# Picosecond/THz acoustic measurements of Semiconductor Devices




Srikanthreddy Devireddy, MPhil

*Thesis submitted to the University of Nottingham,*

*for the degree of Doctor of Philosophy,*

*December 2017.*

# Abstract

This thesis investigates the electron-phonon interactions in fabricated Semiconductor Devices i.e. Schottky Diodes, Quantum Well (QW) embedded *p-i-n* photodiodes, two-dimensional electron gas (2DEG) and two-dimensional hole gas (2DHG) structures all on (311) GaAs substrates. Fast electrical measurements were performed on Schottky diodes fabricated on the (311B) GaAs surface. Optical excitation generates a compressive strain pulse in an Al film which is at the opposite side of the GaAs substrate. Two coherent acoustic phonon modes were generated in the (311B) GaAs substrate: quasi-longitudinal phonons (QLA) and quasi-transverse phonons (QTA). These two modes were detected successfully using the Schottky diode, the dependence of QLA and QTA signals on different applied bias, pump powers and temperatures were investigated.

The dependence of signals on bias reveals that the temporal position of the signals for QLA and QTA moves slightly earlier times with increasing reverse bias because the width of the depletion layer increases with increasing negative bias. The first peak arrival time for QLA phonons in the measured signal moves to earlier times with increasing pump power. This was caused by the nonlinear acoustic properties of the GaAs substrate. Conversely, QTA phonons arrival time was not dependent on pump power which indicates the elastic nonlinear effects are not crucial for QTA signals. Investigation of the temperature dependence reveals that the arrival time changes to later times with increasing temperature because of the decreasing sound velocity with increasing temperature.

The polarity of the experimental signals was compared to the simulated signals of electron-phonon coupling interactions concludes the predominant role of piezoelectric phonon-electric transformation mechanism over deformation potential. Detailed theoretical calculations show the dominance of the piezoelectric mechanism up to frequencies of 70GHz and 250GHz for longitudinal and transverse phonons respectively.

Low dimensional structures *i.e.* Quantum well embedded *p-i-n* photodiode detector (QW-*p-i-n*), two-dimensional electron gas (2DEG) and two-dimensional hole gas (2DHG), fabricated on the (311) GaAs surface, were also investigated as detectors for longitudinal and transverse acoustic signals. The first experimental evidence of high frequency tail in transverse signal is observed using GaAs based QW-*p-i-n* detector. The longitudinal signal confirms the existence of the GHz oscillations, with the most significant occurring 170 GHz, while in transverse acoustic signal we observed a high frequency tail from 300 ps to 800 ps. Fast Fourier transforms (FFT) analysis of this tail shows the existence of high frequency phonons up to 200 GHz. Photocurrent pump-probe measurements was also performed with three different Al film thicknesses (20nm, 30nm and 100nm). Experiments performed with 20nm film thickness clearly shows a weak signal at 250 GHz in the amplitude spectrum which is not observed for 30 nm and 100 nm aluminium films. This observation indicates that the thinner aluminium films can generate higher frequency phonons. The longitudinal and transverse signals were also detected by the 2DHG; for QLA predominantly the peak is negative while for QTA it is positive in contrast to the 2DEG experiments due to the reason that in 2DEG experiments the origin of the signal is due to the decrease in carrier density but for 2DHG the signal is due to the increase in carrier density.

This thesis studies the interaction of subterahertz acoustic phonons with charge carriers with the aim of developing high speed acoustoelectric detectors for subterahertz compressional and shear acoustic waves, and it has been shown that the Schottky diodes are successful in this application.

# Publications and Conferences

**Journal Publications:**

D. Srikanthreddy, B. A. Glavin, C. L. Poyser, M. Henini, D. Lehmann, Cz. Jasiukiewicz, A. V. Akimov, and A. J. Kent, "Piezoelectric response to coherent longitudinal and transverse acoustic phonons in a semiconductor Schottky diode", Physical Review Applied 7, 024014, February 2017.

URL:https://journals.aps.org/prapplied/pd/10.1103/PhysRevApplied.7.024014.

C. L. Poyser, W. B. York, D. Srikanthreddy, B. A. Glavin, T. L. Linnik, R. P. Campion, A. V. Akimov, and A. J. Kent, "Phonon Spectroscopy with Chirped Shear and Compressive Acoustic Pulses", Physical Review Letters, 119, 255502, December 2017.

URL:https://journals.aps.org/prl/pdf/10.1103/PhysRevLett.119.255502

**The work detailed in chapter 4 was selected for a contributed oral presentation at the following conference:**

International Conference "13th School on Acousto-Optics and Applications", SAO2017, 19-23 June 2017, National University of Science and Technology (MISIS), Moscow, Russia, funding gratefully received from the University of Nottingham School of Physics & Astronomy - Kilby Scholarship, and the University of Nottingham Graduate School Travel Prize.

# Acknowledgements

First and foremost, I convey my eternal gratitude, sincere and honest thanks to my Supervisor, Professor. Tony Kent for introducing me to this topic and his valuable time for guiding me throughout my PhD work. His encouragement for deep understanding with a view to gain knowledge has made this work successful. I am deeply indebted to him for timely help to me for the completion of the thesis within the stipulated time. With immense pleasure, I convey my sincere thanks and deep gratitude to Prof. Andrey Akimov for his continuous support and teaching me the laboratory skills and experimental techniques along with efficient and voluminous discussions.

I would also like to extend my thanks to Professor Mohamed Henini and Dr. Richard Campion for growing the samples used throughout this thesis. I am thankful to the School of Physics and Astronomy for allowing me the generous use of facilities in the department. Thanks also to the School of Physics and Astronomy technical staff, especially Jas Chauhan and Dave Taylor for their advice and help in clean room. Chris Pallender and Dave Holt for often providing liquid helium at short notice.

I would like to thank all the THz Acoustics group members, both past and present – Eric Young, Sarah Heywood, William York, Josh Whale, Daniel Moss and Ryan Beardsley. Special thanks must be given to Dr. Caroline Poyser for her continuous help, especially in the early days for revising me the clean room processing techniques and indispensable assistance throughout my PhD work.

I gratefully acknowledge the camaraderie and encouragement from my friends Carl Andrews, Mohammed, Navjot, Michal, Tshaiya Devi and Prasujya Gogoi, especially Debi Prasad Pattnaik. I am thankful to all my tea room friends and each person who has supported me during my PhD work.

Finally, my parents for their blessings and to my life Mentor – brother, Dr. Rakesh Reddy who has always been there for me; without you I wouldn't have been able to reach this doctorate, and for that I will be eternally grateful.

# Contents

**Abstract** i

**Publications and Conferences** iii

**Acknowledgements** iv

**List of Figures** x

**List of Tables** xxii

**1 Introduction** 1

1.1 PicosecondAcoustics……..1

1.2 Low symmetry planes of (311) GaAsproperties……4

1.3 Electron-phonon coupling mechanisms…….8

1.3.1 Deformation potential coupling…….9

1.3.2 Piezoelectric potential coupling…….9

1.3.3 Pekar Mechanism……10

1.3.4 Ripple Effect……. 10

1.4 Motivation for work and Thesis Outline……..11

**2 Background** 14

2.1 Strain pulses…… 14

2.1.1 Generation…… 15

2.1.2 Propagation…….. 18

2.1.3 Detection……. 21

2.2 Strain Sensitive Devices……21

2.2.1 *p-n* junction…… 22

2.2.2 Schottky Diode…….. 26

2.2.3 *p-i-n* Diode…….. 30

2.2.4 Quantum Well (QW) embedded *p-i-n* photodiode detector……. 34

**3 Experimental Details 39**

3.1 Microfabrication Processes ..... 39

3.1.1 Cutting and Cleaning ..... 39

3.1.2 Mechanical polishing ..... 40

3.1.3 Photolithography and Wet etching..... 42

3.1.4 Contact Formation and Annealing ..... 45

3.1.5 Sample Packaging ..... 46

3.1.6 Sample wire bonding ..... 47

3.2. Sample Structures..... 48

3.2.1 NU927 ..... 48

3.2.2 RC34 ..... 49

3.2.3 RC80 ..... 51

3.2.4 NU2080 ..... 52

3.2.5 NU1074 ..... 55

3.3. Lasers…….56

3.3.1 Health and Safety……..56

3.3.2 Amplifier…….. 57

3.3.3 Oscillator…….. 57

3.4 Cryostat ..... 57

3.4.1 Bath Cryostat…… 58

3.4.2 Continuous Flow Cryostat……. 59

3.5 Transport measurements…… 59

3.6 Fast electrical measurements…… 63

3.7 Photocurrent pump-probe measurements…….65

**4 Piezoelectric response to coherent longitudinal and transverse acoustic phonons in a semiconductor Schottky diode 69**

4.1 Introduction…….. 69

4.2 NU927 Current-Voltage characteristics……... 73

4.3 Interaction of coherent transverse and longitudinal acoustic phonons with electrons in a (311 B) GaAs Schottky diode……75

4.3.1 Electrical detection of QLA and QTA Coherent Phonons……..81

4.3.2 Dependence of QLA and QTA Signals on Bias…… ….84

4.3.3 Dependence of QLA and QTA Signals on Pump Laser Power……...87

4.3.4 Dependence of QLA and QTA Signals on Temperature…….90

4.4 Theoretical Analysis of coupling mechanisms to the electrical response of the Schottky contact……93

4.5 (311 A) GaAs Schottky diode Results……102

4.6 Conclusions……108

**5 Electron-Phonon Interactions in Two-Dimensional Structures: Quantum Wells, 2DEGs/2DHGs 110**

5.1 Introduction…… 110

5.2 Photocurrent Measurements ……111

5.3 Longitudinal and Transverse Phonons detection by Quantum Well (QW) embedded *p-i-n* photodiode detector…… 114

5.3.1 Longitudinal acoustic signal detection with various Aluminium film thickness……119

5.3.2 Dependence of Longitudinal acoustic signal on Bias…… 122

5.3.3 Dependence of Longitudinal acoustic signal on Pump Laser Power. 123

5.3.4 Transverse acoustic signal detection with various Aluminium film thickness…….125

5.4 Longitudinal acoustic signal detection using *p-i-n* device embedded with InGaAs QW……129

5.5 Fast acoustic-electric transformation of Longitudinal and Transverse phonons using 2DEG and 2DHG structures……..131

5.5.1 Current-Voltage characteristics of NU2080/NU1074…….132

5.5.2 Electrical detection of QLA and QTA Coherent Phonons by 2DEG.134

5.5.3 Dependence of QLA and QTA signals on Bias Magnitude……137

5.5.4 Laser Power Dependence on QLA and QTA signals……..142

5.5.5 Preliminary work on 2DHG structure detecting acoustic signals……144

5.6 Conclusions ..... 149

**6 Conclusions and Future Work** **152**

6.1 Conclusions …….. 152

6.2 Future Research…… 155

6.2.1 Investigation of smaller size Schottky Devices to detect high frequency acoustic phonons experimentally…… 155

6.2.2 Investigation of shear acoustic modes using *p-i-n* device embedded with InGaAs QW…… 156

6.2.3 Fast electrical measurements on 2DEG structure processed in different orientation…… 157

**Bibliography** **160**

# List of Figures

**Figure 1.1:** Schematic of the conventional unit cell of gallium arsenide (GaAs) in its zinc-blende structure. ..... 5

**Figure 1.2:** Schematic representation of (311) A and (311) B planes of GaAs. ..... 7

**Figure 2.1:** Calculated temporal shape of the initial strain pulse generated by using equation 2.3, and the pulse is bipolar in shape using values given in table 2.1. ..... 17

**Figure 2.2:** Simulated temporal evolution of an initial strain pulse (A), showing shockwave development (B) and soliton formation (C). The arrows marked on the initial strain pulse show the relative velocities of different sections of the strain pulse. Traces B and C are offset vertically for clarity. ..... 19

**Figure 2.3:** (a) Uniformly doped *p*- and *n*-type semiconductors before the junction is formed. (b) The electric field in the region and the energy band diagram of a *p*-*n* junction in thermal equilibrium (V = 0). ..... 23

**Figure 2.4:** Schematic of p-n junction band diagram. $E_F$ is the Fermi energy, $E_V$ is the valence band energy, $E_C$ is the conduction band energy and $V_{bi}$ is the inbuilt potential. (a) shows the junction when a forward bias $V_F$ is applied and (b) shows the junction when reverse bias $V_R$ is applied. ..... 25

**Figure 2.5:** Current-voltage characteristic of a typical *p*-*n* junction. ..... 25

**Figure 2.6:** Schematic energy band diagrams of an *n*-type Schottky diode with $e\Phi_m > e\Phi_s$, where $e\Phi_{m,s}$ is the work function of the metal or semiconductor, respectively. When the metal and the semiconductor are brought into contact the Fermi levels must align at thermal equilibrium. This leads to bending of the energy bands in the semiconductor by an amount $eV_0$, the formation of a potential barrier $e\Phi_B$ and the formation of a depletion region W. $E_{Fm,s}$ are the Fermi levels in the metal and the semiconductor when separate, whereas $E_F$ is the Fermi level of the Schottky diode at

equilibrium. $E_{C,V}$ are the conduction and valence bands in the semiconductor and $e\chi$ is the electron affinity of the semiconductor…… 28

**Figure 2.7:** Schematic energy band diagrams of an *n*-type Schottky diode under different biasing conditions i.e. unbiased condition, forward bias and reverse bias. A bias applied across the Schottky diode changes the size of the contact potential and so changes the number of electrons that can diffuse from the semiconductor into the metal. ..... 29

**Figure 2.8:** Schematic of energy band structure of GaAs in the absence of strain (left), and (right) under compressive uniaxial [111] strain. The conduction band and valence band depicted at the top and bottom of the figure, respectively. In unstrained GaAs (left), the two-degenerate light-hole (LH) and heavy-hole (HH) valence bands (J = 3/2) are separated from CB by the energy $E_0$, whilst the split-off (SO) band (J = ½, $m_J = \pm 1/2$) transition to CB is separated by an energy $E_0+\Delta_0$. Splitting of the degenerate HH and LH bands ($m_J = \pm 1/2$ and $m_J = \pm 3/2$, respectively) happens under applied uniaxial compressive strain, whilst the hydrostatic component increases valence band – conduction band transition energies. Note that similar observations were made for stress along both [100] and [110] directions, and that the polarisations refer to incident light used in piezoelectroreflectance measurements. ..... 33

**Figure 2.9:** Schematic of photocurrent generation in a *p*-*i*-*n* photodiode incorporating a QW at its centre in the intrinsic region. A reverse voltage across the device V results in an energy shift of *e*V and the device is illuminated by a photon of energy $\sim\omega$ on the *p*-doped side. $E_0$ represents the separation of the energy levels in the QW. ..... 35

**Figure 2.10:** Schematic to demonstrate how the strain is detected by quantum well embedded *p*-*i*-*n* device. The figure on the left demonstrates the processes in the QW, while the figure on the right demonstrates the size of the photocurrent varies for the three different scenarios, *i.e.* (a) represents no strain, (b) represents compressive strain and (c) represents tension. The light blue represents the laser energy and the black line represents the energy level in the well. ..... 37

**Figure 3.1:** Polishing setup: Left, polishing system, Right, a polishing jig with weights. ..... 41

**Figure 3.2:** Polishing jig with disc mount for sample. ..... 41

**Figure 3.3:** Optical alignment system designed to ensure surfaces are parallel to avoid the stretching of the phonon pulse by aligning the sample beam (dotted) to the reference beam (solid red line), which are caused by reflections from the sample surface and glass plate, respectively. ..... 42

**Figure 3.4:** (a) Optical access devices, patterned using the "Sheffield" mask. (b) Ground contact produced using Sheffield bottom mask. (c) The Robin Hood photomask set used to produce electrical mesas with no optical access. (d) The NU1080 photomask set used to produce 2DEG and 2DHG structures. ..... 44

**Figure 3.5:** Picture of sample holder with a sample attached using GE varnish..... 47

**Figure 3.6:** Device bonded with 25μm diameter Aluminium wire. ..... 48

**Figure 3.7:** Schematic of NU927 layer structure. Silicon doping concentration of 1.5 μm-thick n-GaAs layer is 1 x $10^{17}$ $cm^{-3}$. The Schottky contact was bonded to central SMA pin whereas Ohmic contact to ground plate of the sample holder. ..... 49

**Figure 3.8:** Schematic of RC34 layer structure. All contact layers are doped to $10^{18}$ $cm^{-3}$, p-type contact layers are Si doped while n-type contact layers are Te doped. All AlGaAs layers feature 33% Aluminium. ..... 50

**Figure 3.9:** Schematic of RC80 Layer structure. All contact layers are doped to $2x10^{18}$ $cm^{-3}$, both p-type and n-type contact layers are Si doped. The buffer layers between the substrate and the active device are required for a high-quality MBE growth but do not have a significant effect on the experiments. ..... 52

**Figure 3.10:** Layer structure of NU2080 wafer. GaAs/AlGaAs heterostructure, which forms a two-dimensional electron gas (2DEG) at the material interface. ..... 53

**Figure 3.11:** Schematic of Two-Dimensional Electron Gas energy band diagram based on GaAs/AlGaAs heterostructure layers. The red portion represents the 2DEG region..... 54

**Figure 3.12:** Processed 2DEG sample on the sample holder with indium bonding. 54

**Figure 3.13:** Schematic of Two-Dimensional Hole Gas energy band diagram based on GaAs/AlGaAs heterostructure layers. The Valence Band is shifted upwards to cross the Fermi level energy to cause the creation of 2DHG region represented by red portion. ..... 55

**Figure 3.14:** Layer structure of NU1074 wafer. GaAs/AlGaAs heterostructure, which forms a two-dimensional hole gas (2DHG) at the material interface. Silicon doping concentration of n-GaAs layer is 5 x $10^{17}$ $cm^{-3}$. ..... 56

**Figure 3.15:** Screen shot of current voltage graphical user interface..... 61

**Figure 3.16:** Flow chart for current voltage graphical user interface..... 62

**Figure 3.17:** Experimental Setup for fast electrical measurements. The electrical connections between the Cryostat and Oscilloscope are shown in figure 3.18. ..... 64

**Figure 3.18:** Schematic of circuit used for Fast electrical measurements..... 65

**Figure 3.19:** Experimental Setup for *p-i-n* experiments. The pump beam path is shown by a dotted line and the probe by a solid line. The electrical connections between the Cryostat and Oscilloscope are shown in this figure 3.20..... 67

**Figure 3.20:** Schematic of circuit used for *p-i-n* experiments. The device was biased and electrically probed using the given circuit, in which the signal was fed through a 20x gain high impedance amplifier and the change in photocurrent was measured through a Stanford Research Systems SR830 DSP Lock-In Amplifier referenced to the chopper. ..... 68

**Figure 4.1:** (a) Electron band diagram of the Schottky diode (degenerate) under equilibrium conditions (i.e. no strain); (b) the schematic demonstration of the effect of the strain pulse incident on the edge of the depletion layer at distance $xd$ from the GaAs/Au interface. (Figure adapted from D. M. Moss et al. [145]). ..... 72

**Figure 4.2:** Current voltage characteristics of the Schottky diode at T=5K. ..... 74

**Figure 4.3:** Temperature dependent I-V characteristics of the Schottky diode at various temperatures *i.e.* (20K, 40K, 80K, 100K, 160K, 200K & 300K). ..... 74

**Figure 4.4:** Schematic of the experiment with coherent QLA and QTA phonons; solid and dashed arrows indicate the direct and reflected phonon fluxes detected by the Schottky contact respectively. ..... 77

**Figure 4.5:** Electrical response measured for QLA signal in a full temporal range, .... with a bias of $V_B$ = 0V at pump fluence $W$=4 mJ/cm$^2$. ..... 82

**Figure 4.6:** Electrical response measured for QTA signal in a full temporal range, with a bias of VB = 0V at pump fluence W=4 mJ/cm2. ..... 83

**Figure 4.7:** (a) Phonon induced signals measured at pump fluence $W$=4 mJ/cm$^2$ for various bias voltages $V_B$ for QLA phonons. (b) Phonon induced signals measured at pump fluence $W$=4 mJ/cm$^2$ for various bias voltages $V_B$ for QTA phonons..... 85

**Figure 4.8:** First peak position dependence on applied bias $V_B$ for QLA phonons. The squares are the experimental data and the red line is a theoretical fit to the experimental data. ..... 86

**Figure 4.9:** First peak position dependence on applied bias VB for QTA phonons. The squares are the experimental data and the red line is a theoretical fit to the experimental data. ..... 86

**Figure 4.10:** Phonon induced signals measured at zero bias, $V_B$=0V with different pump fluences for QLA phonons. The inset shows negative peaks extracted to layers for clarity to observe the first peak temporal shift to earlier times with the increase of *W* for QLA phonons. ..... 88

**Figure 4.11:** Phonon induced signals measured at zero bias, $V_B$=0V with different pump fluences for QTA phonons. The inset shows signals extracted to layers for clarity, vertical dotted line indicates the absence of the first peak temporal shift to earlier times with the increase of *W* for QTA phonons. ..... 89

**Figure 4.12:** First peak position dependence on optical excitation densities *W* for QLA phonons. The squares are the peak position obtained from experimental signals and the red line is a theoretical fit to the experimental data. ..... 89

**Figure 4.13:** Experimentally measured signals at four different temperatures *T* (5K, 80K, 160K and 289K) for QLA phonons. ..... 91

**Figure 4.14:** Experimentally measured signals at four different temperatures *T* (5K, 80K, 160K and 289K) for QTA phonons. ..... 91

**Figure 4.15:** First peak position dependence on different temperatures *T* for QLA phonons. The squares are the peak position obtained from experimental signals and the red line is a theoretical fit to the experimental data. ..... 92

**Figure 4.16:** First peak position dependence on different temperatures *T* for QTA phonons. The squares are the peak position obtained from experimental signals and the red line is a theoretical fit to the experimental data. ..... 92

**Figure 4.17:** Calculated strain waveforms (a) for QLA, and (b) QTA phonons generated in an Al film with pump fluence *W*~1 mJ/cm$^2$. *Source*: ref. Opt. Express 21, 16473 (2013). ..... 96

**Figure 4.18:** The theoretical signals (a) for QLA, and (b) QTA phonons taking into the account of piezoelectric (PE) or deformation potential (DP) in the Schottky diode for two widths of depletion layers and corresponding bias voltage. ..... 99
**Figure 4.19:** The signal after 4-GHz-cutoff low-pass filtering of the calculated signal shown in figure 4.18, (a) for QLA, and (b) QTA phonons at zero bias with depletion layer width 100nm..... 101

**Figure 4.20:** I-V characteristics of the (311A) Schottky diode at T=5K. ..... 103

**Figure 4.21:** Electrical response measured for Schottky diodes fabricated on (311A) GaAs surface in a full temporal range with a bias of $V_B$ = 0V, (a) for QLA, and (b) QTA phonons. ..... 104

**Figure 4.22:** Phonon induced signals measured at pump fluence $W$=4 mJ/cm$^2$ at zero bias, $V_B$=*0*V for QLA phonons (second spike enlarged). Arrow indicates the change of polarity(positive), with respect to (311B) surface. ..... 105

**Figure 4.23:** Phonon induced signals measured at pump fluence W=4 mJ/cm2 at zero bias, VB=0V for QTA phonons (third spike enlarged). Arrow indicates the change of polarity(negative), with respect to (311B) surface. ..... 105

**Figure 4.24:** Phonon induced signals measured for Schottky diodes fabricated on (311A) GaAs surface at pump fluence $W$=4 mJ/cm$^2$ with different bias voltages $V_{B,}$ (a) for QLA, and (b) QTA phonons. ..... 106

**Figure 4.25:** Phonon induced signals measured for Schottky diodes fabricated on (311A) GaAs surface at zero bias, $V_B$=0V with different pump fluences (a) for QLA, and (b) QTA phonons..... 107

**Figure 5.1:** I-V measurements of the RC34 *p-i-n* device when illuminated by continuous-wave laser light at two laser energies and in the dark. ..... 113

**Figure 5.2:** I-V measurements of the RC80 *p-i-n* device when illuminated by continuous-wave laser light at three laser energies and in the dark. ..... 113

**Figure 5.3:** Longitudinal acoustic signal detected using a *p-i-n* device on a (311) GaAs substrate. Feature (a) represents the strain pulse reaching the quantum well for the first time, feature (b) represents the strain passing through the QW in the detector a second time after reflecting at the surface. ..... 115

**Figure 5.4:** Schematic showing the origin of the strain pulses shown in figure 5.3. The path (a) represents the strain pulse reaching the quantum well for the first time, path (b) represents the strain passing through the QW in the detector a second time after reflecting at the surface. ..... 117

**Figure 5.5:** Amplitude spectrum obtained from the signal shown in figure 5.3 by Fast Fourier Transforms (FFT). Black line represents amplitude spectrum of full 400 ps signal, red represents the amplitude spectrum of the tail from 131 ps to 390 ps. 118

**Figure 5.6:** Longitudinal acoustic signal detected using a *p-i-n* device on a (311) GaAs substrate, black line represents 446µm thickness and red represents 160µm thickness. (Figure taken from C. L. Poyser *et al* [67]). ..... 119

**Figure 5.7:** Longitudinal acoustic signal detected using a *p-i-n* device on a (311) GaAs substrate with 20 nm Aluminium film. Feature (a) represents the strain pulse reaching the quantum well for the first time, feature (b) represents the strain passing through the QW in the detector a second time after reflecting at the surface. ..... 120

**Figure 5.8:** Longitudinal acoustic signal detected using a *p-i-n* device on a (311) GaAs substrate with newly evaporated 30 nm Aluminium film. Feature (a) represents the strain pulse reaching the quantum well for the first time, feature (b) represents the strain passing through the QW in the detector a second time after reflecting at the surface. ..... 121

**Figure 5.9:** Longitudinal acoustic signal detected using a *p-i-n* device on a (311) GaAs substrate with 100 nm Aluminium film. ..... 121

**Figure 5.10:** Longitudinal acoustic signal detected using a *p-i-n* device on a (311) GaAs substrate at two different bias voltages. Feature (a) represents the strain pulse reaching the quantum well for the first time, feature (b) represents the strain passing through the QW in the detector a second time after reflecting at the surface. ..... 122

**Figure 5.11:** Longitudinal acoustic signal detected using a *p-i-n* device on a (311) GaAs substrate at various pump densities *W*. Feature (a) represents the strain pulse reaching the quantum well for the first time, feature (b) represents the strain passing through the QW in the detector a second time after reflecting at the surface. The vertical dotted line shows the absence of arrival time shift of the incident and reflected strain pules with increasing *W*. ..... 123

**Figure 5.12:** Photocurrent changes when the incident strain pulse is passing the quantum well of the *p-i-n* device for various pump densities *W* at bias $V_B$= 1V. .... 124

**Figure 5.13:** The dependence of the changes of photocurrent amplitude ΔP (for definition see figure 5.12) on pump density *W*. ..... 125

**Figure 5.14:** Transverse acoustic signal detected using a *p-i-n* device on a (311) GaAs substrate. Feature (a) represents the strain pulse reaching the quantum well for the first time, feature (b) represents the strain passing through the QW in the detector a second time after reflecting at the surface. ..... 126

**Figure 5.15:** High frequency tail of the transverse acoustic signal from 300 ps to 800 ps time window. ..... 126

**Figure 5.16:** Amplitude spectrum obtained from the Fast Fourier Transforms (FFT) of the temporal signal shown in figure 5.14. ..... 127

**Figure 5.17:** Amplitude spectrum obtained from the Fast Fourier Transforms (FFT) of the high frequency tail shown in figure 5.8. Black line represents the time window from 328 ps to 478 ps, red line shows the time window from 478 ps to 628 ps and blue line represents the time window from 628 ps to 778 ps. ..... 128

**Figure 5.18:** Transverse acoustic signal detected using a *p-i-n* device on a (311) GaAs substrate with 100 nm Aluminium film. Feature (a) represents the strain pulse reaching the quantum well for the first time, feature (b) represents the strain passing through the QW in the detector a second time after reflecting at the surface. ..... 129

**Figure 5.19:** The longitudinal acoustic signal detected using a *p-i-n* device fabricated on RC 80 of (311) GaAs substrate with 30 nm Aluminium film. Feature (a) represents the strain pulse reaching the quantum well for the first time, feature (b) represents the strain passing through the QW in the detector a second time after reflecting at the surface. ..... 130

**Figure 5.20:** Longitudinal acoustic signal detected using a *p-i-n* device fabricated on RC 80 of (311) GaAs substrate with 100 nm Aluminium film. Feature (a) represents the strain pulse reaching the quantum well for the first time, feature (b) represents the strain passing through the QW in the detector a second time after reflecting at the surface. ..... 131

**Figure 5.21:** Current voltage characteristics of the two-dimensional electron gas structure at temperature T=5K. ..... 133

**Figure 5.22:** Current voltage characteristics of the two-dimensional hole gas structure at temperature T=5K. ..... 133

**Figure 5.23:** Schematic of the 2DEG structure displaying the excitation spots at the Al film were displaced at some angle relative to the device. (a) shows pump spot for detecting QLA signal while (b) shows pump spot for detecting QTA signal. ..... 135

**Figure 5.24:** Electrical response measured from 2DEG structure in a full temporal range, consists of both QLA and QTA phonons with a bias of VB = 400 mV at pump fluence W=4.8 mJ/cm2. ..... 135

**Figure 5.25:** Electrical response measured from 2DEG structure in a full temporal range, for QLA phonons with a bias of $V_B$ = 400 mV at pump fluence $W$=4.8 mJ/cm$^2$. ..... 136

**Figure 5.26:** Electrical response measured from 2DEG structure in a full temporal range, for QTA phonons with a bias of $V_B$ = 400 mV at pump fluence $W$=4.8 mJ/cm$^2$. The vertical dotted red arrow indicates the presence of QLA phonon mode..... 137

**Figure 5.27:** Electrical response measured from 2DEG structure at pump fluence $W$=4 mJ/cm$^2$ for various positive bias voltages $V_B$ for QLA phonons..... 138

**Figure 5.28:** Electrical response measured from 2DEG structure at pump fluence $W$=4 mJ/cm$^2$ for various negative bias voltages $V_B$ for QLA phonons..... 138

**Figure 5.29:** Electrical response measured from 2DEG structure at pump fluence $W$=4 mJ/cm$^2$ for various positive bias voltages $V_B$ for QTA phonons..... 139

**Figure 5.30:** Electrical response measured from 2DEG structure at pump fluence $W$=4 mJ/cm$^2$ for various negative bias voltages $V_B$ for QTA phonons..... 139

**Figure 5.31:** Schematic to demonstrate the origin of 2DEG signals. (a) represents no strain, (b) with strain, the red colour curve indicates the tunnelling of charges out of the channel while the black arrow represents the decrease in carrier density. (c) Dependence of electrical response measured from 2DEG structure at pump fluence $W$=1.6 mJ/cm$^2$ for QLA phonons on bias. The inset shows current voltage characteristics of the two-dimensional electron gas structure at temperature T=5K for comparison. ..... 141

**Figure 5.32:** Electrical response measured from 2DEG structure at bias, $V_B$=400 mV with different pump fluences for QLA phonons. ..... 143

**Figure 5.33:** Electrical response measured from 2DEG structure at bias, $V_B$=400 mV with different pump fluences for QTA phonons. ..... 143

**Figure 5.34:** First peak position dependence on optical excitation densities $W$ for QLA phonons. The squares are the peak position obtained from experimental signals and the red line is a theoretical fit to the experimental data..... 144

**Figure 5.35:** Electrical response measured from 2DHG structure in a full temporal range, consists of both QLA and QTA phonons with a bias of $V_B$ = 100 mV at pump fluence $W$=4.8 mJ/cm$^2$. ..... 145

**Figure 5.36:** Electrical response measured from 2DHG structure at pump fluence $W$=4.8 mJ/cm$^2$ for various positive bias voltages $V_B$ for QLA phonons..... 146

**Figure 5.37:** Electrical response measured from 2DHG structure at pump fluence $W$=4.8 mJ/cm$^2$ for various positive bias voltages $V_B$ for QTA phonons..... 147

**Figure 5.38:** Schematic to demonstrate the origin of 2DHG signals. The red colour curve indicates the tunnelling of holes while the black arrow represents the increase in carrier density..... 148

**Figure 5.39:** Electrical response measured from 2DHG structure at bias, $V_B$=100 mV with different pump fluences for QLA phonons. ..... 148

**Figure 5.40:** Electrical response measured from 2DHG structure at bias, $V_B$=100 mV with different pump fluences for QTA phonons. ..... 149

**Figure 6.1:** Schematic of NU927 sample structure modified to fabricate air-bridge Schottky devices..... 156

**Figure 6.2:** (a) Schematic of 2DEG sample investigated in chapter 5. (b) Schematic of 2DEG sample fabricated in different orientation..... 158

**Figure 6.3:** Electrical response measured from 2DEG structure fabricated in different orientation, consists of both QLA and QTA phonons with a bias of $V_B$ = 500 mV at pump fluence $W$=4.8 mJ/cm$^2$. ..... 158

# List of Tables

Table 1.1: Referenced general properties of gallium arsenide at Room Temperature.. ..... 6

Table 2.1: Parameters used for the generation of the temporal shape of the initial strain pulse in GaAs substrate. ..... 17

Table 4.1: Turn-On voltage of Schottky diode at different temperatures. ..... 75

Table 4.2: Different arrival timings of the multiple reflections in the GaAs substrat. ..... 84

# Chapter 1

# Introduction

Laser picosecond acoustics has numerous applications in material characterization and in understanding light- matter interactions. Generation and detection of longitudinal acoustic phonon pulses in thin films, multilayer structures and nanostructures has been reported in various experiments [1–10]. Acoustic waves with frequency from 10 GHz to 1 THz (~5-500 nm) reveal the details of bonding, sound velocities, and thickness of film. These techniques are convenient, non-destructive and very precise [5, 6].

The work presented in this thesis investigates the effects of picosecond/THz acoustic measurements on (311) GaAs based semiconductor devices, and their potential applications. Devices fabricated on low symmetry planes of GaAs, such as (311), provide the opportunity for the generation of coherent transverse phonons exists, due the different symmetry considerations of the crystal in this orientation. Transverse acoustic waves would have advantages for use in picosecond acoustic experiments due to their shorter wavelength compared to longitudinal waves. This chapter provides a general description of picosecond acoustics with an overview of some previous work on semiconductor devices. It will be followed by the description of the properties of low symmetry planes of GaAs. A summary of different electron-phonon coupling mechanisms that are relevant when considering the effects of strain on the electronic properties of a semiconductor devices is presented. The concluding section of this chapter explains the motivation behind the present research, and briefly outlines the structure of the thesis.

### 1.1 Picosecond Acoustics

Picosecond acoustics is a pump-probe technique in which an ultrashort optical pump pulse is partially absorbed by a thin metallic transducing layer, deposited onto the surface of the sample, and launches by “instantaneous” thermal expansion a

longitudinal acoustic wave packet with a characteristic spectrum extending in the 40–400 GHz region.

The acoustic pulse then travels inside the sample and its motion is monitored by a delayed optical probe pulse with wavelength $\lambda_{pr}$. The probe pulse is reflected by the strain wave through a (stimulated) Brillouin scattering process, i.e., interacting with a single phonon frequency $v=c*q/(2\pi) = 2n*c*cos(\theta)/(\lambda_{pr})$, where c is the sound velocity, q the acoustic wave vector, n($\lambda_{pr}$) the refractive index of the medium and θ the scattering angle. The Brillouin scattered intensity interferes with the portion of probe beam reflected by the fixed surface of the sample, leading to time-dependent oscillations with a periodicity T set by the Bragg condition: $T=\lambda_{pr}/(2n*c*cos(\theta))$, i.e., corresponding to the period of the phase-matched acoustic phonon. The periodicity and damping of such oscillations then gives direct access to acoustic parameters such as sound velocity and attenuation.

Picosecond acoustics was initially used as a non-destructive testing technique for thin films, calculations of acoustic velocities in materials, and the determination of various phenomena, such as electron-phonon scattering rates. In these experiments a thin film is pumped with ultrafast laser, and the changes in optical reflectivity is probed due to the phononic effects [11-13]. Acoustic phenomena such as phonon dispersion [14], were examined by superlattices [15-17] as an alternative to thin films for the generation and detection of acoustic pulses.

Investigation of the use of phonons to modulate electronic properties in existing devices was performed by many researchers; Heat pulse-induced conductivity measurements in silicon metal-oxide semiconductor field-effect transistors were explored by Kent et al. [18]. The possibility of thermally generated, non-equilibrium acoustic phonon-assisted tunnelling within double barrier structures was experimentally demonstrated by Ouali et al [19]. The ability to control charge transport through devices using optically transduced coherent phonons was later revealed by Fowler et al. [20] where the experimental setup is different from other experiments because the system was optically pumped and probed electrically.

The ultrafast gating of photocurrent in a quantum well embedded *p-i-n* diode using coherent acoustic wavepackets was demonstrated by Moss et al. [21]. In another paper, the same authors explained the possibility of using such a *p-i-n* diode as a hypersonic detector [22]. In the same year, ultrafast control of the device's electrical properties by strain pulses using Schottky diodes was investigated [23]. These general applications of strain in semiconductor devices has opened different paths for further research.

The advanced technology of crystal growth allows the possibility to deposit high quality GaAs/AlAs superlattices along high index growth directions, such as [011], [211], and [311] differing from the conventional [100] growth direction. Although (100) GaAs substrates are widely used for experimental picosecond acoustics, generation and detection of shear acoustic waves was not observed. However, using high-index substrates/low symmetry surfaces of a semiconductor material, i.e. (311) GaAs substrates, the generation and detection of both compressive and shear acoustic modes by ultrafast lasers becomes possible [24]. The superlattices grown along [311] direction has the interesting feature of reduced symmetry as compared with the tetragonal (100)-oriented structures. As a result, these structures are optically anisotropic in the plane of the superlattice layers.

Coherent generation and detection of monochromatic acoustic phonons in the terahertz range plays significant role in phonon spectroscopy of nanostructures and high-speed optical modulation applications. Coherent generation of longitudinal (LA) acoustic phonons in GaAs/AlAs superlattices has been investigated by various researchers [25-28] using ultrafast optical excitation. Coherent transverse phonons (TA) are not observed directly in multilayers grown on the high symmetry [100] crystal direction. Coherent generation and detection of TA phonons in bulk GaAs has been demonstrated by O. Matsuda et. al. [29]. This involved ultrafast excitation of GaAs crystals cut so that the excitation laser was parallel to the low symmetry [411] direction. The disadvantage of using bulk material is that the accessible TA phonon frequencies are low, 27.4GHz [29], because the acoustic dispersion is not folded. Hurley et. al [30] demonstrated that coherent TA phonons could be generated by reflection of an LA phonon pulse from an interface with an anisotropic crystal. Zone

folded acoustic modes have been studied [31-34] using Raman scattering for GaAs/AlAs multilayers grown along [012], [311] and [211] crystal directions. In these papers, acoustic phonon modes were observed for each of the LA and the two TA polarisations which were predicted to be Raman active.

Popovic et. al [35] performed Raman measurements on GaAs/AlAs multilayers grown along the [111] direction. Longitudinal acoustic phonons were observed but TA modes were not, even though they were predicted to be Raman active. The authors suggest that the TA modes were not observable because the elastically scattered light signal was too strong at the TA mode frequencies. R. N. Kini et. al [36] showed the first evidence of coherent generation and detection of high frequency monochromatic TA phonons in a low-symmetry periodic multilayer structure. Coherent phonons at ~400GHz were generated by ultrafast excitation of a GaAs/AlAs periodic multilayer structure grown along the [311] direction on a GaAs substrate. In phonon spectroscopy studies, shear modes are more sensitive to defects and these modes are important for studying piezoelectric electron-phonon interactions since LA phonons couple via both piezoelectric and deformational potential interactions.

### 1.2 Low symmetry planes of (311) GaAs properties

The work presented in this thesis is entirely focused on devices processed on (311) gallium arsenide substrate. This section briefly covers some general properties of GaAs with more emphasis on the properties of (311) GaAs. The (311) GaAs suitability for the formation of heterostructures, and its advantages over the more commonly used (100) GaAs substrates will be discussed in brief. Gallium arsenide is a type III-V semiconductor composed of the element gallium (Ga) from column III and the element arsenic (As) from column V of the periodic table of the elements. The material has high electron mobility and a high saturated electron velocity compared to silicon. GaAs was first created by Victor Goldschmidt and reported in 1929, but the first reported electronic properties of III–V compound as semiconductors did not appear until 1952 [ 37]. The GaAs crystal is composed of two sub-lattices, each face centred cubic (fcc) and offset with respect to each other

by half the diagonal of the fcc cube [38]. This crystal configuration is known as cubic sphalerite or zinc blende structure as shown in figure 1.1.

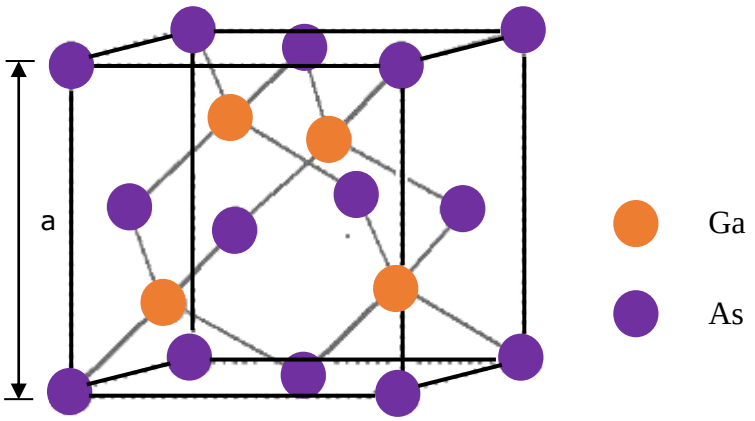



**Figure 1.1:** Schematic of the conventional unit cell of gallium arsenide (GaAs) in its zinc-blende structure.

Some of the general material characteristics and properties of GaAs at room temperature is listed in Table 1.1 [39,14]. Analyses of the structure and more detailed properties of Gallium Arsenide can be found in many other references [40-45].

| **Property** | **Value** | **Units** |
|---|---|---|
| Lattice Constant (a) | 5.65 | (Å) |
| Density | 5.32 | ($g/cm^3$) |
| Atomic Density | $4.5x10^{22}$ | (atoms/ $cm^3$) |
| Molecular weight | 144.64 | (g/mol) |
| Bulk Modulus | $7.55x10^{11}$ | (dyn/ $cm^2$) |
| Sheer Modulus | $3.26\ x10^{11}$ | (dyn/ $cm^2$) |
| Coefficient of thermal expansion | $5.8\ x10^{-6}$ | ($K^{-1}$) |
| Specific Heat | 0.327 | (J/g-K) |
| Thermal Diffusivity | 0.31 | ($cm^2\ s^{-1}$) |
| Relative Permittivity | 12.9 | ----- |
| Band Gap | 1.42 | (eV) |
| Electron Mobility (undoped) | 8500 | ($cm^2\ V^{-1}s^{-1}$) |

| | | |
|---|---|---|
| Hole Mobility (undoped) | 400 | ($cm^2\ V^{-1}s^{-1}$) |
| Melting Point | 1238 | (ºC) |
| Effective Mass $m^*$ | $5.74\ x10^{-32}$ | (kg) |
| Longitudinal Acoustic Velocity | 4730 | ($ms^{-1}$) |
| Transverse Acoustic Velocity | 3350 | ($ms^{-1}$) |
| Dispersion Parameter in [100] orientation | $7.40\ x10^{-18}$ | ($m^3s^{-1}$) |
| Second Order elastic constant in [100] orientation | 119 | GPa |

**Table 1.1:** Referenced general properties of gallium arsenide at Room Temperature.

The amount of energy required for an electron to move from the Valence Band (VB) to the Conduction Band (CB) referred as "energy band gap" depends on the temperature, the semiconductor material, and the material's purity and doping concentration. GaAs is a direct band gap semiconductor, which means that the minimum of the conduction band is directly over the maximum of the valence band. Transitions between the valence band and the conduction band require only a change in energy, and no change in momentum, unlike indirect band-gap semiconductors such as silicon. This property of GaAs makes it a very useful material for the manufacturing of light emitting diodes and semiconductor lasers, since a photon is emitted when an electron changes energy levels from the conduction band to valence band. Alternatively, an incident photon can excite an electron from the valence band to the conduction band, allowing GaAs to be used in photo detectors.

Due to the excellent lattice matching between the GaAs and AlAs materials; GaAs-based heterostructures are generally processed with AlAs and intermediary Al alloys of $Al_xGa_{1-x}As$. AlAs has relatively much larger band gap of 2.16 eV compared to GaAs at room temperature; however, their lattice constants differ only by $8\ x\ 10^{-3}$ Å (= 0.14 %) [44] which allows the formation of excellent material interfaces that reduce both discontinuities and defects within the overall crystal. This is utilized herein to form the various nanostructures that are modulated

by incoming strain pulses; further details regarding the fabrication of these nanostructures, and their wafer profiles can be found in Chapter 3.

The appearance of periodic interface corrugation is another interesting feature of superlattices grown along the high indices direction. In (311)-oriented structures this interface corrugation is particularly large [46,47]. The (311) GaAs surface is categorized into two types i.e. (311) A-GaAs and (311) B-GaAs depending on the surface termination. The surface reconstruction of (311) A and (311) B GaAs details can be found in many other references [48, 49]. In atomistic configurations, the (311) surface exhibits (100) terraces and (111) step-edge atoms. To reduce the surface free energy this micro step formation is attributed to faceting of the growing GaAs and AlAs surface [46]. The (311) GaAs surface contains equal number of (100)-like atoms with two surface-dangling bonds and (111)-like atoms with one surface-dangling bond [50] as shown in figure 1.2. The type A surface contains (100)-like As atoms and (111) A-like Ga atoms whereas the type B surface contains (100)-like Ga atoms and (111) B-like As atoms.

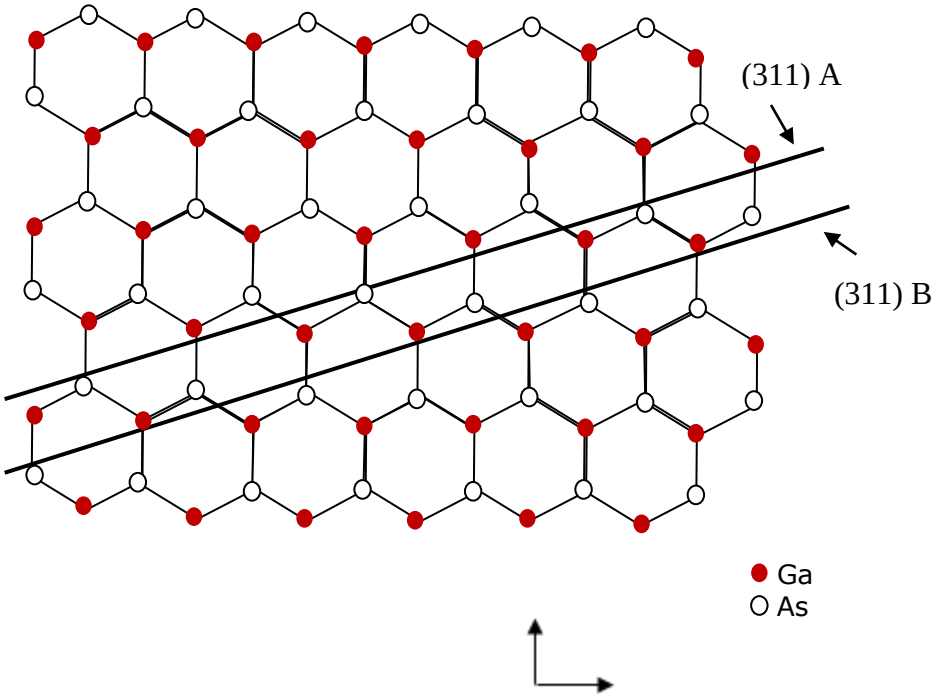



**Figure 1.2:** Schematic representation of (311) A and (311) B planes of GaAs.

Over the past few years there has been a constant interest in using (311) GaAs substrates for the following reasons.

- The Si-doped (311) GaAs conductivity can be controlled by changing growth temperatures and Ga/As flux ratios while maintaining high crystal quality [51,52] which allows exciting optoelectronic applications.
- The surface corrugation observed in (311) GaAs offers considerable potential for the fabrication of quantum dot and quantum wire structures [46].
- For the growth of uniform quantum dot arrays [53,54] and for specific engineering of quantum dot shapes, both the (311) A and (311) B GaAs surfaces was used as templates. It can also act as a good template for the smooth surface of quantum well growth [55].
- GaAs (311) A-(4x1) and GaAs (311) B-(2x1), two surface reconstructions were observed [49]. These surfaces are stable during MBE growth and can play a significant role in understanding the optoelectronic properties of (311) GaAs-based structures.

### 1.3 Electron-phonon coupling mechanisms

This section will briefly address the different electron-phonon coupling mechanisms that are relevant when considering the effects of strain on the electronic properties of a semiconductor device. These include the deformation potential [56], the piezoelectric effect [57], the Pekar mechanism [58, 59] and the ripple effect [60].

The deformation potential and the piezoelectric effect are the two dominant effects in this work, and so this section will concentrate on these two. The deformation potential is the main coupling mechanism for longitudinal acoustic phonons, whereas in the case of transverse acoustic phonons it is the piezoelectric effect.

### 1.3.1 Deformation potential coupling

Bardeen and Shockley [56] defined deformation potential as the motion of energy band boundaries (i.e. conduction band (CB) and valence band (VB)) under acoustic waves of high frequency. Strain propagating through a lattice modulates the interatomic spacing, and thus changes the energy separation (band gap) between the CB and VB of the bulk material. The magnitude of the shift in energy (δE) caused by the strain (ε) is defined by a constant known as the deformation potential constant [61], at small values of strain this is linear and can be represented in equation 1.1. For GaAs along the (100) the value of deformation potential constant is $\Xi_d \sim 10$ev [61].

$$\delta E = \Xi_d \, \varepsilon \tag{1.1}$$

### 1.3.2 Piezoelectric potential coupling

An additional effect of deformation on crystals that lack inversion symmetry, i.e. ionic crystals, is the production of an electric field. This arises either from the formation of electric dipoles when atomic species are separated, e.g. the gallium and arsenic atoms in GaAs, or from the alignment of existing regions of aligned electric dipoles. This induced electric field shifts the energy levels of electrons and holes due to the Stark effect. Similar to the deformation potential, the piezoelectric effect can depend on crystalline direction, for example in GaAs, along the (100) there is no effect but, as inferred from the piezoelectric tensor [62], other directions, such as (111), do exhibit such an effect. Strain (S) induced electric polarization field *E* can be expressed by equation 1.2 [63].

$$\varepsilon_{lm} \, E_m = e_{lmn} \, S_{mn} \, , \tag{1.2}$$

where $\boldsymbol{e_{lmn}}$ and $\varepsilon_{\boldsymbol{lm}}$ are, respectively the components of the piezoelectric and dielectric tensors.

### 1.3.3 Pekar Mechanism

The mechanism that provides coupling between electrons and phonons in a crystal in the presence of an external filed is referred as Pekar mechanism [58]. This coupling arises due to the dependence of dielectric permittivity on strain. Because of this dependence, an acoustic phonon can induce an effective AC electric field at the same frequency leading to an additional coupling with electrons. Glavin et al. [59] observed that, as the dimensions of the sample are reduced to the scale of typical nanostructures, the confined electric fields generated in these nanostructures can result in the Pekar mechanism being the dominant electron-phonon interaction. It was also noted that the mechanism in these nanostructures could be controlled by an external electric field, is more important for non-piezoelectric materials, and is not dependent on crystal symmetry/asymmetry, unlike the piezoelectric coupling mechanism discussed in 1.3.2.

However, given the size and composition of the nanostructures examined in this thesis, there was a negligible Pekar mechanism contribution to strain-induced transport compared to deformation potential coupling, as calculated kindly by B. A. Glavin for similar structures [22].

### 1.3.4 Ripple Effect

When strain is applied to a nanostructure, such as a Quantum Well (QW), the change in dimensions causes a shift in the energies of the confined electron states, known as the “ripple-effect” [64]. In quantum wells, this would result in either an expansion or a contraction of the well width, thus resulting in a modulation of the confined quantum well energy levels. The ripple effect domination over deformation potential was observed by Knipp and Reinecke [64] in InGaAs-based quantum dot (QD) sizes less than 50nm. For a QW, the magnitude may be estimated by considering shifts in the energy of the ground state electron of an infinite square well potential due to changes in well thickness $a$. The ground state energy for an electron in such a potential is [65]:

$$E_1 = \frac{\hbar^2 \pi^2}{2\, m^* a^2}, \tag{1.3}$$

where m* is the effective mass of the electron and for the GaAs conduction band, m* ~ $0.067m_e$ [66].

The derivative of the equation 1.3 is taken with respect to the thickness of the well, *a,* to calculate changes in well thickness which leads to equation 1.4.

$$\left|\frac{dE}{da}\right| = \frac{\hbar^2 \pi^2}{m^* a^3} \tag{1.4}$$

Now consider a strain pulse with amplitude $\varepsilon_m$ propagating through the well: the change in well thickness due to the pulse is $da = a\varepsilon_m$ and therefore the shift in ground state energy is:

$$|\mathrm{d}E| = \frac{\hbar^2 \pi^2}{\mathrm{m}^* \mathrm{a}^2} \varepsilon_m \approx \mathrm{A_r} \varepsilon_m, \tag{1.5}$$

where $A_r$ is an effective ripple constant. Evaluating equation 1.5 for the well thickness of *a* = 5nm QW subjected to a strain of $10^{-3}$ results in a shift of energy of 0.5 meV, which is negligible when compared with the deformation potential mechanism i.e. $A_r << \Xi_d$.

### 1.4 Motivation for work and Thesis Outline

The motivation of this work is to fabricate Semiconductor Devices i.e. Schottky Diodes, two-dimensional electron gas structures (2DEG), two-dimensional hole gas structures (2DHG) and Quantum Well (QW) embedded *p-i-n* photodiodes on (311) GaAs substrates over the more commonly used (100) GaAs substrates to investigate shear acoustic modes and to examine the role of various electron-phonon coupling mechanisms. In (100) GaAs substrates, if the excitation laser spot size is much larger

than the penetration depth of the laser, generation of coherent shear waves is not possible. However, for samples grown on low symmetry planes of GaAs, such as (311), the opportunity for the generation of coherent transverse phonons exists, due the different symmetry considerations of the crystal in this orientation. In picosecond acoustic experiments, generation and detection of transverse acoustic waves has advantages due to their shorter wavelength compared to longitudinal waves. The use of (311) GaAs substrates also has interest from the point of view of fundamental physics since GaAs is piezoactive in this direction leading to the possibility of new effects due to the interactions between electrons and phonons in structures grown on these substrates.

This thesis consists of five additional chapters that explains relevant theory, microfabrication, experimental details and results along with its analysis in subsequent chapters. Chapter 2 provides theoretical description of strain pulse generation, propagation and detection.

Chapter 3 gives the experimental details and is divided into seven main sections. The first section describes the microfabrication techniques, with specific emphasis on all aspects required to produce good samples for measurements. The second section explains the sample structures grown at the University of Nottingham by molecular beam epitaxy (MBE) either by Professor M. Henini or Dr R. P. Campion used to process semiconductor devices. The third section describes the two laser systems i.e. amplifier laser system, oscillator laser system used to perform fast electric and pump-probe measurements respectively along with health and safety measures while working with lasers. The fourth section discusses briefly about the two cryostats used to perform measurements at low temperatures. The following sections generally outline the transport measurements used to determine sample characteristics, experimental setups for fast electric and pump-probe measurements used to obtain results respectively.

Chapter 4 and 5 contain experimental results acquired from two different experiments and the discussion of those results. Chapter 4 investigates the dominant role of piezoelectric mechanism in a semiconductor Schottky diode. A Schottky

contact fabricated on a low-symmetry surface of a semiconductor material which does not possess a centre of inversion symmetry serves as an efficient piezoelectric transducer for both compressive and shear perturbations associated with coherent quasi longitudinal (QLA) and quasi transverse (QTA) phonons, respectively. In this chapter, the first direct experimental evidence of the piezoelectric transformation from QLA and QTA coherent phonons to an electrical signal at microwave (gigahertz) frequencies was demonstrated, and the method is theoretically predicted to work up to sub-terahertz frequencies.

Chapter 5 explores the detection of longitudinal and transverse acoustic phonons using two-dimensional structures *i.e.* Quantum well embedded *p-i-n* photodiode detector (QW-*p-i-n*), two-dimensional electron gas (2DEG) and two-dimensional hole gas (2DHG) fabricated on (311) GaAs substrates. C. L. Poyser *et al* [67] performed some initial investigations to obtain longitudinal and transverse acoustic signals using QW-*p-i-n* photodiode however succeed only to detect longitudinal acoustic waves but unable to detect quasi-transverse signal which is predicted to be present [68], as the alignment necessary to see the transverse signal was not clear. This is investigated from the Schottky experiments and successfully detected quasi-transverse phonons. Finally, Chapter 6 concludes this thesis and summarises the investigations presented in the previous chapters and makes suggestions for further work in this field.

# Chapter 2

# Background

This chapter provides some of the background theory that is relevant to the experiments performed in this thesis and the associated discussions. This includes theory behind the thermoelastic generation of coherent strain pulses in thin metal films along with the mathematical models used to simulate initial strain profiles. This is followed by the description of these phonons propagation, focussing on attenuation and dispersion. The balancing of dispersive effects and crystal nonlinearity leads to the formation of solitons which is considered in next section. Existing optical techniques for the detection of these phonons are then described very briefly followed by the explanation of the devices that are sensitive to strain.

## 2.1 Strain pulses

The experiments described in this report utilise optical pumping to induce ultrafast strain pulses which pump the device structures. A typical strain pulse can be depicted as the derivative of the displacement and consists of coherent phonons with multiple frequencies generated within a sub-nanosecond timescale. The time duration of strain pulses used in this thesis is in picosecond range with phonon frequencies in the GHz and subteraherzt regimes. In a thin film transducer, at generation the shape of the pulse is bipolar, however its shape changes with propagation.

Generation and propagation of ultrafast strain pulses have been studied over the past three decades by the pump-probe technique. Using ultrafast laser pulses, a thin transducer film on a sample is pumped with light, which penetrates through to sub-surface levels and a coherent phonon wavepacket is generated due to thermoelastic effects. This acoustic wavepacket then propagates through the sample and may interact with sample interfaces and/or reflect off the sample surfaces. By optical probing of the sample, either on the same or opposing surface of the pump excitation, the resultant strain pulse is detected. The optical probe pulse consists of laser pulses

identical to the pump pulses but with much lower power. Because of the change in optical reflectivity on the sample surface by the strain pulse, probing is achieved. The reflected optical probe pulse is directed towards a photodiode where these changes in optical reflectivity is detected. The generation, propagation and subsequent detection of these pulses are clearly explained below in the next three sections.

### 2.1.1 Generation

An ultra-short optical pulse, incident on a thin metal transducer film will induce picosecond strain pulses due to the thermo-elastic effect. This effect will be analysed and modelled from a *macroscopic* point of view [13]. Consider an ultra-short pulse of light with fluence $W$ and duration incident on a transducer film. The light absorption depth is $\xi$, and it is assumed that this is much less than the film thickness $d$. It is also assumed that the energy from the pulse is imparted instantaneously into the film. In such a case, the resulting temperature rise at a distance, x, into the film is given by:

$$\Delta T\ (x) = \frac{(1-r)W}{C\xi} exp(-\frac{x}{\xi}), \tag{2.1}$$

where $r$ is the optical reflectivity and $C$ is the specific heat capacity per unit volume of the film. The temperature rise induces an isotropic thermal stress in the film given by:

$$\sigma = -3B\beta\Delta T\ (x), \tag{2.2}$$

where $\beta$ the linear-expansion coefficient and $B$ is the bulk modulus. Longitudinal acoustic waves resulting from this stress are launched into the film. Strain waves originating from each point are launched in both positive and negative directions. The waves propagating in the negative direction, which is towards the free surface of the film, are reflected there with a polarity change, which gives rise to the bipolar shape of the pulse.

After a long time compared with the time for sound to propagate through a distance equal to the absorption depth $\xi/s$ ($s$ is the sound velocity), the form of the strain pulse in the film may be given by [69]:

$$\varepsilon(t) = \frac{2A\xi}{(s\tau^2)(1-R)\Sigma_{j=0}^{\infty}R^j o(t)} \times exp\left[-\frac{1}{\tau^2}o(t)^2\right] \qquad (2.3)$$

where $$A = \frac{3(1-r)W\beta B}{2C\xi\rho s^2}\ , \qquad o(t) = t - \frac{(2j+1)d}{s}\ , \qquad (2.4)$$

and $R$ is the reflection coefficient for longitudinal sound waves at the film/substrate interface; $s$ is the speed of longitudinal sound in the metal; $d$ the thickness of the metal film; $\rho$ the density and the $W$ pump fluence. The summation term in equation (2.3) is to account for multiple reflections of the photo-induced strain pulse from the film/substrate interface and free surface. In the same equation, $\tau$ is an adjustable parameter which accounts for electron diffusion by modifying the temporal shape away from the ideal situation where $\tau = \xi/s$ and defines the temporal width of the pulse.

This model has its limitations because it is based on a macroscopic approach which assumes that the material can be characterised by a temperature profile and that energy transport can be calculated solely from the macroscopic thermal conductivity i.e. the macroscopic contribution to heat capacity due to the lattice is dominant and the electronic contribution may be ignored. However, the later contribution is significant: the energy from the light pulse is initially absorbed by electrons which diffuse into the film, imparting energy to the lattice through electron-phonon coupling. Typically for metals the electron diffusion is about a hundred times larger than the macroscopic thermal diffusion coefficient, and thus electron diffusion dominates. A microscopic model may be used which assigns separate depth-dependent temperature profiles to the lattice and electron gas, known as the two-temperature model [13]. However, the model presented above was found to be sufficient for the analysis of strain pulse experiments, like those described in this thesis, such as in Akimov *et al* [70] and therefore was utilised in later strain analysis. An example of a strain pulse generated by the equation (2.3) is shown in figure 2.1.

The various symbols used in the equation (2.3) & (2.4) and the values used for calculations in this work are defined in table 2.1.

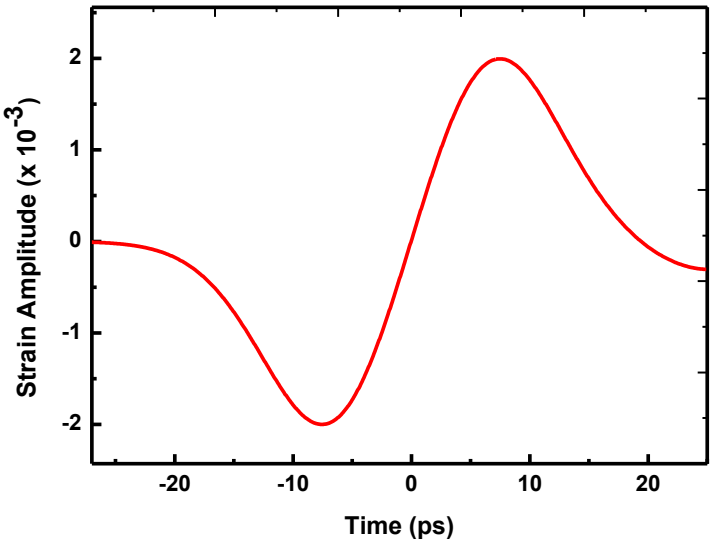



**Figure 2.1:** Calculated temporal shape of the initial strain pulse generated by using equation 2.3, and the pulse is bipolar in shape using values given in table 2.1.

| Symbol | Value | Description | Reference |
|---|---|---|---|
| $\beta$ | $23.1 \times 10^{-6}$ K$^{-1}$ | Linear expansion coefficient | [71] |
| $\rho$ | $2.7 \times 10^{3}$ kg m$^{-3}$ | Density | [72] |
| $\xi$ | 6.4 nm | Optical Absorption length of 800 nm light in the film | [13] |
| $s_{al}$ | 6420 m s$^{-1}$ | Speed of sound (in Al) | [73] |
| $R$ | 0.164 | Reflection coefficient | Measured |
| C | $2.422 \times 10^{6}$ Jm$^{-3}$ K$^{-1}$ | Specific heat capacity | [73] |
| $r$ | 0.86 | Reflectivity (800nm) | [74] |
| $B$ | $76 \times 10^{9}$ Pa | Bulk Modulus | [73] |
| $d$ | 100 nm | Al film thickness | Measured |
| $\tau$ | 2.5 ps | Temporal width of the pulse | [75] |
| $W$ | 5 mJ m$^{-2}$ | Pump fluence | Measured |

**Table 2.1:** Parameters used for the generation of the temporal shape of the initial strain pulse in GaAs substrate.

### 2.1.2 Propagation

The previous subsection described picosecond strain pulse generation in a substrate-adhered metal film. In this section propagation of this stain pulse through a GaAs substrate is considered in detail. For low strain amplitude, where the strain pulse is constituted of low frequency components (e.g. up to ~ 100 GHz) with in the limit of low temperatures, both dispersion and attenuation are negligible. Consequently, propagation is linear, and both the pulse amplitude and temporal profile are preserved during propagation. However, for large strain amplitudes, non-linear effects grow in magnitude and can balance phonon dispersion, leading to the generation of a train of pulses which maintain their temporal shape and travel at a constant speed. These pulse forms, known as solitons, were first seen by John Scott Russell (1808–1882) in the water waves propagating in a canal. Acoustical solitons were first observed by Maris *et al* [69] in gallium arsenide and later in sapphire by Dijkhuis *et al* [76]. These pulses are sub-picosecond in duration and have been generated and studied in a variety of different experiments [71, 77].

The formation of acoustical solitons is illustrated in figure 2.2 for three stages denoted by A, B and C. The simulated evolution of a high amplitude strain pulse propagating in a GaAs substrate is under the combined influence of nonlinearity and dispersion. The initial strain pulse, shown in stage A, includes a secondary pulse (at around 40 ps) formed due to reflection of the generated strain pulse, first at the interface between the metal film and GaAs substrate and then at the free surface of the film. Further pulses will be present after the appropriate time intervals but, are not shown for clarity. In general, such reflections occur when an acoustic pulse travels from any given medium of acoustic impedance $Z_1$ into another of acoustic impedance $Z_2$ and the reflection coefficient (R) is given by equation 2.5 as follows.

$$R = \frac{Z_2 - Z_1}{Z_2 + Z_1}. \qquad (2.5)$$

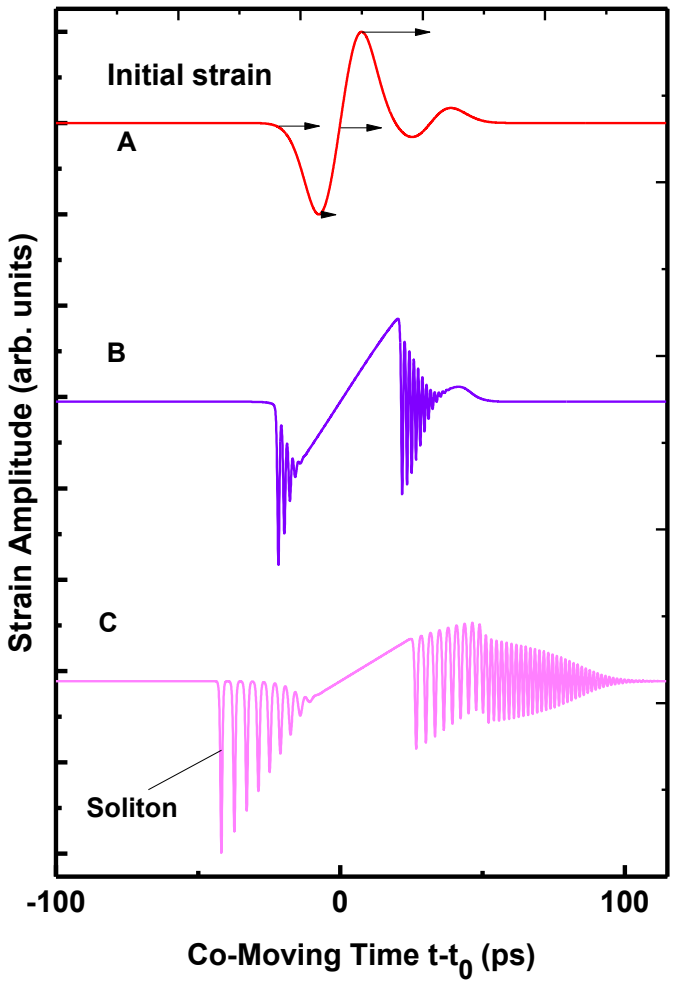



**Figure 2.2:** Simulated temporal evolution of an initial strain pulse (A), showing shockwave development (B) and soliton formation (C). The arrows marked on the initial strain pulse show the relative velocities of different sections of the strain pulse. Traces B and C are offset vertically for clarity.

In equation 2.5, $Z_1$ is the acoustic impedance of film and $Z_2$ is the acoustic impedance of the substrate. The main reason for the use of aluminium films in this work is that aluminium and GaAs, the substrate material used in these experiments, have similar acoustic impedances which results in a small R and minimal reflection at this interface. Following its generation in the metal film, the strain pulse changes its shape as it propagates through the substrate, this will be considered now very

briefly. Due to the dependence of acoustic velocity on strain at high amplitude, the positive peak of a propagating pulse travels faster than the leading edge, and the negative peak slower than the trailing edge (see arrows on stage A in figure 2.2), resulting in a sharpening of both leading and falling edges of the pulse, described as a shock wave (stage B). The formation of a steep shock wave implies the presence of very high frequency, terahertz components in the wavepacket for which acoustic dispersion is greatly enhanced. Consequently, these terahertz components lag the wavefront and give rise to an oscillating disturbance in the wavepacket. On the trailing edge of the pulse, where strain is compressive, non-linear effects and phonon dispersion add together leading to a dispersive tail, whereas on the leading edge, where large positive strain amplitudes are present, a balance between phonon dispersion and non-linear effects leads to soliton formation (stage C). The acoustical pulse propagation and the formation of the soliton may be described mathematically by the Korteweg-de Vries equation [71, 78] as follows:

$$\frac{\partial \varepsilon}{\partial t} = -\frac{C}{2\rho v_s}\varepsilon\frac{\partial s}{\partial x} - \beta\frac{\partial^3 \varepsilon}{\partial x^3}\ , \qquad (2.6)$$

where $\beta$ is the first order dispersion parameter, $C$ is the non-linear parameter, $s$ is the acoustic attenuation factor and $\rho$ is the density. Solving equation 2.6 numerically allows us to track the evolution of the strain pulse. The analysis presented in this thesis uses a simulation of acoustic pulse propagation written in Matlab provided by Emmanuel Péronne [71]. This simulation uses co-moving time coordinates ($t-t_0$), where $t_0$ is the arrival time of the low frequency components of the strain pulse– the time origin is the centre of the strain pulse. All figures that shows results from this simulation, presented throughout this thesis, use this coordinate frame.

### 2.1.3 Detection

In optical pump-probe experiments, detection of the acoustic pulse typically involves measuring changes in the optical reflectivity of the sample. One commonly used method is the observation of changes in the probe beam reflected from the surface using a photodiode detector [1, 13, 70, 79]. Alternatively, an interferometric method can be used that allows the investigation of both the amplitude and the phase changes of the reflected beam caused by changes in the refractive index and the surface deflection [71, 78, 80, 81]. In both cases a laser beam is split into two parts to form the pump and probe. The optical probe pulse is identical to the pump beam except that it is of lower power, and travels on a delayed optical path so that the complete profile of the strain pulse can be observed. This delayed optical path can be quite long depending on the propagation distance. For a GaAs substrate of 444 μm thickness, detection of single pass through the substrate would require a temporal delay of approximately 81.03ns which is equal to optical path distance of 24.31 meters. It is difficult to establish such a long delay therefore techniques to use later laser pulses to introduce the time delay can be employed to reduce the delay path length [14]. In all the optical methods mentioned in above references, the probe beam is reflected off a surface or sub-surface region and directed towards a photodiode to measure the reflectivity changes. These changes occur due to the modification of real and complex refractive indices of the material by strain interaction [1].

## 2.2 Strain sensitive devices

Investigating strain induced transport effects is an alternative method to the optical detection. This method exploits devices whose carrier transport characteristics can be modulated by an incoming wavepacket due to electron-phonon interaction. These interactions are explained in section 1.3, and lead to specific effects in these devices described as the piezojunction effect. In this thesis, such devices like Schottky diode and QW-embedded *p-i-n* diode are used for investigations in chapter 4 and chapter 5 respectively.

As is appropriate, a brief description of a *p*-*n* junction and Schottky diode will be provided first in Section 2.2., after which the *p*-*i*-*n* diode and an overview of piezojunction effect will be given. The operation of a QW-embedded *p*-*i*-*n* diode which is a modified version of *p*-*i*-*n* diode is presented in section 2.2.4.

### 2.2.1 *p*-*n* junction

The *p*-*n* junction is a key element for most semiconductor devices. This is formed between a *p*-type (with positively charged carriers) and an *n*-type (with negatively charged carriers) semiconductor. It is used widely in rectification, switching, amplification, etc. There are two types of *p*-*n* junctions: (1) The homojunction, made of one semiconductor and (2) The heterojunction, made of different semiconductors.

Figure 2.3a shows two semiconductors with uniformly *p*- and *n*-type doping. The p-type material contains a concentration $N_A^-$ of negatively charged acceptors and density of free holes $p = N_A^-$. The n-type material contains concentration $N_D^+$ of positively charged donors and density of free holes $n = N_D^+$. Therefore, the Fermi level $E_F$ is near the valence band edge in the *p*-type material and near the conduction band in the *n*-type material. When these two semiconductors are in contact, the carrier concentration gradient at the junction causes diffusion [82]. As the free carriers move through the junction, they leave behind ionized acceptors ($N_A^-$) and donors on each side of the junction. This space charge creates an electric field, $\mathcal{E}$, and induces a drift current opposite to the diffusion current (see figure 2.3b). Therefore, a state of equilibrium occurs leading to a *potential difference*, $V_{bi,}$ across the junction as the negatively charged acceptors repel the electrons and the positively charged donors repel the holes. At equilibrium, the net current is zero and the Fermi level is constant across the sample. The regions on either side of the junction become completely depleted of free carriers in comparison to the *p*- and *n*-type materials further away from the junction. This area around the *p*-*n* junction is called the "depletion region".

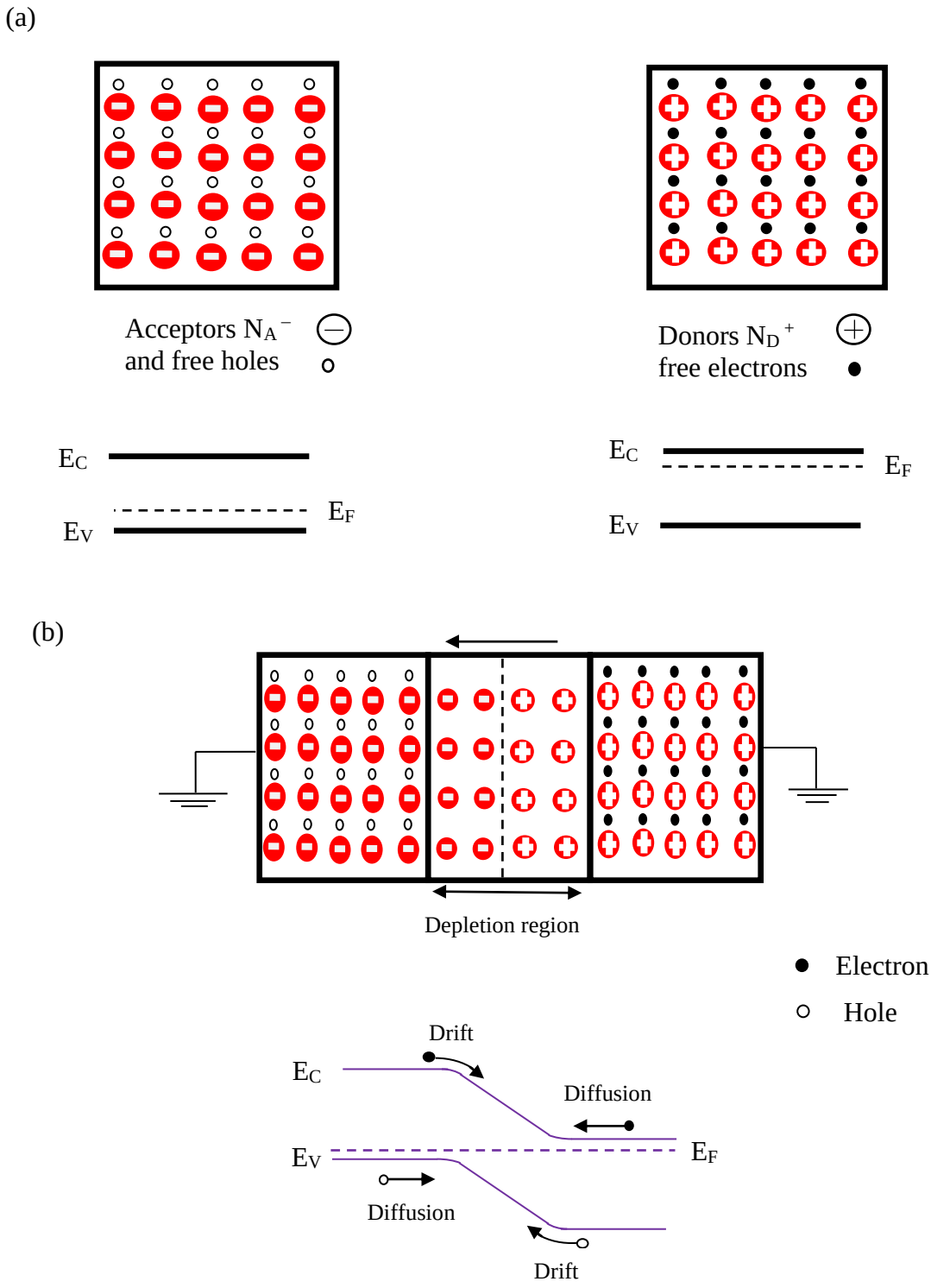



**Figure 2.3:** (a) Uniformly doped *p*- and *n*-type semiconductors before the junction is formed. (b) The electric field in the region and the energy band diagram of a *p*-*n* junction in thermal equilibrium (V = 0).

When we apply a positive voltage on the *p*-side, the junction becomes forward biased. Majority carriers, electrons and holes, are attracted towards the junction and the depletion region becomes narrower. Electrons are injected into the *p*-side and holes are injected into the *n*-side, thus resulting into a large forward current (see figure 2.4 a). When we apply a negative voltage on the *p*-side (see figure 2.4 b), the junction becomes reverse biased. Majority carriers move far away from the junction thus broadening the depletion region. Some electrons are injected into the *p*-side and some holes are injected into the *n*-side thus resulting into a small reverse current.

The rectifying behaviour of a *p*-*n* junction is the most important characteristic, i.e. the current easily flows only in one direction. The current-voltage (*I*-*V*) characteristic of a typical *p*-*n* junction is shown in Figure 2.5. At the forward bias condition, the current increases rapidly with increasing applied bias and at the reverse bias, virtually no current flows till a critical voltage is reached, at which point the current suddenly increases. This sudden increase in current is referred to as the junction breakdown. The breakdown mechanisms are the Zener tunnelling effect and avalanche multiplication, both occurring under a large applied electric filed. A valence electron can make a transition from the valence band to the conduction band by penetrating through the energy gap. This effect is referred as tunnelling. Also, an electron can gain sufficient kinetic energy to break a bond thus creating an electron-hole pair. The newly created electron-hole pairs both acquire kinetic energy from the electric filed and create additional pairs. This process is therefore called avalanche multiplication [73].

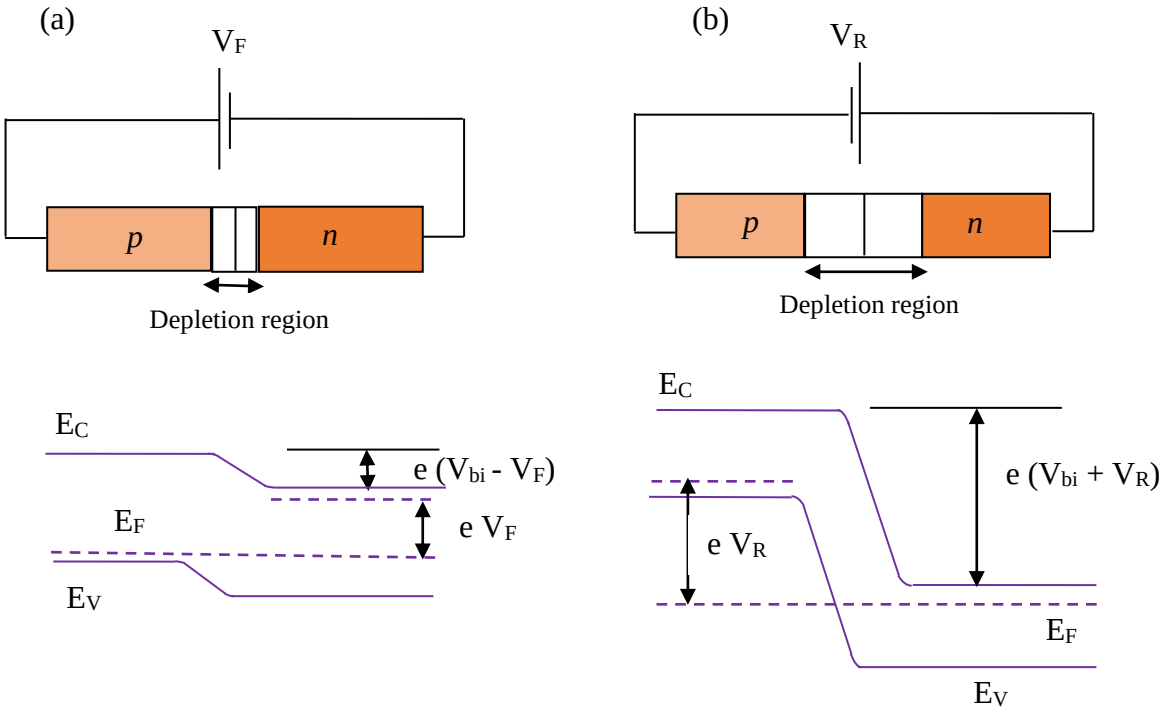



**Figure 2.4:** Schematic of p-n junction band diagram. $E_F$ is the Fermi energy, $E_V$ is the valence band energy, $E_C$ is the conduction band energy and $V_{bi}$ is the inbuilt potential. (a) shows the junction when a forward bias $V_F$ is applied and (b) shows the junction when reverse bias $V_R$ is applied.

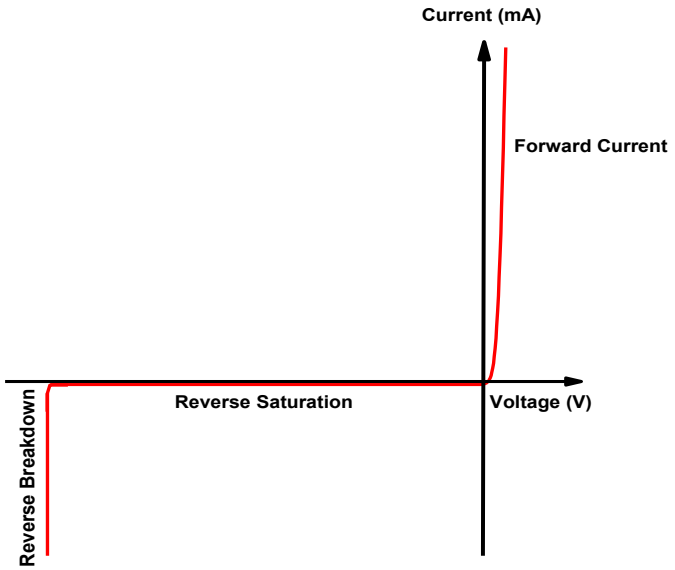



**Figure 2.5:** Current-voltage characteristic of a typical *p-n* junction.

### 2.2.2 Schottky Diode

A Schottky diode is a metal-semiconductor junction that forms a potential barrier at the interface [82], as shown in figure 2.6. As mentioned in previous section that the *p*-*n* junction can respond on fast time scales (~ GHz) to a picosecond strain pulse. However, Schottky junctions are majority carrier devices, known to exhibit an ultra-fast response (~ THz) to changes in applied bias. Injection of majority carriers is faster than that of minority carriers, so these types of device are often chosen for fast switching speeds and therefore high frequency applications [83]. It has been demonstrated by Moss et al. that Schottky diodes can be used to detect ultrafast strain pulses without the need for a laser as part of the detection scheme [23]. This suggests that Schottky diodes are a strong candidate as detection devices for all-electronic picosecond acoustics experiments.

The Schottky diode is an ideal candidate for strain sensitive devices because in comparison to the *p*-*n* diode it has faster response times. This can be explained by the roles that majority and minority carriers play in each device's operation. The *p*-*n* junction is a minority carrier device - the minority carriers diffuse across the junction, form the "diffusion" current, and recombine. Since diffusion and recombination are slow processes, the smallest reverse recovery times is ~ 10ps for a fast *p*-*i*-*n* diode [84]. By comparison, the Schottky diode is a majority carrier device. If the semiconductor is *n*-doped, then electrons are the majority carriers. They are quickly injected into the conduction band of the metal contact on the other side of the diode, becoming free moving electrons. In contrast to *p*-*n* diodes, there is no slow recombination of *n*- and *p*-type carriers, therefore no reverse recovery time and the switching time can be as low as ~100 fs [85]. In fact, many Schottky diode device structures have been developed which can operate at terahertz frequencies [86]. Thus, as a strain-sensor for a picosecond strain pulse, where component frequencies can extend into the terahertz range which makes Schottky diode a perfect choice. For the above-mentioned reasons, Schottky diodes were used for investigating the interaction of coherent traverse and longitudinal acoustic phonons with electrons in a (311B) GaAs Schottky diode as detailed in chapter 4.

Consider the case where $e\Phi_m > e\Phi_s$, for an n-type semiconductor [87], where the work function $e\Phi_{m,s}$ is the energy required to remove an electron from the Fermi level of the metal ($E_{Fm}$) or the semiconductor ($E_{Fs}$), respectively, to the vacuum level. As the metal and semiconductor are brought together, charge must be transferred so that the Fermi levels align at thermal equilibrium ($E_F$). Electrons from the *n*-type semiconductor conduction band ($E_C$) diffuse into the metal, leaving behind positively charged donor ions. The Fermi level in the semiconductor is lowered by an amount $eV_0 = e(\Phi_m - \Phi_s)$, where $V_0$ is the equilibrium contact potential. This potential, and the associated electric field, prevents further electrons from diffusing into the metal. Another potential barrier, with height $e\Phi_B = e(\Phi_m - \chi)$ stops electron injection from the metal to the semiconductor. Here the electron affinity, $e\chi$, is the energy required to remove an electron from the bottom of the conduction band of the semiconductor to the vacuum level. A depletion region, W, is formed in the semiconductor by the presence of the positively charged donor ions. The built-in electric field occurs across this region, along with an associated voltage drop. The width of the depletion region can be calculated from the Poisson equation [82] as follows:

$$W = \sqrt{\frac{2\epsilon_r\epsilon_0}{eN_D}\left(V_0 - V - \frac{k_B T}{e}\right)}, \tag{2.7}$$

where $\epsilon_r$ is the relative permittivity of the semiconductor, $\epsilon_0$ is the permittivity of free space, e is the charge of an electron, $N_D$ is the donor concentration of the *n*-doped semiconductor, $V$ is the external bias applied to the Schottky diode, $k_B$ is the Boltzmann constant and T is the temperature. In general, the depletion width for any given Schottky junction is dependent on the applied bias.

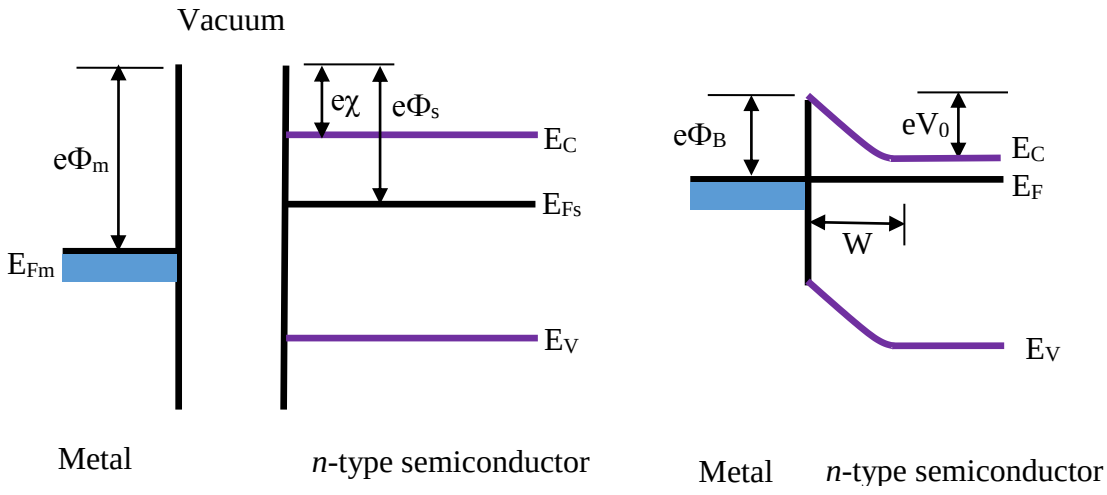



**Figure 2.6:** Schematic energy band diagrams of an *n*-type Schottky diode with $e\Phi_m > e\Phi_s$, where $e\Phi_{m,s}$ is the work function of the metal or semiconductor, respectively. When the metal and the semiconductor are brought into contact the Fermi levels must align at thermal equilibrium. This leads to bending of the energy bands in the semiconductor by an amount $eV_0$, the formation of a potential barrier $e\Phi_B$ and the formation of a depletion region W. $E_{Fm,s}$ are the Fermi levels in the metal and the semiconductor when separate, whereas $E_F$ is the Fermi level of the Schottky diode at equilibrium. $E_{C,V}$ are the conduction and valence bands in the semiconductor and $e\chi$ is the electron affinity of the semiconductor.

The band structure of the *n*-type Schottky diode is illustrated in Figure 2.7 for a device under forward, reverse and unbiased condition. When a forward bias voltage $V_F$ is applied to the Schottky barrier, defined as a positive bias being applied to the metal, the contact potential is reduced from $V_0$ to $(V_0 - V_F)$ as shown in figure 2.7. A reduction in the contact potential allows more electrons from the semiconductor conduction band to diffuse into the metal causing a forward current to flow. When a reverse bias voltage $V_R$ is applied, the contact potential is increased to $(V_0 + V_R)$ and the electron flow from the semiconductor to the metal is reduced. As the potential barrier for the flow of electrons from the metal to the semiconductor is independent of applied bias, it is possible to increase current flow in the forward direction but not the reverse direction and the junction behaves as a rectifier.

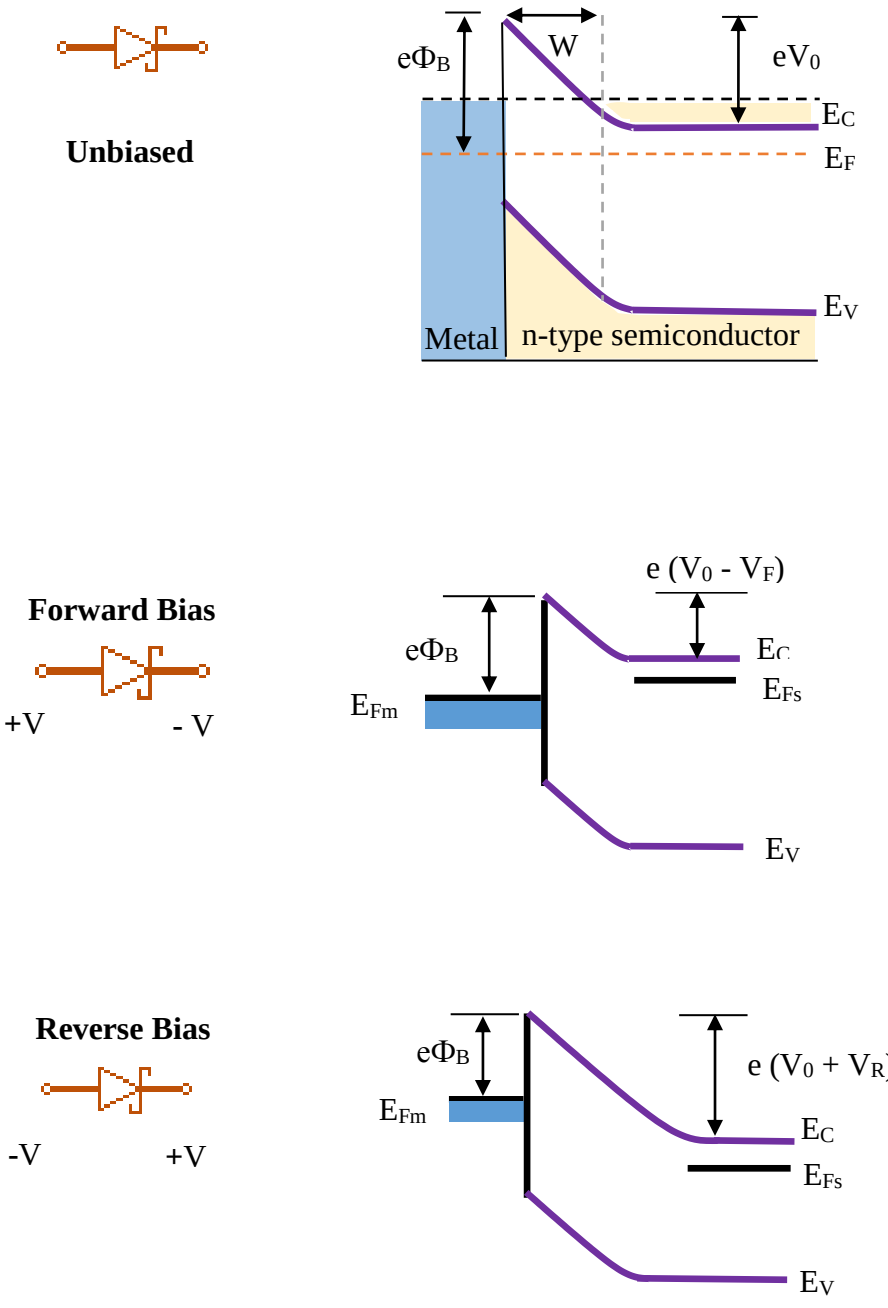



**Figure 2.7:** Schematic energy band diagrams of an *n*-type Schottky diode under different biasing conditions i.e. unbiased condition, forward bias and reverse bias. A bias applied across the Schottky diode changes the size of the contact potential and so changes the number of electrons that can diffuse from the semiconductor into the metal.

### 2.2.3 *p-i-n* Diode

The *p-i-n* diode has an intrinsic (*i*) region sandwiched between heavily doped p- and n-type semiconductors. In practice, the idealized intrinsic region is approximated by either a high-resistivity *p*-layer or a high-resistivity *n*-layer [88]. The *p-i-n* diode has two characteristics: (1) after turn-on the device resistance varies approximately linearly with increasing forward bias; (2) the diode capacitance is constant under reverse bias [89]. It has wide applications: in attenuator applications where resistance is required to be controlled by the current; as DC controlled microwave switch; as a modulating device, due to its variable forward resistance characteristics; as photodetectors in fibre optic systems; as light emitting diodes [82].

Under forward bias, holes from the p-type region and electrons from n-type the region are injected into the *i*-region. In a *p-i-n* diode, the depletion region exists completely within the *i*-region. This depletion region is much larger than in a *p-n* diode, and almost constant size, independent of the reverse bias voltage. This increases the volume where electron-hole pairs can be generated by an incident photon. In reverse bias, most incident photons on the diode are absorbed in the intrinsic region and leads to the photogeneration of electron-hole pairs. These pairs later drift as minority carriers towards their respective opposing regions. In comparison to the diffusion process the drift process is relatively fast [89], this allows *p-i-n* photodetector diode for the fast detection of incoming photons, hence the requirement that most electron-hole pairs are generated within the intrinsic region, and not the doped regions. In this work, a Quantum Well(QW) embedded *p-i-n* photodiode detector, which is a modified version of *p-i-n* diode, is used for strain-induced transport detection. This is discussed in more depth in 2.2.4.

#### The Piezojunction Effect

The application of strain to junction-based devices such as the *p-n* diode or transistor gives rise to a change in electrical characteristics as was demonstrated by Harry H. Hall [90]. This behaviour is known as the piezojunction effect and can be exploited to make stress sensitive sensors [91]. The piezojunction effect is primarily attributable to the effect of strain on the relative position of valence and conduction band edges in a semiconductor which arises due to piezoelectric and deformation

potential interactions. The symmetry of the crystal is disturbed hence modifying its electronic structure, such as the band gap, and therefore it's conductivity [91]. In a *p-n* junction, where the current decreases exponentially with band-gap energy, this gives rise to notable change in observed current-voltage (*I-V*) characteristics. In addition, strain can affect carrier mobility and the valence band density of states, which can also contribute to changes in the *I-V* characteristics.

In mechanical stress sensors such as microphones, accelerometers and pressure sensors [92] the static piezojunction effect is employed. The effect of static strain on a *p-n* junction, specifically that the junction resistance should depend critically on the band-gap energy $E_g$ therefore pressure, was first predicted by Shockley [93]. In fact, it is well understood that for the energy level structure of any diamond-type lattice, such as germanium or silicon, the energy gap $E_g$ between valence and conduction bands increases with decreasing atomic spacing and therefore pressure [94]. This was shown experimentally by Bardeen *et al* in germanium-based *p-n* junctions at room temperature in [90] where it was explained that as $E_g$ increases with pressure there is a reduction in minority carrier populations and therefore diffusion current. In the low voltage limit the junction resistance is:

$$R_0 = Ae^{(E_g/kT)}, \tag{2.8}$$

where $A$, which is a product of the effective density of states for electrons and holes in the conduction and valence bands, can be taken as a constant since changes in $A$ with pressure have negligible effect on resistance compared with changes in $E_g$. This is because of the large value of the exponent ($kT \sim 0.025$ eV) for Ge at room temperature), a very small fractional change in the band gap $E_g$ results in a large effect on $R_0$.

Rindner *et al.* [95], in later studies, showed the effect of pressure on diffusion current in GaAs *p-n* junctions and the conclusions from these studies were that the resistance changes here are primarily due to the band-gap widening, as well as defects in the diode itself. These studies, based on previous calculations by Pollak

[96], considering the effect of uniaxial strain on a GaAs junction. By considering the electron-phonon coupling effects in stressed bulk substrates one can understand these studies clearly. Stressed bulk GaAs studies by Pollak *et al.* [96, 97] and Chandrasekhar *et al.* [98] indicated that there would be a splitting of the degenerated GaAs valence band in the presence of uniaxial compressive strain, hence causing an energy separation between the light-hole (LH) and heavy-hole (HH) valence bands. Pollak determined that, when a uniaxial compressive stress is applied to GaAs, the transition at $k = 0$ between the top of the doubly degenerate valence band ($E_v$) and bottom of the lowest conduction band ($E_c$) is split by an amount $\delta E$ due to a splitting of the degenerate valence band. The splitting of this transition may be defined as follows:

$$\Delta(E_c - E_v) = a(S_{11} + 2S_{12})X \pm \frac{\delta E}{2}, \tag{2.9}$$

where

$$\delta E_{100} = 2b(S_{11} + S_{12})X \tag{2.10}$$

$$\delta E_{111} = dS_{44}X\sqrt{3} \tag{2.11}$$

$$\delta E_{110} = \left[b^2(S_{11} - S_{12})^2 + \frac{d^2 S_{44}^2}{4}\right]^{1/2} X \tag{2.12}$$

for [100], [111] and [110] stress respectively; $X$ is the stress; $a$ is the hydrostatic pressure deformation potential; $b$ and $d$ are deformation potentials for strains of tetragonal and rhombical symmetries, respectively and $S_{11}$, $S_{12}$, and $S_{14}$ are the elastic compliance constants. The hydrostatic component of uniaxial compressive strain would result a further separation between the conduction band and valence band i.e. a larger band gap, and a reduction in the energy separation between the split-off (SO) band and HH band [96], as shown in Figure 2.8 for [111] strain. Deformation potential is the important mechanism for these effects, as explained in Section 1.3.1. Both the LH-HH splitting and increased band gap energy are directly proportional to hydrostatic and shear deformation potentials [42, 96]. Rindner *et al.* observed stress-induced band gap widening caused changes of up to ~30 % in the

measured current in both forward and reverse biases at room temperature experiments with [111] GaAs *p-n* junctions.

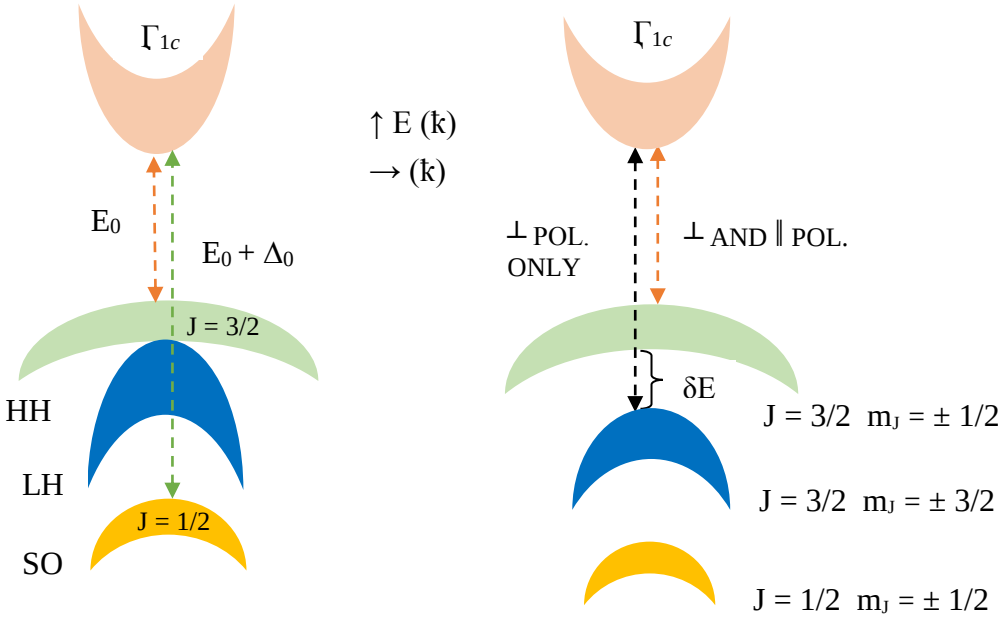



**Figure 2.8:** Schematic of energy band structure of GaAs in the absence of strain (left), and (right) under compressive uniaxial [111] strain. The conduction band and valence band depicted at the top and bottom of the figure, respectively. In unstrained GaAs (left), the two-degenerate light-hole (LH) and heavy-hole (HH) valence bands (J = 3/2) are separated from CB by the energy $E_0$, whilst the split-off (SO) band (J = ½, $m_J$ = ±1/2) transition to CB is separated by an energy $E_0+\Delta_0$. Splitting of the degenerate HH and LH bands ($m_J$ = ±1/2 and $m_J$ = ±3/2, respectively) happens under applied uniaxial compressive strain, whilst the hydrostatic component increases valence band – conduction band transition energies. Note that similar observations were made for stress along both [100] and [110] directions, and that the polarisations refer to incident light used in piezoelectroreflectance measurements.

In contrast to the experiments described above, which concentrated only on slowly varying stress on a *p-n* junction, the strain pulses generated in this thesis were modulated on a much faster timescale. Moss *et al.* [99] investigated such a case by using femtosecond optical pulses to generate acoustic wavepackets. In this work, authors showed that the coherent phonons modified the electronic structure of the

junction via the deformation potential. This caused a change in the measured current due to the sudden change in electrostatic potential by the strain pulse.

### 2.2.4 Quantum Well (QW) embedded *p-i-n* photodiode detector

A quantum well (QW) embedded *p-i-n* photodiode can be used as a sensitive detector of coherent acoustic waves which provides detection sensitivity of up to 1000 times than that of traditional pump-probe techniques [22]. The energy levels in a QW are sensitive to strain. Incorporating QW in the centre of an undoped intrinsic region, located between the *n* and *p*-type regions of a *p-i-n* diode structure (QW-*p-i-n*) allows strain induced shifts in the energy levels of the QW to be characterised in terms of a photocurrent. The depletion region, which is almost completely contained within the intrinsic layer, is much larger than that present in a *p-n* diode and almost constant in size with no effect of applied voltage, under reverse bias.

The previous sections have given a general description of the operation of a *p-n* junction and *p-i-n* diode with brief explanation of various strain-induced effects it exhibits. A modified version of *p-i-n* diode with QW incorporated in intrinsic region is used for investigations detailed in chapter 5, so details of its operation will be given here. The main principle of a measurement of strain with a *p-i-n* photodiode is to monitor changes in the photocurrent generated in the device as the strain pulse travels through. As mentioned, a *p-i-n* diode detector can be fabricated by growing an intrinsic region between the *p*- and *n*-doped regions. This functions in the same way as a standard *p-n* diode [82], with the intrinsic region acting like an extended depletion zone. The device can be made more sensitive to strain by the inclusion of a QW in the intrinsic region.

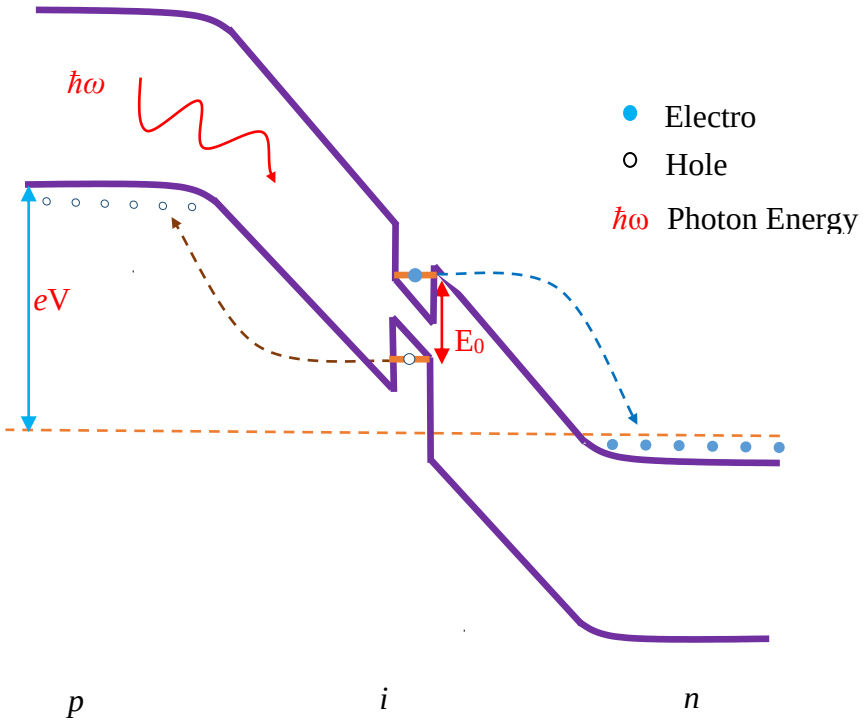



**Figure 2.9:** Schematic of photocurrent generation in a *p-i-n* photodiode incorporating a QW at its centre in the intrinsic region. A reverse bias voltage across the device V results in an energy shift of *e*V and the device is illuminated by a photon of energy ~ω on the *p*-doped side. $E_0$ represents the separation of the energy levels in the QW.

The process of photocurrent-generation in the *p-i-n* diode is shown in Figure2.9, where the device is reverse biased to use as a detector and the QW has a ground state exciton energy $E_0$. When photons with energy $\hbar\omega \sim E_0$ are incident on the QW, electron-hole pairs are created which tunnel out of the well into the intrinsic region, separate, due to the electric field, and drift across the device to the contacts, thus generating a photocurrent. The large width of the intrinsic region here is beneficial, because it ensures that the magnitude of the in-built electric field is low, a large electric field would reduce the barrier thickness for electrons to tunnel into and out of the well and thus increase background current. In addition to the QW, electron-hole pairs may also be generated in other parts of the intrinsic region and these, separated by the electric field, may tunnel through the QW and contribute to a background

current. However, in experiments, this background can be minimised by photo-excitation of the QW with an energy below that of the bulk.

In a quantum well, the absorption of light inside the well exhibits a sharp resonance when the energy of the light matches the exciton resonance of the well. An exciton is formed when an electron and hole are coupled through the Coulomb interaction acting like a hydrogen particle with the hole acting as the nucleus. The masses of the constituents of this hydrogen like particle are determined by the effective masses in the appropriate energy bands. The probability of absorbing light then becomes equal to the probability of creating this particle. This is a particularly strong transition when the particle created would correspond to the 1s state of the hydrogen atom. For this state, the probability of creating the particle is related to the proximity of the hole and electron to each other, which is enhanced by confinement in a QW [100]. This sharp transition contributes to the high sensitivity of the device.

When a quantum well is subjected to strain wave it causes a change in its energy levels. At this point these changes can tune or detune the QW from resonance with the laser energy leading to strong changes in the photocurrent generated, if the device is excited by light. This is demonstrated in figure 2.10. Moss *et al.* [22] investigated that due to deformation potential the strain induced shifts occurs in the QW.

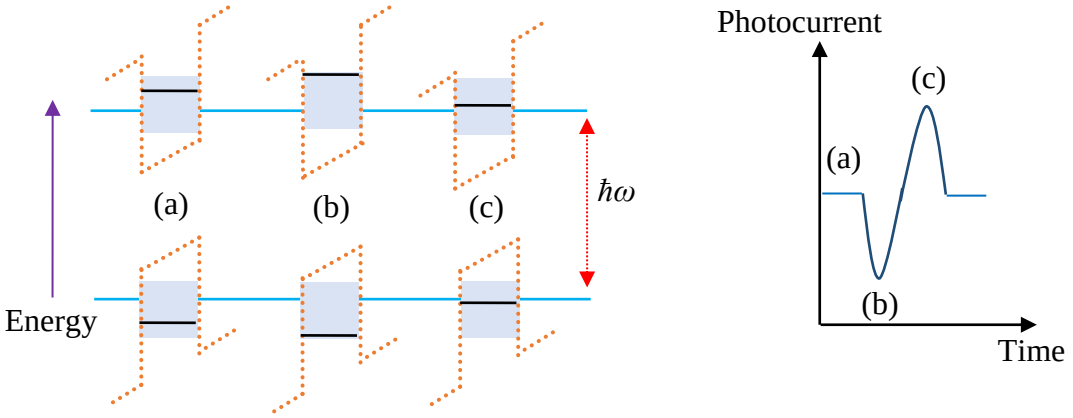



**Figure 2.10:** Schematic to demonstrate how the strain is detected by quantum well embedded *p-i-n* device. The figure on the left demonstrates the processes in the QW, while the figure on the right demonstrates the size of the photocurrent varies for the three different scenarios, *i.e.* (a) represents no strain, (b) represents compressive strain and (c) represents tension. The light blue represents the laser energy and the black line represents the energy level in the well.

To achieve the highest detection sensitivity, the device is tuned so the maximum of the laser energy is slightly smaller than the QW energy gap when no strain is present. In this case, there will be some photocurrent generated in the device but not the maximum amount possible. A compressive strain moves the energy levels within the well further from the maximum of the laser energy, this will lead to a reduction of the photocurrent in the device, whereas the tension moves the energy levels closer, causing more photocurrent.

The operation of the device can be optimised at different wavelengths by adjusting the level of bias applied to the *p-i-n* diode. This can cause large shifts in the exciton resonance of the QW. These large shifts are possible due to a process known as the quantum-confined Stark effect, which is caused by the confinement of the exciton in the QW which preventing it from being ionised. The Stark shifts can then be seen because of the applied field on the exciton [100]. Using this effect, the detector can operate at a range of wavelengths. However, as larger biases are applied the exciton peak is broadened and the device will start to lose sensitivity. This means

that width of the QW in the device needs to be chosen to give an appropriate energy gap for the required wavelength of operation. The potential wavelengths of operation for each device can be tested using the photocurrent measurements detailed in section 3.6. The width of the quantum well is also a consideration with regards to the frequency requirements of the detector. When the wavelength of the phonon incident on the detector is shorter than the width of the quantum well it is possible for both tension and rarefaction to be present within the well which will lead to the signal being averaged out. Therefore, narrower QWs provide better sensitivity to high frequency waves.

# Chapter 3

# Experimental Details

This chapter will explain the microfabrication processes and experimental methodologies used in this work. First, the general sample processing methods will be discussed. After this, sample structures fabricated using above methods will be discussed in detail. This will be followed by general details of the equipment used in the experiments. Finally, the different experimental methods along with optical arrangements will be described in more detail with a brief discussion of the data acquisition.

## 3.1 Microfabrication Processes

The microfabrication processes used to create the semiconductor devices will be discussed in this section. Several samples used in the following experiments were processed from gallium arsenide (GaAs) based semiconductor wafers which are grown at the University of Nottingham by molecular beam epitaxy (MBE) either by Professor M. Henini or Dr R. P. Campion with wafer names prefixed as 'NU' and 'RC' respectively. The samples were grown on 2-inch diameter [311] orientated GaAs semi-insulating substrates. These were then processed to different semiconductor devices in the School of Physics and Astronomy clean room facility, by the methods described in the following sub sections.

### 3.1.1 Cutting and Cleaning

Before any processing can take place, the wafer must be cut to form a device chip and cleaned. Cleaning is also required at various stages throughout the development of the final device. A standard method of cutting GaAs is to scribe the wafer surface with a diamond tipped scribe and crack the wafer along the scribed valley. A typical chip used in the following experiments was approximately 5 mm x 5 mm in dimension. Once a chip had been obtained, the well-established four solvent clean (ethyl lactate, acetone, methanol and isopropanol) was used to remove any contamination from the surface. It is important to dehydrate the chip in the oven

following the cleaning process to avoid degradation of the photoresist in the later stages. The temperature at which the dehydration is performed should be greater than the temperature of the photoresist bake. In our case 115$^{o}$C was sufficient.

### 3.1.2 Mechanical polishing

The NU samples used in this thesis were mounted in the MBE machine using indium on the back face of the sample which makes back surface of the wafer both rough and contaminated. This surface must be removed to acquire a smooth, flat, contaminant free surface. Mechanical and mechanochemical polishing was used to both ensure that a sample has a high degree of optical flatness, and to remove surface contaminants and sub-surface damage. This was important in pump-probe experiments for two reasons: firstly, a metal film adhered to a rough substrate surface will scatter light from the pump which could directly excite devices, and secondly, sub-surface damage and surface contaminants can strongly scatter acoustic phonons.

The chip was polished on a Logitech PM2A lapping & polishing machine (Figure 3.1). The machine consists of a base with a motorised spindle onto which, different polishing laps may be placed. The sample is stuck to a plate mounted in a jig (Figure 3.2) that is held on top of the lap. To make sure the sample thinned uniformly it is important that the surface of the sample to be polished is level with the edge of the polishing jig. This is achieved using the optical alignment detailed in (Figure 3.3), which involves comparing a laser spot reflected off the sample with a spot reflected off an optical flat. As the lap spins, the jig simultaneously rotates and moves laterally. Weights are placed on top of the jig so that the sample surface is pressed into the lap. Post lapping, mechanochemical polishing was performed to achieve an optically flat mirror finish to the surface using sodium hypochlorite chemical polish (Chemlox) fluid, applied to a cloth lapping plate.

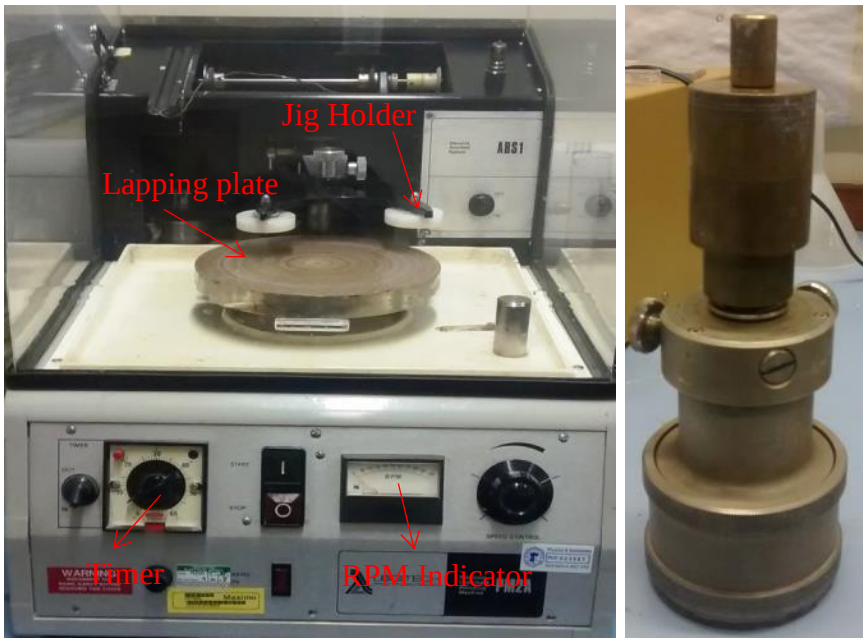



**Figure 3.1:** Polishing setup: Left, polishing system, Right, a polishing jig with weights.

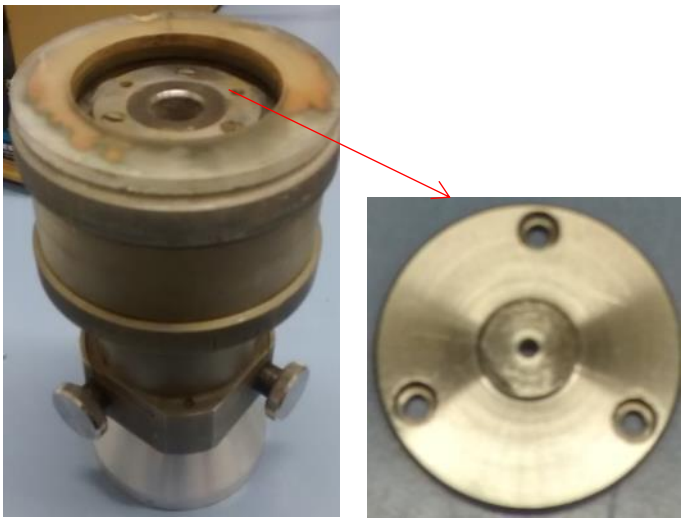


**Figure 3.2:** Polishing jig with disc mount for sample.

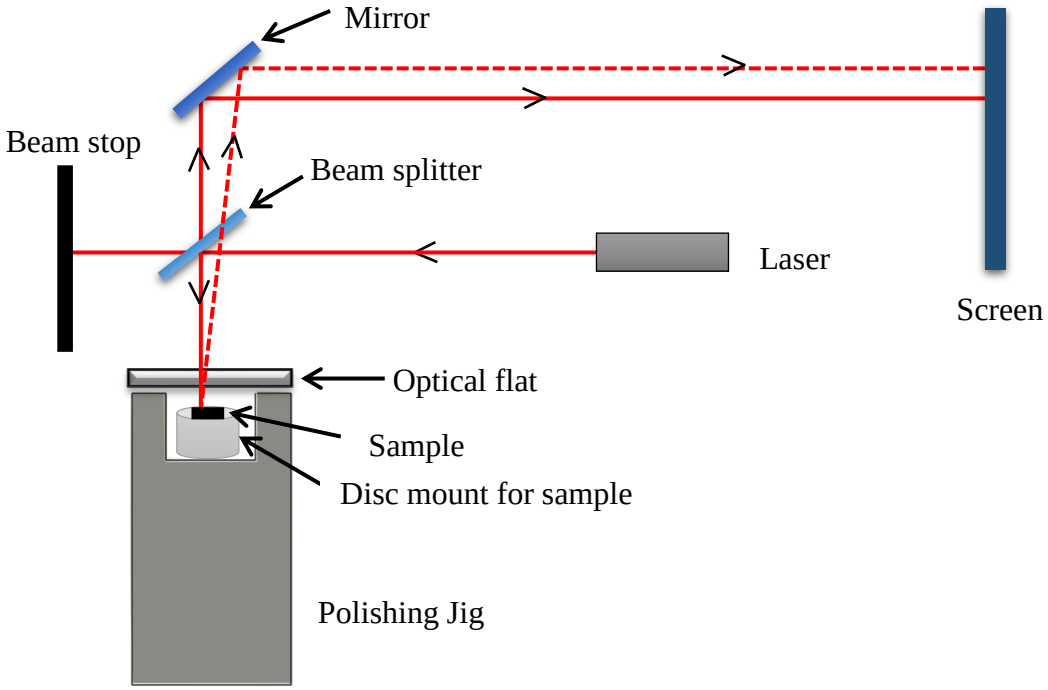



**Figure 3.3:** Optical alignment system designed to ensure surfaces are parallel to avoid the stretching of the phonon pulse by aligning the sample beam (dotted) to the reference beam (solid red line), which are caused by reflections from the sample surface and glass plate, respectively.

### 3.1.3 Photolithography and Wet etching

UV lithography or optical photolithography is the process by which a required pattern can be applied to a given surface; this pattern is used for further processes to obtain the desired device, such as by wet etching or evaporation. It is achieved by applying chemical photoresist to the sample surface in an even layer, hardening it, and exposing the relevant areas to ultraviolet radiation. Depending on whether a positive or negative photoresist is used, the UV radiation photochemically destabilises or stabilises the exposed areas, respectively. The less stable regions are therefore more soluble when immersed in photoresist developing solution and are thus removed to leave the required pattern.

In this thesis, the devices were patterned by employing standard photolithographic techniques whereby a positive photo resist (BPRS 150) was used to form the mesa pattern, ranging from 30 μm to 400 μm, through the exposure of UV light from a Karl Suss MJB 3 mask aligner. Positive photoresist was spun onto the samples at 4000 rpm to get an even coat and the samples were then baked at 90 °C for 2min on a hot plate. This soft baked sample was then exposed to UV for 6seconds with a mercury lamp power of 11mW. The UV exposed pattern was developed using a positive developer solution, AZ 400k, with a ratio of 1:8 (developer: water). By using an optical microscope, the development progress was checked regularly to prevent overdeveloping of the photoresist.

The "Sheffield" mask set was used to produce devices from 200 μm to 400 μm in diameter where optical access is required to the mesa as shown in figure 3.4a. Due to the distinct horseshoe shape of the contact mask, quantum well embedded *p-i-n* photodiodes were fabricated for the experiments described in Chapter 5. This photomask set consists of etch, top contact, and bottom contact masks which allows different top and bottom contact materials evaporation. A ground contact will be formed by the square around the edge which is marked in 3.4b.

The "Robin Hood" mask set shown in figure 3.4c. will provide electrical mesas from 30 μm to 800 μm in diameter. These mesas had no optical access and were used to fabricate the Schottky diodes discussed in Chapter 4. The Robin Hood photomask set comprises an etch mask, and a contact mask which is identical for both top and bottom contacts, so different contact material evaporation is not possible with this mask set. For Schottky diodes fabrication, combination of Robin Hood contact mask (Schottky contact) and Sheffield bottom mask (Ohmic contact) was used to get different contact materials evaporation. The "NU1080" photomask set shown in figure 3.4d. is used to fabricate two-dimensional electron and hole gas structures discussed in chapter 5. The NU1080 photomask set comprises an etch mask, and a contact mask. Dum-bell shaped 2DEG and 2DHG devices with active mesa area 200 x 200 μm wide with end contact pads were defined by wet etching using the etch mask.

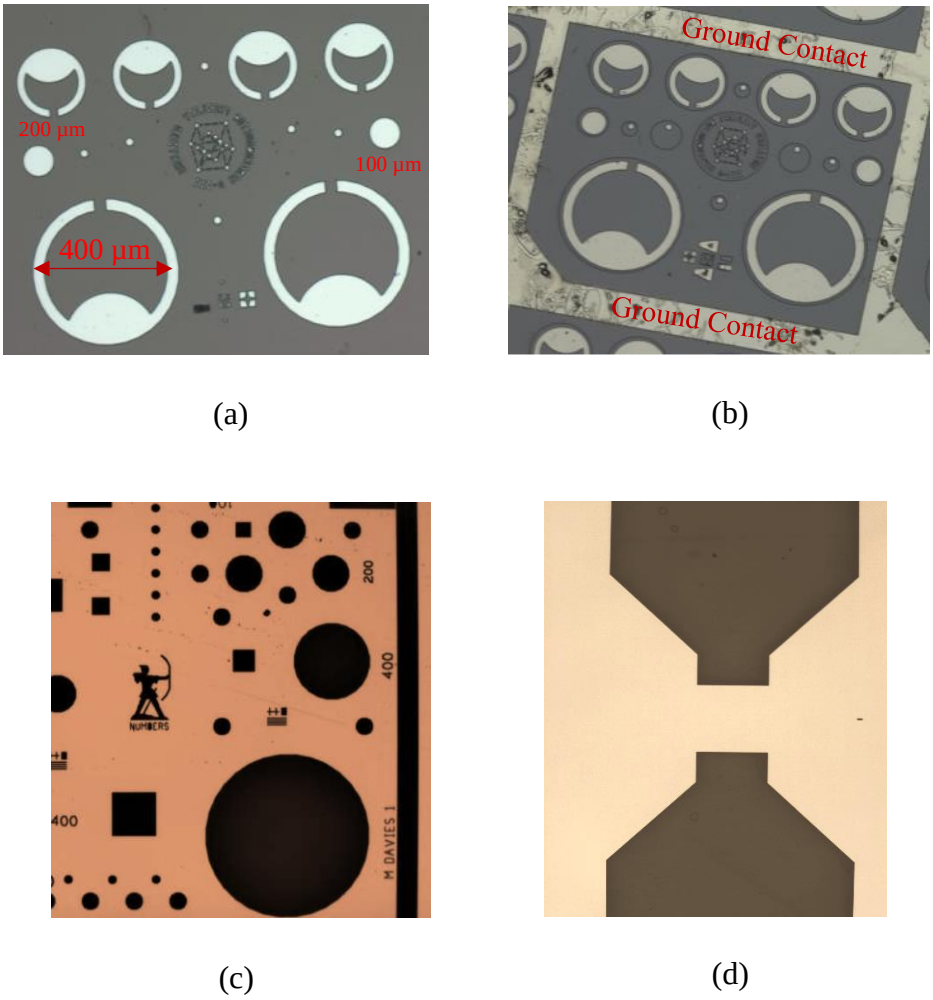



**Figure 3.4:** (a) Optical access devices, patterned using the "Sheffield" mask. (b) Ground contact produced using Sheffield bottom mask. (c) The Robin Hood photomask set used to produce electrical mesas with no optical access. (d) The NU1080 photomask set used to produce 2DEG and 2DHG structures.

Chemical wet etching is a material removal process that uses liquid chemicals or etchants to remove layers which are not necessary for experiments, and to reach specific sample layers. Materials that are not protected by the masks are etched away by liquid chemicals. For the devices discussed in this work, wet chemical etching was performed to access the bottom contact layer of each sample, which allows to apply voltage across the active region of the device. The intended height of the mesa was obtained by standard wet etching techniques using $H_2O_2$:$H_3PO_4$:$H_2O$, 10:1:20,

with a typical etch rate of ≈5nms$^{-1}$. The etch rate was monitored every 30 s intervals using a KLA Tencor D-120 Alpha Step surface stylus profiler.

### 3.1.4 Contact Formation and Annealing

Contacts were made by thermal evaporation technique under high vacuum, where the contact thickness can be controlled to sub-nanometre accuracy and annealing at a specific temperature. The desired material was evaporated by a heated filament and expanded into the chamber, before condensing onto the sample surface. An oxide etch with 1:1 solution of hydrochloric acid and distilled water was performed for 60s before loading the samples into evaporator to remove surface oxides from the sample. The sample and the sources of material to be deposited are placed in a chamber which is pumped down to pressures in the $10^{-7}$ mbar range to decreases the risk of contamination. The material sources are then heated via a current placed through a refractory metal boat until the source material starts to evaporate. A quartz crystal microbalance present within the evaporator acts as a film thickness monitor to control the amount of depositing material. The current through the boat is varied to achieve a stable evaporation rate and then a shutter is opened allowing the metal to be deposited on the sample. The shutter is closed again when the desired layer thickness is achieved. This allows the deposition of metal across the whole of the sample. To remove the excess metal, lift-off was performed by soaking the sample in warm acetone. n-type metallisations were conducted in an Edwards E306A coating system, while p-type metallisations were performed in an Edwards Auto 305 Turbo evaporator.

To form Ohmic contacts to different semiconductor materials an appropriate metal must be chosen that will diffuse into the semiconductor upon annealing. Different metals are required to form good p-type and n-type contacts. For n-type Ohmic contacts 60 nm Ge, 60 nm Au, 30 nm Ni and 150nm Au capping layer (GeAuNiAu) was used. The Ge is the dopant and the nickel layer is used to control diffusion. When forming Ohmic contacts on p-doped semiconductors, a layer of 20nm Mg was deposited followed by a 150 nm Au capping layer. For 2DEG and 2DHG structures, large-area (1 mm$^2$) diffused 15 nm Au, 30 nm Zn and 120 nm Au

(Au/Zn/Au) p-type contacts were evaporated using the contact mask to minimize the contact resistance and hence unwanted phonon radiation from contacts.

Ohmic contacts were annealed by a rapid thermal annealing (RTA) technique, which allows the diffusion of the metal into the semiconductor. An Anealsys AS-One Rapid Thermal Processing furnace with $H_2$ /Argon processing gas and graphite susceptor plate was used for this work. The rapid heating in the RTA is provided by a series of heat lamps. To ensure that this heat is transferred efficiently to the samples they are positioned within a graphite susceptor plate. The temperature can be monitored by a combination of a pyrometer and a thermocouple attached to the plate. The samples were heated to temperatures of between 350 °C to 420 °C for dwell times of 30s and then cooled back to room temperature. A purge gas of 5% $H_2$ in Argon was used to reduce oxidation of the contacts at high temperatures. Schottky contacts require an abrupt barrier between the semiconductor and metal and are not annealed. A thin 15 nm Ti layer was first evaporated to give good adhesion between the semiconductor and the thick 150 nm Au contact.

### 3.1.5 Sample Packaging

Processed samples were mounted onto a copper plated printed circuit board holder using a small quantity of GE/IMI 7031 Varnish, which is an insulating glue capable of withstanding the large temperature changes the samples are subjected to during cryogenic experiments. Figure 3.5 shows an attached sample on its holder. The copper pattern on the holder provides a ground plane and a 50 Ω strip line was connected to an SMA cable launcher.

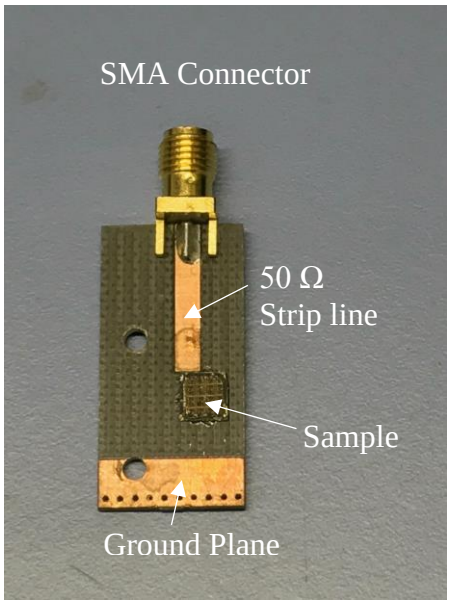



**Figure 3.5:** Picture of sample holder with a sample attached using GE varnish.

### 3.1.6 Sample wire bonding

The contacts on each processed device need to be electrically bonded to the PCB header. The bonding process was carried out using an ultrasonic aluminium wire wedge-bonder which involves the use of force, time and ultrasonics to join two materials. The wire is pressed against the contact surface at low force and vibrated for a limited period until bonding is achieved. The ultrasonic energy frees the molecules of the metal and dislocates them from their pinned positions, which allows the metal to flow under the low compressive forces of the bond. The applied force, ultrasonic energy and bonding duration were adjusted to ensure good mechanical adherence and electrical contact. Figure 3.6 shows 25μm diameter Aluminium wire bonded to a 200μm device. The quality of bond adherence can be tested by pulling on the bonded wire with a pair of tweezers. This is an important stage, as a poorly bonded contact may not exhibit Ohmic electrical properties and may come off when cooled to low temperature.

The bonding process is as follows: firstly, the free end of the aluminium wire is pressed into the first contact forming the “primary” bond; secondly, the aluminium wire is pressed into the secondary chosen contact and cut by the bonder forming the “secondary” bond.

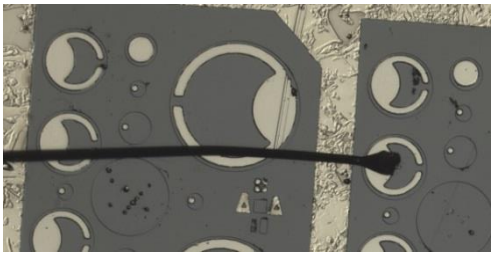


**Figure 3.6:** Device bonded with 25μm diameter Aluminium wire.

### 3.2. Sample Structures

This section will describe the five different sample structures investigated in this work. All the samples were grown on 2-inch diameter [311] orientated GaAs semi-insulating substrates using the combination of GaAs and AlGaAs. Due to the similar lattice constants of this combination, the formation of strain within the structures will be prevented. In addition, as GaAs is a direct bandgap semiconductor, with high electron mobility making it ideal for the creation of devices which is good in optical and electronic properties. Schottky diodes, two-dimensional electron gas structures (2DEG) and two-dimensional hole gas structures (2DHG) were processed on NU927, NU2080 and NU1074 wafers respectively whereas Quantum Well (QW) incorporated between AlGaAs *p-i-n* photodiodes on RC34 and InGaAs based *p-i-n* photodiodes on RC80 were processed as described in section 3.1.

#### 3.2.1 NU927

Figure 3.7 shows the sample structure of NU927 wafer on which Schottky diodes were processed. A 1.5 μm-thick n-GaAs layer, doped with Si to a density of $n_D$ =1 x $10^{17}$ $cm^{-3}$, was grown by molecular beam epitaxy on a (311B) surface of the 380 μm thick semi-insulating GaAs substrate. On the top of this, a 150 nm-thick Au Schottky contact was deposited as described in section 3.1. The structure was processed (as described in section 3.1) into 100 μm-diameter and 0.8 μm-tall vertical device mesas, and a GeAuNiAu Ohmic contact was made to the n-GaAs layer. A 100nm thick Al film was deposited by thermal evaporation as described in section 3.1.4 on the

opposite face of the substrate. The Schottky and bottom contacts were Al wire bonded to the central SMA pin and the ground plate respectively. Measurements were then performed with the experimental setup as described in section 3.6.

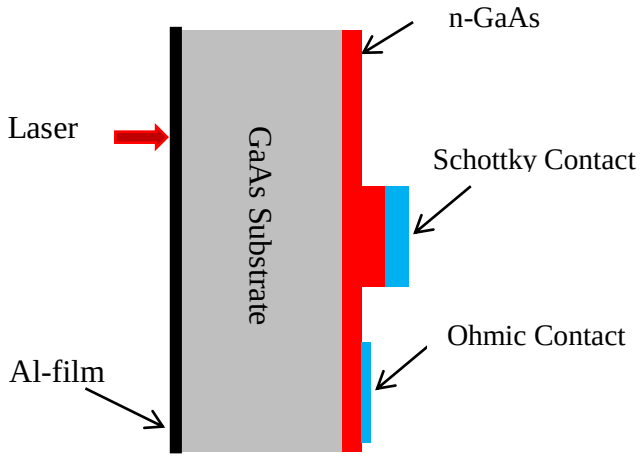



**Figure 3.7:** Schematic of NU927 layer structure. Silicon doping concentration of 1.5 μm-thick n-GaAs layer is 1 x $10^{17}$ $cm^{-3}$. The Schottky contact was bonded to central SMA pin whereas Ohmic contact to ground plate of the sample holder.

### 3.2.2 RC34

Figure 3.8 shows the sample structure of RC34 wafer on which QW *p-i-n* diodes were processed. The p-layer was grown first in this sample, as opposed to the n-layer being grown first in normal samples. This was found to be necessary due to the growth requirements for doped AlGaAs on a (311) substrate. The stepped layer of the surface makes it more prone to roughening. Also, the nature of the exposed bonds on this surface mean that the doping must be treated differently to doping of (100) grown GaAs. In the structure shown in figure 3.8, p-doping (bottom contact) is provided by Si and the n-doping (top contact) is provided by Te, the doping in both cases is $10^{18}$ $cm^{-3}$ as is usual for contact layers. This structure was grown on the *A* face of the (311) substrate where it is possible for Si to act as a p-dopant, rather than as the n-dopant it normally forms in (100) GaAs. This was necessary because the carbon which is often used as a p dopant was not found to be effective on the (311) orientation of GaAs. This wafer consists a 200nm thick p-type $Al_{0.33}Ga_{0.67}As$ bottom

contact layer grown on top of a commercially available 445 µm thick semi-insulating GaAs substrate. A 7.5nm undoped GaAs QW is located between two 100nm undoped $Al_{0.33}Ga_{0.67}As$ intrinsic regions of the device. A top contact layer was deposited above the intrinsic region, which consists of 200nm thick n-type $Al_{0.33}Ga_{0.67}As$. The buffer layers between the substrate and the active device are required for a high-quality MBE growth but do not have a significant effect on the experiments hence not detailed here. The sample was processed into optical access mesas as described in section 3.1 using the Sheffield mask, and were mounted onto the sample holder as shown in figure 3.5. On the rear surface of the substrate a 30nm thick Aluminium film transducer was deposited by thermal evaporation as described in section 3.1.4. The top and bottom contacts were Al wire bonded to the central SMA pin and the ground plate respectively. Measurements were then performed with the experimental setup as described in section 3.7.

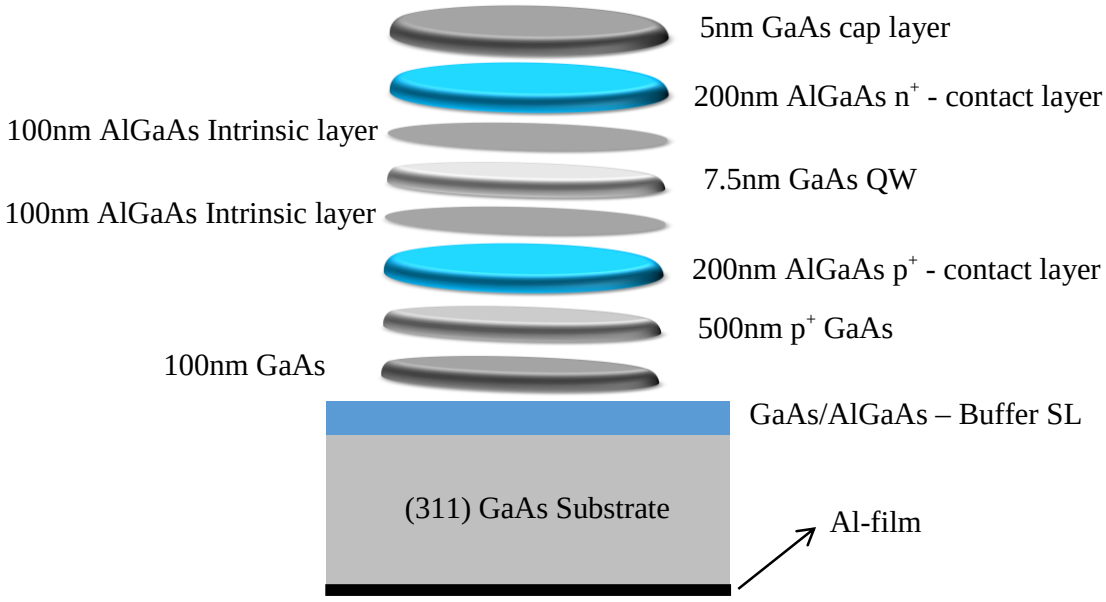



**Figure 3.8:** Schematic of RC34 layer structure. All contact layers are doped to $10^{18}$ $cm^{-3}$, p-type contact layers are Si doped while n-type contact layers are Te doped. All AlGaAs layers feature 33% Aluminium.

### 3.2.3 RC80

On a (311) substrate, the AlGaAs intrinsic layers have a somewhat rough interface which affects the quality of a GaAs QW. In RC80 wafer, instead of AlGaAs layers, GaAs barriers were used with smaller gap material for QW. Figure 3.9 shows the sample structure of RC80 wafer on which InGaAs based QW-*p*-*i*-*n* diodes were processed. In the structure shown in figure 3.9, both p doping (bottom contact) and n doping (top contact) is provided by Si, the doping in both cases is $2x10^{18}$ $cm^{-3}$ as is usual for contact layers. This structure is very like RC34 structure expect the thickness of quantum well. The basic difference in this structure is all AlGaAs layers were replaced with GaAs layers. This wafer consists a 500nm thick p-type GaAs bottom contact layer grown on top of a commercially available 448 μm thick semi-insulating GaAs substrate. A 5nm undoped InGaAs QW is located between two 100nm undoped GaAs intrinsic regions of the device. A top contact layer was deposited above the intrinsic region, which consists of 500nm thick n-type GaAs. Finally, a 30nm undoped GaAs cap layer was deposited which is not necessary for the experiments hence it was etched as described in section 3.1.3. The sample was processed into optical access mesas as described in section 3.1 using Sheffield mask, and were mounted onto the sample holder. On the rear surface of the substrate a 30nm thick Aluminium film transducer was deposited by thermal evaporation as described in section 3.1.4. The top and bottom contacts were Al wire bonded to the central SMA pin and the ground plate respectively. Measurements were then performed with the experimental setup as described in section 3.7.

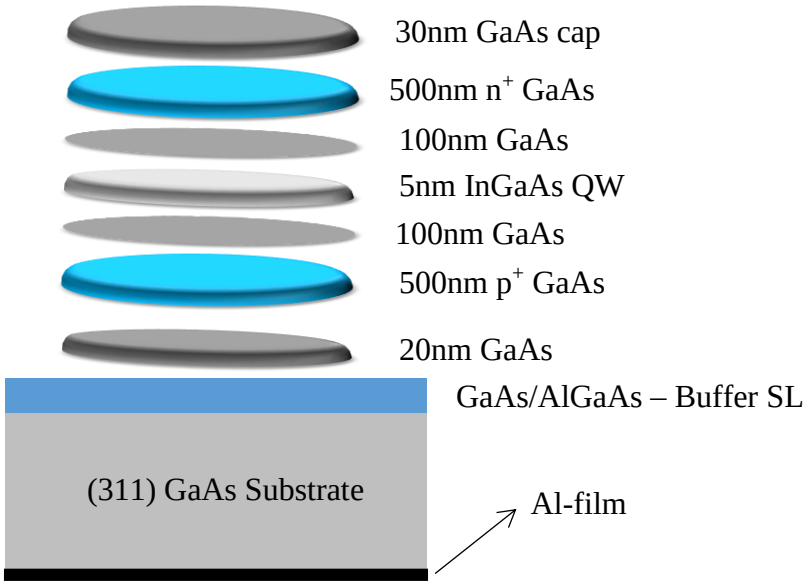



**Figure 3.9:** Schematic of RC80 layer structure. All contact layers are doped to $2x10^{18}$ $cm^{-3}$, both p-type and n-type contact layers are Si doped. The buffer layers between the substrate and the active device are required for a high-quality MBE growth but do not have a significant effect on the experiments.

### 3.2.4 NU2080

The two-dimensional electron gas (2DEG) trapped at a doped heterojunction is a very important low-dimensional system for electronic transport. 2DEGs offer a stable system of extremely high mobility electrons, especially at low temperatures. Using gallium arsenide (GaAs) to replace silicon as semiconductor material in active devices has been of great interest because electron mobility in GaAs is six times higher than that for silicon (8,600 $cm^2/Vs$ for GaAs and 1,350 $cm^2/Vs$ for Si at room temperature). Figure 3.10 shows the layer structure of NU2080 on which two-dimensional electron gas structures were processed as described in section 3.1. It is important to note that (311) A GaAs is very anisotropic in nature, and to obtain the highest mobility the hall bar should be oriented [-233] direction. The structure consists of 500nm thick undoped GaAs layer grown on top of a commercially available 380 μm thick semi-insulating GaAs substrate. This undoped layer has significantly lower band-gap than the 40nm thin $Al_{0.33}Ga_{0.66}As$-doped layer. Doping

is provided by Si to a density of $1.3 \times 10^{18}$ $cm^{-3}$. The different band-gap is because of the electrons generated in the n-type AlGaAs thin layer all migrate to the GaAs layer left empty by the previous layer due to the heterojunction formed by the two materials having a different band-gap, forming a quantum well in the GaAs conduction band. In this case, electrons can move freely without scattering from ionized impurities because the electrons are confined inside an un-doped layer. The resultant effect is the formation of a very thin inversion layer called two-dimension electron gas as shown in figure 3.11, having a high electron concentration and high carrier mobility, giving the channel very low resistivity. On the rear surface of the substrate a 30nm thick Aluminium film transducer was deposited by thermal evaporation as described in section 3.1.4. Figure 3.12 shows a processed 2DEG sample which is mounted on the sample holder and indium bonding was performed manually.

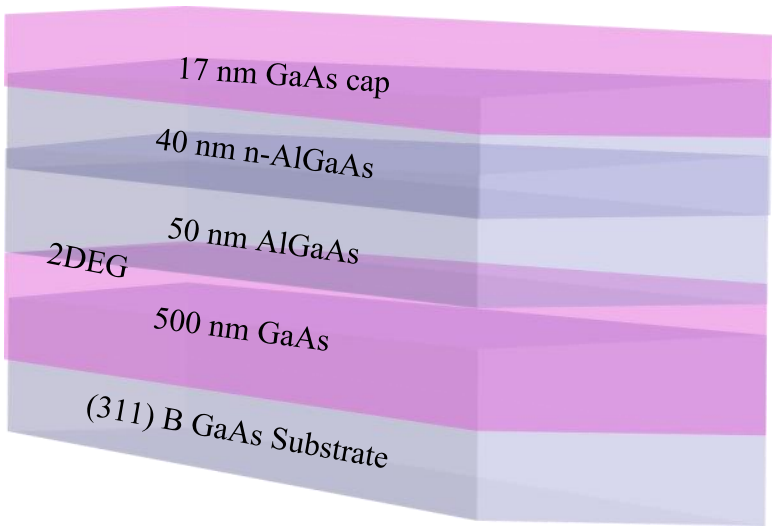



**Figure 3.10:** Layer structure of NU2080 wafer. GaAs/AlGaAs heterostructure, which forms a two-dimensional electron gas (2DEG) at the material interface.

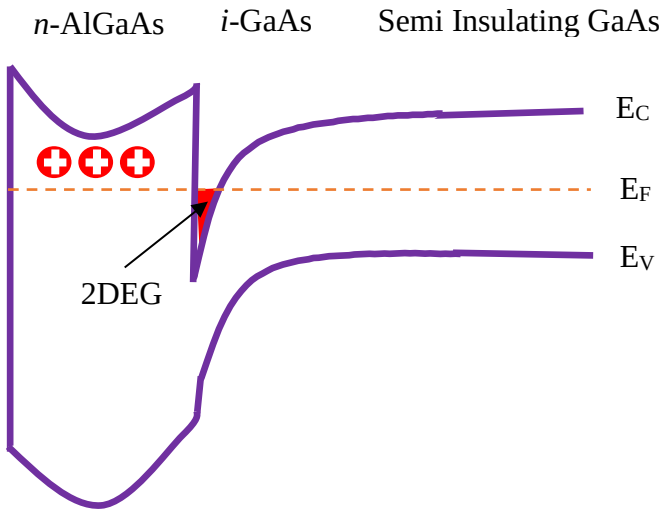



**Figure 3.11:** Schematic of Two-Dimensional Electron Gas energy band diagram based on GaAs/AlGaAs heterostructure layers. The red portion represents the 2DEG region.

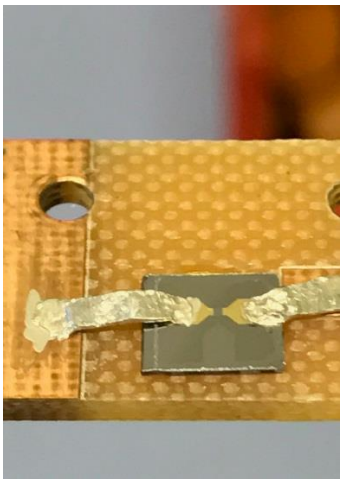


**Figure 3.12:** Processed 2DEG sample on the sample holder with indium bonding.

### 3.2.5 NU1074

The analogous construct of holes is called a two-dimensional hole gas (2DHG), figure 3.14 shows the layer structure of NU1074 on which two-dimensional hole gas structures were processed using the methods described in section 3.1. The structure consists of 500nm thick undoped GaAs layer grown on top of a commercially available 385 µm thick semi-insulating GaAs substrate. The 2DHG is confined in a single GaAs/$Al_{0.33}Ga_{0.67}As$ heterostructure with a Si doping layer to a density of $5x10^{17}$ $cm^{-3}$ placed at 80 nm from the interface. Figure 3.13 shows the schematic of Two-Dimensional Hole Gas energy band diagram, Holes (missing electrons in the valence band) collect at the interface creates 2DHG region represented by red portion. On the rear surface of the substrate a 30nm thick Aluminium film transducer was deposited by thermal evaporation as described in section 3.1.4. Processed 2DHG sample which is mounted on the sample holder and indium bonding was performed manually is similar as shown in figure 3.12.

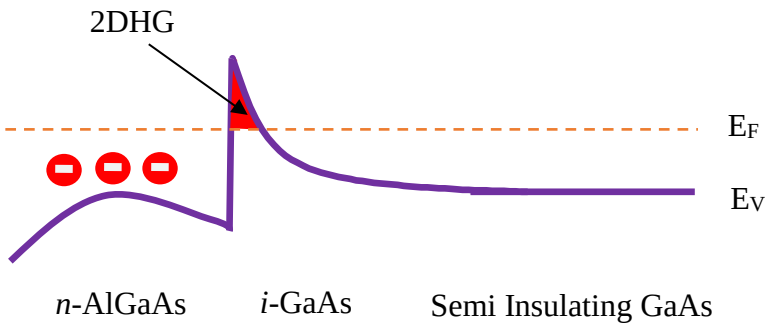



**Figure 3.13:** Schematic of two-dimensional hole gas energy band diagram based on GaAs/AlGaAs heterostructure layers. The valence band is shifted upwards to cross the Fermi level energy to cause the creation of 2DHG region represented by red portion.

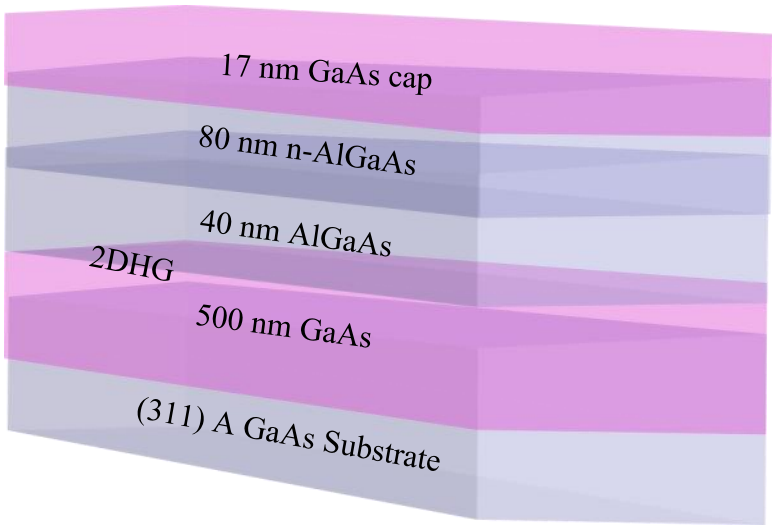



**Figure 3.14:** Layer structure of NU1074 wafer. GaAs/AlGaAs heterostructure, which forms a two-dimensional hole gas (2DHG) at the material interface. Silicon doping concentration of n-GaAs layer is 5 x $10^{17}$ $cm^{-3}$.

### 3.3. Lasers

Two laser systems were used in this work: a high power amplified system and an oscillator system. The amplified system can achieve pump powers of the order of mJs with low repetition rate; while oscillator system generates pump powers of nJs with a higher repetition rate. These systems will be discussed along with health and safety measures in this section.

#### 3.3.1 Health and Safety

Appropriate health and safety measures should be taken when performing experiments with lasers, especially the class IV lasers discussed herein. Laser safety goggles should be worn, which have appropriate safety ratings, by all personnel. The laboratory should be kept clean and tidy to remove trip hazards, windows should be covered to prevent accidental transmission or reflection of stray beams, interlock systems should be installed at all doors, and appropriate warning signs and signals should also be installed.

When aligning systems, laser power should be reduced as much as possible and, when removing reflective objects such as lens and mirrors, the laser must be suitably blocked to prevent stray reflections, and only one system per laboratory should be in operation at any one time. A more detailed account of health and safety measures can be found in various literatures, such as the CVCP Notes of Guidance [101].

### 3.3.2 Amplifier

The fast-electrical measurements were performed using an amplified titanium sapphire laser system consisting four main components manufactured by Spectra-Physics. The Millennia Pro solid state continuous-wave (CW) green laser pumping a Tsunami ultrafast titanium sapphire oscillator to produce optical pulses. These pulses were directed into a Spitfire Pro amplifier pumped by an Empower diode-pumped pulsed green laser. For the experiments described in this report, the output of the laser is centred at wave length 800 nm with 80 fs duration, and 5 kHz repetition rate.

### 3.3.3 Oscillator

A Spectra Physics Ti: Sapphire Tsunami laser system was used to perform photocurrent pump-probe measurements. The Ti: Sapphire rod is pumped using a Spectra Physics Millenia Xs Nd:$YVO_4$ diode laser. The accessible wavelength range of this laser system is 690-1080 nm with 120 fs pulse duration and a repetition rate of 82 MHz. The wavelength is tuned using a prism and slit arrangement. Prisms are used to introduce negative dispersion into the system and a movable slit selects the wavelength region required.

## 3.4 Cryostat

All experiments described in this thesis were performed at low temperatures to prevent the attenuation of high frequency phonons as they propagate through the substrate and to reduce the influence of the thermal background in samples unless until specified separately. Two different cryostats were used is briefly described here.

### 3.4.1 Bath Cryostat

For low temperature pump – probe measurements, the 'Optistat Bath Cryostat' made by Oxford Instruments was used. This cryostat contains several layers to insulate the sample space from the outer environment and 'hold' the low temperature during experiments. The sample space is at the core of the cryostat, surrounded by a radiation shield thermally coupled to a liquid helium reservoir. Liquid or gas helium was then supplied to the sample space through a needle valve. An adjustable needle valve control, located at the top of the cryostat is used to optimise the flow of helium. Surrounding the liquid helium reservoir, and insulated from it by a vacuum space, is a liquid nitrogen reservoir, acting as a radiation shield and therefore, substantially reducing the helium boil-off rate. The outermost layer incorporates a shell of vacuum space (pumped down to at least 10-4 mbar) to isolate the inner cryostat from the room temperature surroundings. Encompassing the sample space at the bottom end are five indium sealed quartz windows for optical access.

Experiments were conducted at temperatures between 10 and 1.5 K, achieved by pumping on the sample space using a rotary pump. A manostat, situated between the pump and the cryostat, was used to set (lock) the pressure at a certain level to maintain the required temperature. Accurate measurements of the temperature within ± 0.05 K was achieved using the Allen Bradley resistor that was mounted on the sample probe together with a heater. Below 4.5 K (in liquid helium), stable temperature was achieved by stabilising the helium flow through a combination of the needle valve position and the manostat pressure. Above 4.5 K (in helium vapour), optimum temperature stability of the desired temperature was achieved using the heater. Stabilised temperature was controlled in both cases using the resistor by means of software, implementing a proportional-integral-derivative (PID) feedback loop.

By having a good vacuum and a filled nitrogen reservoir, to minimise helium boil-off rates, low temperatures are maintained in the system up to a full day, without the need to refill the liquid helium reservoir during experiments. The sample holder is mounted at the bottom of the sample rod. Coaxial pin connections are available from the head of the rod that may be used to make connections to any devices on the

sample. A Vernier micrometer, also located at the rod head, provided height control for the sample holder. It was also possible to rotate the rod to make the sample's surface in parallel with one of the cryostat windows if required.

### 3.4.2 Continuous Flow Cryostat

For the fast-electrical measurements, an Oxford instruments Optistat CF-V liquid helium Continuous Flow cryostat was used. In this system helium was transferred continuously from a helium Dewar to the cryostat using a well-insulated transfer tube. A needle valve located on the transfer tube was used to control the flow. The sample was mounted on a heat exchanger that thermally couples the liquid helium to the sample. Through a combination of the heater and sensor incorporated in the heat exchanger, stable temperatures were attained. The temperature was measured and controlled by the ITC 503S temperature controller that used a PID feedback system. Temperatures as low as 3.8 K may be achieved under constant pumping from a large rotary pump.

## 3.5 Transport measurements

To understand the transport characteristics of a device, it is necessary to obtain the current-voltage (I-V) characteristics of the device before using the device for experiments. Matlab GUI (also known as Graphical User Interfaces) was used for this purpose which provides point-and-click control of software applications, eliminating the need to type commands to run the program. Current Voltage Measurements Graphical User Interface (GUI) was created using matlab and for this purpose we used a Keithley 2401 source meter interfaced via a low-cost Prologix GPIB-USB controller. This GPIB-USB controller converts any computer with a USB port into a GPIB Controller or Device. In Controller mode, the GPIB-USB controller can remotely control GPIB enabled instruments such as Oscilloscopes, Logic Analysers, and Spectrum Analysers. In Device mode, the GPIB-USB controller converts the computer into a GPIB peripheral for downloading data and screen plots from the instrument front panel. In both modes, the GPIBUSB controller interprets high level commands received from the host computer and performs the appropriate

low-level GPIB protocol handshaking. Each GPIB object is associated with one controller and one instrument. The GPIB address consists of the board index of the GPIB controller, and the primary address and (optionally) the secondary address of the instrument and the term "board index" is equivalent to the term "logical unit". We must specify the board index and instrument primary address values during GPIB object creation and the same should be used during programming. If the instrument has a secondary address, we can specify its value during or after object creation by configuring the secondary address property. We can perform the Write and Read Operations using “fprintf” and “fscanf” respectively.

fprintf → Write text to an instrument.
fscanf → Read data from an instrument and format as text.

By using GPIB configurator we can select the available devices and verify the communication with an instrument. Figure 3.15 shows the screen shot of Current Voltage GUI and the flow chart (see figure 3.16) describes how it works. For the programming details, see appendix A.

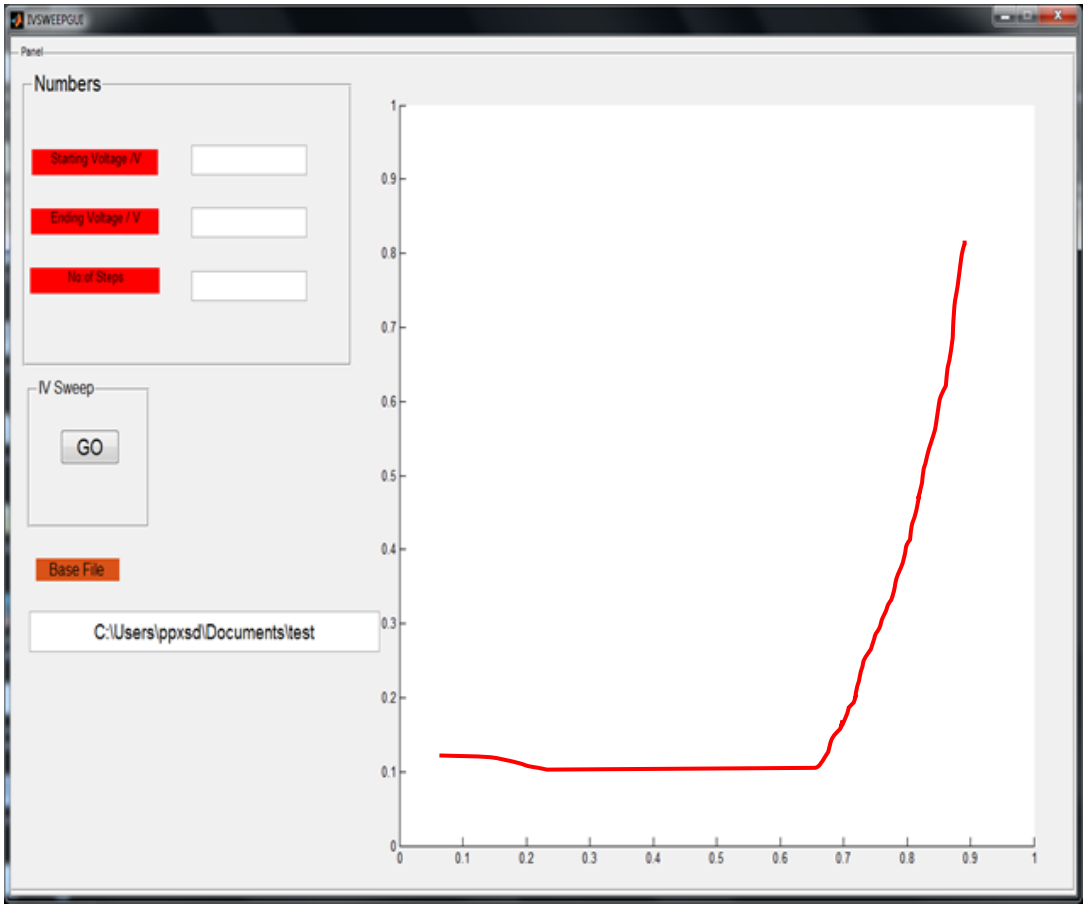



**Figure 3.15:** Screen shot of current-voltage graphical user interface.

Horizontal axis = Voltage (V)

Vertical axis = Current (mA)

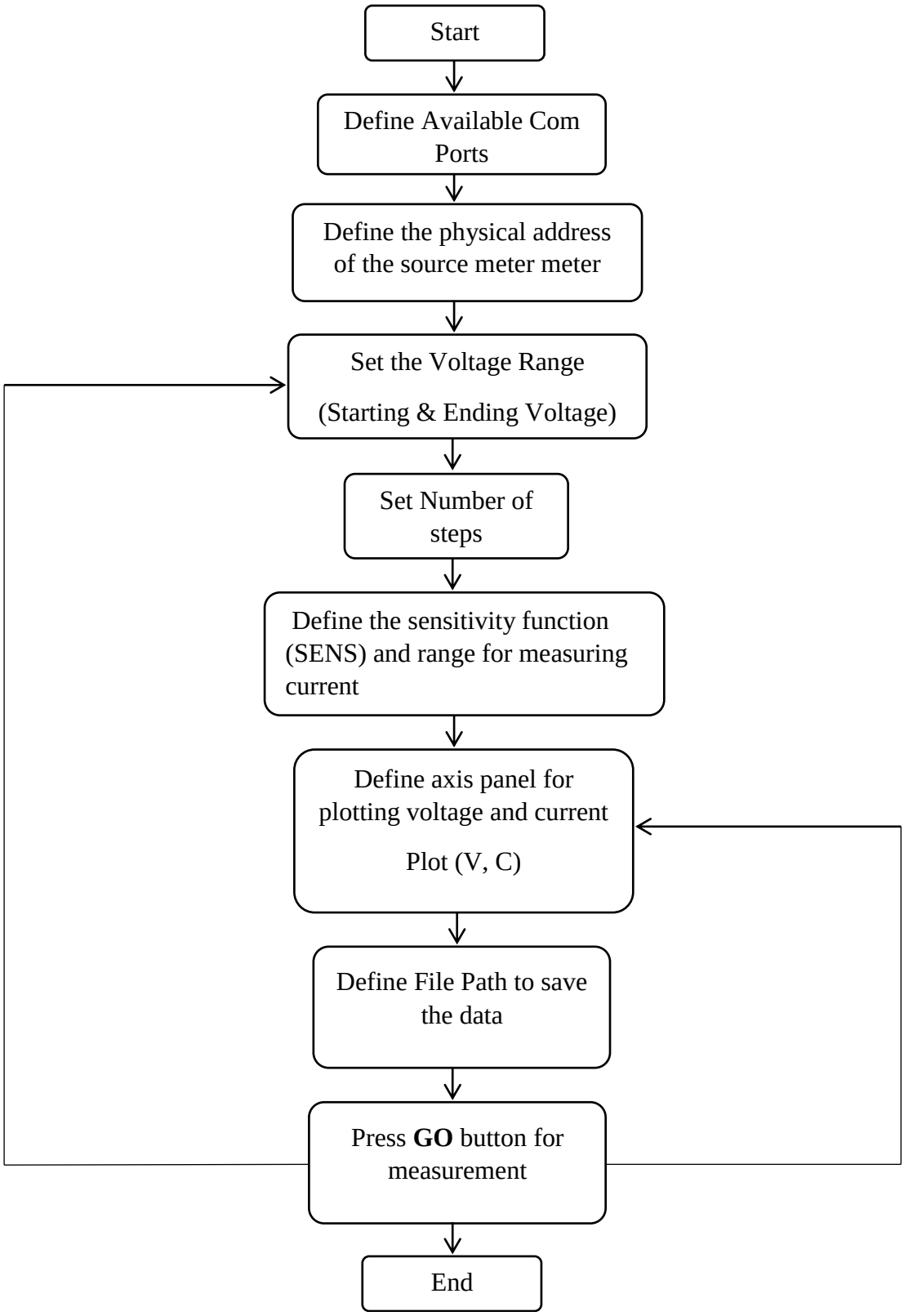



**Figure 3.16:** Flow chart for current voltage graphical user interface.

### 3.6 Fast electrical measurements

Fast electrical measurements were performed on Schottky Diodes and two-dimensional electron and hole gas structures as detailed in chapter 4 and 5 using the experimental scheme shown in figure 3.17, where the sample is maintained at 5K with liquid helium. Amplified pulses from the Spitfire Pro were directed through various optical components so that 800nm wavelength pulses were focused to a beam spot diameter of 50 μm. The spot was aimed onto an Al film evaporated on the rear surface of the sample directly behind the connected device. For blue light experiments (without Al film) 400 nm wavelength was produced by the combination of a doubler and a 400 nm interference filter.

A voltage bias was applied externally to the device using a Keithley 230 programmable voltage source, and the electrical signal from the device was passed through two 10dB amplifiers before being recorded on a 12.5 GHz analogue bandwidth Tektronix DPO 71254 digital oscilloscope, which will allow real time observation of strain-induced effects in Schottky Diode. A maximum fluence of 10 $mJ/cm^2$ was incident on the Al film thus generating bipolar strain pulse via thermoelastic effects. The oscilloscope was triggered by the triggering photodiode shown in figure 3.17 and data was recorded with a 4ps resolution and 10000 averages.

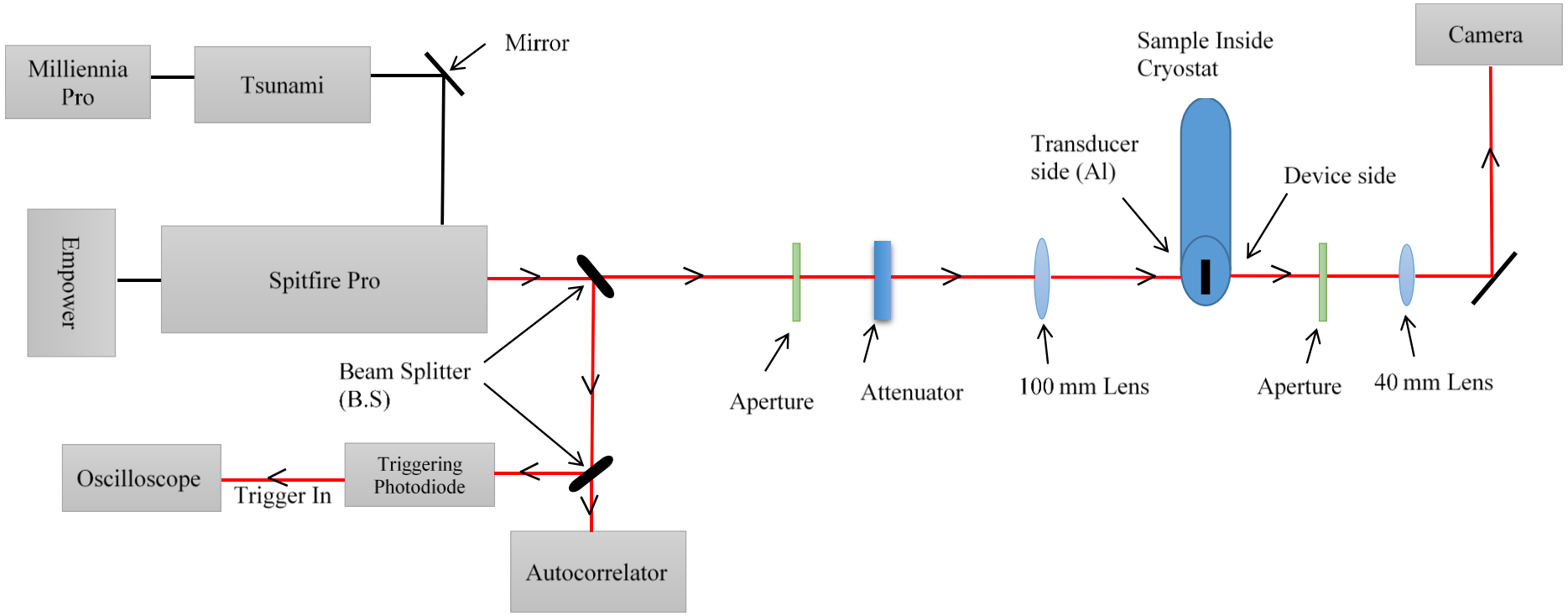



**Figure 3.17:** Experimental Setup for fast electrical measurements. The electrical connections between the Cryostat and Oscilloscope are shown in figure 3.18.

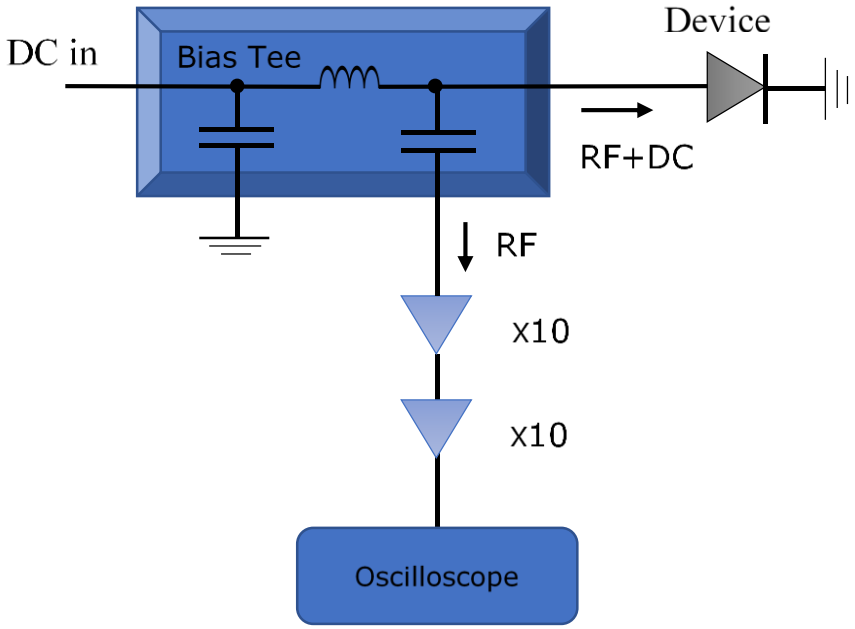



**Figure 3.18:** Schematic of circuit used for fast electrical measurements.

### 3.7 Photocurrent pump-probe measurements

Photocurrent pump-probe measurements were performed on *p-i-n* photodiode detector fabricated from RC34 and RC80 using the experimental scheme shown in figure 3.19. These measurements required a pump-probe arrangement, using the oscillator laser described in section 3.3.3. This technique is commonly used to investigate relaxation processes in various samples types. Though there are many variations on this technique, they all share a common principle which is an intense laser pulse (pump pulse) is incident on the sample, followed after a known time delay by a less intense pulse (probe pulse). The less intense pulse, which is normally transmitted or reflected, is collected and measured to reveal information about the sample at the known time delay. In this work, the absorbed pulse is generating photocarriers, which are electrically probed by using the circuit shown in figure 3.20. A general description of pump-probe techniques can be found elsewhere in the literature [102]. The pump and probe spots were incident on the transducer and *p-i-n* detector, respectively. To align the probe spot on the *p-i-n* detector a camera is used, and a luminescence signal which can be seen from the pump spot through the

substrate is used to align it opposite. The delayed probe beam will excite carriers in the quantum well at approximately the same time as the arrival of the strain pulse which allows to measure strain induced effects. This delay is dependent on the propagation of the strain pulse through sample and in this case, it was calculated to be 81.03ns for a GaAs substrate thickness of 444 μm which is equal to optical delay path of 24.31 meters. In general, to achieve this delay two parallel bar mirrors will be used for multiple reflections. Even using high quality mirrors, the beam diverges and the power decreases significantly. Therefore, this experiment is performed with the oscillator laser described in section 3.3.3, because of its high repetition rate it is possible to lower the path length requirements. The oscillator has a pulse repetition rate (T=12 ns) which is an order of magnitude smaller than the time of flight for a strain pulse through the substrate. Time delays corresponding to multiples of the 12-ns time separation between the laser pulses can be achieved simply by using a later pulse to probe. The optical delay provided by the laser path then only needs to cover the remainder left when the time required is divided by 12 ns. A manual delay stage is included in the probe beam for ease of fine tuning of the probe path to match this condition. The sample in these measurements was maintained at 10K by using the bath cryostat described in section 3.4.1.

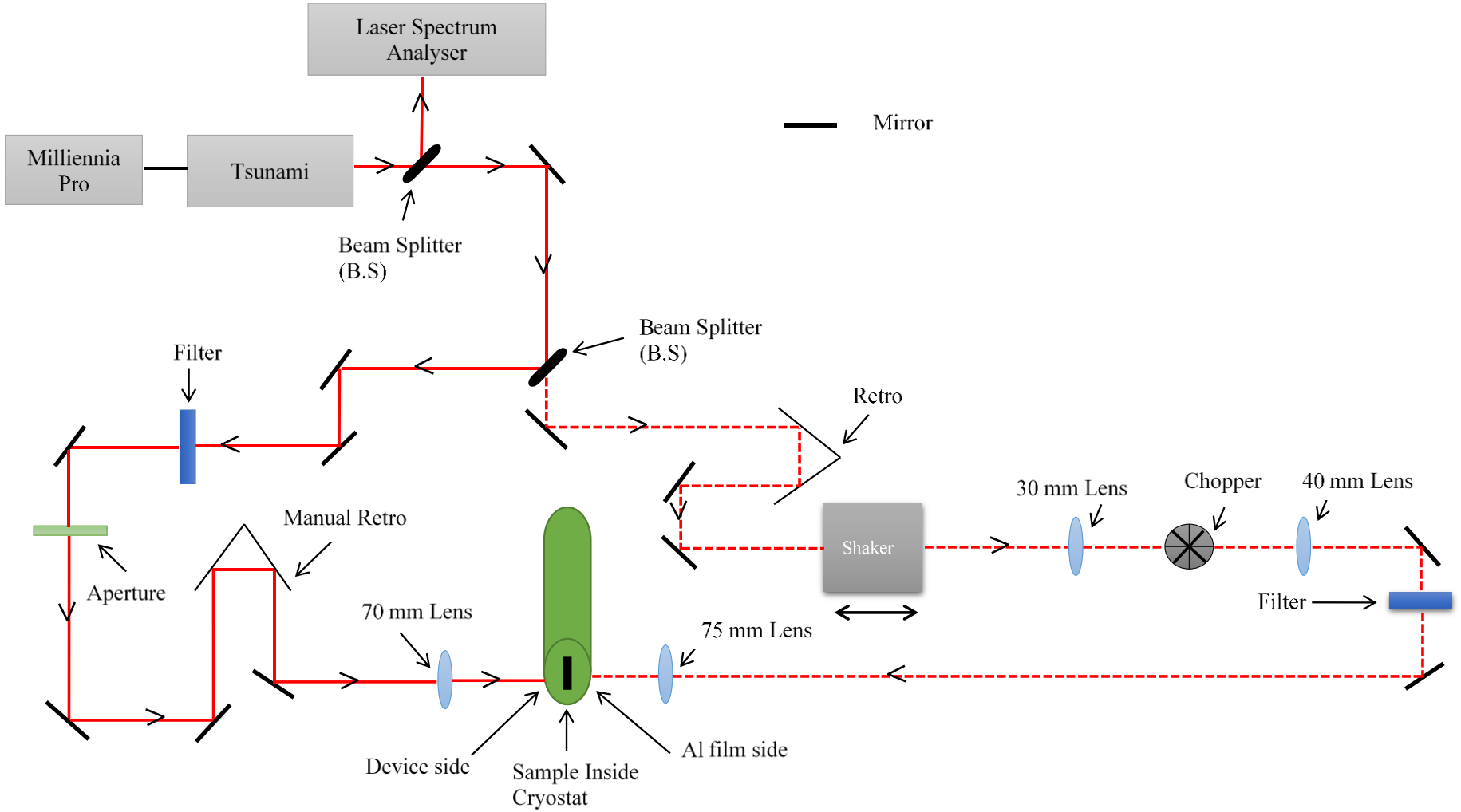



**Figure 3.19:** Experimental Setup for *p-i-n* experiments. The pump beam path is shown by a dotted line and the probe by a solid line. The electrical connections between the Cryostat and Oscilloscope are shown in this figure 3.20.

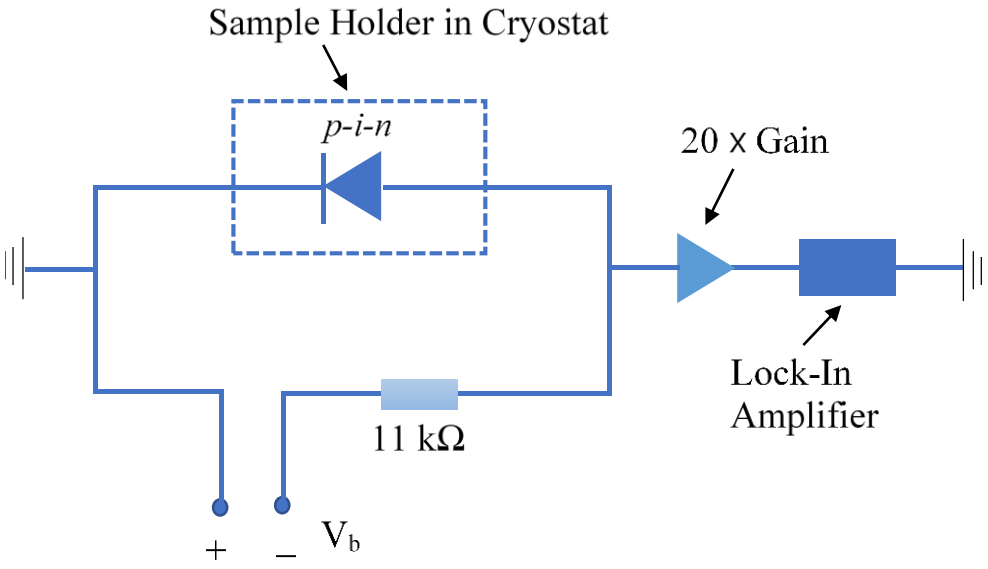



**Figure 3.20:** Schematic of circuit used for *p-i-n* experiments. The device was biased and electrically probed using the given circuit, in which the signal was fed through a 20x gain high impedance amplifier and the change in photocurrent was measured through a Stanford Research Systems SR830 DSP Lock-In Amplifier referenced to the chopper.

# Chapter 4

# Piezoelectric response to coherent longitudinal and transverse acoustic phonons in a semiconductor Schottky diode

## 4.1 Introduction

Schottky diodes can be used to detect ultrafast strain pulses without the need for a laser as part of the detection scheme, as was demonstrated by Moss *et al.* [23]. This suggests that Schottky diodes are a strong candidate for detection devices for all-electronic picosecond acoustics experiments. In that work, the phonon-induced electrical signals in a Schottky diode fabricated on high-symmetry (100) crystallographic planes was governed exclusively by the deformation potential mechanism and are not sensitive to the shear strain components (Transverse Phonons).

In picosecond strain-pulse experiments, the static piezojunction model as described in section 2.2.4 breaks down because of two reasons. Firstly, these experiments were predominantly carried out at low temperatures (T ~ 5K) where minority carrier populations and therefore diffusion current, the dominant contribution to the static effect, was small in magnitude. Secondly, since the picosecond temporal duration of the pulse leads to ultrafast changes in the band structure of a semiconductor, the equilibrium condition assumed by the static model no longer applied.

In the static piezojunction effect, the strain modifies the carrier population transfer through the Schottky barrier due to variation in barrier height or tunneling transmission. In previous experiments with a static or slowly varying strain in semiconductor junctions, the response was proportional to forward bias and very small at reverse bias [95]. Conversely, experiments performed by D. M. Moss *et al.* [23] observed a substantial response of the device to the strain at reverse bias ($V_b$ < 0). Therefore, authors in this paper considered a mechanism that is fundamentally different from the static case. The proposed mechanism in this work gives a strong electrical response due to the dynamical screening of the potential perturbations in the semiconductor band structure induced by the strain pulse. Electron redistribution in the semiconductor causes such screening which gives rise to a displacement current through the diode. In bulk semiconductors, there is a uniform distribution of carriers, and so no net charge flow but in the Schottky diode, the strongly non-uniform distribution of carriers give rise to an electrical response -no conventional current flows since the diode is reverse biased. The figure 4.1 (a) (*Source*: ref. D. M. Moss et al. [23]) shows the conduction band diagram of the (degenerate) Schottky diodes under equilibrium conditions (i.e. no strain). For $V_b$ < 0 there is negligible current flow and the electron density at a distance $x$ into the semiconductor interface $n(x)$ is close to the equilibrium value $n_o(\mu(x))$, a function of the local electro-chemical potential $\mu\ (x) = E_F - \varphi\ (x)$, where $E_F$ is the Fermi energy, and $\varphi\ (x)$ the equilibrium band edge potential energy which can be found from the solution of the Poisson equation with the relevant boundary conditions. The approximate depletion region width $x_d$ is shown in equation 2.7.

Figure 4.1 (b) (taken from [23]) demonstrates the case of the Schottky diode band diagram fragment in the presence of a symmetric bipolar strain pulse $\varepsilon\ (x,\ t)$ propagating in the GaAs towards the Schottky barrier. At each $x$ and $t$, the strain modifies the energy of the band edges, shifting them in accordance with the deformational potential model on a value: $U\ (x,\ t) = \Xi\ \varepsilon\ (x,\ t)$, where $\Xi$ is the deformation potential constant for electrons in GaAs. Under uniaxial stain, this value is in the range $\Xi \approx -6.3$ to $-13.5$ eV, taken from studies of the optical band gap [97, 103]. This perturbation is partially screened by the free electrons, which undergo a

spatial redistribution. The total charge $Q$ induced by the electron redistribution is given as by equation 4.1:

$$Q(t) = -eA \int dx \{ \varepsilon_0 ( \mu' (x,t) ) - \varepsilon_0 (\mu (x,t))\} . \quad (4.1)$$

In equation 4.1 the electron density is given by $\varepsilon (x,t) = \varepsilon_0 ( \mu' (x,t))$, where $\mu' (x,t) = E_F - \varphi (x) - U (x, t) - \delta \varphi (x, t)$, $\delta \varphi$ is electrostatic energy induced by redistribution of the electrons and $A$ is the cross-sectional area of the device. If the strain pulse is localised in a region of the device that has a uniform carrier distribution, $Q$ is constant and therefore no current is induced. However, when the strain pulse passes through a non-uniform region, $Q$ is not constant and so a current is generated. As seen in Figure 4.1 (b), the first non-uniform region encountered by the strain pulse, as it propagates towards the GaAs-Au interface, is the edge of the depletion region at $x = -x_d$ . Since the position of this edge is bias dependent, it was expected that the first peak in electrical response would move to earlier times with increasing negative bias $V_b$.

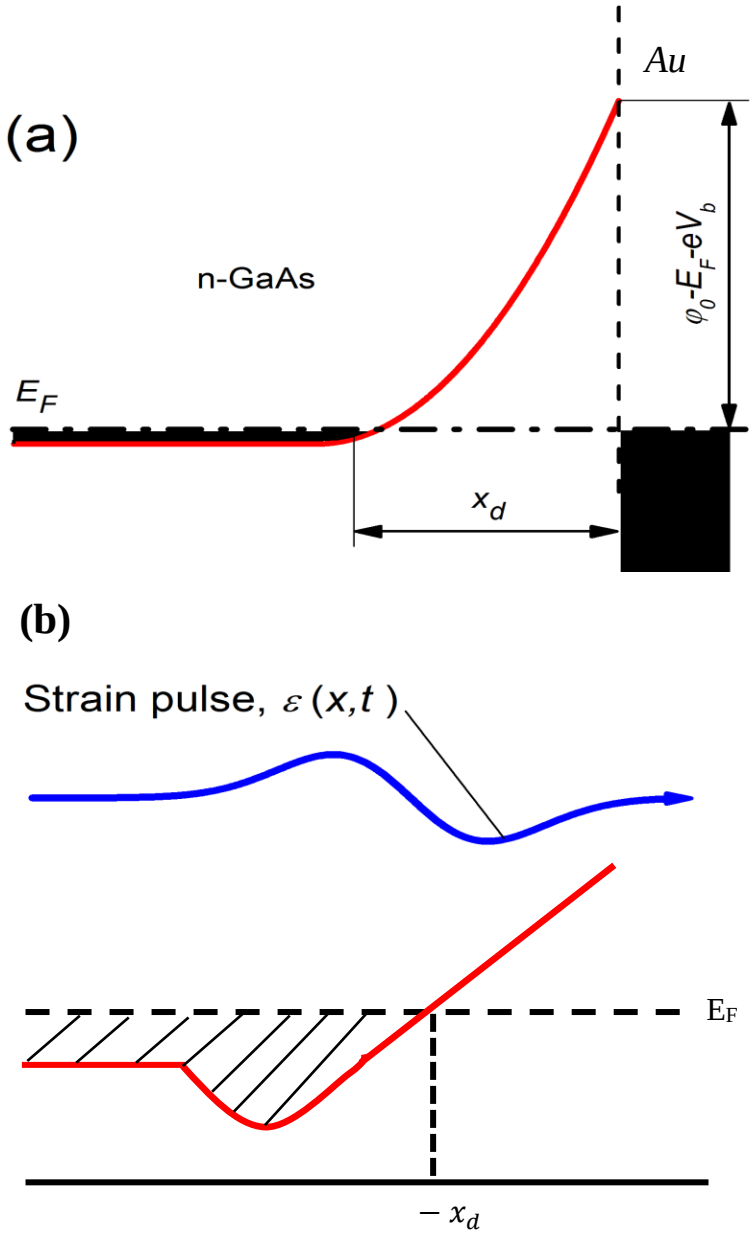



**Figure 4.1:** (a) Electron band diagram of the Schottky diode (degenerate) under equilibrium conditions (i.e. no strain); (b) the schematic demonstration of the effect of the strain pulse incident on the edge of the depletion layer at distance $x_d$ from the GaAs/Au interface. (Figure adapted from D. M. Moss et al. [23]).

This chapter investigates the piezoelectric response to both coherent longitudinal and transverse acoustic phonons in a Schottky diode fabricated on a low-symmetry surface of a semiconductor material which is the fundamental difference from the previous investigations [23]. First, transport measurements

performed on fabricated Schottky diode at different temperatures is presented. Fast acousto-electrical measurements conducted on (311 B) GaAs Schottky diode and results along with theoretical analysis will be discussed in next section. Finally, results obtained from (311 A) GaAs Schottky diode is presented, after which an overall conclusion on electron-phonon interactions in a Schottky diode is presented.

### 4.2 NU927 Current-Voltage characteristics

Transport measurements were conducted on all samples to verify the quality of the processed devices and their correct operation. These measurements were taken in a continuous flow cryostat at a temperature of 5 K as later experiments required the low temperature to reduce the scattering of acoustic phonons. Prior to wire bonding, individual Schottky devices were selected according to their reverse-bias breakdown voltage, obtained from room temperature *I-V* characteristics using probe station in clean room. Selected devices were then bonded as described in section 3.1.6 and further *I-V* measurements were taken at different temperatures.

The current-voltage (I-V) characteristics of the Schottky diodes were measured using the Current Voltage Graphical User Interface as described in section 3.5. The Schottky diode I-V characteristics at a temperature of $T$=5 K is shown in figure 4.2. The turn on voltage of this device is 0.7 V, at a forward bias and reverse bias breakdown voltage is at -5 V. Current-voltage measurements were also performed at various temperatures (20K, 40K, 80K, 100K, 160K, 200K & 300K) to observe the temperature dependent effects on Schottky Diode as shown in figure 4.3. The turn on voltage at each temperature is given in table 4.1. All these I-V measurements were performed using continuous flow cryostat as described in section 3.4.2.

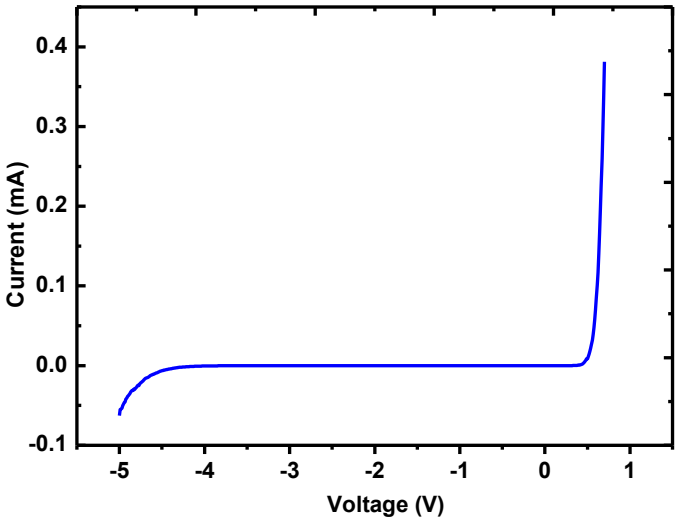



**Figure 4.2:** Current voltage characteristics of the Schottky diode at T=5K.

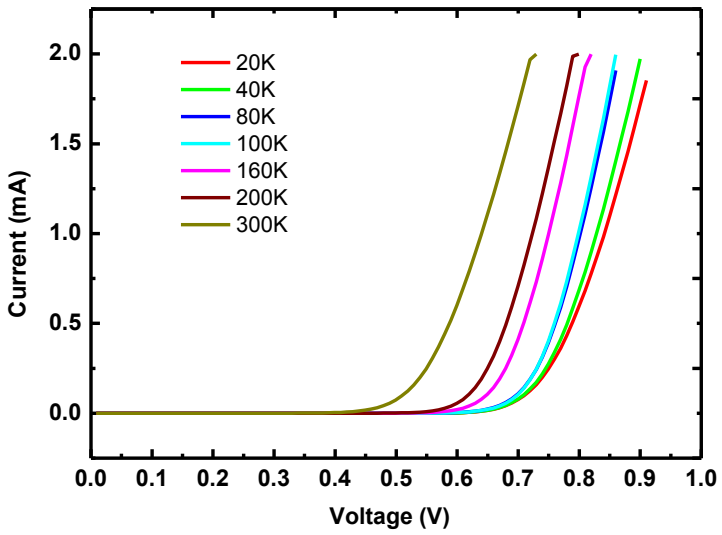



**Figure 4.3:** Temperature dependent I-V characteristics of the Schottky diode at various temperatures *i.e.* (20K, 40K, 80K, 100K, 160K, 200K & 300K).

| Temperature(K) | Turn-On Voltage(V) |
|---|---|
| 20 K | 0.68 |
| 40 K | 0.67 |
| 80 K | 0.65 |
| 100 K | 0.64 |
| 160 K | 0.62 |
| 200 K | 0.59 |
| 300 K | 0.50 |

**Table 4.1:** Turn-On voltage of Schottky diode at different temperatures.

The curves in figure 4.3 and table 4.1 clearly show that the diode "turn-on" voltage decreases with temperature. This is expected, given the decrease in GaAs band-gap energy with temperature [104].

### 4.3 Interaction of coherent transverse and longitudinal acoustic phonons with electrons in a (311 B) GaAs Schottky diode

The Schottky diode-based strain pulse experiments were performed on a setup shown in figure 3.15 and all measurements were at T = 5K unless otherwise specified. The schematic of experiment in the coordinate frame with the *x* and *z* axes along the $[\bar{2}33]$ and [311] crystallographic directions, respectively is shown in figure 4.4. The sample was mounted on a specially designed holder incorporating 50 Ω micro strip line conductor and a microwave coaxial launcher for connection to the wide-bandwidth cryostat wiring. Changes in the voltage across the device caused by the presence of the strain pulse were measured by a fast oscilloscope as described in section 3.6. The pump pulse taken from an amplified Ti: Sapphire laser (800nm wavelength, 80fs pulse duration and 5 kHz repetition rate) was used to generate acoustic signals in an 100nm Al film thermally evaporated on the opposite face of

the (311) GaAs substrate of thickness $d$ = 380μm. The acoustic signal propagates across the substrate of the sample to the Schottky diode. The laser was focused to a spot of diameter 50 μm and the intensity on the Al film did not exceed 10 mJ/cm$^2$. Because of the optical excitation, a compressive strain pulse is generated in the Al film [1] with amplitude, $\varepsilon = 10^{-3}$.

The injection of this strain pulse into the (311) GaAs substrate results three acoustic modes: quasi-longitudinal phonons (QLA), quasi-transverse phonons (QTA) and pure transverse (TA) which propagate along the [311] crystallographic direction in GaAs [68]. The strain pulses injected from the Al transducer into the GaAs substrate along this direction are combinations of these modes, but due to the different sound velocities, $v_i$ ($i$ = QLA, QTA or Pure TA) of the modes they separate in time into isolated pulses of specific polarization. In figure 4.4, the displacement vector for QLA is close to the normal [311] whereas for QTA the displacement vector is close to $[\bar{2}33]$. The pure transverse phonons (TA) mode, which corresponds to the third polarization is not excited in this work due to the symmetry selection rules.

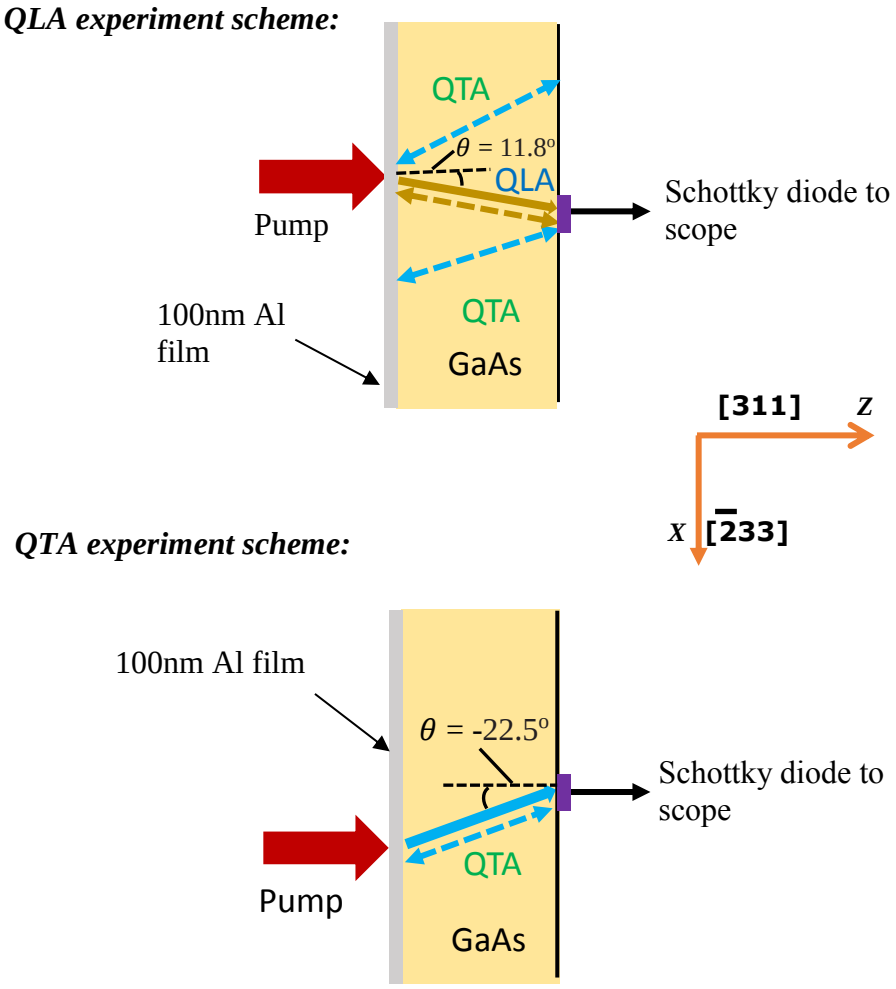



**Figure 4.4:** Schematic of the experiment with coherent QLA and QTA phonons; solid and dashed arrows indicate the direct and reflected phonon fluxes detected by the Schottky contact respectively.

Deformations strains, occur in a body under the action of stresses. In an elastic solid the strain is directly proportional to the stress for small displacements, this is know as Hooke's law. The stiffness tensor $\boldsymbol{C}$ is a fundamental property of a material. In the elastic regime, it generalizes Hooke's law in three dimensions, relating strains and stresses. This states that the six components of stress at any point of a body are in a linear function of the six components of strain as shown in equation 4.2 briefly.

$$\sigma_{ij} = c_{ijkl}\varepsilon_{kl} \tag{4.2}$$

where $\sigma$ is the stress tensor and $\varepsilon$ is the strain tensor. To sum over repeated indices, by using Einstein Summation notation, *ij* may be replaced by *m* according to:

| | |
|---|---|
| 1 → 11; | 4 → 23 or 32; |
| 2 → 22; | 5 → 13 or 31; |
| 3 → 33; | 6 → 12 or 21; |

In tensor notation, the equation 4.2 can be written to equation 4.3.

$$\sigma_m = c_{mn}\varepsilon_n \tag{4.3}$$

Stiffness tensor is generally written as a 6 x 6 matrix as shown below:

$$\begin{pmatrix} \sigma_1 \\ \sigma_2 \\ \sigma_3 \\ \sigma_4 \\ \sigma_5 \\ \sigma_6 \end{pmatrix} = \begin{pmatrix} C_{11} & C_{12} & C_{13} & C_{14} & C_{15} & C_{16} \\ C_{12} & C_{12} & C_{23} & C_{24} & C_{25} & C_{26} \\ C_{13} & C_{23} & C_{33} & C_{34} & C_{35} & C_{36} \\ C_{14} & C_{24} & C_{34} & C_{44} & C_{45} & C_{46} \\ C_{15} & C_{25} & C_{35} & C_{45} & C_{55} & C_{56} \\ C_{16} & C_{26} & C_{36} & C_{46} & C_{56} & C_{66} \end{pmatrix} \begin{pmatrix} \varepsilon_1 \\ \varepsilon_2 \\ \varepsilon_3 \\ 2\varepsilon_4 \\ 2\varepsilon_5 \\ 2\varepsilon_6 \end{pmatrix}, \qquad \text{M (4.4)}$$

where C's are the elastic moduli or stiffness's. The factors of 2 in the strain tensor is to ensure the matrix M4.4 corresponds to equation 4.3 by taking proper care of double counting. The stiffness tensor not only contains information about static deformations, but also about elastic waves traveling through the material. The array of values of the elastic stiffness constants is reduced for a cubic crystal to the matrix M4.5, showing that the non-zero elastic constants of a cubic crystal are just three.

$$\begin{pmatrix}\sigma_1\\ \sigma_2\\ \sigma_3\\ \sigma_4\\ \sigma_5\\ \sigma_6\end{pmatrix}=\begin{pmatrix}C_{11} & C_{12} & C_{12} & 0 & 0 & 0\\ C_{12} & C_{11} & C_{12} & 0 & 0 & 0\\ C_{12} & C_{12} & C_{11} & 0 & 0 & 0\\ 0 & 0 & 0 & C_{44} & 0 & 0\\ 0 & 0 & 0 & 0 & C_{44} & 0\\ 0 & 0 & 0 & 0 & 0 & C_{44}\end{pmatrix}\begin{pmatrix}\varepsilon_1\\ \varepsilon_2\\ \varepsilon_3\\ 2\varepsilon_4\\ 2\varepsilon_5\\ 2\varepsilon_6\end{pmatrix} \qquad \text{M (4.5)}$$

Along the [311] direction, there is only one pure transverse mode (polarized along the $[0\bar{1}1]$ direction) and the other two modes have mixed longitudinal and transverse character. The velocities of these waves can be calculated using the Christoffel equation [105]. The 3-dimensional elastic equation is shown by equation 4.6

$$\rho\frac{\partial^2 u_i}{\partial t^2}=c_{ijkl}\frac{\partial^2 u_l}{\partial x_j\partial x_k} \qquad (4.6)$$

For crystals of high symmetry, where the number of independent elastic moduli is small, the number of terms on the right-hand side of equation 4.6 reduces considerably. For cubic crystals, using the non-zero elastic constants in matrix M4.5 the following three equations (4.7, 4.8, 4.9) are obtained.

$$\rho\frac{\partial^2 u_1}{\partial t^2}=c_{11}\frac{\partial^2 u_1}{\partial x_1^2}+c_{44}\left(\frac{\partial^2 u_1}{\partial x_2^2}+\frac{\partial^2 u_1}{\partial x_3^2}\right)+(c_{12}+c_{44})\left(\frac{\partial^2 u_2}{\partial x_1\partial x_2}+\frac{\partial^2 u_3}{\partial x_1\partial x_3}\right) \qquad (4.7)$$

$$\rho\frac{\partial^2 u_2}{\partial t^2}=c_{11}\frac{\partial^2 u_2}{\partial x_2^2}+c_{44}\left(\frac{\partial^2 u_2}{\partial x_1^2}+\frac{\partial^2 u_2}{\partial x_3^2}\right)+(c_{12}+c_{44})\left(\frac{\partial^2 u_3}{\partial x_2\partial x_3}+\frac{\partial^2 u_1}{\partial x_1\partial x_2}\right) \qquad (4.8)$$

$$\rho\frac{\partial^2 u_3}{\partial t^2}=c_{11}\frac{\partial^2 u_3}{\partial x_3^2}+c_{44}\left(\frac{\partial^2 u_3}{\partial x_2^2}+\frac{\partial^2 u_3}{\partial x_1^2}\right)+(c_{12}+c_{44})\left(\frac{\partial^2 u_1}{\partial x_3\partial x_1}+\frac{\partial^2 u_2}{\partial x_2\partial x_3}\right) \qquad (4.9)$$

The solutions of equation 4.6 represent plane monochromatic elastic waves for which displacement vector has the form as shown in equation 4.10.

$$u=A\boldsymbol{e}(\boldsymbol{q})\exp[i(\omega t-\boldsymbol{q}.\boldsymbol{x})]\,, \qquad (4.10)$$

where the phase, $\omega t-\boldsymbol{q}.\boldsymbol{x}$ , is a linear function of the coordinate *x*. The shape of the wave is determined by the surfaces of constant phase and these at any instant of time

are clearly plane surfaces perpendicular to the vector $\boldsymbol{q}$. The vector $\boldsymbol{q}$, components $\boldsymbol{q_1, q_2, q_3}$ is known as the propagation vector and $\boldsymbol{e(q)}$, components $\boldsymbol{e_i(q)}$ is a unit vector known as the polarization vector. In this work, the wave vector for QLA and QTA phonons, $\mathbf{q_{QLA}}$ and $\mathbf{q_{QLA}}$ , respectively, are parallel to [311] direction. However, due to elastic anisotropy their group velocities, $\mathbf{v}^g_{QLA}$ and $\mathbf{v}^g_{QTA}$, lying in the $(0\bar{1}1)$ plane, point at angles $\theta_{QLA}$ and $\theta_{QTA}$ to [311] direction as shown in figure 4.4. The components of the group velocity parallel to [311] are equal to the corresponding phase velocities and $v_{QLA}$ and $v_{QTA}$. These velocities and angles was obtained by solving elastic equations with the elastic constants for GaAs [106, 107], kindly solved by our collaborator Boris Glavin. The details of these calculations are provided very briefly here. The direction of $\boldsymbol{q}$ in equation 4.10 is selected and substituting $u$ in equations (4.7-4.9) will give three equations involving $e_1(\boldsymbol{q}), e_2(\boldsymbol{q})$ and $e_3(\boldsymbol{q})$. After equating the determinant of the coefficients of $e_1(\boldsymbol{q}), e_2(\boldsymbol{q}), e_3(\boldsymbol{q})$ to zero, we obtain cubic equation for $\omega^2$ in terms of the components of $\boldsymbol{q}$. In the case of [311] growth direction after some algebraic manipulation this equation is represent by a secular equation 4.11.

$$\begin{vmatrix} 9c_{11}+2c_{44}-11\rho\omega^2/k^2 & 3(c_{12}+c_{44}) & 3(c_{12}+c_{44}) \\ 3(c_{12}+c_{44}) & c_{11}+10c_{44}-11\rho\omega^2/k^2 & (c_{12}+c_{44}) \\ 3(c_{12}+c_{44}) & (c_{12}+c_{44}) & c_{11}+10c_{44}-11\rho\omega^2/k^2 \end{vmatrix} = 0 \quad (4.11)$$

Where $c_{ij}$ are the elastic constants and $\rho$ is the mass density. Each value of $\omega$ corresponds to a definite mode of vibration. The polarization directions for each mode can be obtained by substituting back the appropriate valve of $\omega$. By resolving the ratio $e_1(\boldsymbol{q}): e_2(\boldsymbol{q}): e_3(\boldsymbol{q})$ provides the direction $\boldsymbol{e(q)}$. The equations (4.12-4.14) of the sound velocities for the [311] direction obtained from equation 4.11, are:

$$v_T^2 = (c_{11} - c_{12} + 9c_{44})/11\rho\,, \quad (4.12)$$

$$v_{QTA}^2 = (10c_{11} + c_{12} + 13c_{44} - D)/22\rho\,, \quad (4.13)$$

$$v_{QLA}^2 = (10c_{11} + c_{12} + 13c_{44} + D)/22\rho\,, \quad (4.14)$$

where $D = [(8c_{11} - c_{12} - 9c_{44})^2 + 72(c_{12} + c_{44})^2]^{1/2}$ .

Equation 4.12 provides the velocity of a pure transverse (TA) wave polarized along the $[0\bar{1}1]$ axis. Equation 4.13 and 4.14 describes quasi-transverse (QTA) and quasi-longitudinal (QLA) velocities, respectively. Substituting the elastic constants (in GPa) of GaAs, ($c_{11}$ = 119, $c_{12}$ = 53.8 and $c_{44}$ = 59.5) [107], we obtained, $v_{QLA}$ = 5.1 kms$^{-1}$, $v_{QTA}$ = 2.9 kms$^{-1}$, $\theta_{QLA}$ = 11.8$^{o}$ and $\theta_{QTA}$ = -22.5$^{o}$. In figure 4.4, the QLA, QTA and TA modes, propagating along [311] (i.e. the z-direction), the polarizations were found to be $\mathbf{e}_{QLA} = (u_0, 0, \sqrt{1-u_0^2})$, and $\mathbf{e}_{QTA} = (\sqrt{1-u_0^2}, 0, -u_0)$, with $u_0 \approx 0.165$ [32]. The mixed character of the QLA and QTA waves gives rise to their coupling with the pure longitudinal wave generated in the Al film, while the pure TA mode is not excited. To describe quantitatively the evolution of the strain components of the QLA and QTA pulses, it is convenient to introduce the shape functions $\eta_i(t - z/v_i)$ with index *i* marking pulse polarization according to equation 4.15.

$$u_{zz}^{(i)} = e_z^{(i)} \eta_i(t - z/v_i),\ u_{xz}^{(i)} = \left(\frac{e_x^{(i)}}{2}\right) \eta_i(t - z/v_i). \qquad (4.15)$$

The functions $\eta_i(t - z/v_i)$ describes the spatio-temporal evolution of the strain pulses and are determined by the "seed" pulse profile and its transmission through the Al/GaAs interface.

### 4.3.1 Electrical detection of QLA and QTA Coherent Phonons

After the strain pulse propagation through the GaAs substrate in the time $\Delta t_i = d/v_i$, the coherent phonons induce an electrical response in the Schottky contact as described in section 4.2. This electrical response $\delta V(t)$ is monitored by a digitizing oscilloscope with the bandwidth of 12.5 GHz as described in section 3.6. The excitation spots at the Al film were displaced at some angle relative to the Schottky diode (see the pump spot) shown in figure 4.4 for QLA and QTA wave packets, so that the injected phonon fluxes were incident on the device. An example of the

temporal traces $\delta V(t)$ measured for QLA and QTA coherent phonons in a full temporal range is shown in figure 4.5 and figure 4.6, respectively. The traces include several sharp spikes. Firstly, the spike at time $t$=0 corresponds to the response from optical pump breakthrough. The other spikes, marked by vertical arrows are due to coherent phonon wave packets. The second spikes at $t$≈69 ns (figure 4.5) and at $t$≈121 ns (figure 4.6) are the QLA and QTA phonons respectively propagating directly from Al film to Schottky device [see solid arrows in figure 4.4], which is the main point of interest in all further measurements.

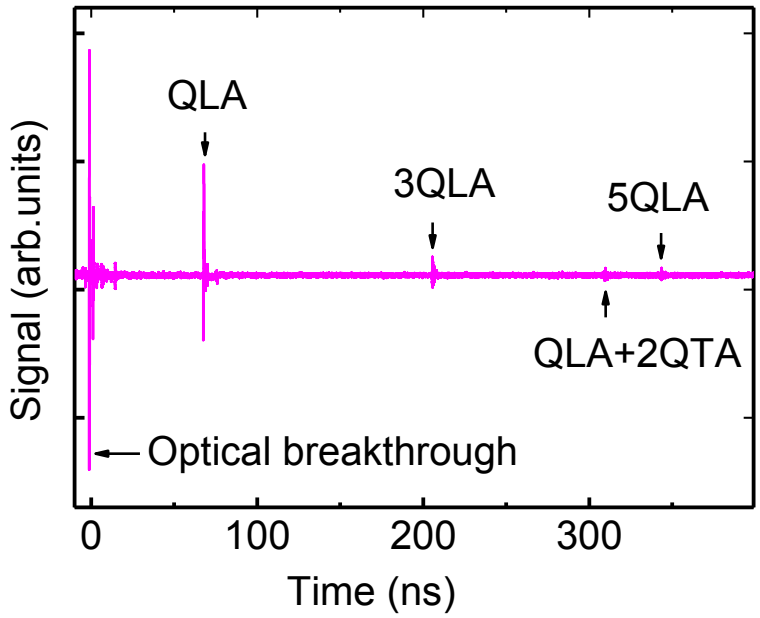



**Figure 4.5:** Electrical response measured for QLA signal in a full temporal range, with a bias of $V_B$ = 0V at pump fluence $W$=4 mJ/cm$^2$.

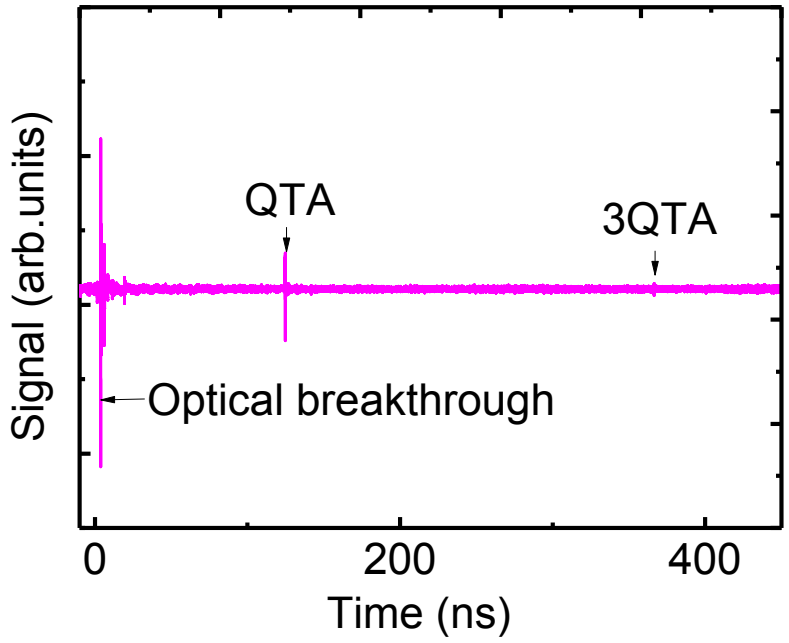



**Figure 4.6:** Electrical response measured for QTA signal in a full temporal range, with a bias of VB = 0V at pump fluence W=4 mJ/cm2.

The sound velocities for these spikes are $v_{QLA} = 5.5$ km/s and $v_{QTA} = 3.1$ km/s for QLA and QTA phonons respectively, which are close to the calculated values. After this, subsequent spikes at *t* = 3QLA, QLA+2QTA and 5QLA in figure 4.5 and *t* = 3QTA in figure 4.6 correspond to the multiple reflections in the substrate without and with mode conversion as shown in figure 4.4 by dashed arrows. The different arrival timings for each reflection is shown in Table 4.2. The possibility that features in $\delta V(t)$ are due to an incoherent heat pulse can be discounted, because they are too short in time duration and are only observed when laser excitation is located directly at the correct angles $\theta$. Only at the GaAs-metal interface, the mode conversion QLA↔QTA take place, which may happen at the side of the GaAs substrate with Al film and at the Schottky Au contact.

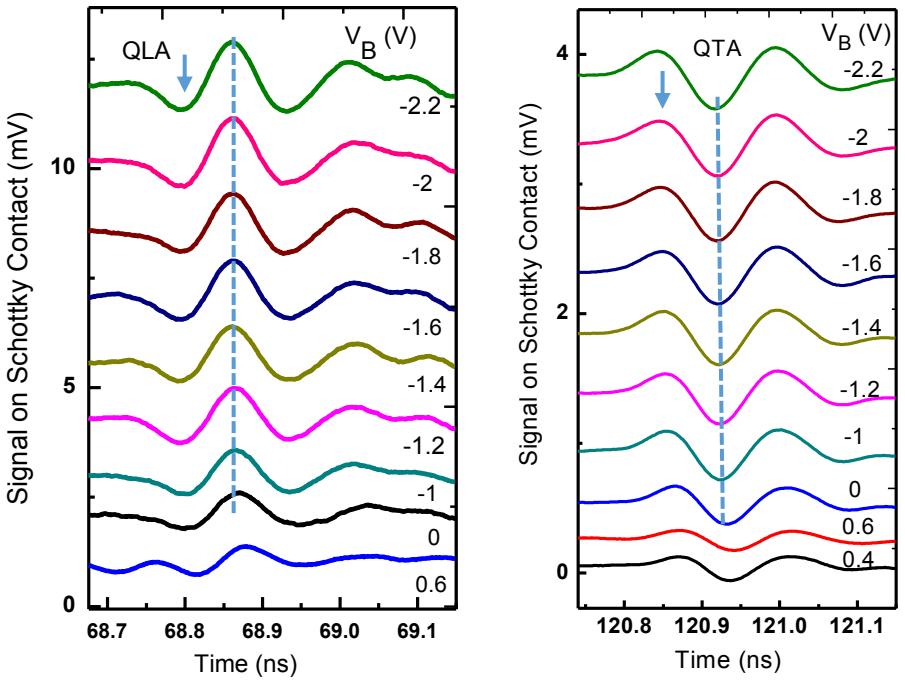
| Spike | Arrival Time(ns) |
|---|---|
| QLA | $t$ = 68.78 |
| 3QLA | $t$ = 206 |
| 5QLA | $t$ = 344 |
| QTA | $t$ = 120.86 |
| QLA+2QTA | $t$ = 310 |
| 3QTA | $t$ = 362 |

**Table 4.2:** Different arrival timings of the multiple reflections in the GaAs substrate.

### 4.3.2 Dependence of QLA and QTA Signals on Bias

The response of the direct QLA and QTA phonons detected at $t$≈69 ns and $t$≈121 ns respectively, was investigated for a range of applied bias ($V_B$ = 0 to −2.2V). The bias was applied to the Schottky diode externally using a Keithley 230 programmable voltage source via a bias tee and the electrical response $\delta V(t)$ was recorded on an oscilloscope (see section 3.6). An example of the electrical signals $\delta V(t)$ (zoomed) for QLA and QTA coherent phonons measured for several bias voltages $V_B$ is shown in figure 4.7 (a) and figure 4.7 (b), respectively. The signals possess oscillatory behavior which is due to the ringing of the electrical resonance of the device and electrical circuit. The important observation from these figures is that the first peak is negative for QLA and positive for QTA phonons, pointed by vertical arrows. Considering the negative peak for QLA and positive peak for QTA, the temporal positions $t_m$ of the first peak minimum (for QLA) and maximum (for QTA) slightly moves to earlier times with the increase of reverse bias as expected (see section 4.1). This observation agrees with the previous experiments performed on Schottky diodes fabricated on high symmetry GaAs surfaces [23]. The positive peaks (marked with vertical dotted line), centred between two negative peaks and a similar, but negative peaks (marked with vertical dotted line), centred between two positive

peaks is shown in figure 4.7 (a) and figure 4.7 (b), respectively is another feature of the signal which is due to the Schottky barrier. The shape of this peak doesn't change with increasing bias, from $V_B$ = 0V to -2.2V and the temporal position of its centre is almost bias independent this is because when a reverse bias voltage $V_R$ is applied, the position of the Schottky barrier doesn't change hence the centre peaks of the signal is completely bias independent as expected.




(a) (b)

**Figure 4.7:** (a) Phonon induced signals measured at pump fluence $W$=4 mJ/cm$^2$ for various bias voltages $V_B$ for QLA phonons. (b) Phonon induced signals measured at pump fluence $W$=4 mJ/cm$^2$ for various bias voltages $V_B$ for QTA phonons.

The first peak position of the electrical response $\delta V(t)$, negative peak for QLA and positive peak for QTA as a function of applied reverse bias is shown in figure 4.8 and figure 4.9, respectively. In accordance to the equation 2.7 and from these figures, we can notice that the electric response moved to earlier times when applying a more negative bias. The shift observed for QLA is 25 ps and for QTA it is 20 ps.

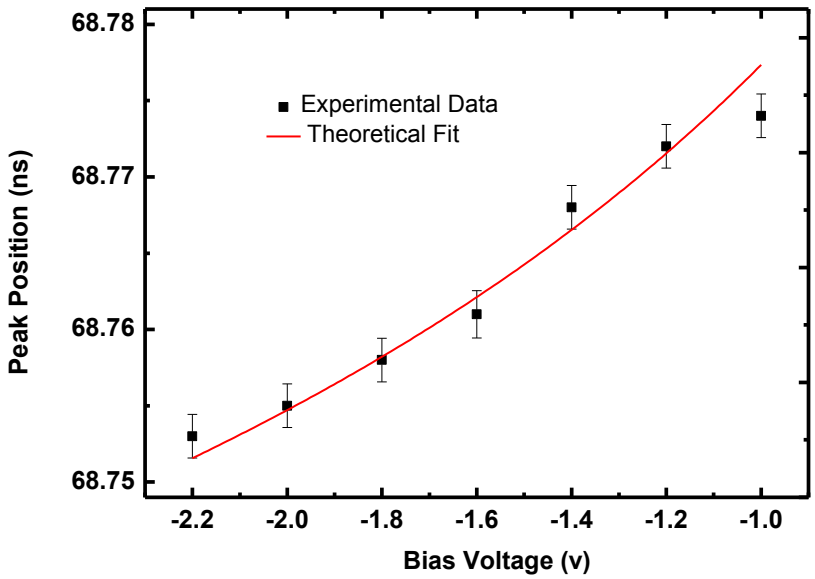



**Figure 4.8:** First peak position dependence on applied bias $V_B$ for QLA phonons. The squares are the experimental data and the red line is a theoretical fit to the experimental data.

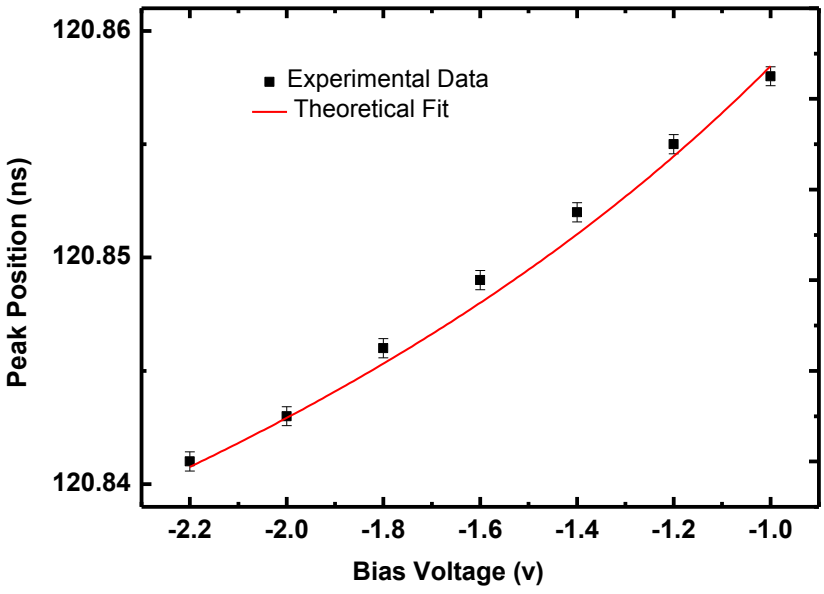



**Figure 4.9:** First peak position dependence on applied bias VB for QTA phonons. The squares are the experimental data and the red line is a theoretical fit to the experimental data.

The change in peak position $\Delta t$ is expressed by equation 4.16 by rearranging the equation 2.7.

$$\Delta t = \frac{\Delta W}{c} = \frac{1}{c}\left[\sqrt{C(V_0 - V)} - \sqrt{CV_0}\right], \qquad (4.16)$$

where $\Delta W$ is the shift of the depletion width, $c$ is the sound speed, $N_D$ is the donor concentration, $V_0$ is the Schottky barrier height and applied voltage $V$ = -1V to -2.2V. In figure 4.8 and figure 4.9, the red curve shows the theoretical fit to the data of the form $y = (\sqrt{(\mathrm{A} - \mathrm{C}x)} - \sqrt{(\mathrm{D})})/\,c$, where A= 1.343 ± 0.009 V/cm$^{-3}$, C = -2.258x10$^{-7}$ cm$^{-3}$, D = 1.342 ± 0.007 V/cm$^{-3}$ and A= 1.343 ± 0.008 V/cm$^{-3}$, C = -9.722x10$^{-8}$ cm$^{-3}$, D = 1.342 ± 0.006 V/cm$^{-3}$, respectively. From these constants obtained by the fit, doping concentration $N_D$ = 1.4x10$^{17}$ cm$^{-3}$ and barrier height $V_0$ = 1V were extracted. The doping concentration and barrier height extracted from the fit are close to the nominal values of $N_D$ = 1x10$^{17}$ cm$^{-3}$ and $V_0$ = 0.9V [82], respectively.

### 4.3.3 Dependence of QLA and QTA Signals on Pump Laser Power

The dependence of the electrical response $\delta V(t)$ on various optical excitation densities $W$ at the Al film was measured. The amplitude of the generated strain pulse within the Al transducer film is proportional to pump fluence (see section 2.1.1). Thus, signal amplitude should increase with the increase of pump fluence $W$. Such behavior was observed in experiments, and the results for $V_B$=0V is shown in figure 4.10 and figure 4.11 for QLA and QTA, respectively. As the strain amplitude increases, the nonlinear properties of the lattice play a crucial role and produce interesting phenomena such as the formation of solitary waves as explained in section 2.2.1. The modification of the shape of the acoustic pulse as the pump fluence is increased also indicates the appearance of nonlinear effects during the strain propagation through substrate. The most important observation is the QLA acoustic pulse arrives at earlier times when the pump fluence is increased. It is explained by the increase of the speed of sound with the increase of the amplitude of the acoustic pulse. In figure 4.10, it is clearly seen that the first peak for QLA phonons moves to earlier times with the increase of $W$ (also see figure 4.12). This

temporal shift has been observed in earlier works performed with picosecond acoustic optical techniques and corresponds to nonlinear acoustic properties of GaAs substrate [71, 77]. The nonlinear equation of propagation is expressed in the comoving frame traveling at the speed of sound by Korteweg-de Vries Burgers equation (see equation 2.6), which acoustic attenuation, acoustic dispersion ($\beta$) and acoustic nonlinearity ($C$). This acoustic nonlinearity, $C = C_{111} + C_{11}$ is a linear combination of second ($C_{11}$) and third-order $C_{111}$ elastic constants depending on the direction of propagation and the symmetry of the crystal [69]. Another interesting phenomenon arises due to nonlinear effect is that the dispersive tail of the acoustic pulse lasts longer with increasing pump fluence. In our experiment for $W$=6.4 mJ/cm$^2$, the temporal shift relatively too small $W$ is equal to ~100 ps (see inset of figure 4.10) which is like the experiments when LA phonons propagate in high-symmetry [100] direction in GaAs. In contrast to QLA, the arrival time for QTA phonons does not depend on $W$ (see dotted line, inset in figure 4.11), which means that elastic nonlinear effects for QTA phonons are not so important [108].

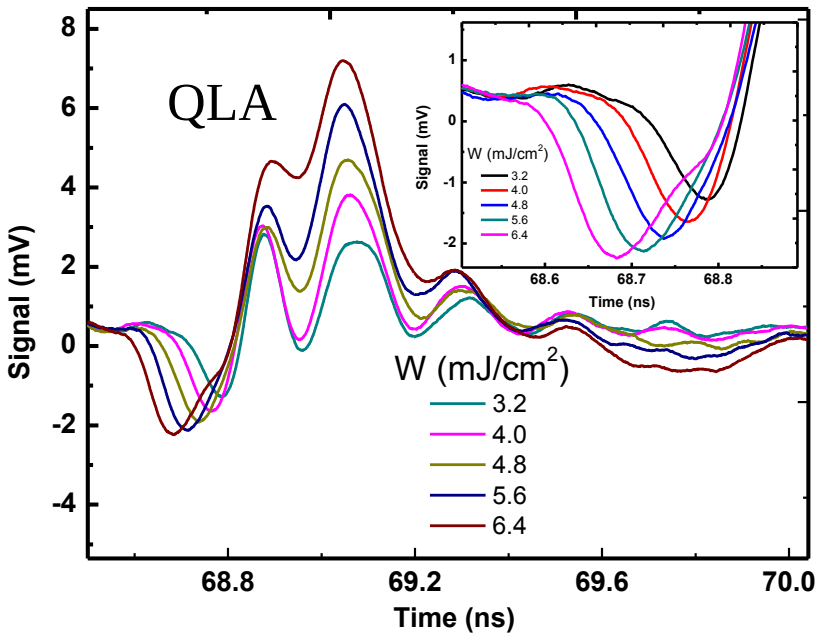



**Figure 4.10:** Phonon induced signals measured at zero bias, $V_B$=0V with different pump fluences for QLA phonons. The inset shows negative peaks extracted to layers for clarity to observe the first peak temporal shift to earlier times with the increase of $W$ for QLA phonons.

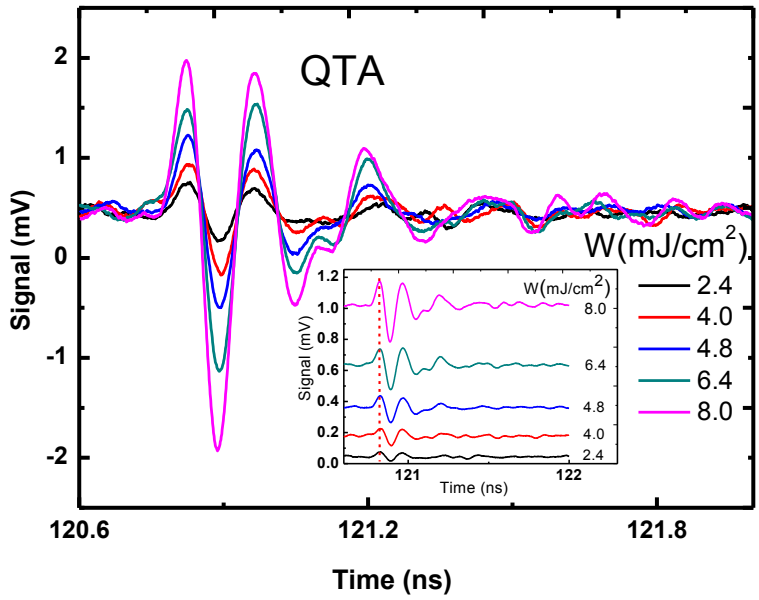



**Figure 4.11:** Phonon induced signals measured at zero bias, $V_B$=0V with different pump fluences for QTA phonons. The inset shows signals extracted to layers for clarity, vertical dotted line indicates the absence of the first peak temporal shift to earlier times with the increase of *W* for QTA phonons.

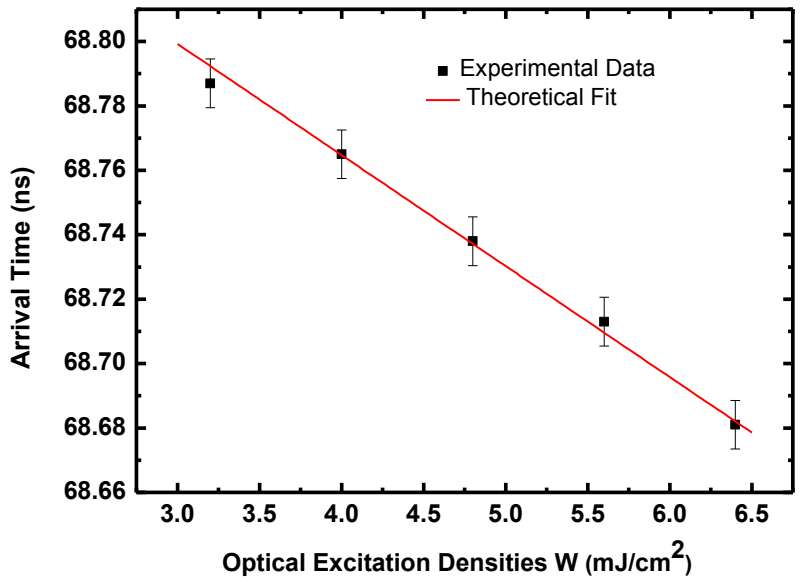



**Figure 4.12:** First peak position dependence on optical excitation densities *W* for QLA phonons. The squares are the peak position obtained from experimental signals and the red line is a theoretical fit to the experimental data.

By solving equation 2.6, the velocity of the soliton is expressed by equation 4.17.

$$U = c + \frac{C_3 \varepsilon_0}{6\rho c} , \qquad (4.17)$$

where $U$ is the velocity of the soliton, $C_3$ is the third order elastic constant along [311] direction, $\varepsilon_0$ is the peak strain amplitude, $\rho$ is the density and $c$ is the sound speed. By substituting the constant values and rearranging equation 4.17, the change in the arrival time $\Delta t$ can expressed by equation 4.18.

$$\Delta t = \frac{d}{c + (C_3 \times 1.53 \times 10^{-12})} , \qquad (4.18)$$

where $d$ is the GaAs substrate thickness. In figure 4.12, the red line shows the theoretical fit to the data of the form $y = d/(c + (a \times x))$, where $a$ = 0.002772 ± 0.0006. Form this constant, the third order elastic constant $C_3$ = -9.26x$10^{11}$ N/m$^2$ was extracted for the GaAs along [311] direction which has not been reported previously. For GaAs along [100] direction, this third order elastic constant is $C_3$ = -3.186x$10^{11}$ N/m$^2$. The significant difference of this third order elastic constant along [311] direction could be due to the uncertainty in the peak strain amplitude in the measurements.

### 4.3.4 Dependence of QLA and QTA Signals on Temperature

Measurements were also conducted at different temperatures up to 298K. Figure 4.13 and figure 4.14 shows the measured signal for QLA and QTA respectively at various temperatures from T= and 5K to 298 K. The important observation is, that the temporal shape of the signals is almost identical which indicates that the device operates even at room temperature. The arrival time shifts as a function of temperature (*T*) as shown in figure 4.15 and figure 4.16 for QLA and QTA signals, respectively. The arrival time for both QLA and QTA changes to later time with increasing temperature. This temporal shift corresponds to the decrease of sound velocities with the increase of *T*. This shift observed was approximately 1% which agrees with earlier measurements [79]. Another important observation is that the

amplitude of the signals does not decrease much with increasing temperature which is also in agreement with the previous experiments of the attenuation for phonons if we assume the frequencies we are detecting to are mostly < 100 GHz [79].

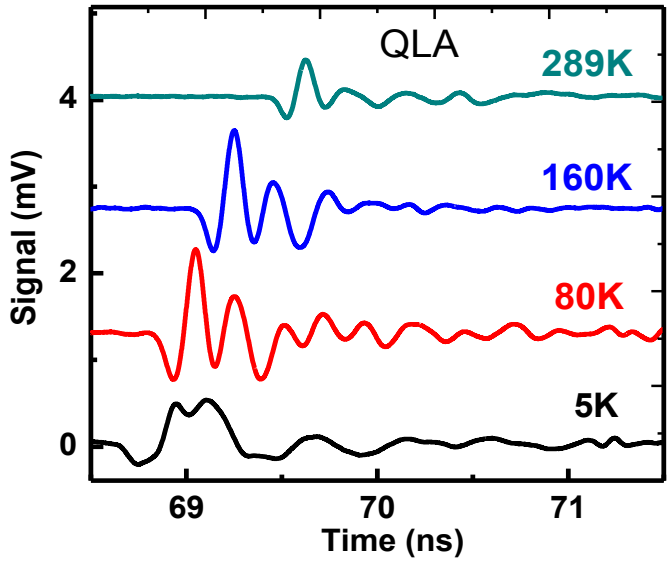



**Figure 4.13:** Experimentally measured signals at four different temperatures *T* (5K, 80K, 160K and 289K) for QLA phonons.

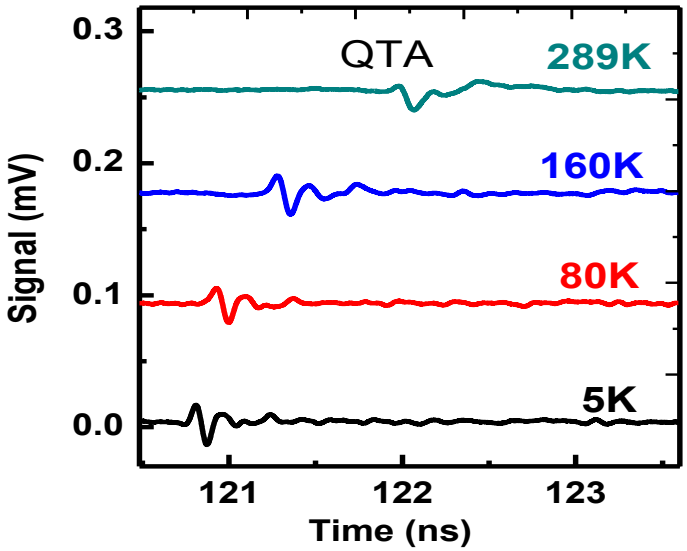



**Figure 4.14:** Experimentally measured signals at four different temperatures *T* (5K, 80K, 160K and 289K) for QTA phonons.

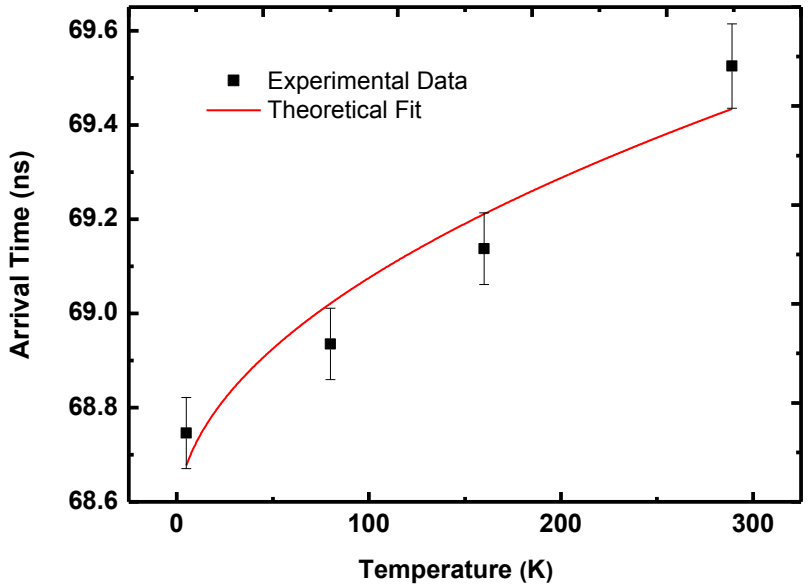



**Figure 4.15:** First peak position dependence on different temperatures *T* for QLA phonons. The squares are the peak position obtained from experimental signals and the red line is a theoretical fit to the experimental data.

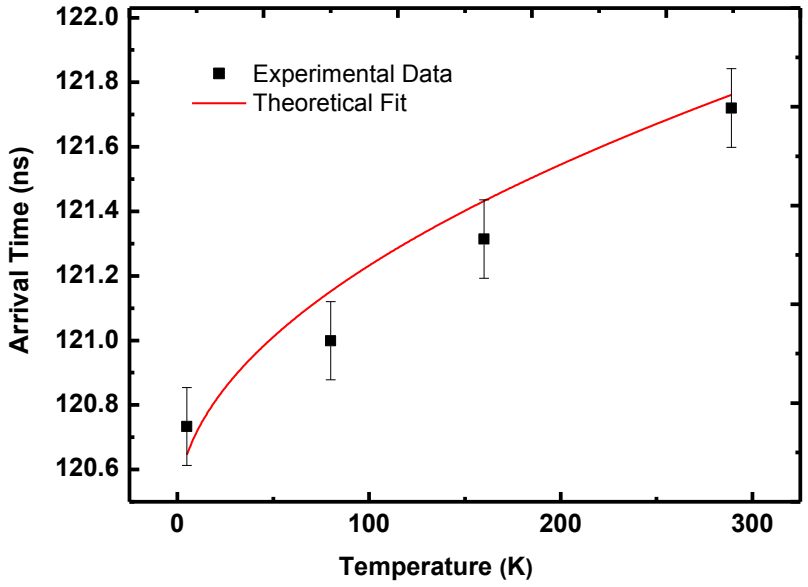



**Figure 4.16:** First peak position dependence on different temperatures *T* for QTA phonons. The squares are the peak position obtained from experimental signals and the red line is a theoretical fit to the experimental data.

The sound velocities along the [311] direction for QTA and QLA phonons can be expressed by equation 4.19 and equation 4.20, after rearranging the equations 4.13 and 4.14, respectively.

$$v_{QTA} = \left(\frac{10C_{11} + C_{12} + 13C_{44}}{22\rho}\right)\sqrt{T} - \frac{D}{22\rho} \qquad (4.19)$$

$$v_{QLA} = \left(\frac{10C_{11} + C_{12} + 13C_{44}}{22\rho}\right)\sqrt{T} + \frac{D}{22\rho} \qquad (4.20)$$

In figure 4.15, the red line shows the theoretical fit to the data of the form $y = d/A\sqrt{T} + B$, where $A$= 0.05 ± 0.010 m/s and $B$ = 68.56 ± 0. 12 m/s. For QTA phonons shown in figure 4.16, the red line shows the theoretical fit to the data of the form $y = d/A\sqrt{T} - B$, where $A$= 0.07 ± 0.024 m/s and $B$ = 120.47 ± 0. 286 m/s. From figures 4.15 and 4.16 we can see a close fit to the experimental data within the associated error. By substituting the elastic constants of GaAs [107] in equation 4.19 and 4.20, A= 0.065 m/s, $B$ = 118.47 m/s and A= 0.047 m/s, $B$ = 68.47 m/s values were calculated, respectively. These calculated values are quite close to the values obtained from the theoretical fit.

## 4.4 Theoretical Analysis of coupling mechanisms to the electrical response of the Schottky contact

The previous sections described the experimental detection of both QLA and QTA phonons and signal dependence on bias, pump power and temperature. The main aim of this section is to understand the coupling mechanisms of the electrical response of the Schottky contact to the incident coherent phonons by theoretical analysis. The two-important electron-phonon coupling mechanisms considered in this thesis are Deformation potential coupling and Piezoelectric potential coupling as described in section 1.3.1 and section 1.3.2, respectively. The energy diagram of the Schottky diode is shown in figure 2.7, the current across a metal-semiconductor junction is

mainly due to majority carriers. This can be explained by three different mechanisms: diffusion of carriers from the semiconductor into the metal, thermionic emission of carriers across the Schottky barrier and quantum-mechanical tunneling through the barrier. According to the diffusion theory, the driving force is distributed over the length of the depletion layer, but thermionic emission theory assumes that only energetic carriers, those, which have an energy equal to or larger than the conduction band energy at the metal-semiconductor interface, contribute to the current flow. Quantum-mechanical tunneling through the barrier considers the wave-nature of the electrons, allowing them to penetrate through thin barriers. For the static piezojunction model, the strain modifies the carrier transfer through the Schottky barrier due to variation in barrier height or tunnelling transmission. When an acoustic wave propagates through the structure, the related strain induces the potential acting on electrons. This potential is described within the deformation potential model [109], where redistribution of charge carriers gives rise to the perturbation of the electric field in the system. Furthermore, the acoustic wave induces a lattice polarization which perturbs the electric field in a piezoelectric semiconductor. The currents induced by strain components $u_{zz}$ and $u_{xz}$ are the displacement currents which appear due to electron screening of the potential perturbation (can be either due to DP or PE polarization) induced by dynamical strain as described in section 4.2. When an acoustic wave is propagating along the *z*-axis, which is normal to the flat metal-semiconductor interface in one-dimension, the perturbed potential $\delta\varphi$ satisfies the Poisson equation which can be expressed by equation 4.21.

$$\frac{d\delta\varphi}{dz} = \frac{e}{\varepsilon_s \varepsilon_0}\delta n + \frac{1}{\varepsilon_s \varepsilon_0}\frac{dP_Z}{dz} \quad , \tag{4.21}$$

where $\delta n$ is perturbation of the electron concentration, $\varepsilon_s$ and $\varepsilon_0$ are the dielectric constant of the semiconductor and the absolute permittivity, respectively. $P_Z$ , is the *z*-component of the piezoelectric polarization. In this work, the characteristic frequency of coherent phonons is much less than the inverse dielectric relaxation time but much higher than $(RC)^{-1}$ ($R$ and $C$ are the resistance and capacitance of the

diode) and then the induced voltage changes $\delta V$ on the Schottky contact is expressed [106] by equation 4.22.

$$\delta V = V_{PE}(Z_0) - V_{PE}(Z_d) + \frac{\varepsilon_s + \varepsilon_m}{2\varepsilon_m} V_{DP}(Z_0) - V_{DP}(Z_d) \qquad (4.22)$$

where $V_{PE}(Z)$ and $V_{DP}(Z)$ are the strain induced changes in the potential at a coordinate $z$ due to PE and DP polarizations respectively; $Z_0$ and $Z_d$ are the coordinates of the semiconductor/metal interface and the edge of the depletion layer in the semiconductor respectively; and $\varepsilon_{s,m}$ are the lattice permittivities of the semiconductor and metal.

For further analysis, we consider the generation and injection of strain pulses in an Al film. In the narrow near surface region of an Al film, the optically generated hot carriers diffuse into the Al film and pass their energy to the lattice. The combined effect of the increased lattice temperature and nonequilibrium carriers initiates the mechanical stress which generates the strain pulse. The generated strain pulse is pure LA since, due to the polycrystalline nature of the Al film structure, it can be treated as an elastically isotropic medium. However, in this work because of mode conversion under reflection at the interface with the anisotropic (311) GaAs substrate the TA component appears in the film [68]. By using the standard elasticity equations [110] for the temporal Fourier components of the displacement $\mathbf{u}$ in the aluminum film we can calculate the injected QLA and QTA strain pulses in the (311) GaAs substrate. The calculated strain waveforms for QLA and QTA phonons generated in an Al film with pump fluence $W$=1 mJ/cm$^2$ is shown in figure 4.17(a) and figure 4.17(b) (*Source*: ref. A.V. Scherbakov et al. [68]), respectively. These waveforms do not include the nonlinear acoustic properties of GaAs.

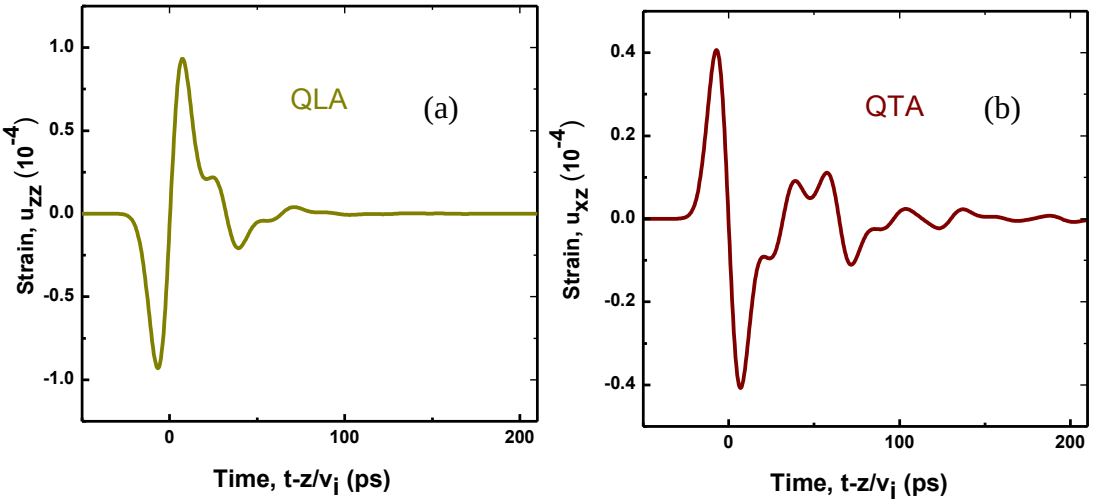



**Figure 4.17:** Calculated strain waveforms (a) for QLA, and (b) QTA phonons generated in an Al film with pump fluence $W$~1 mJ/cm$^2$. *Source*: ref. Opt. Express 21, 16473 (2013).

Now, we will be considering the theoretical signals for QLA and QTA phonons taking into account the piezoelectric (PE) and deformation potential (DP) mechanisms of phonon-electric transformations in the Schottky diode. The GaAs conduction band is isotropic, so deformation potential coupling to the QTA mode is expected to be very weak. The QLA mode may couple via both the piezoelectric and deformation potential interactions.

The electric field (**E**) generated by a set of stationary charges can be written as the negative gradient of a scalar potential ($V$) by equation 4.23.

$$\vec{\boldsymbol{E}} = -\nabla V \tag{4.23}$$

The partial differential equation for this scalar potential can be obtained by combining the field equation 4.24 which gives Poisson's equation as shown in equation 4.25.

$$\boldsymbol{\nabla}.\vec{\boldsymbol{E}} = \frac{\rho}{\varepsilon_0} \tag{4.24}$$

$$\frac{\rho}{\varepsilon_0} = \boldsymbol{\nabla}.\vec{\boldsymbol{E}} = \nabla.(-\nabla V) = -\nabla^2 V \tag{4.25}$$

The potential ($V$) due to deformation potential ($V_{DP}$) in a semiconductor is determined by the standard expression for electrons in the Γ-valley as shown in equation 4.26.

$$V_{DP} = -\left(\frac{E_1}{e}\right)\nabla \cdot \mathbf{u}, \tag{4.26}$$

where $\mathbf{u}$ is the displacement and $E_1 \sim -10$ eV is the DP constant of GaAs [111]. In an equivalent way, the potential ($V$) due to piezoelectric coupling ($V_{PE}$) is expressed by equation 4.27 using Poisson's equation.

$$\nabla^2 V_{PE} = \left(\frac{1}{\varepsilon_s \varepsilon_0}\right)\nabla \cdot \mathbf{P}\ , \tag{4.27}$$

where **P** is PE polarization and boundary condition are $V_{PE}(-\infty) = 0$. The equations 4.26 and 4.27 can be expressed with respect to the spatio-temporal evolution function $\eta_i(t - z/v_i)$ of the strain pulses for deformation potential and piezoelectric mechanisms by equation 4.28 and 4.29, respectively.

$$V_{DP} = -\left[\frac{E_1 e_z^{(i)}}{(e)}\right]\eta_i(t - z/v_i)\ , \tag{4.28}$$

$$V_{PE} = -\left[\frac{e_{eff}}{(\varepsilon_s \varepsilon_0)}\right]\mu_i(t - z/v_i)\ , \tag{4.29}$$

where $e_{eff}$ is the effective PE constant and $\mu_i' = -v_i \eta_i$ represents the shape of displacement in the pulse, the prime represents differentiation over the argument of $\mu_i, t - z/v_i$.

The effective PE constant obtained from the experimental scheme (see figure 4.4) is shown in equation 4.30.

$$e_{eff} = -\left[\frac{2e_{14}}{\left(11^{3/2}\right)}\right]\left[9\boldsymbol{e}_z^{(i)} + \left(\frac{16}{\sqrt{2}}\right)\boldsymbol{e}_x^{(i)}\right], \qquad (4.30)$$

where $e_{14} = -0.16$ C/m$^2$ is the GaAs PE constant. The important observation is that the sign of the effective PE constant depends on the kind of (311) face at which the Schottky contact is fabricated [(311B) or (311A)]. The above expression corresponds to the (311B) while for (311A) the sign of $e_{eff}$ is reversed and the corresponding experimental results are presented in section 4.6.

The calculated temporal evolutions of the signal for QLA and QTA phonons considering piezoelectric and deformation potential mechanisms for two different depletion layer widths kindly done by our collaborator Boris Glavin is shown in figure 4.18 (a) and figure 4.18 (b), respectively. For the deformation potential contribution, only the response corresponding to the depletion layer edge in the semiconductor was considered. This is because the deformation constant in metals is not well known [112]. The available data so far suggests that it is less (in absolute value) than that of GaAs [112]. It can be seen clearly from simulated signals that for deformation potential the polarity didn't change for QLA and QTA phonons and in addition the QTA signal amplitude is very small, almost negligible. However, for the piezoelectric mechanism the QLA and QTA have opposite polarity, which agrees with experimental results. This theoretical analysis considering the DP and PE coupling mechanism separately indicate that the piezoelectric mechanism is the dominant mechanism in the induced voltage changes on the Schottky contact for both QLA and QTA modes. This difference is much larger (~20 times) for QTA phonons. The calculated response to the strain pulse extends to 100 GHz spectral range. The temporal signal slightly increases its amplitude and shifts to earlier times

with the increase of reverse bias $V_b$ which is due to the increase of the depletion layer width in the semiconductor as described section 4.2.

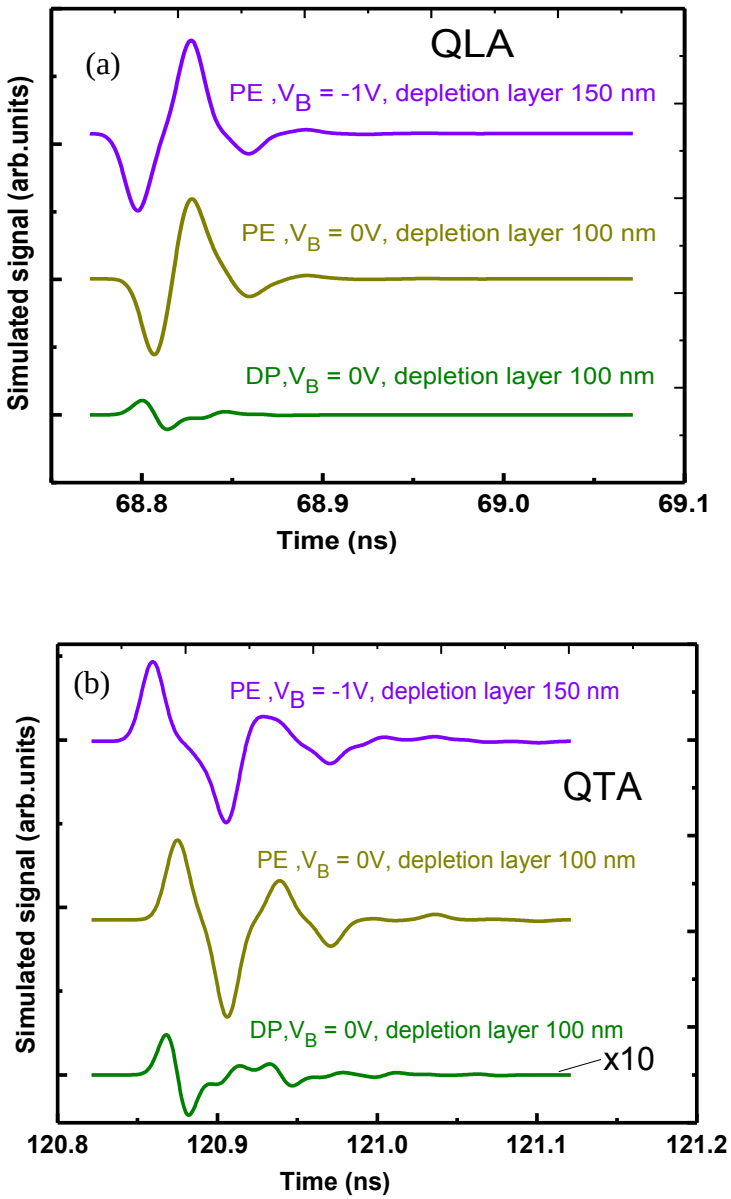



**Figure 4.18:** The theoretical signals (a) for QLA, and (b) QTA phonons taking into the account of piezoelectric (PE) or deformation potential (DP) in the Schottky diode for two widths of depletion layers and corresponding bias voltage.

Because of the high-frequency limitations of the experimental setup, a quantitative comparison of the experimental and calculated temporal shapes and the

amplitudes of the induced voltage changes on the Schottky contact is difficult. In the experimental signals shown in figure 4.7 (a) and figure 4.7 (b), we can see the ringing oscillations with lower frequency, approximately 4-GHz, because of the parasitic capacitance (approximately 0.1 pF) and inductance (approximately 10 nH) of the sample holder and bonding wires. The frequency response characteristics in the experiment also depends on the bias-dependent equivalent circuit. In the case of increasing reverse bias, the capacitance of the Schottky contact decreases. This capacitance decrease leads to an increase of the signal amplitude with increasing negative bias which can be seen clearly in figure 4.7 (a) and figure 4.7 (b).

By using the $V_{DP}$ and $V_{PE}$ equations 4.28 and 4.29, respectively, we obtained the threshold acoustic frequency ($f_{th}$), expressed in equation 4.31, for which deformation potential and piezoelectric mechanisms provided equal contributions to the Schottky-diode response.

$$f_{th} = \left[ \frac{\left(e_{eff} v_i e\right)}{2\pi\varepsilon_s \varepsilon_0 E_1 e_z^{(i)}} \right] \tag{4.31}$$

In this work, the threshold acoustic frequency for QLA phonons is $f_{th} \approx 70$GHz, while for QTA is $f_{th} \approx 250$GHz. Both frequencies are considerably higher than the bandwidth of the oscilloscope used in this thesis. Therefore, to know the origin of the results, comparison of the experimental and calculated signals was done by applying a low-pass filter with a cut-off frequency at 4-GHz to the calculated PE responses at zero bias with depletion layer width 100nm shown in figure 4.18 (a)&(b). The filtered signal is shown in figure 4.19 (a) and figure 4.19 (b) for QLA and QTA phonons, respectively. This filtering does not include the parasitic ringing observed in the experimental results.

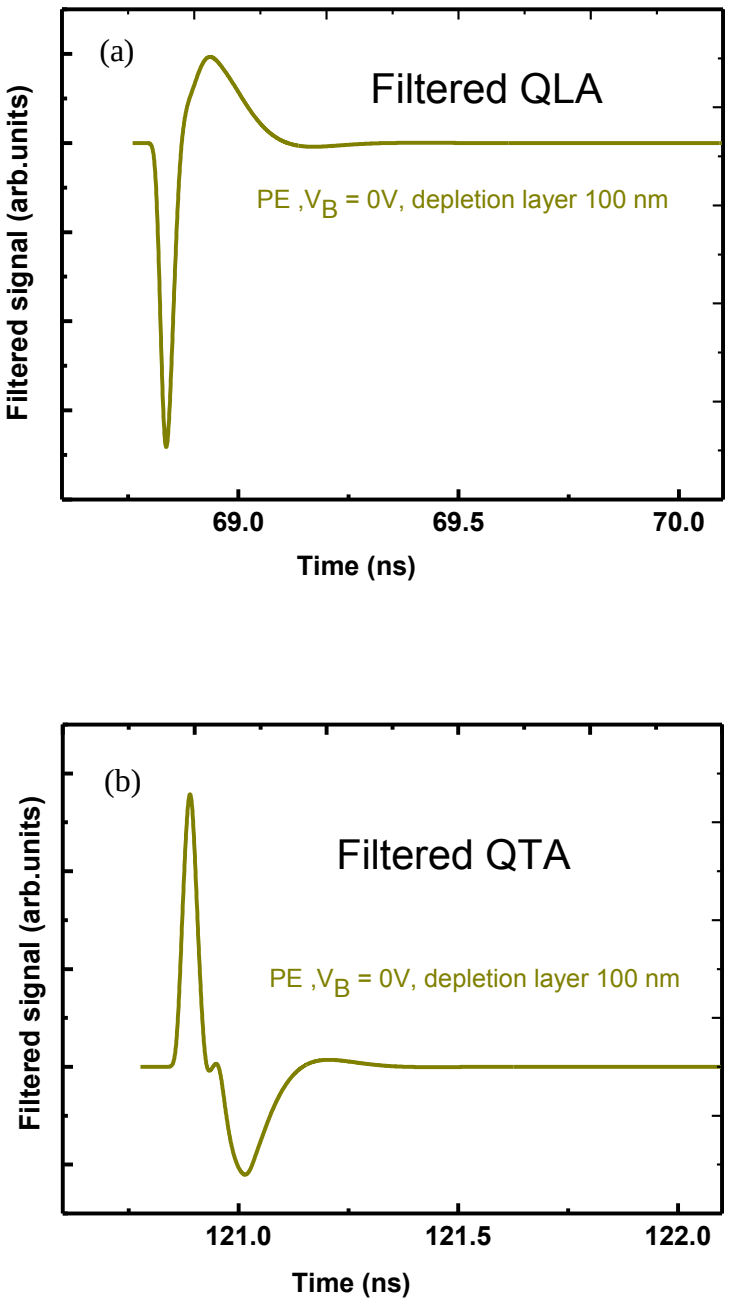



**Figure 4.19:** The signal after 4-GHz-cutoff low-pass filtering of the calculated signal shown in figure 4.18, (a) for QLA, and (b) QTA phonons at zero bias with depletion layer width 100nm.

Because of the filtering the signals possess low amplitude, but still sufficient to be measured with our experiment setup. The crucial point is that the polarity of the first peak in the filtered signal is the same as in the simulated signals. In addition, the filtered signals for PE mechanism agree with the experimental results polarity which is negative for QLA and positive for QTA phonons. This analysis leads to the conclusion that the piezoelectric phonon-electric transformation mechanism is dominant over the deformation potential.

### 4.5 (311 A) GaAs Schottky diode Results

Previous sections described the experiments performed on Schottky didoes fabricated on (311B) GaAs surface. This section discusses the results obtained from (311A) GaAs surface. For further confirmation of the earlier conclusion *i.e.* to prove the predominant role of piezoelectric phonon-electric transformation mechanism over deformation potential mechanism, similar fast electrical measurements (as described in section 3.6) with Schottky diodes fabricated on (311A) GaAs surface were performed. These Schottky diodes were fabricated on the NU1094 wafer. The sample structure is like NU927 as shown in figure 3.7 expect the doping density. The doping density in this wafer is $n_D$ =1.2 x $10^{18}$ $cm^{-3}$. Figure 4.20 shows the (311A) Schottky diode I-V characteristics at a temperature of $T$=5 K. The device turns on at a forward bias of 0.6 V and reverse breakdown occurs at about -3 V which is different from (311B); the reason might be due to the high doping concentration.

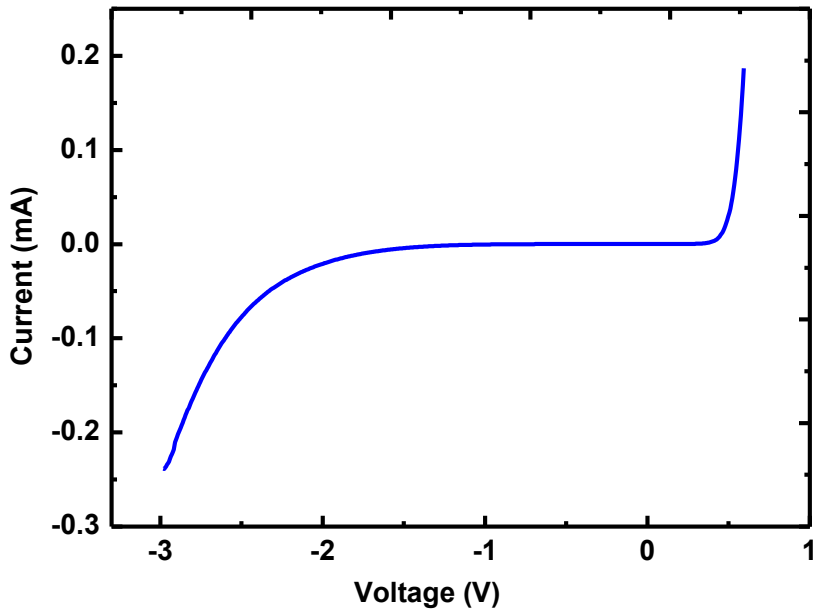



**Figure 4.20:** I-V characteristics of the (311A) Schottky diode at T=5K.

An example of the temporal traces $\delta V(t)$ measured at pump fluence $W$=4 mJ/cm$^2$ at zero bias, $V_B$=*0*V for QLA and QTA coherent phonons on (311A) GaAs surface in a full temporal range is shown in figure 4.21 (a) and figure 4.21 (b), respectively. The signals include several spikes as for signals obtained from (311B) GaAs. The second spike for QLA, third for QTA which is direct phonons were zoomed for comparison. These spikes at $t$≈58 ns (figure 4.22) and at $t$≈116 ns (figure 4.23) are the QLA and QTA phonons respectively propagating directly from Al film to the Schottky device [see solid arrows in figure 4.4]. The timings of these phonons are different from (311B) results (QLA, $t$≈69 ns and QTA, $t$≈121 ns) because of the different sample thickness, 318 μm.

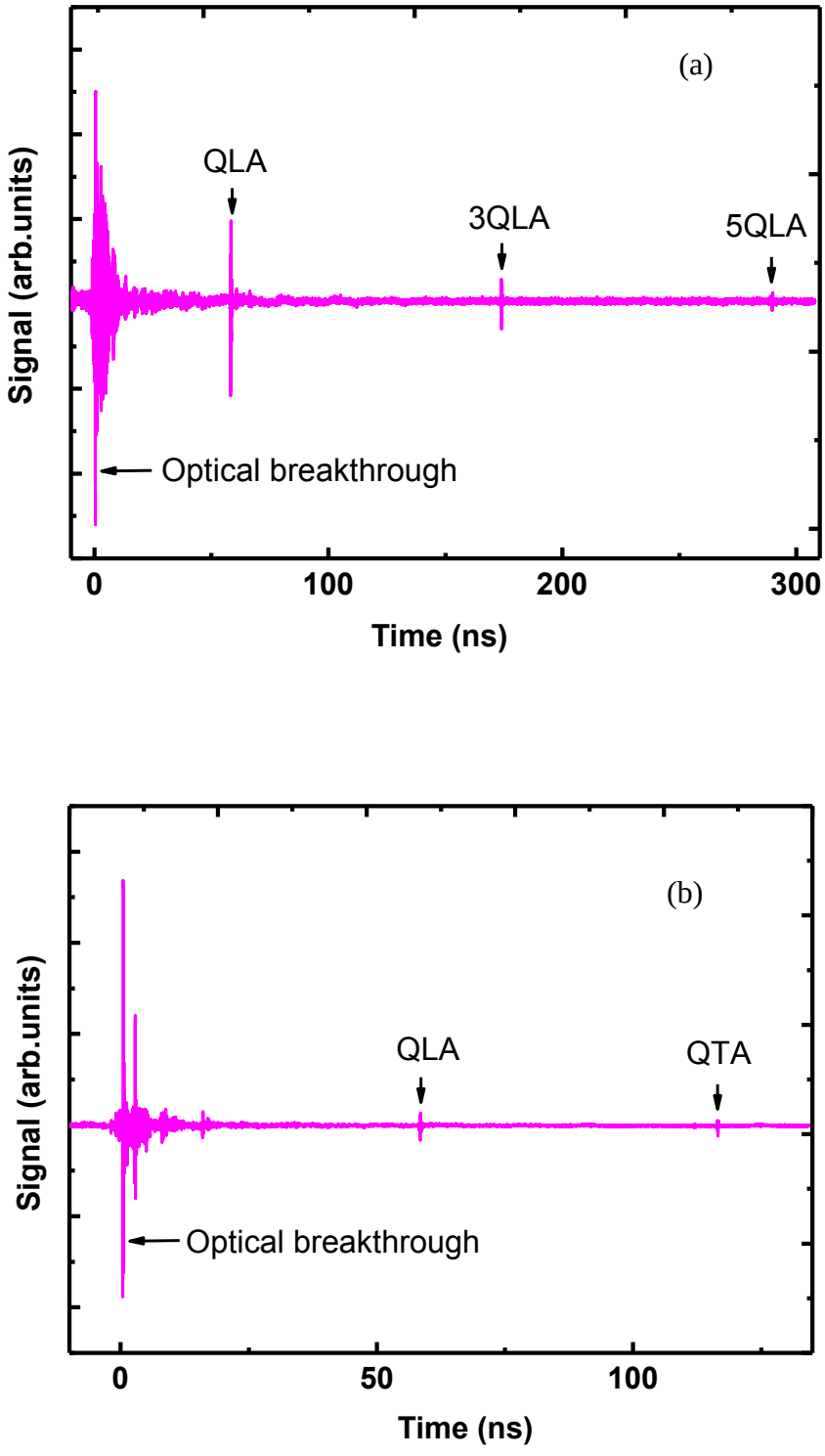



**Figure 4.21:** Electrical response measured for Schottky diodes fabricated on (311A) GaAs surface in a full temporal range with a bias of $V_B$ = 0V, (a) for QLA, and (b) QTA phonons.

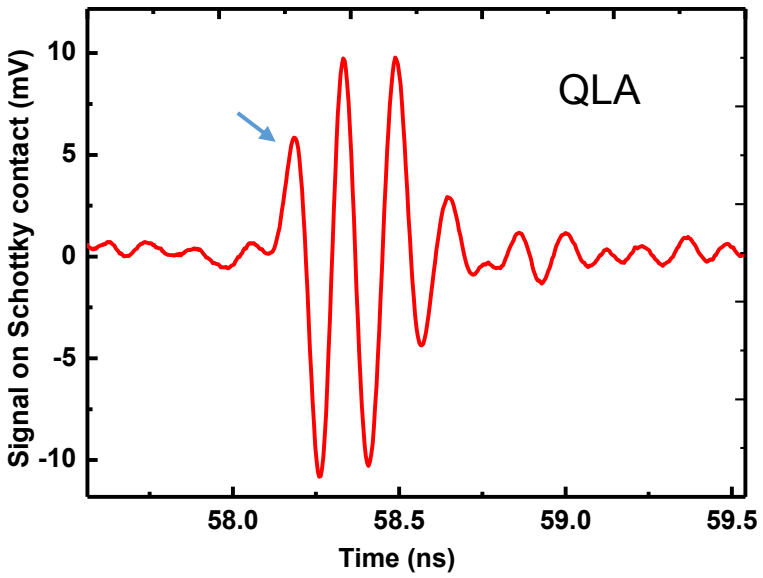



**Figure 4.22:** Phonon induced signals measured at pump fluence $W$=4 mJ/cm$^2$ at zero bias, $V_B$=0V for QLA phonons (second spike enlarged). Arrow indicates the change of polarity(positive), with respect to (311B) surface.

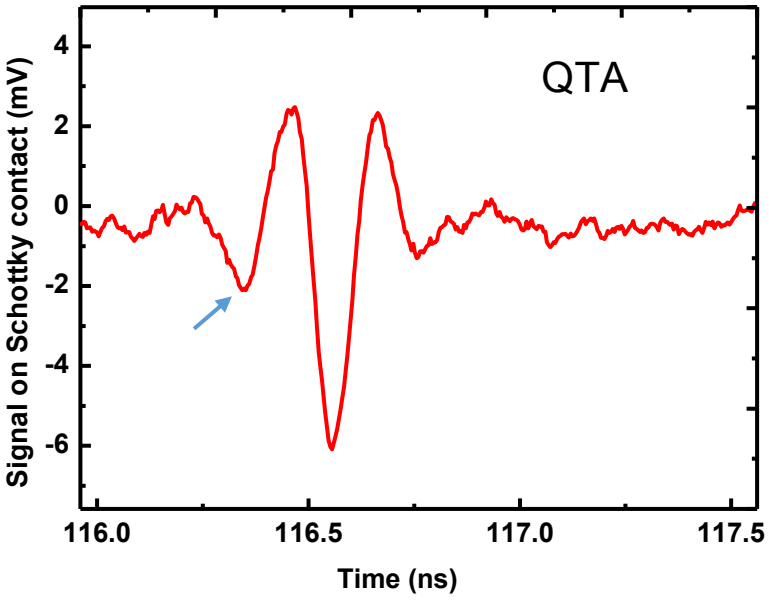
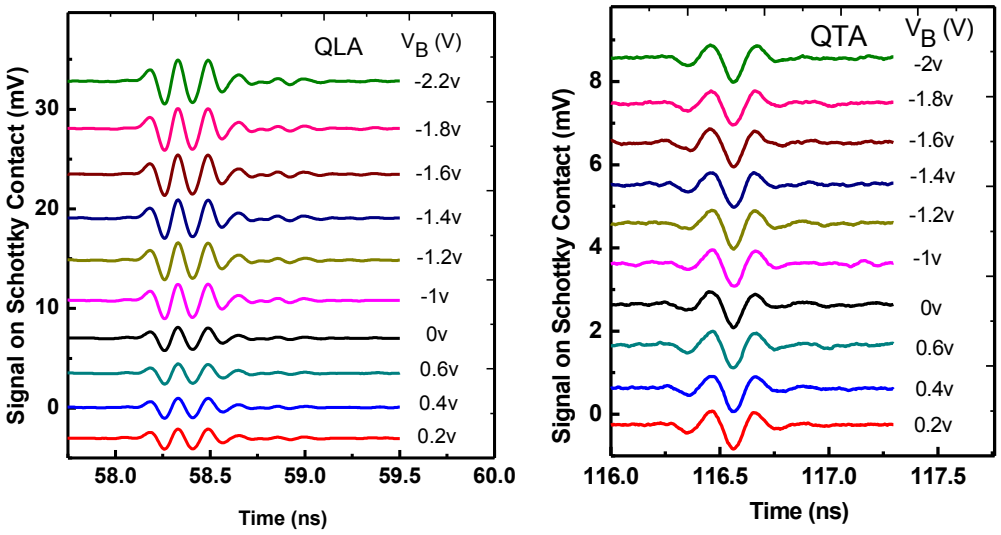



**Figure 4.23:** Phonon induced signals measured at pump fluence W=4 mJ/cm2 at zero bias, VB=0V for QTA phonons (third spike enlarged). Arrow indicates the change of polarity(negative), with respect to (311B) surface.

The important observation is that the polarity of the direct phonons in the measured signal for (311A) surface reverses compared to (311B), indicated by an arrow: for QLA (figure 4.22) it becomes positive, and for QTA (figure 4.23) it becomes negative which is opposite for (311B) results (see figure 4.7 (a) & figure 4.7 (b)). This polarity changes between (311B) surface and (311A) agrees with the theoretical predictions for the piezoelectric mechanism.

The response of the direct QLA ($t$≈58 ns) and QTA ($t$≈116 ns) phonons was investigated for range of applied bias and pump fluences. Dependence of QLA and QTA on bias is shown in figure 4.24 (a)&(b), respectively.




(a) QLA Signals (b) QTA Signals

**Figure 4.24:** Phonon induced signals measured for Schottky diodes fabricated on (311A) GaAs surface at pump fluence $W$=4 mJ/cm$^2$ with different bias voltages $V_{B,}$ (a) for QLA, and (b) QTA phonons.

The temporal positions of the first peak (positive) for QLA and QTA (negative) slightly moves to earlier times with the increase of reverse bias as expected (see section 4.1), which is consistent with (311B) results. The QLA signals shows strong ringing oscillations which is because of the parasitic capacitance and inductance. The amplitude of the QTA signal is small in comparison with QLA signals.

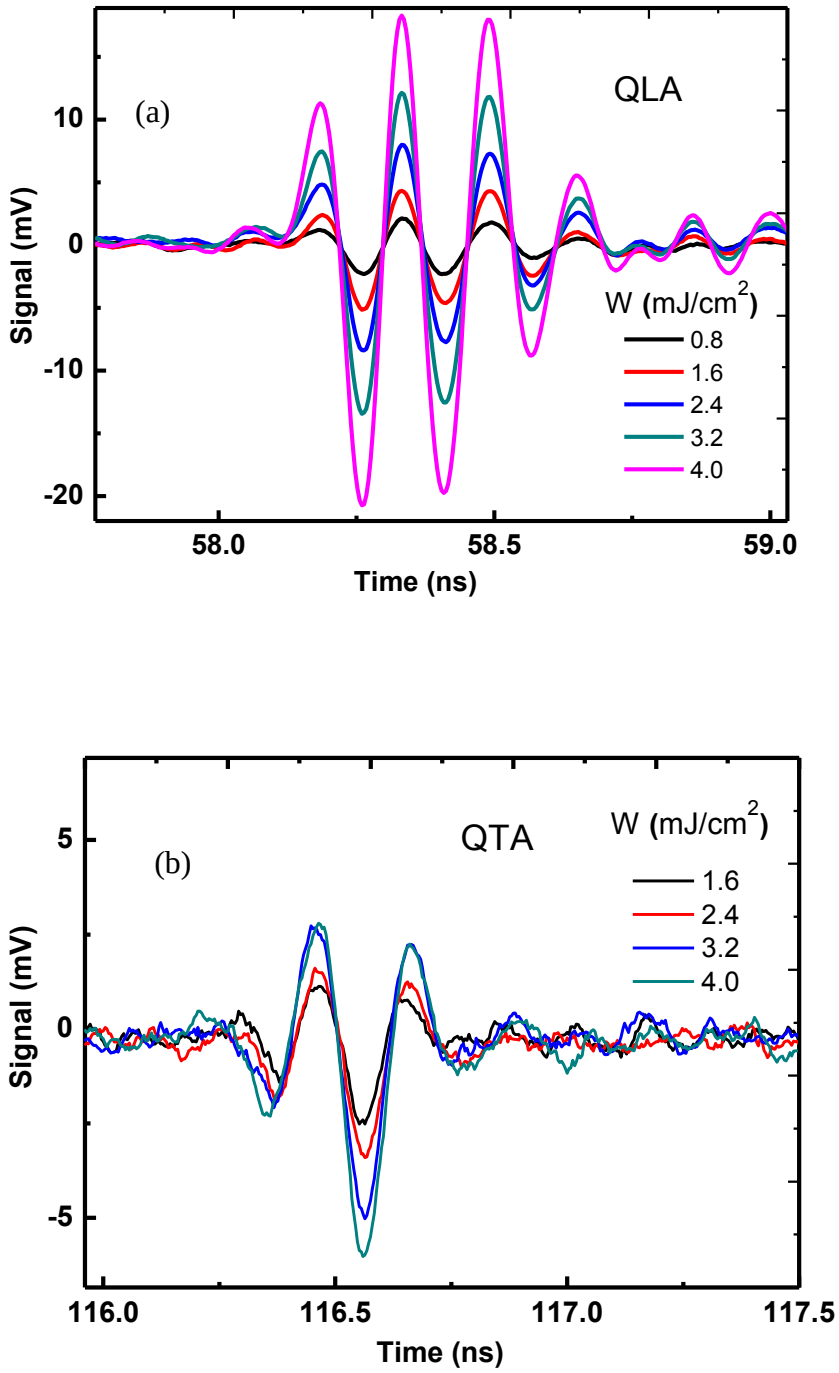



**Figure 4.25:** Phonon induced signals measured for Schottky diodes fabricated on (311A) GaAs surface at zero bias, $V_B$=0V with different pump fluences (a) for QLA, and (b) QTA phonons.

QLA and QTA signals dependence on pump fluence was performed at zero bias, shown in figure 4.25 (a)&(b), respectively. The arrival time for QLA phonons moves slightly to earlier times with increasing pump fluence, which indicates for Schottky diodes fabricated on (311A) GaAs surface, the nonlinear acoustic properties of GaAs are crucial. However, for QTA phonons there is no such shift in arrival time and this is due to the elastic nonlinear effects does not play significant role [108]. Dependence of QLA and QTA signals on pump fluence in the case of (311A) GaAs surface is consistent with the results obtained for (311B) GaAs surface.

Fast electrical measurements performed on the Schottky devices fabricated at (311B) and (311A) GaAs surfaces and comparison with calculated signals clearly shows that the piezoelectric transformation from coherent phonons to the polarization is the main mechanism. Conversely, in the case of Schottky devices fabricated on high-symmetry (100) crystallographic planes the detected electrical signals (phonon-induced), deformation potential is the dominant mechanism. As mentioned in previous sections, due to the band with limitation of the Oscilloscope used in this thesis, is it not possible to experimentally detect the higher frequencies calculated. However, using specially designed sample holders and smaller devices one should be able to detect high frequency phonons by Schottky didoes. It is possible, to detect frequencies up to at least 100 GHz experimentally by using Schottky contacts of few microns size with capacitance of order 10 fF [113].

## 4.6 Conclusions

In this chapter, Schottky diodes fabricated on (311B) GaAs surface and (311A) GaAs has been investigated to understand the interaction of subterahertz acoustic phonons with charge carriers with the aim of developing high speed acoustoelectric detectors for subterahertz compressional and shear acoustic waves. It has been shown that the Schottky diodes are successful in this application.

Optical excitation generates a compressive strain pulse in an Al film which is at the opposite side of the GaAs substrate, which generates QTA and QLA modes. These optical modes were later detected and their dependence on applied voltage bias, power and temperature was investigated.

The investigations revealed that the temporal position of the signal is moved to slightly earlier timescales by incrementing the reverse bias voltage. This is due to the increase in the depletion layer width. The dependence of the QLA and QTA modes on the power identified that QLA times were lower due to the nonlinear acoustic properties of the GaAs substrates, while the QTA times were unchanged. The inverse dependence of the sound velocities with temperature, was reflected in the arrival times of the QLA and QTA modes.

By comparing the experimental results with the calculated signals, the predominant role of piezoelectric phonon-electric transformation mechanism over deformational potential was concluded. Similar experimental measurements performed on GaAs (311A) confirmed these results and have discussed in detail in chapter 4. Due to experimental setup limitations the validity of the theoretically calculated dominance of the piezoelectric mechanism up to 70 GHz and 250 GHz cannot be performed.

In this thesis, I have successfully demonstrated that the Schottky devices processed on a low symmetry ordered semiconductor substrate efficiently serves to function as a piezoelectric transducer for longitudinal and transverse phonons up to 10GHz. In the future by designing devices of a few microns scale and with low capacitance value, transducers to detect sub-THz frequencies can be detected and resolved.

# Chapter 5

# Electron-Phonon Interactions in Two-Dimensional Structures: Quantum Wells, 2DEGs/2DHGs

## 5.1 Introduction

This chapter investigates the detection of longitudinal and transverse acoustic phonons in two-dimensional structures *i.e.* Quantum well embedded *p-i-n* photodiode detector (QW-*p-i-n*), two-dimensional electron gas (2DEG) and two-dimensional hole gas (2DHG) fabricated on (311) GaAs substrates. Previous work with (311) GaAs by P. Walker *et al* [24] has shown the possibility for the generation and detection of transverse modes in low symmetry directions using pump-probe in a superlattice where the pump and probe beam were both aligned on the superlattice device. The problem with detecting and generating in the same superlattice is the longitudinal and transverse components of the signal are mixed, leading to difficulties in separating the different contributions. A more recent work by A. V. Scherbakov *et al* [68] used detection on the opposite side of the substrate to the generation of the acoustic pulses. The different speeds of transverse phonons compared to acoustic phonons in GaAs substrates cause a separation of the two pulses in this configuration making the separation of the different modes easier.

C. L. Poyser *et al* [67] performed some initial investigations to obtain Longitudinal and Transverse acoustic signal using Quantum Well (QW) embedded p-*i-n* photodiode detector. Growing a *p-i-n* device, which incorporates a QW with the superior quality optical resonance, which is necessary for the creation of a sensitive detector of acoustic waves, is challenging on a (311) substrate. They successfully created a device and detected longitudinal acoustic waves but unable to

detect the quasi-transverse signal which is predicted to be present [68], as the alignment necessary to see the transverse signal was not clear. The extension of this work is to detect quasi-transverse signal. The transverse signal will not travel perpendicular to the (311) substrate due to acoustic anisotropy. This is an effect seen in anisotropic crystals where the group velocity and wavevector of a phonon wave may point in different directions meaning that the phonon energy flux is decreased in some directions and increased in others [114]. It is expected that the energy of the transverse phonons will be decreased in the [311] direction. This means the laser should not be aligned directly opposite the device to obtain a clear signal. From the Schottky experiments as described in chapter 4, we can estimate the angle and laser alignment to detect quasi-transverse phonons.

The experiments described in this chapter are divided into two sections according to processed devices and employed laser system, which were described previously in section 3.2 and section 3.3, respectively. The first section discusses longitudinal and transverse phonons detection by Quantum Well (QW) embedded *p-i-n* photodiode detector: GaAs Quantum well (RC34) and InGaAs Quantum well (RC80). These experiments were performed using a low power with high repetition rate Oscillator laser system as described in section 3.3.3. The second section discusses longitudinal and transverse phonons detection by two-dimensional electron gas (NU2080) and two-dimensional hole gas (NU1074) structures using a high power with low repetition rate amplifier laser system as described in section 3.3.2.

## 5.2 Photocurrent Measurements

Laser excitation of semiconductor samples creates carriers, which with the application of bias leads to the generation of a photocurrent. This can be used to get information about the quality of the optical resonances in the sample. This is important in the characterisation of the *p-i-n* photodiode detector. The variation of the photocurrent with bias in the device can be obtained using I-V measurements. These measurements were done using the oscillator laser described in section 3.3.3 in continuous wave mode. When the laser operates in this mode it emits a narrower energy pulse giving a better estimation of the wavelength dependence of the current

generated. To find out the *p-i-n* photodiode sensitivity and the wavelength dependence of its sensitivity a photocurrent experiment was performed.

These measurements were performed on two different wafers RC34 and RC80, GaAs Quantum well embedded between two AlGaAs intrinsic layers (see figure 3.8) and InGaAs Quantum well incorporated between two GaAs layers (see figure 3.9), respectively. Although many devices were utilized as a part of the investigations presented in this chapter, only a single set of photocurrent measurements will be shown here. At the point when distinctive devices are processed from a similar wafer there is a chance of difference, regardless of the obviously indistinguishable structure, because of unavoidable processing irregularities. In any case, the distinctions seen between the diverse *p-i-n* devices utilized were sufficiently small to be irrelevant to the outcomes of these investigations.

Figure 5.1 and figure 5.2 show the I-V characteristics of the devices fabricated on RC34 and RC80, respectively when in the dark and when illuminated with different laser energies at 10K. In the dark, the device fabricated on both wafers shows the diode characteristics. Device fabricated on RC34 shows turn on voltage 0.5 V, at a forward bias and reverse breakdown occurs at about -2.25 V. The device fabricated on RC80 shows turn on voltage 1.5 V, at a forward bias and reverse breakdown occurs at about -1. 5 V.

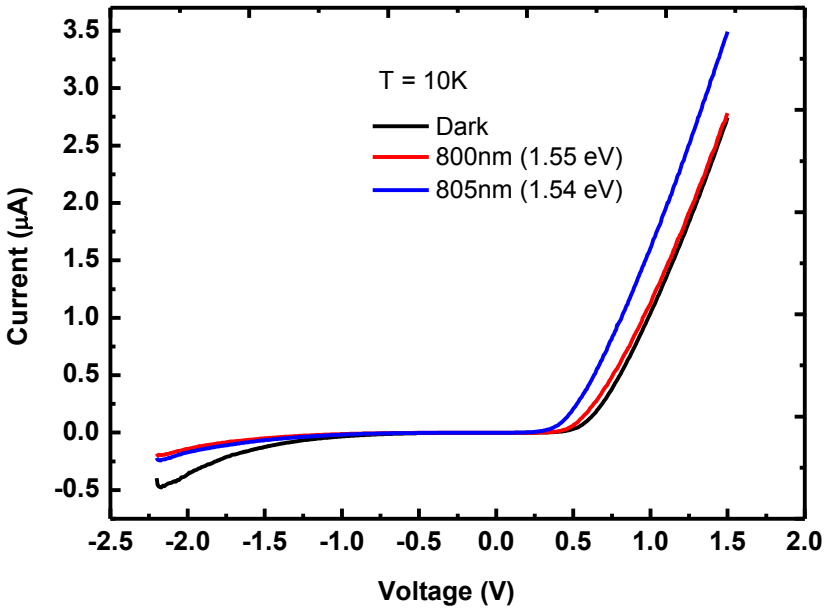



**Figure 5.1:** I-V measurements of the RC34 *p-i-n* device when illuminated by continuous-wave laser light at two laser energies and in the dark.

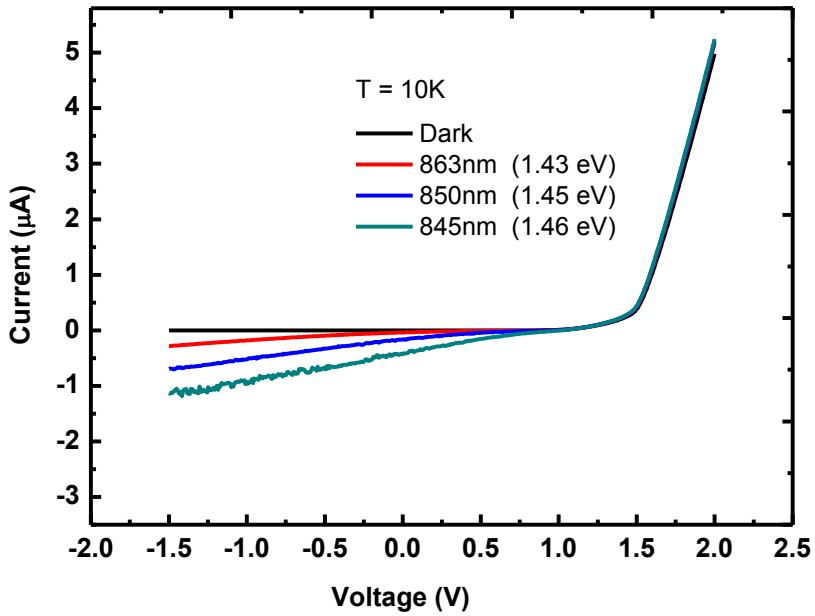



**Figure 5.2:** I-V measurements of the RC80 *p-i-n* device when illuminated by continuous-wave laser light at three laser energies and in the dark.

When a *p-i-n* device is illuminated with laser light it is possible to generate a photocurrent if the light has an energy greater than the band gap energy of the semiconductor it consists of. The diode (see figure 3.8) used in this experiment is mainly constructed of $Al_{0:3}Ga_{0:7}As$. At 10K the band gap energy of $Al_{0:3}Ga_{0:7}As$ is 1.8985 eV. The laser energies used to excite the sample in figure 5.1 and figure 5.2 are significantly lower than this. The operation of the *p-i-n* device as a detector depends on a quantum well in the intrinsic region. Exciting the device with light energy less than the bandgap of the main device is necessary to ensure that all absorption is occurring in the quantum well.

In the ideal I-V of an *p-i-n* diode, a peak is expected to occur when the laser excitation energy is equal to the exciton resonance of the quantum well [115]. Changing the bias applied to the device decreases this resonance energy, due to the quantum-confined Stark effect for excitons. The way this contributes to the *p-i-n* detection mechanism is detailed in section 2.2.4. In figure 5.1 and figure 5.2 there is no such peak and moreover, with light illumination only a slight change in current of a few micro amps is observed. This might be due to the quantum well grown in (311) GaAs not being of very good in quality compared to (100) GaAs substrates.

## 5.3 Longitudinal and Transverse Phonons detection by Quantum Well (QW) embedded *p-i-n* photodiode detector

Despite the questionable quality of the QW, photocurrent pump-probe measurements as described in section 3.7 were performed on quantum well incorporated *p-i-n* photodiode detector (QW-*p-i-n*) fabricated from RC34 and RC80 wafers, using the experimental scheme shown in figure 3.17. All measurements were performed at T = ~10K by using bath cryostat described in section 3.4.1. The optical pump induces strain pulses in Al film deposited on the polished face of a GaAs substrate opposite to the QW-*p-i-n* structure. The strain pulse injected from the Al film to the GaAs substrate and reaches the *p-i-n* structure after traversing the GaAs substrate in a time $t = d/s_L$ = 87ns where $d$ = 444μm is the thickness of the GaAs substrate and $s_L$= 5.1 $kms^{-1}$ is the longitudinal sound velocity in GaAs [116]. The diode is excited by a

probe pulse split from the pump. The probe is delayed with respect to the pump by passing through a step-motor optical delay line – producing a time delay *t*. The probe beam excited carriers in the quantum well, a considerable proportion of which could escape the well to form the photocurrent. The presence of the strain pulse passing through the QW changed the exciton energy to bring it in and out of resonance with the energy of the laser. This led to a change in the number of carriers generated in the QW, and hence changed the size of the photocurrent (see figure 2.10). The probe is focused to a spot size of 50μm on the optically flat surface of the mesa with energy density <50 μJ/cm$^2$. The photocurrent induced by the probe pulse, measured as a function of the delay *t* between pump and probe, was temporally integrated and amplified. The photocurrent in the absence of a strain pulse was isolated by chopping the pump pulse at 15 kHz using an acousto-optic modulator and a lock-in amplifier was used to obtain the strain induced photocurrent signal. The longitudinal acoustic signal detected by the quantum well fabricated on RC34, after generation in an 30nm aluminium film transducer and propagation through the 444 μm (311) substrate, is shown in figure 5.3.

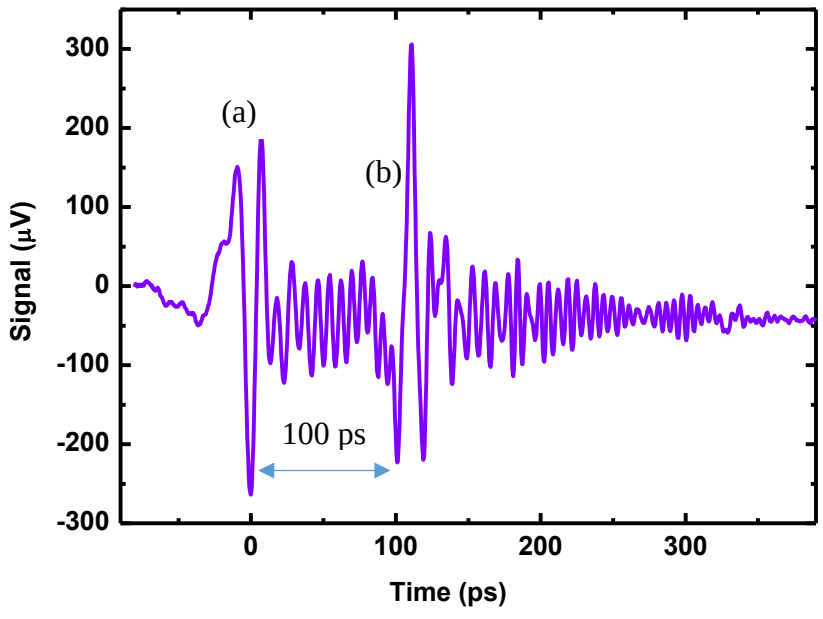



**Figure 5.3:** Longitudinal acoustic signal detected using a *p-i-n* device on a (311) GaAs substrate. Feature (a) represents the strain pulse reaching the quantum well for the first time, feature (b) represents the strain passing through the QW in the detector a second time after reflecting at the surface.

Figure 5. 4 demonstrates the origin of the strain pulse and its propagation through the RC34/RC80 sample structure that corresponds to the detected photocurrent signal features using *p-i-n* photodiode detector as shown in figure 5.3. The strain pulses present in figure 5.3 are due to the nature of the *p-i-n* photodiode detector. As explained in section 2.2.4, previous work [22] has shown that the signal seen in this detector originates from the quantum well grown in its intrinsic region. This QW is 305nm from the surface, an interface between the semiconductor sample and air. This interface is known to produce a near-complete reflection of strain with a $\pi$ phase change [1]. The first observed pulse, marked as (a) in figure 5.3 (also see figure 5.4, (a)) is the change in the photocurrent due to the strain pulse propagating through the QW on the way to the surface of the device. Upon reaching the top surface of the device, the strain pulse experiences a $\pi$ phase change and it was detected again in the QW (reflected) on the second pass which is marked as (b) in figure 5.3 (also see figure 5.4, (b)). In figure 5.3, the 100 ps difference in the arrival time of the incident and reflected pulses to the quantum well is the propagation time for the longitudinal polarised sound over the distance of 610 nm from the quantum well to the surface and back. The incident and reflected pulses have opposite phases due to phase change at reflection.

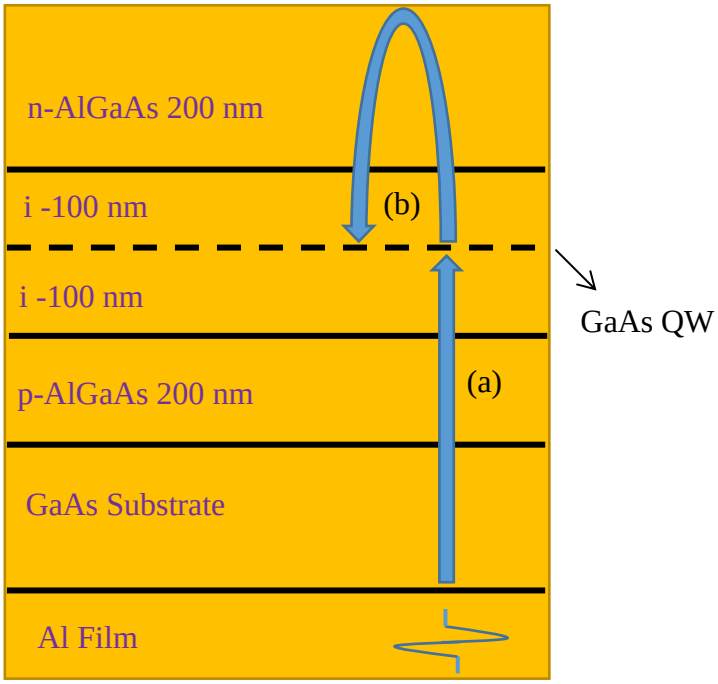



**Figure 5.4:** Schematic showing the origin of the strain pulses shown in figure 5.3. The path (a) represents the strain pulse reaching the quantum well for the first time, path (b) represents the strain passing through the QW in the detector a second time after reflecting at the surface.

Figure 5.5 shows the Fourier transform of the signal shown in figure 5.3. The amplitude spectrum of the tail from 131 ps to 390 ps, shows the dominant frequency at 150 GHz and a weaker signal at 200 GHz. The gaps between frequencies within this spectrum are due to taking account of forward and reflected pulses in Fast Fourier transforms (FFT). The FFT of the longitudinal signal confirms the existence of the GHz oscillations, with the most significant occurring 170 GHz.

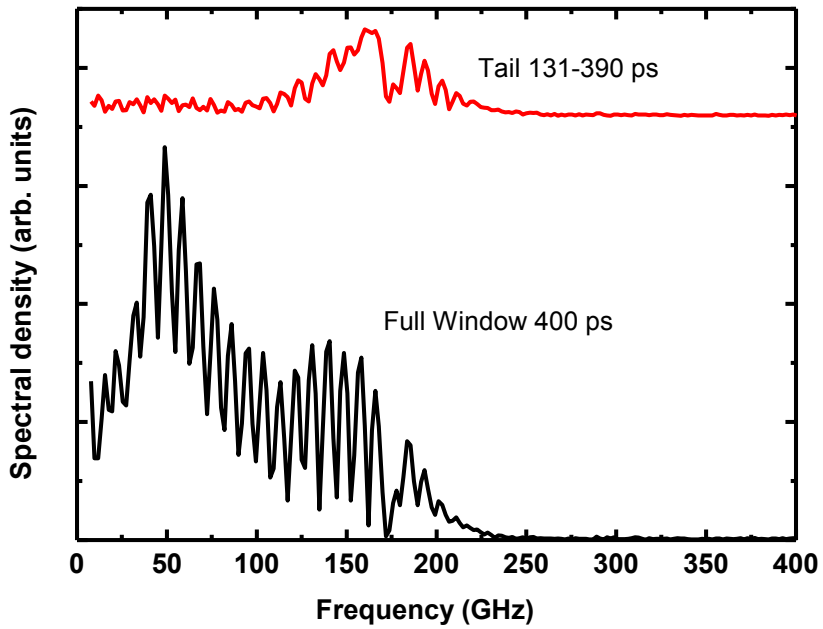



**Figure 5.5:** Amplitude spectrum obtained from the signal shown in figure 5.3 by Fast Fourier Transforms (FFT). Black line represents amplitude spectrum of full 400 ps signal, red represents the amplitude spectrum of the tail from 131 ps to 390 ps.

This agrees with the earlier photocurrent pump-probe measurements carried out on this sample by C. L. Poyser *et al* [67]. The longitudinal acoustic signals detected after generation in a 30nm aluminium film transducer and propagation through the 446 μm/160 μm (311) GaAs substrate by C. L. Poyser *et al* [67] is shown in figure 5.6. The two features marked as (a) and (b) in the figure 5.6 correspond to the arrival to the quantum well of incident and reflected strain pulses propagating from the GaAs substrate toward the top surface of the *p-i-n* structure and back from the surface toward the GaAs substrate, respectively (see figure 5.4). The oscillations between the incident and reflected strain pulses disappears as the substrate thickness reduces to 160 μm.

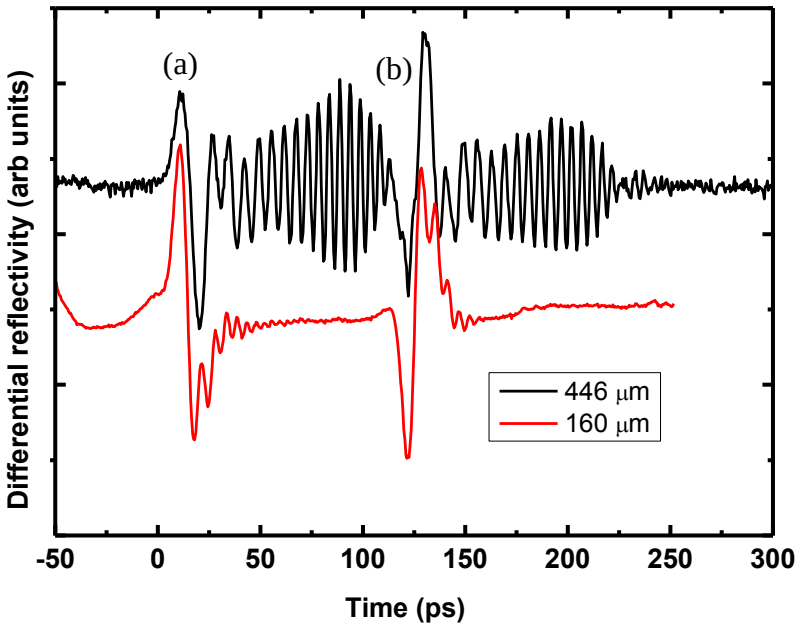



**Figure 5.6:** Longitudinal acoustic signal detected using a *p-i-n* device on a (311) GaAs substrate, black line represents 446μm thickness and red represents 160μm thickness. (Figure taken from C. L. Poyser *et al* [67]).

### 5.3.1 Longitudinal acoustic signal detection with various Aluminium film thickness

Photocurrent pump-probe measurements were also performed as described in section 3.7 on devices fabricated on RC34 with three different Al film thicknesses (20nm, 30nm and 100nm) with wavelength at 780nm. The longitudinal signal detected with a 20-nm aluminium film is shown in figure 5.7, inset shows the amplitude spectrum obtained for the signal by the Fast Fourier Transforms (FFT). It is clearly seen from the amplitude spectrum that a weak signal at 250 GHz (see inset vertical arrow) which is not observed for 30 nm and 100 nm aluminium films.

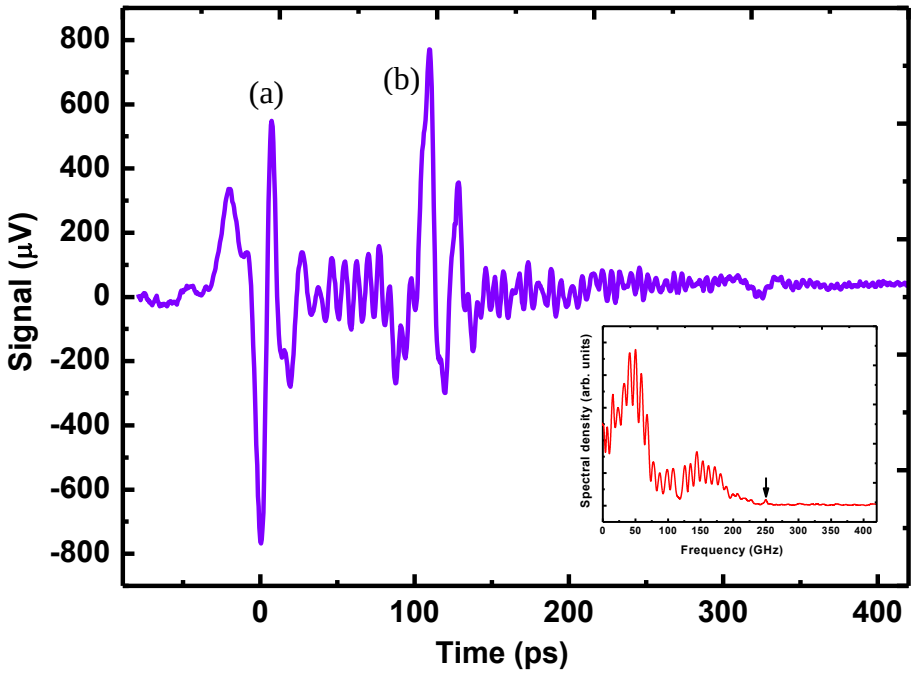



**Figure 5.7:** Longitudinal acoustic signal detected using a *p-i-n* device on a (311) GaAs substrate with 20 nm Aluminium film. Feature (a) represents the strain pulse reaching the quantum well for the first time, feature (b) represents the strain passing through the QW in the detector a second time after reflecting at the surface.

The longitudinal signal detected with newly evaporated 30 nm aluminium film at pump density *W*, 45 μJ/cm$^2$ is shown in figure 5.8. This signal is slightly different in comparison to the signal shown in figure 5.3 which is also measured for 30 nm aluminium film. The reason for the slightly different temporal shape is due to the non-uniformity of the adhesion of the evaporated aluminium film. The amplitude spectrum of the signal shown in figure 5.8 is like the spectrum shown in figure 5.5 with dominant frequency at 170 GHz. In figure 5.9, the longitudinal signal detected using 100 nm aluminium film, inset shows the amplitude spectrum obtained for the signal by the Fast Fourier Transforms (FFT) which consists dominant frequency at 50 GHz.

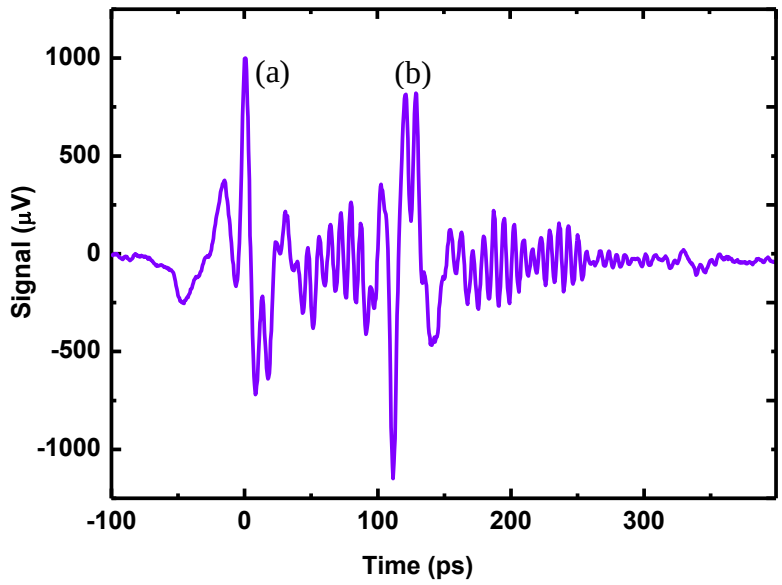



**Figure 5.8:** Longitudinal acoustic signal detected using a *p-i-n* device on a (311) GaAs substrate with newly evaporated 30 nm Aluminium film. Feature (a) represents the strain pulse reaching the quantum well for the first time, feature (b) represents the strain passing through the QW in the detector a second time after reflecting at the surface.

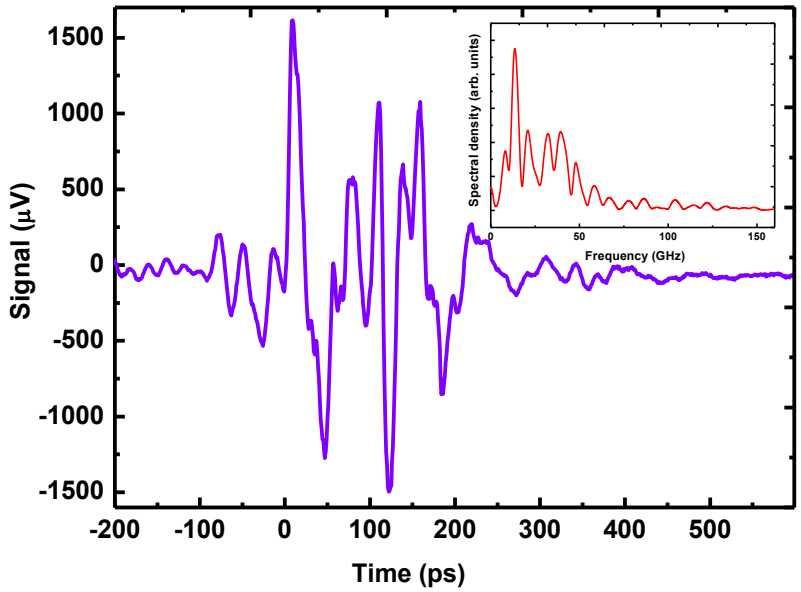



**Figure 5.9:** Longitudinal acoustic signal detected using a *p-i-n* device on a (311) GaAs substrate with 100 nm Aluminium film.

From the measurements performed with three different aluminium film thickness, it is clearly observed that in the thick Al film (100nm) the second strain pulse of the longitudinal signal due to the strain passing through the QW in the detector a second time after reflecting at the surface is not clear (see figure 5.9). This might be due to the multiple reflections in the aluminium film.

### 5.3.2 Dependence of Longitudinal acoustic signal on Bias

The longitudinal acoustic signal detected using the *p-i-n* device fabricated on wafer RC 34 was measured at two different applied bias voltages to observe the dependence of signal on bias. In figure 5.10, the black line shows the signal measured for positive 1V bias and the red line represents the signal measured for negative 1V bias. It is clearly seen from figure 5.10, that the temporal shape of the signal is exactly same for two different applied biases. This indicates the shape and signal amplitude ΔP (for definition see figure 5.12) is independent of applied bias, because the kinetic parameters (*i.e.* time of carrier tunneling from the QW and carrier recombination time in the QW) are stain-independent, which is consistent with previous work performed by D. M. Moss *et al* [21].

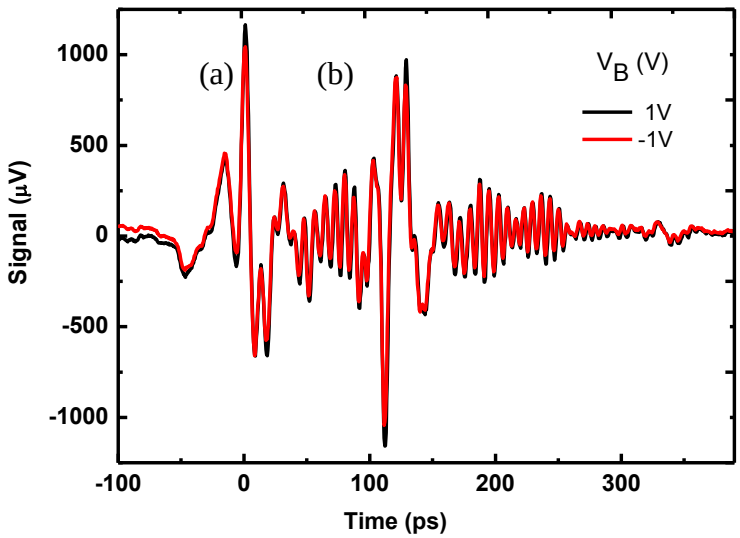



**Figure 5.10:** Longitudinal acoustic signal detected using a *p-i-n* device on a (311) GaAs substrate at two different bias voltages. Feature (a) represents the strain pulse reaching the quantum well for the first time, feature (b) represents the strain passing through the QW in the detector a second time after reflecting at the surface.

### 5.3.3 Dependence of Longitudinal acoustic signal on Pump Laser Power

The longitudinal acoustic signal detected using the *p-i-n* device fabricated on wafer RC 34 measured at various pump densities is shown in figure 5.11. In figure 5.11, with the excitation pump densities *W*, the temporal profile of the signal is independent of *W*. The arrival time of the incident and the reflected strain pulses (see figure 5.11 (a) and (b), respectively) is also independent of *W*. The vertical dotted lines in the figure 5.11, represents the absence of arrival time shift of the incident and reflected strain pulses with increasing *W*. This observation shows that there are no nonlinearities in the mechanism of detection of strain pulses for the pump density *W* values used in our experiments.

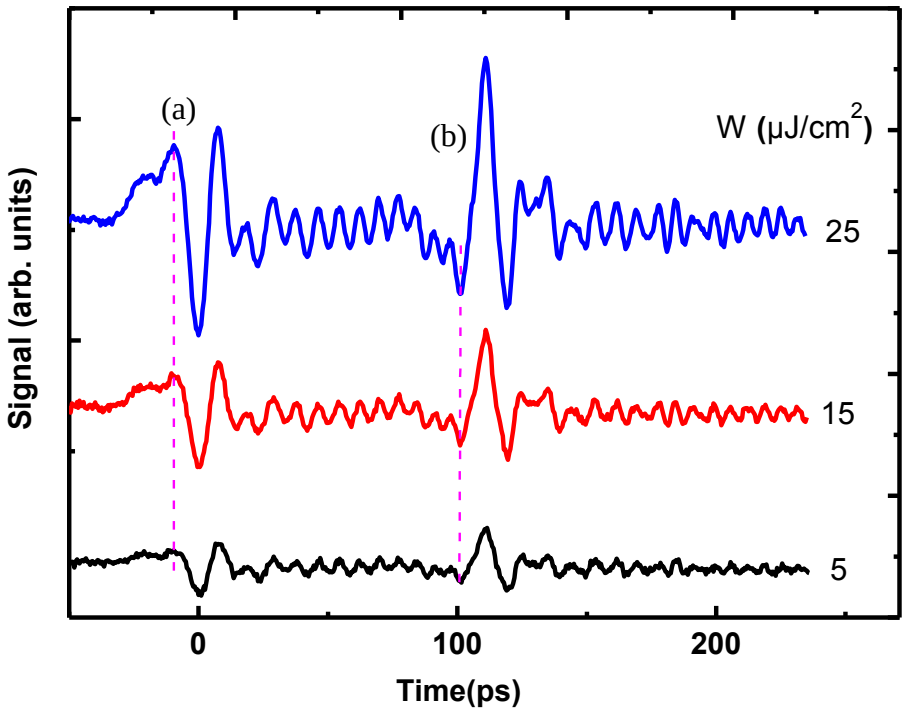



**Figure 5.11:** Longitudinal acoustic signal detected using a *p-i-n* device on a (311) GaAs substrate at various pump densities *W*. Feature (a) represents the strain pulse reaching the quantum well for the first time, feature (b) represents the strain passing through the QW in the detector a second time after reflecting at the surface. The vertical dotted line shows the absence of arrival time shift of the incident and reflected strain pules with increasing *W*.

The incident strain pulse shown in figure 5.11 (a) is zoomed for clarity to understand the dependence of the signal amplitude ΔP of the ultrafast photocurrent changes for various pump densities *W* at bias $V_B$= 1V, which is shown in figure 5.12. The signal amplitude ΔP for different powers was obtained from figure 5.12 and plotted against pump densities *W* as shown in figure 5.13. From figure 5.13, it is clearly seen that as the pump density *W* increases the changes of photocurrent amplitude ΔP increases, which is consistent with previous work performed by D. M. Moss *et al* [22].

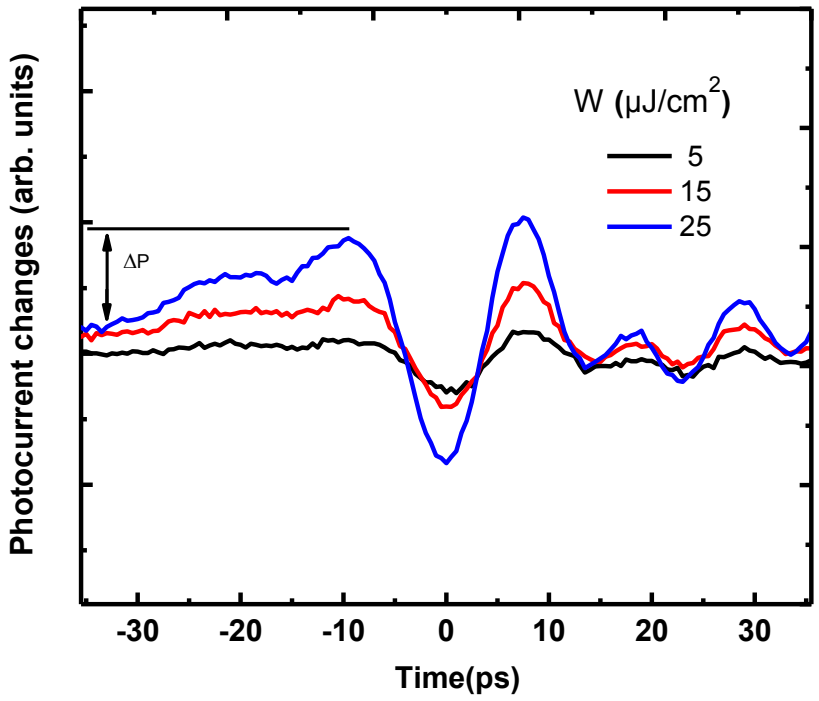



**Figure 5.12:** Photocurrent changes when the incident strain pulse is passing the quantum well of the *p-i-n* device for various pump densities *W* at bias $V_B$= 1V.

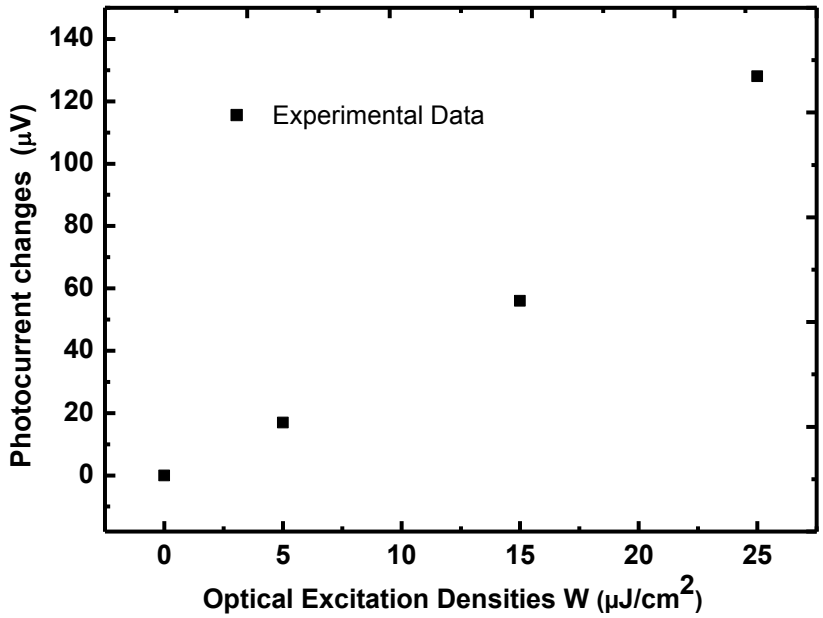



**Figure 5.13:** The dependence of the changes of photocurrent amplitude ΔP (for definition see figure 5.12) on pump density *W*.

### 5.3.4 Transverse acoustic signal detection with different aluminium film thickness

The most interesting investigation of the RC34 sample is the transverse acoustic signal detection by the quantum well fabricated on RC34, after generation in an 30nm aluminium film transducer and propagation through the 444 μm (311) substrate, which is shown in figure 5.14. In the transverse acoustic signal, figure 5.14, we observed high frequency tail which no one has reported previously. This high frequency tail is from 300 ps to 800 ps which can be seen clearly in figure 5.15. For the transverse acoustic signal, the 200 ps difference in the arrival time of the incident and reflected pulses to the quantum well is the propagation time for the longitudinal polarised sound over the distance of 610 nm from the quantum well to the surface and back. The incident and reflected pulses have opposite phases (indicated by red arrows, see figure 5.14) due to phase change at reflection.

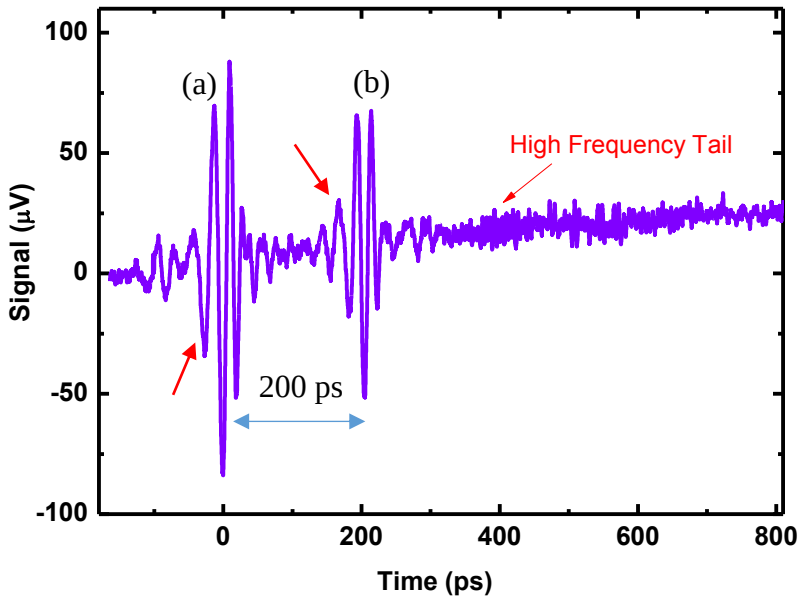



**Figure 5.14:** Transverse acoustic signal detected using a *p-i-n* device on a (311) GaAs substrate. Feature (a) represents the strain pulse reaching the quantum well for the first time, feature (b) represents the strain passing through the QW in the detector a second time after reflecting at the surface.

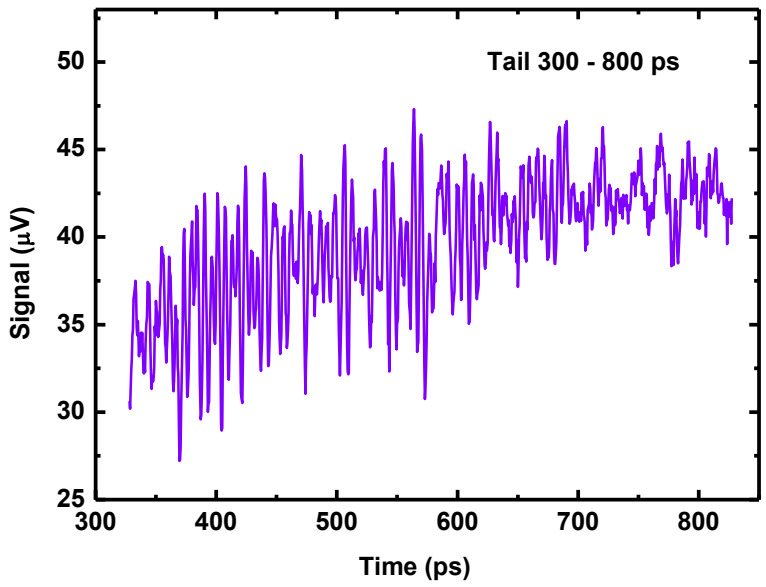



**Figure 5.15:** High frequency tail of the transverse acoustic signal from 300 ps to 800 ps time window.

Fast Fourier transforms (FFT) analysis was performed on this signal with different time windows to obtain the amplitude spectrum. Fourier transform of the temporal signal that includes both incident and reflected strain pulses with high frequency tail (1 ns – time window) is shown in figure 5.16. It can be seen that the dominant frequency in the signal is 50 GHz with a weaker signal at 170 GHz. The gaps between frequencies within this spectrum are due to taking account of forward and reflected pulses in FFT.

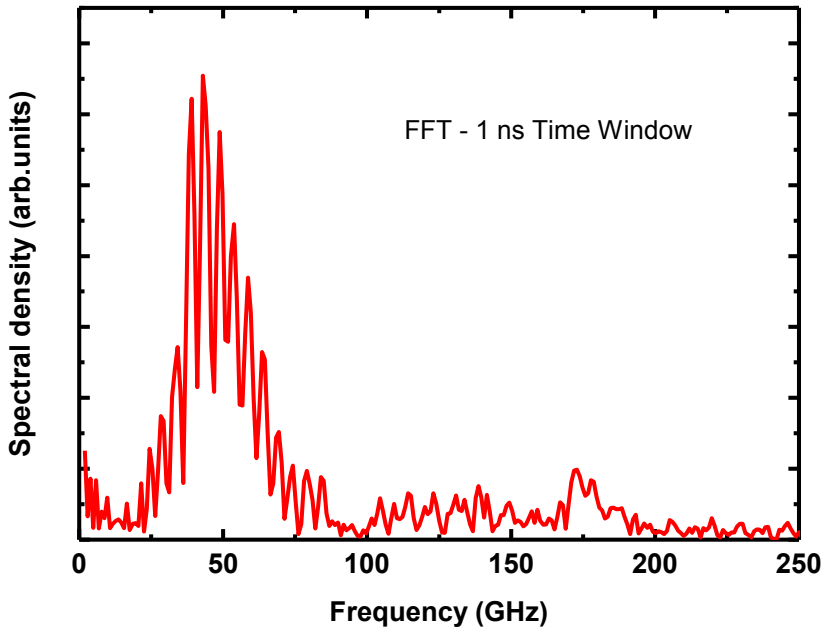



**Figure 5.16:** Amplitude spectrum obtained from the Fast Fourier Transforms (FFT) of the temporal signal shown in figure 5.14.

To confirm the origin of the high frequency 170 GHz observed in figure 5.16, the Fourier transforms were performed on the high frequency tail shown in figure 5.15 with different time windows as shown in figure 5.17. The time window from 328 ps to 478 ps gives two signals, a weaker signal at 130 GHz and strong signal at 170 GHz whereas time window from 478 ps to 628 ps gives three signals, a low frequency signal at 50GHz and two strong signals at 130 GHz and 170 GHz. The time window from 628 ps to 778 ps has three signals, a low frequency signal at 50 GHz with dominant frequency at 170 GHz and a weaker signal at 200 GHz. It is

clearly seen from the figure 5.17 that all the time windows show the dominant frequency at 170 GHz.

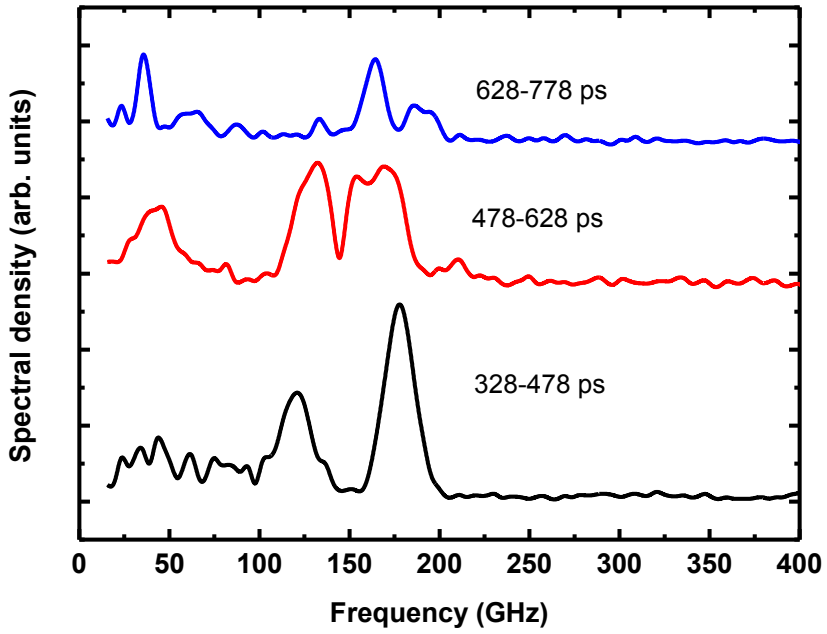



**Figure 5.17:** Amplitude spectrum obtained from the Fast Fourier Transforms (FFT) of the high frequency tail shown in figure 5.8. Black line represents the time window from 328 ps to 478 ps, red line shows the time window from 478 ps to 628 ps and blue line represents the time window from 628 ps to 778 ps.

The transverse acoustic signal detected using a 100 nm Aluminium film is shown in figure 5.18. The second strain pulse for the transverse signal is observed but the signal looks noisier and the oscillations are not clear which is again due to the multiple reflections in the aluminium film. The amplitude spectrum of this signal was obtained which consists dominant frequency at 50 GHz, which clearly indicates that the thick aluminium films are not capable of generating high frequencies. Investigations were additionally performed to detect transverse signal in 20nm Al film, yet we were unsuccessful.

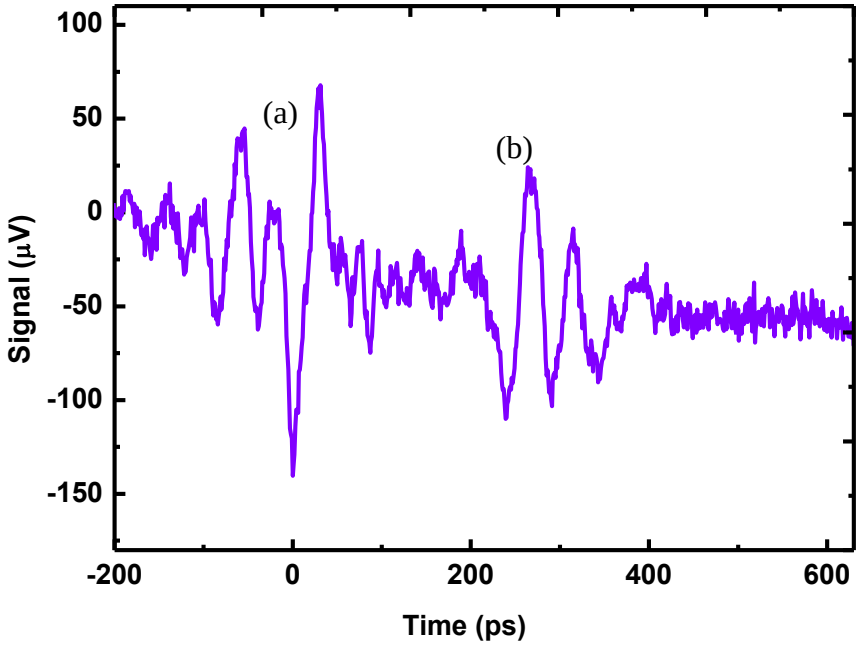



**Figure 5.18:** Transverse acoustic signal detected using a *p-i-n* device on a (311) GaAs substrate with 100 nm Aluminium film. Feature (a) represents the strain pulse reaching the quantum well for the first time, feature (b) represents the strain passing through the QW in the detector a second time after reflecting at the surface.

## 5.4 Longitudinal acoustic signal detection using *p-i-n* device embedded with InGaAs QW

Photocurrent pump-probe measurements as described in section 3.7 were also performed on InGaAs quantum well incorporated *p-i-n* photodiode detector fabricated on RC80 wafer, using the experimental scheme shown in figure 3.17. The reason for selecting p-*i*-*n* device embedded with InGaAs QW is described in detail section 3.2.3, to summarise: GaAs grows better than AlGaAs layers on (311) surface. After a series of iterations of device processing and testing, a *p-i-n* device embedded with InGaAs QW was fabricated which could detect longitudinal acoustic signal. The longitudinal acoustic signal detected by the quantum well fabricated on RC80, after generation in an 30nm aluminium film transducer and propagation through the 448μm (311) substrate, is shown in figure 5.19. The probe is focused to a spot size of

50μm on the optically flat surface of the mesa with energy density <50 μJ/cm$^2$. In figure 5.19, the 200 ps difference in the arrival time of the incident and reflected pulses to the quantum well is the propagation time for the longitudinal polarised sound over the distance of 1260 nm from the quantum well to the surface and back. The incident and reflected pulses have opposite phases due to phase change at reflection, indicated by vertical arrows.

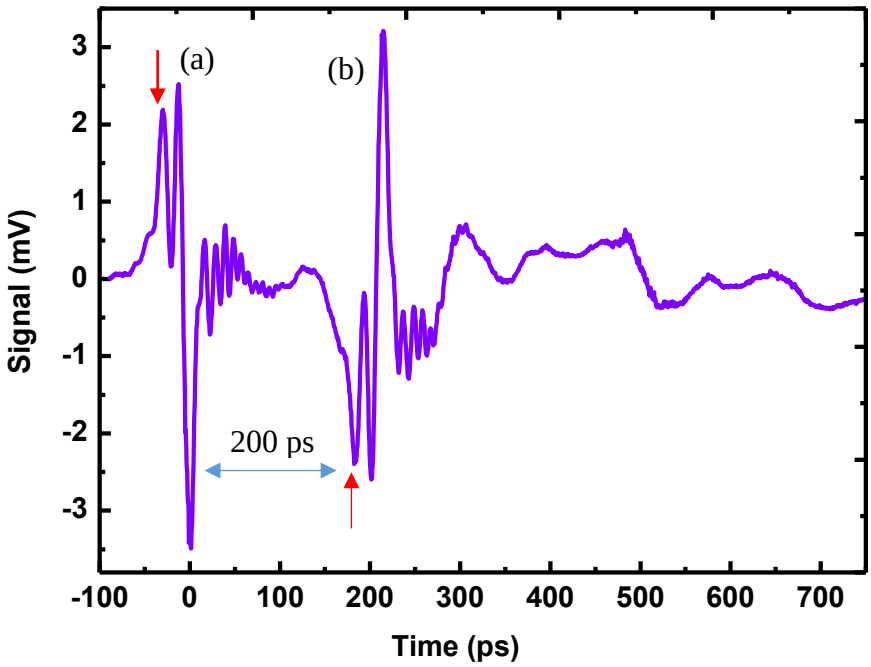



**Figure 5.19:** The longitudinal acoustic signal detected using a *p-i-n* device fabricated on RC 80 of (311) GaAs substrate with 30 nm Aluminium film. Feature (a) represents the strain pulse reaching the quantum well for the first time, feature (b) represents the strain passing through the QW in the detector a second time after reflecting at the surface.

The temporal shape of the signal is different compared to the longitudinal signal obtained from GaAs quantum well (RC 34) as shown in figure 5.3. This might be due to the inadequate quality of the quantum well and device processing. Figure 5.20 shows the longitudinal signal detected with a 100 nm aluminium film. The temporal shape is different from 30 nm aluminium film and the signal-to-noise is lower. The

reasons for this temporal shape difference with different aluminium films, power, temperature and bias were not yet investigated by optimising the sample structure, which opens a large scope for future reasearch work.

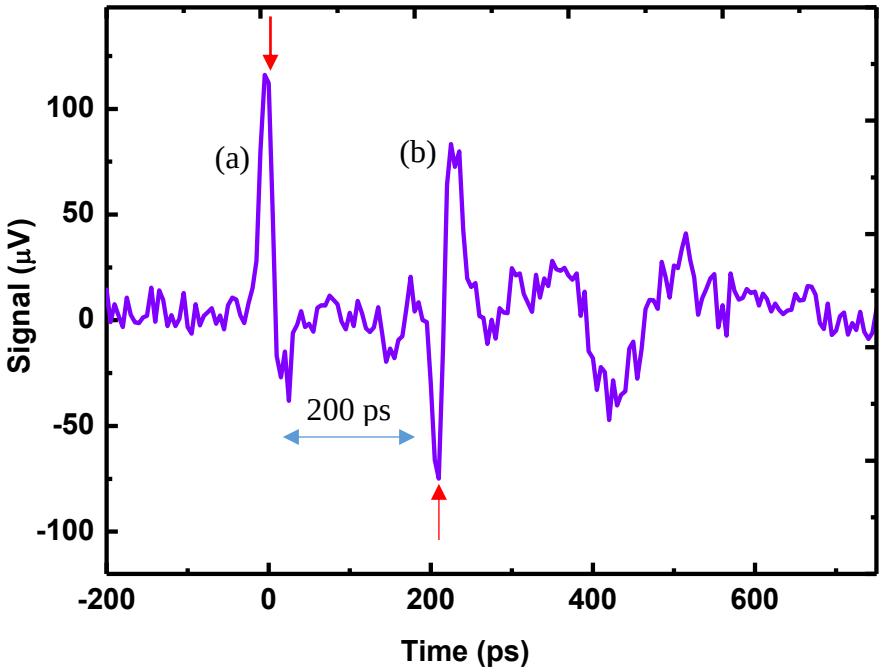



**Figure 5.20:** Longitudinal acoustic signal detected using a *p-i-n* device fabricated on RC 80 of (311) GaAs substrate with 100 nm Aluminium film. Feature (a) represents the strain pulse reaching the quantum well for the first time, feature (b) represents the strain passing through the QW in the detector a second time after reflecting at the surface.

## 5.5 Fast acoustic-electric transformation of Longitudinal and Transverse phonons using 2DEG and 2DHG structures

In layered semiconductor heterojunction structures conduction band variations can lead to formation of a quasi two-dimensional electron layer known as a two-dimensional electron gas (2DEG) as shown in figure 3.11, the analogous construct of holes is called a two-dimensional hole gas (2DHG). At low temperatures

the interaction with phonons has strong effects on device performance and can become dominant particularly in the heterojunction system where growth techniques allow physical separation of the parent donor atoms and the two-dimensional electron gas layer thus reducing ionized impurity scattering. Clearly, such systems are ideal for experimental study of the electron-phonon interaction. Previous sections of this chapter described the longitudinal and transverse phonons detection using by Quantum Well (QW) embedded *p-i-n* photodiode detector. This section investigates the longitudinal and transverse phonons detection by two-dimensional electron gas (NU2080) and two-dimensional hole gas (NU1074) structures.

### 5.5.1 Current-Voltage characteristics of NU2080/ NU1074

The current-voltage (I-V) characteristics of the two-dimensional electron gas and two-dimensional hole gas structures were measured before experiments using Current Voltage Graphical User Interface as described in section 3.5. The two-dimensional electron gas and two-dimensional hole gas I-V characteristics at a temperature of $T$=5 K is shown in figure 5.21 and figure 5.22, respectively. In figure 5.21, when applied forward voltage is changing from low to high values, there appear three regions that show different relationships between current and voltage. At the low forward voltages, there is a linear relation where the Ohm's law is obeyed, and the current linearly increases with voltage. With further increasing voltage, the relation becomes sublinear, which is because the electron energy reaches threshold for optical phonon scattering, leading to electron mobility decrease and a sublinear dependence between current and voltage is observed due to velocity saturation. Finally, when the voltage is above 0.7 V, the current gradually rises into the saturation region because of saturation drift velocity. In figure 5.22, at the low forward voltages, there is a linear relation between applied voltage and current.

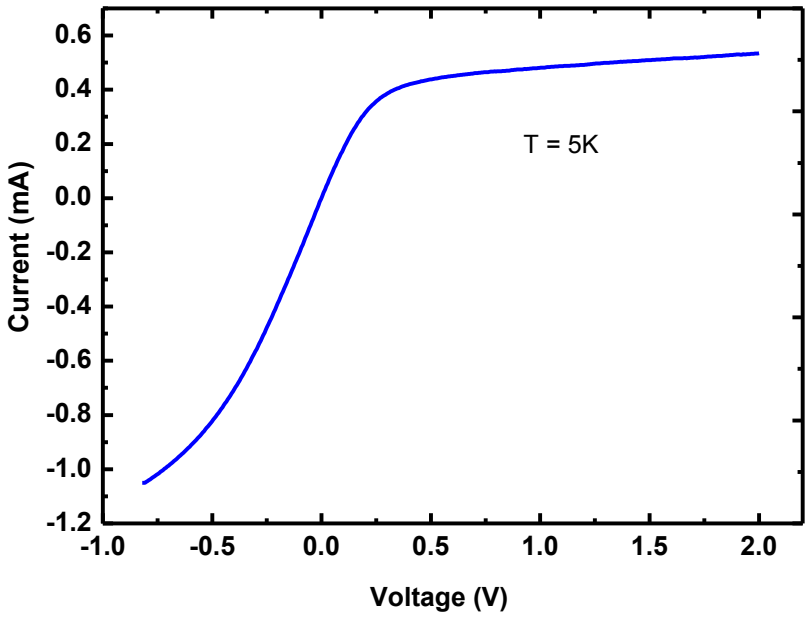



**Figure 5.21:** Current voltage characteristics of the two-dimensional electron gas structure at temperature T=5K.

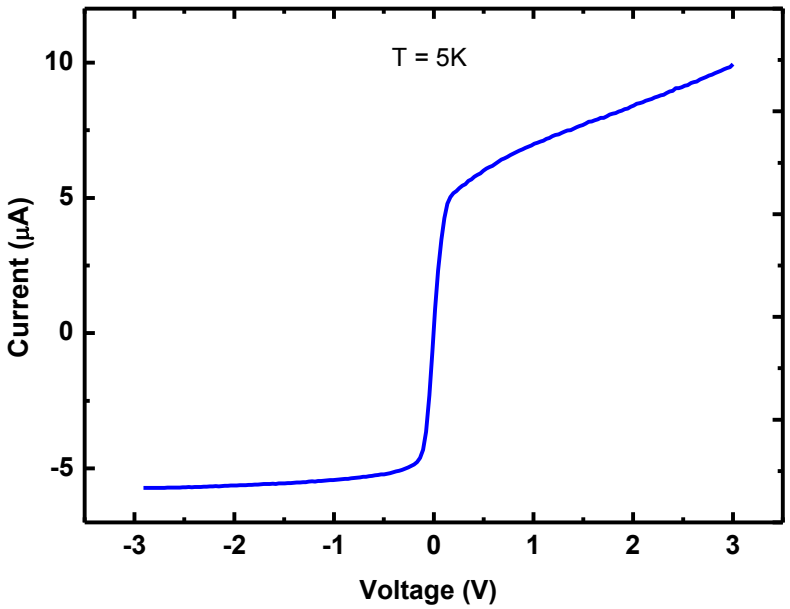



**Figure 5.22:** Current voltage characteristics of the two-dimensional hole gas structure at temperature T=5K.

### 5.5.2 Electrical detection of QLA and QTA Coherent Phonons by 2DEG

The strain pulse based fast-electrical measurements, like for the Schottky diode experiments (vertical devices), described in chapter 4 were performed using two-dimensional electron gas and two-dimensional hole gas structures (lateral devices). The experimental setup is shown in figure 3.16 where the normal lens was replaced with cylindrical lens and all measurements were at T = 5K unless otherwise specified. The sample was mounted on a specially designed holder incorporating 50 Ω micro strip line conductor and a microwave coaxial launcher for connection to the wide-bandwidth cryostat wiring. Changes in the voltage across the device caused by the presence of the strain pulse were measured by a fast oscilloscope as described in section 3.6. The pump pulse taken from an amplified Ti: Sapphire laser (800nm wavelength, 80fs pulse duration and 5 kHz repetition rate) was used to generate acoustic signals in an 30nm Al film thermally evaporated on the opposite face of the (311) GaAs substrate of thickness $d$ = 328μm.

After the strain pulse propagation through the GaAs substrate in the time $\Delta t_i = d/v_i$ ($i$ = QLA, QTA or Pure TA modes), the coherent phonons induce an electrical response in the two-dimensional structures. This electrical response $\delta V(t)$ is monitored by a digitizing oscilloscope with the bandwidth of 12.5 GHz as described in section 3.6. The excitation spots at the Al film were displaced at some angle relative to the device for QLA and QTA wave packets as shown in figure 5.23(a) and 5.23(b), respectively to detect the injected phonon fluxes by the two-dimensional structures. Unlike the Schottky diode experiments, in the two-dimensional structure measurements the pump spots appear like a vertical line (see figure 5.23) as the cylindrical lens creates a strip across the device, because of this even after aligning the pump spot only for QLA we can still expect QTA signal. An example of the temporal trace $\delta V(t)$ measured that includes both QLA and QTA coherent phonons as expected in a full temporal range is shown in figure 5.24. The trace includes three sharp spikes. Firstly, the spike at time $t$=0 corresponds to the response from optical pump breakthrough. The other spikes marked by vertical arrows are due to coherent phonon wave packets. The second spikes at $t$≈59 ns (figure 5.24) and at $t$≈104 ns

(figure 5.24) are the QLA and QTA phonons respectively propagating directly from Al film to 2DEG, which is the main point of interest in all further measurements.

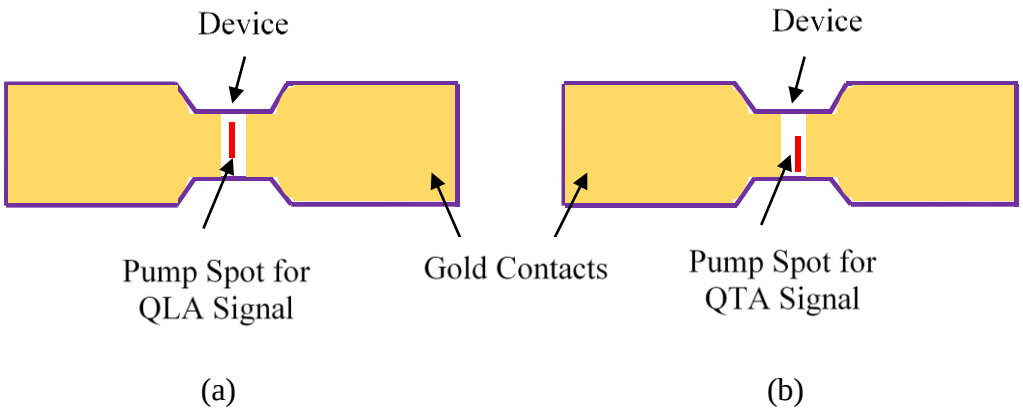



**Figure 5.23:** Schematic of the 2DEG structure displaying the excitation spots at the Al film were displaced at some angle relative to the device. (a) shows pump spot for detecting QLA signal while (b) shows pump spot for detecting QTA signal.

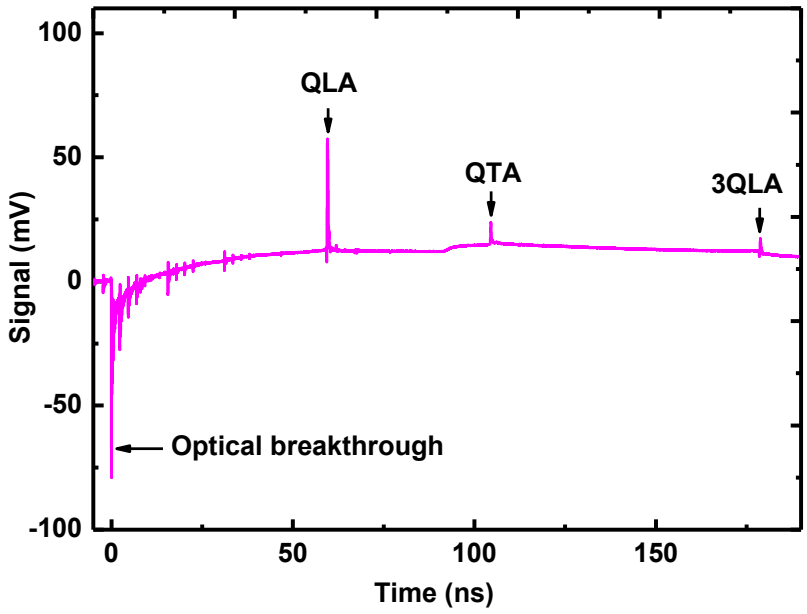



**Figure 5.24:** Electrical response measured from 2DEG structure in a full temporal range, consists of both QLA and QTA phonons with a bias of VB = 400 mV at pump fluence W=4.8 mJ/cm2.

The third spike at $t \approx 177$ ns (3QLA), is the QLA reflection after three times. For further analysis, by using two cylindrical lenses the pump spot is tightly focused to separate the QLA and QTA phonon modes. Figure 5.25 shows the only QLA signal in the full temporal range with the absence of QTA phonon mode. The QTA signal in the full temporal range is shown in figure 5.26, however the QLA phonon mode is not completely absent as marked at $t \approx 59$ ns by vertical dotted red arrow in figure 5.26. This is maybe due to the reason that a small amount of the pump beam is scattered behind the contacts and hence the QLA is not separated completely in QTA trace. For QLA, the signal is amplitude is 100 mV (see figure 5.25) while for QTA the signal is amplitude is 30 mV (see figure 5.26).

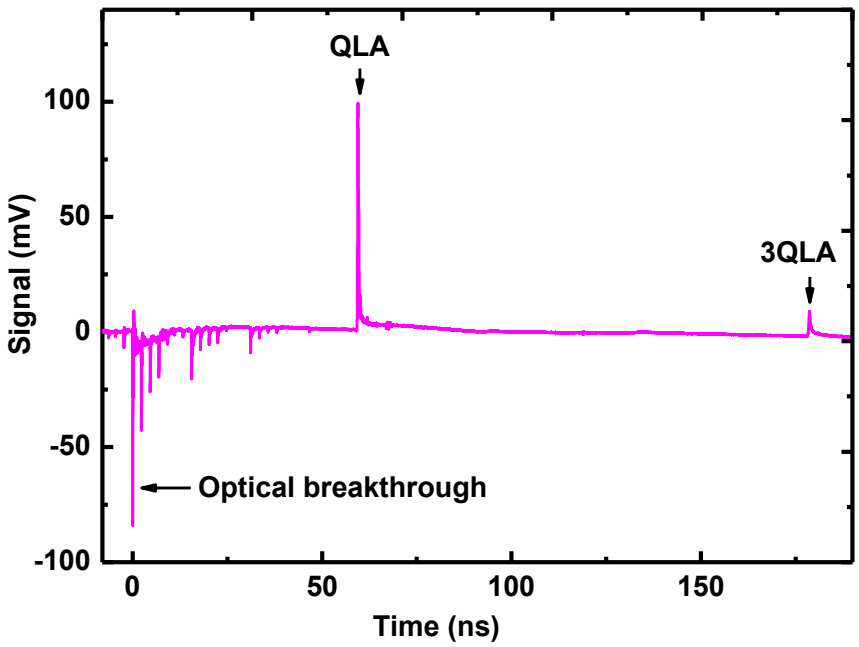



**Figure 5.25:** Electrical response measured from 2DEG structure in a full temporal range, for QLA phonons with a bias of $V_B = 400$ mV at pump fluence $W = 4.8$ mJ/cm$^2$.

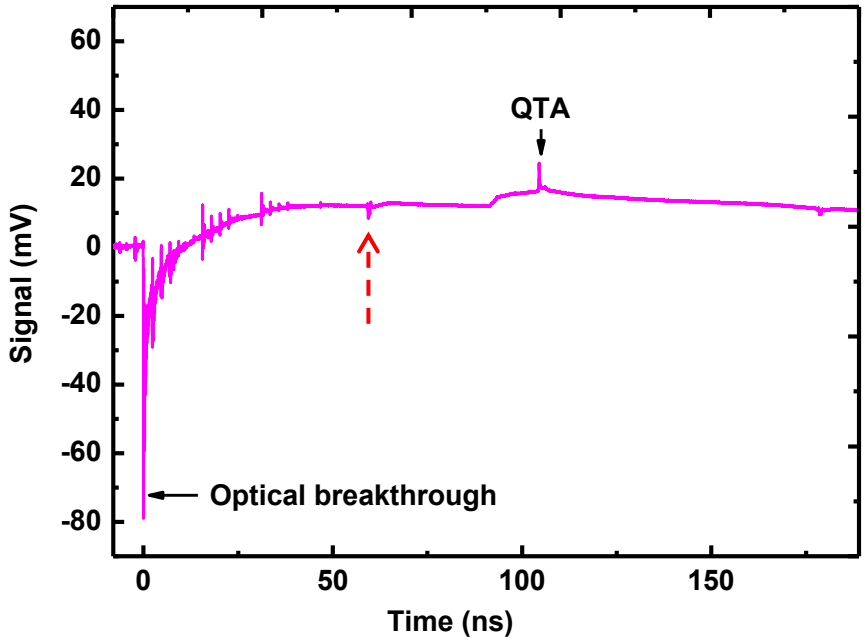



**Figure 5.26:** Electrical response measured from 2DEG structure in a full temporal range, for QTA phonons with a bias of $V_B$ = 400 mV at pump fluence $W$=4.8 mJ/cm$^2$. The vertical dotted red arrow indicates the presence of QLA phonon mode.

### 5.5.3 Dependence of QLA and QTA signals on Bias Magnitude

The response of the direct QLA and QTA phonons, detected at $t$≈59 ns and $t$≈104 ns respectively, was investigated for a range of applied positive and negative biases ($V_B$ = 0 to 500 mV). The bias was applied to the 2DEG externally using a Keithley 230 programmable voltage source via a bias tee and the electrical response $\delta V(t)$ was recorded on an oscilloscope (see section 3.6). An example of the electrical signals $\delta V(t)$ (zoomed) for QLA phonons measured for several positive and negative bias voltages $V_B$ is shown in figure 5.27 and figure 5.28, respectively while figure 5.29 and figure 5.30 shows QTA phonons measured for several positive and negative bias voltages $V_B$.

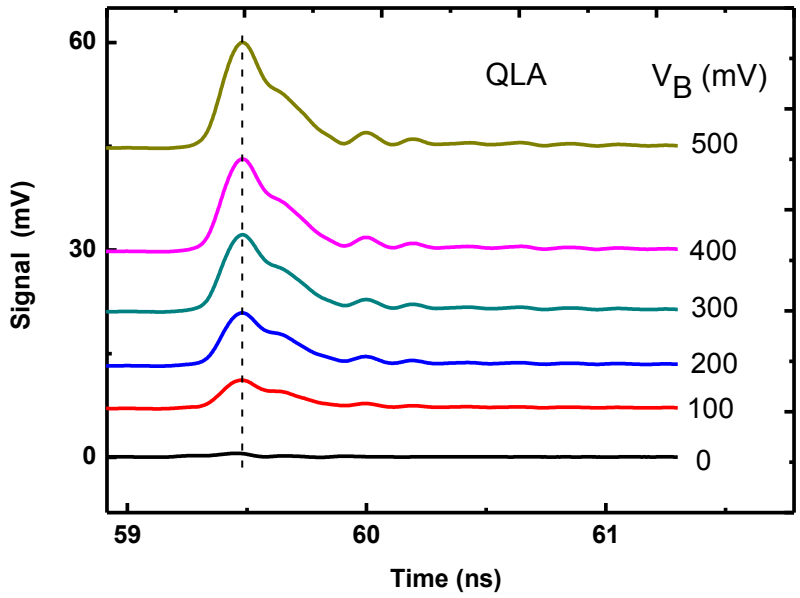



**Figure 5.27:** Electrical response measured from 2DEG structure at pump fluence $W$=4 mJ/cm$^2$ for various positive bias voltages $V_B$ for QLA phonons.

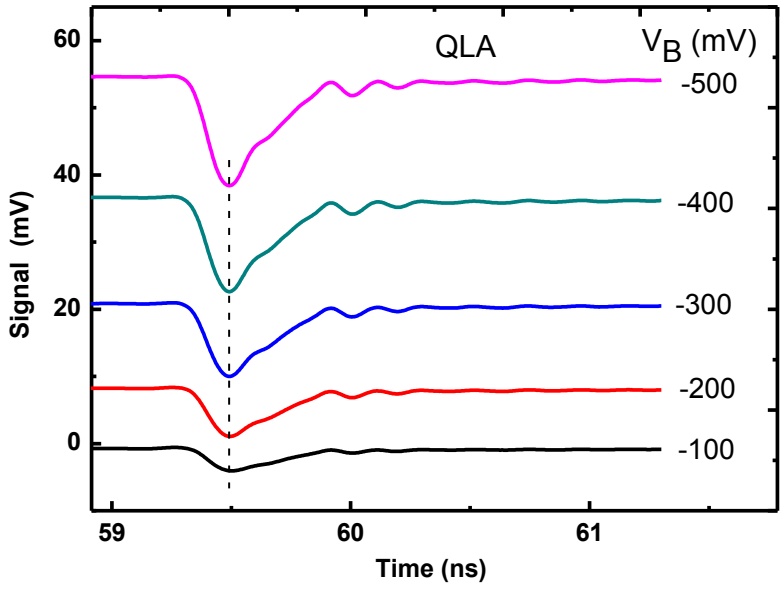



**Figure 5.28:** Electrical response measured from 2DEG structure at pump fluence $W$=4 mJ/cm$^2$ for various negative bias voltages $V_B$ for QLA phonons.

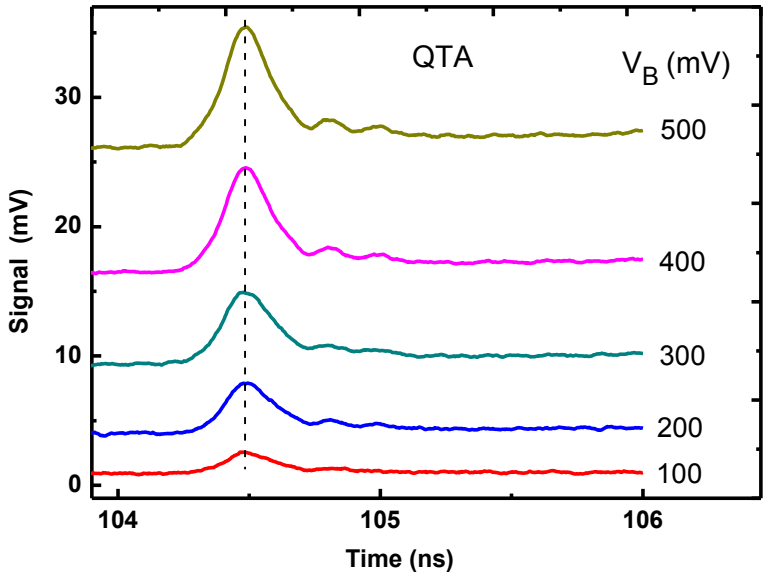



**Figure 5.29:** Electrical response measured from 2DEG structure at pump fluence $W$=4 mJ/cm$^2$ for various positive bias voltages $V_B$ for QTA phonons.

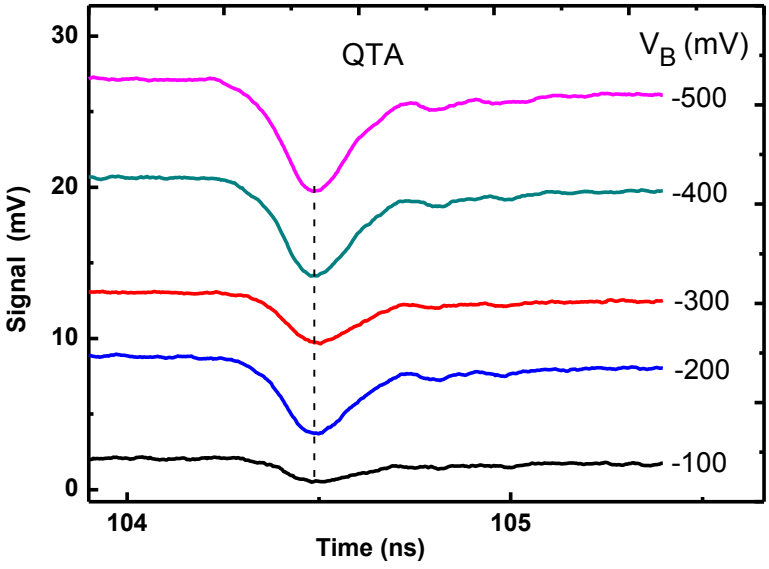



**Figure 5.30:** Electrical response measured from 2DEG structure at pump fluence $W$=4 mJ/cm$^2$ for various negative bias voltages $V_B$ for QTA phonons.

When a strain pulse propagates across the substrate at the speed of sound in 2DEG, it causes change in conductivity of the channel. The presence of a phonon constitutes a periodic modulation of the lattice constant for which there is a corresponding shift in the conduction and valence band energies. Such shifts give rise to an effective potential experienced by the electron which can induce electronic transitions. At low temperatures the deformation potential interaction is the dominant coupling mechanism between electrons and acoustic phonons. The polarity of the signal for both QLA and QTA is identical with applied bias as QLA modes are coupled with deformational potential whereas the QTA modes are coupled with piezoelectric potential. However, the QLA and QTA signal reverses when the bias polarity is revered (see figures 5.27 to 5.30). The peak position of the QLA and QTA signals remains the same with increasing positive/negative bias which is marked by vertical dotted lines (see figures 5.27 to 5.30). For $V_B$ = 0 mV, the electrical response $\delta V(t)$ for both QLA and QTA is negligible. From these results, it is evident that the incident strain pulse causes an increase in resistance of the 2DEG channel. This might be due to the deformation potential associated with strain modulating the electronic band structure, causing depletion of the charges in the channel through increased tunnelling of charges out of the channel (see figure 5.31(b)). Alternatively, the strain pulse could cause a decrease of mobility of the electrons in the channel through heating or electron-phonon scattering.

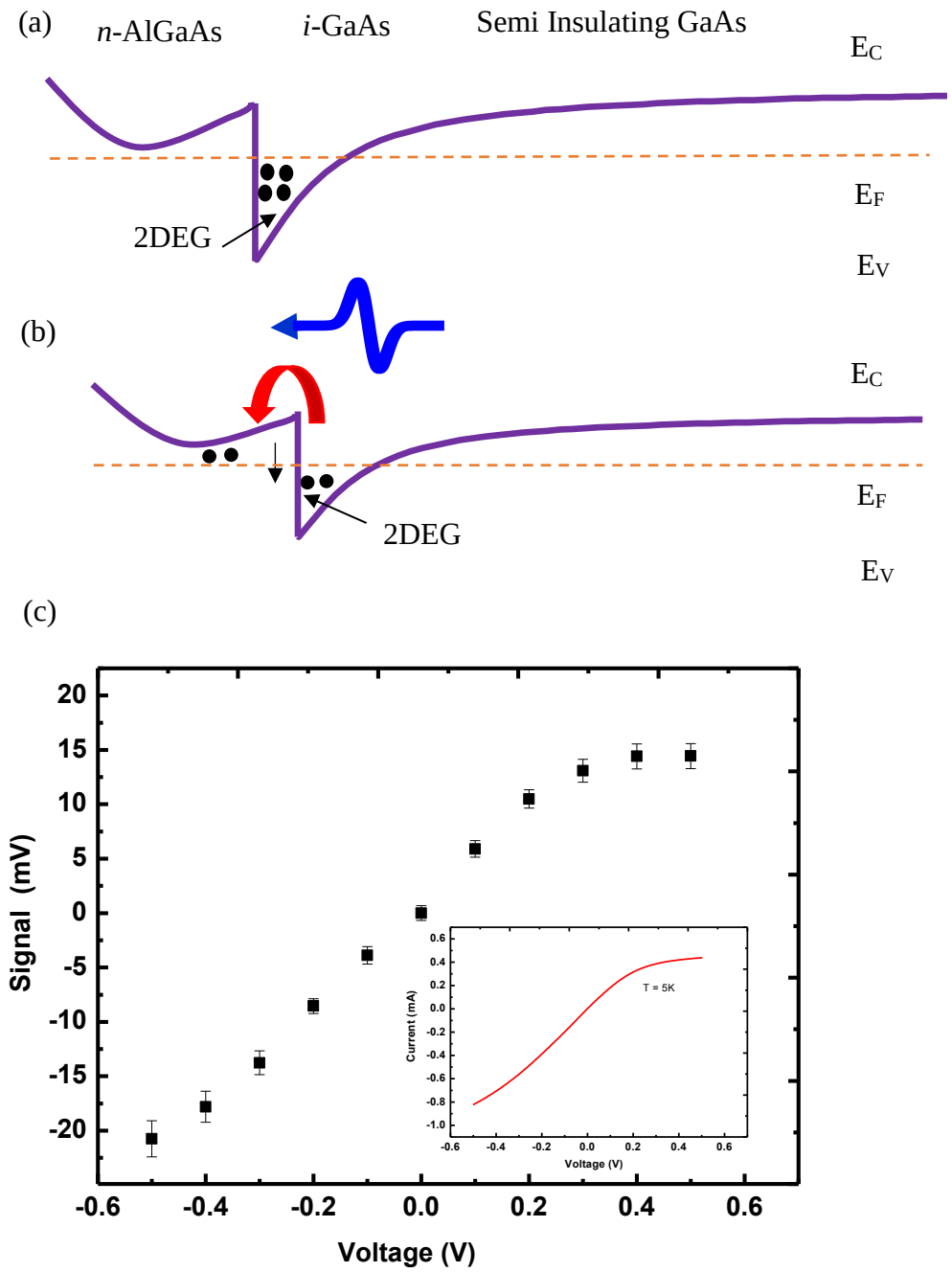



**Figure 5.31:** Schematic to demonstrate the origin of 2DEG signals. (a) represents no strain, (b) with strain, the red colour curve indicates the tunnelling of charges out of the channel while the black arrow represents the decrease in carrier density. (c) Dependence of electrical response measured from 2DEG structure at pump fluence $W$=1.6 mJ/cm$^2$ for QLA phonons on bias. The inset shows current voltage characteristics of the two-dimensional electron gas structure at temperature T=5K for comparison.

The electrical response measured from 2DEG structure at pump fluence $W$=1.6 mJ/cm$^2$ for QLA phonons as a function of applied bias voltage is shown in figure 5.31(c). The important observation is that the shape of the electrical response as function of bias is identical to the IV characteristics of the device (see inset of figure 5.31(c)). This observation confirms that the origin of 2DEG signals is due to the decrease in carrier density. Ideally if we assume that the origin of signals is due to the changes in the mobility, the amplitude of the signal is expected to decrease strongly however it is not observed in this work.

### 5.5.4 Laser Power Dependence on QLA and QTA signals

The dependence of the electrical response $\delta V(t)$ on various optical excitation densities $W$ at the Al film was measured. The amplitude of the generated strain pulse within the Al transducer film is proportional to pump fluence (see section 2.1.1). Thus, signal amplitude should increase with the increase of pump fluence $W$. Such behavior was observed in experiments, and the results for $V_B$=400 mV is shown in figure 5.32 and figure 5.33 for QLA and QTA, respectively. In figure 5.32, it is clearly seen that the first peak for QLA phonons moves to earlier times with the increase of $W$ (also see figure 5.34). This temporal shift has been observed in earlier works performed with picosecond acoustic optical techniques and corresponds to nonlinear acoustic properties of GaAs substrate [71, 77]. In contrast to QLA, the arrival time for QTA phonons does not depend on $W$ (see dotted line, inset in figure 5.33), which means that elastic nonlinear effects for QTA phonons are not so important [108].

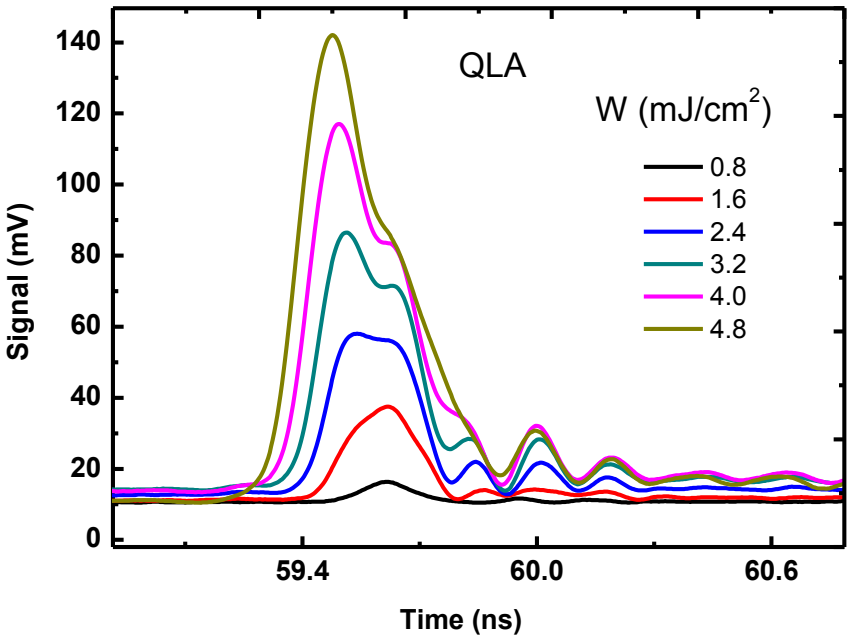



**Figure 5.32:** Electrical response measured from 2DEG structure at bias, $V_B$=400 mV with different pump fluences for QLA phonons.

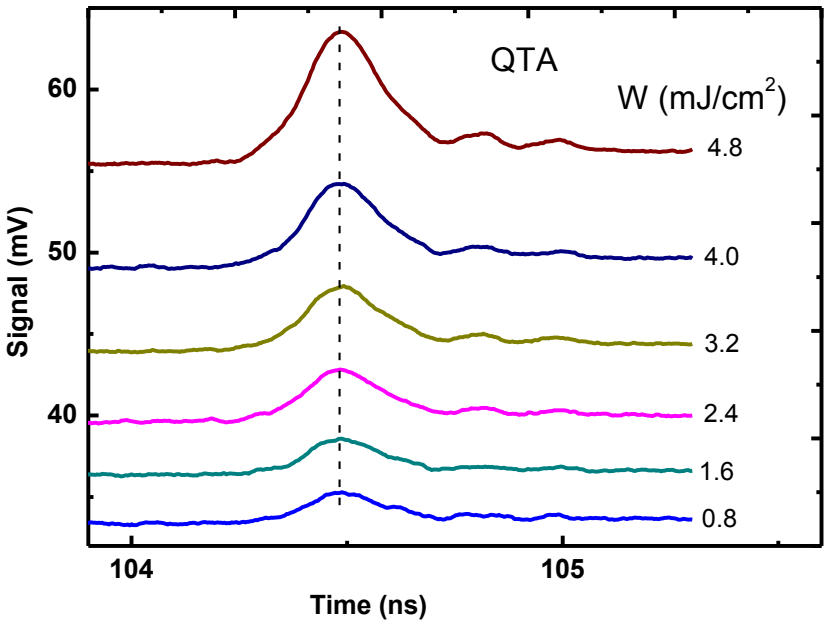



**Figure 5.33:** Electrical response measured from 2DEG structure at bias, $V_B$=400 mV with different pump fluences for QTA phonons.

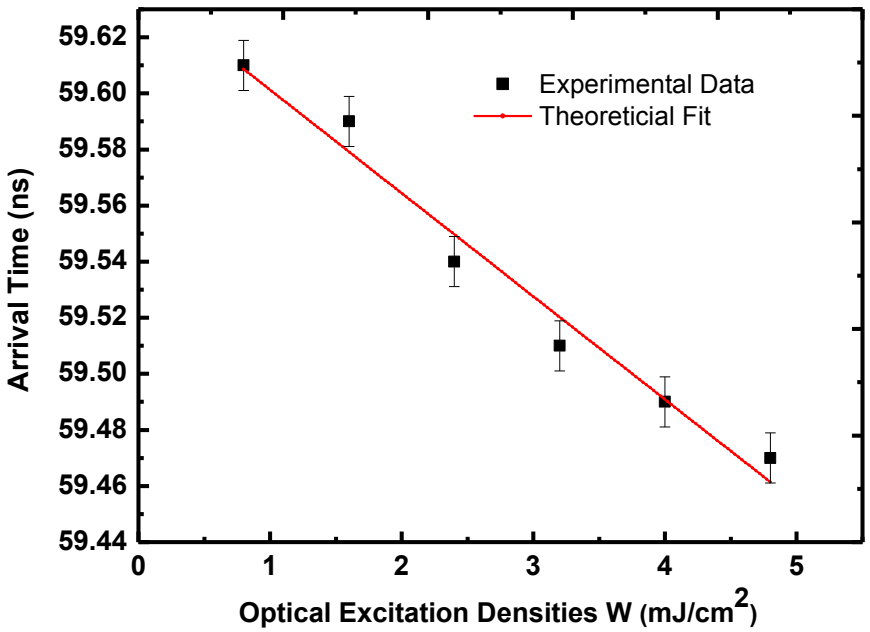



**Figure 5.34:** First peak position dependence on optical excitation densities *W* for QLA phonons. The squares are the peak position obtained from experimental signals and the red line is a theoretical fit to the experimental data.

In figure 5.34, the red line shows the theoretical fit to the data of the form $y = (d/(c + (a \times x))) + b$ (see equations 4.17 and 4.18), where $a$ = 0.003424 ± 0.0004 and $b$ = 0.164 ± 0.001. Form these constants, the third order elastic constant $C_3$ = -9.67x$10^{11}$ N/m$^2$ was extracted for the GaAs along [311] direction which is close to the Schottky diode measurements. This indicates that the third order elastic constant extracted from the theoretical fit could be the actual value.

### 5.5.5 Preliminary work on 2DHG structure detecting acoustic signals

Similar fast-electrical detection of QLA and QTA phonons like the 2DEG experiments described in section 5.5.2 were also performed using two-dimensional hole gas structure on a setup shown in figure 3.15 and all measurements were at T = 5K unless otherwise specified. The GaAs substrate of thickness $d$ = 350μm and a

30nm aluminium film is evaporated on the opposite side of the substrate. An example of the temporal trace $\delta V(t)$ measured that includes both QLA and QTA coherent phonons in a full temporal range is shown in figure 5.35. The trace includes three sharp spikes. Firstly, the spike at time $t$=0 corresponds to the response from optical pump breakthrough. The other spikes marked by horizontal arrows are due to coherent phonon wave packets. The second spikes at $t$≈64 ns (figure 5.35) and at $t$≈112 ns (figure 5.35) are the QLA and QTA phonons respectively propagating directly from Al film to 2DHG, which is the main point of interest in all further analysis. The signal amplitude for both QLA and QTA signals is same at maximum pump power. The different arrival times for 2DEG ($t$≈59 for QLA, $t$≈104 for QTA) and 2DHG ($t$≈64 for QLA, $t$≈112 for QTA) structures is because of the different substrate thickness ($d$ = 328μm for 2DEG structure, $d$ = 350μm for 2DHG structure).

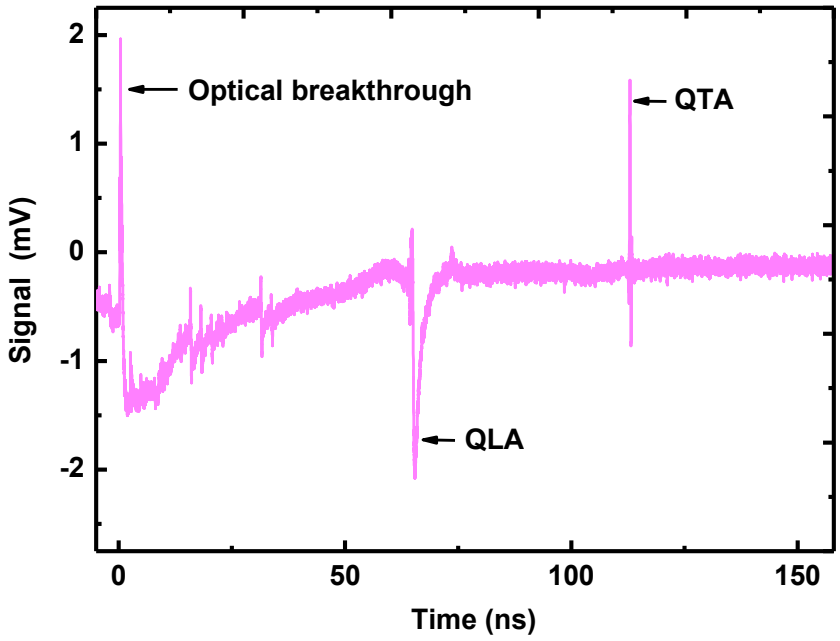



**Figure 5.35:** Electrical response measured from 2DHG structure in a full temporal range, consists of both QLA and QTA phonons with a bias of $V_B$ = 100 mV at pump fluence $W$=4.8 mJ/cm$^2$.

The direct QLA and QTA modes were zoomed for clarity and measured for various positive bias voltages $V_B$ is shown in figure 5.36 and figure 5.37, respectively. The interesting observation from these bias measurements was that the polarity of the signal changes, for QLA predominantly the peak is negative while QTA it is positive in contrast to the 2DEG experiments. From figure 5.36 and figure 5.37, it is clearly observed that the temporal shape of the signal is almost independent of applied positive bias. The arrival time for both QLA and QTA phonons is also independent to the applied bias.

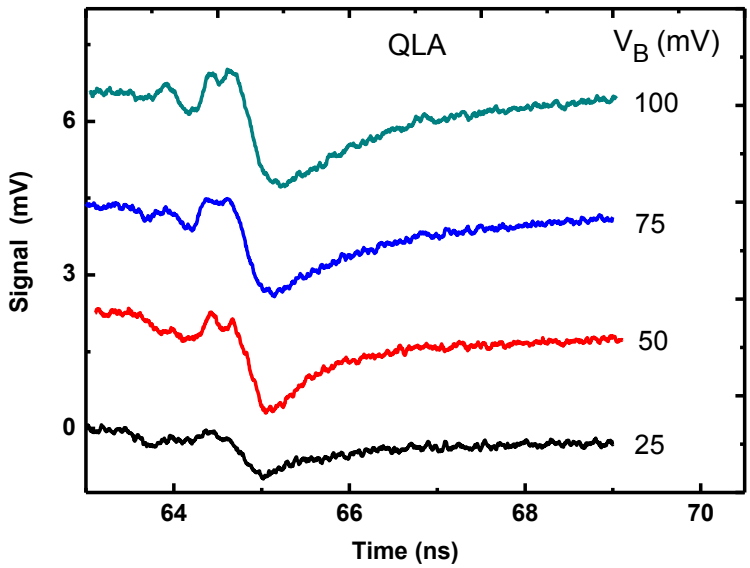



**Figure 5.36:** Electrical response measured from 2DHG structure at pump fluence $W$=4.8 mJ/cm$^2$ for various positive bias voltages $V_B$ for QLA phonons.

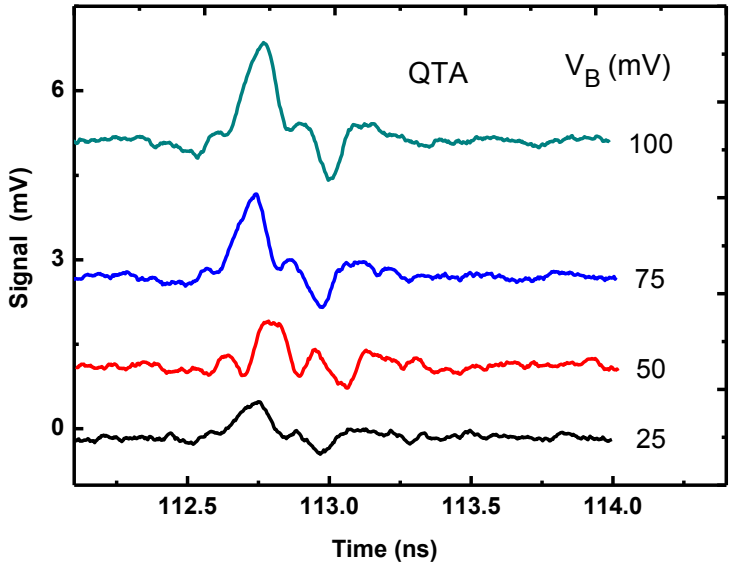



**Figure 5.37:** Electrical response measured from 2DHG structure at pump fluence $W$=4.8 mJ/cm$^2$ for various positive bias voltages $V_B$ for QTA phonons.

In section 5.5.3, for the 2DEG it is evident from results that the increase in resistance of the 2DEG channel is the main cause of the signal, alternatively the incident strain pulse might cause a decrease in resistance. From figure 5.35, it is clearly seen that the strain pulse causes a decrease in resistance of the 2DHG channel. This might be due to the deformation potential associated with the strain modulating the electronic band structure, causing an increase in the carrier density as holes tunnel through the channel (see figure 5.38), which is the origin of 2DHG signals hence the polarity of the signals is reversed. The other reason for the change in polarity for QLA (negative) and QTA (positive) is due to phonons couple to carriers in GaAs via deformational potential and via piezoelectric interaction. In conduction band of GaAs there is a single deformation potential constant which couple electrons to longitudinal acoustic phonons only. In the valence band, however, there are three independent constants [117], which can couple holes to all phonon modes. Wiley *et. al.* [118] showed that it is sufficient to use a single effective valence band deformational potential ($\Xi_d$) to account for the transport properties in p-type GaAs. As the deformational potential constant in valence band

for holes was found to be $\Xi_v$ = 4.9 eV [117], the QLA mode is negative in comparison with electrons and QTA mode is positive.

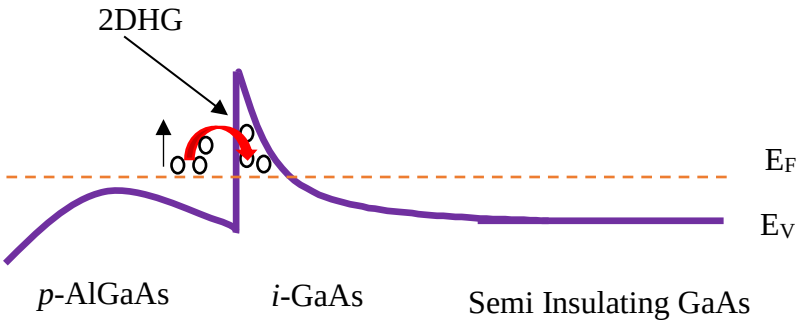



**Figure 5.38:** Schematic to demonstrate the origin of 2DHG signals. The red colour curve indicates the tunnelling of holes while the black arrow represents the increase in carrier density.

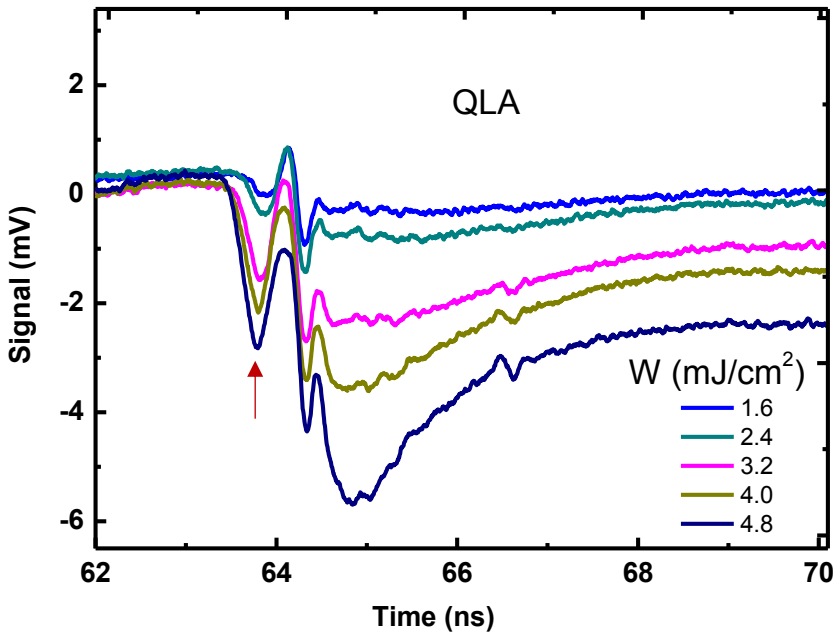



**Figure 5.39:** Electrical response measured from 2DHG structure at bias, $V_B$=100 mV with different pump fluences for QLA phonons.

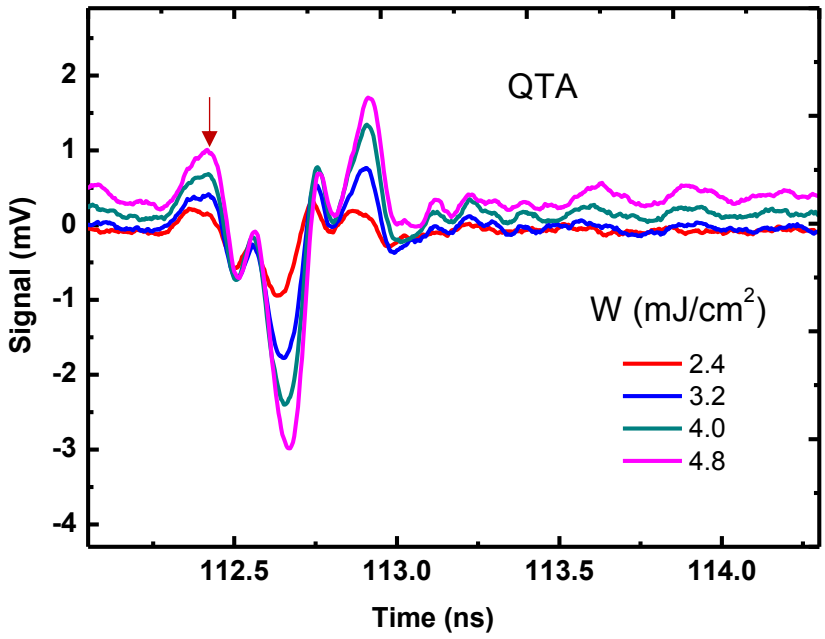



**Figure 5.40:** Electrical response measured from 2DHG structure at bias, $V_B$=100 mV with different pump fluences for QTA phonons.

The dependence of the electrical response $\delta V(t)$ on various optical excitation densities $W$ at the Al film was measured for both QLA and QTA is shown in figure 5.39 and figure 5.40, respectively. The amplitude of the signal increases with increasing pump power as described on section 4.4.3. The first peak position marked by vertical red arrow for QLA (negative) and QTA (positive) phonons remains same with increasing pump power. This observation is in contrast with the 2DEG experiments where for QLA phonons the first peak moves earlier times due to the nonlinear acoustic properties of GaAs substrate [158, 159].

## 5.6 Conclusions

In this chapter, low dimensional structures *i.e.* Quantum well embedded *p-i-n* photodiode detector (QW-*p-i-n*), two-dimensional electron gas (2DEG) and two-dimensional hole gas (2DHG) were fabricated on (311) GaAs surface. These structures were investigated as detectors for longitudinal and transverse acoustic signals. The first experimental evidence of high frequency tail in transverse signal is observed using GaAs based QW-*p-i-n* detector.

Initially, a GaAs based QW embedded *p-i-n* photodiode detector was used to detect longitudinal and transverse acoustic signals. The longitudinal signal confirms the existence of the GHz oscillations, with the most significant occurring 170 GHz, while in transverse acoustic signal we observed high frequency tail which is from 300 ps to 800 ps. Fast Fourier transforms (FFT) analysis of this tail shows the existence of high frequency phonons at 200 GHz. Photocurrent pump-probe measurements was also performed with three different Al film thicknesses (20nm, 30nm and 100nm). Experiments performed with 20nm film thickness clearly shows a weak signal at 250 GHz in the amplitude spectrum which is not observed for 30 nm and 100 nm aluminium films. This observation indicates that the thinner aluminium films can generate high frequency phonons. Longitudinal acoustic signal detected was measured at two different applied bias voltages to observe the dependence of signal on bias. The temporal shape of the signal is exactly same for two different applied biases. This indicates the shape and signal amplitude of the signal is independent of applied bias, which is consistence with previous work performed by D. M. Moss et al [21].

The detected longitudinal acoustic signal was also measured at various pump densities to observe the dependence of the signal. These measurements show that with increasing excitation pump densities *W*, the temporal profile of the signal is independent of *W*. The arrival time of the incident and the reflected strain pulses is also independent of *W*. This observation shows that there are no nonlinearities in the mechanism of detection of strain pulses for the pump density *W* values used in our experiments. The signal amplitude ΔP of the ultrafast photocurrent changes for various pump densities *W* at bias $V_B$= 1V was analysed which clearly shows that with increasing pump density *W*, the changes of photocurrent amplitude ΔP increases, which is consistence with previous work performed by D. M. Moss et al [22]. Inaddition, photocurrent pump-probe measurements performed on InGaAs quantum well incorporated *p-i-n* photodiode detector. Longitudinal and transverse acoustic signals was observed successfully. The data taken was not of a sufficient quality to determine the temporal shape of the signals and its dependence on applied bias, power and temperature.

In later sections of this chapter, fast electrical measurements were performed on a two-dimensional electron gas (2DEG) and a two-dimensional hole gas (2DHG) structures fabricated on (311) GaAs substrates. The optical excitation generates compressive strain pulse in the Al film which is at the opposite side of the GaAs substrate. Because of this strain pulse injection two coherent acoustic phonon modes were generated in the (311) GaAs substrate: quasi-longitudinal phonons (QLA) and quasi-transverse phonons (QTA). These two modes were detected successfully, later the dependence of QLA and QTA signals on different applied bias, pump powers were measured. The dependence of signals on applied positive and negative bias reveals that the temporal position of the signals for QLA and QTA remains same with increasing bias.

The QLA and QTA signals dependence on different pump fluences was investigated. This suggested that the first peak arrival time for QLA phonons in the measured signal moves to earlier times with increasing pump power. This was caused by the nonlinear acoustic properties of the GaAs substrate. Conversely, QTA phonons arrival time was not dependent on pump power which indicates the elastic nonlinear effects are not crucial role for QTA signals. The longitudinal and transverse signals detected by 2DHG, for QLA predominantly the peak is negative while for QTA it is positive in contrast to the 2DEG experiments due to the reason that in 2DEG experiments the origin of the signal is due to the decrease in carrier density but for 2DHG the signal is due to the increase in carrier density.

# Chapter 6

# Conclusions and Future Work

This concluding chapter will summarise this thesis by providing an overview of the experiments performed on semiconductor devices, and by revisiting the main conclusions from the previous chapters. Possibilities for future research arising from these conclusions will then be discussed.

## 6.1 Conclusions

In the initial chapters of this thesis, general description of picosecond acoustics with an overview of some previous work on semiconductor devices were discussed alongside with various electron-phonon coupling mechanisms. This was followed by detailed explanation of theoretical background knowledge. This background covers the stain pulses generation, propagation and detection together with the description of strain sensitive devices used in this work.

The microfabrication techniques that were essential for the processing of viable devices for the thesis alongside with various sample structures were explained in Chapter 3. In later sections of this chapter, the different laser systems and cryostats employed to perform experiments in this thesis were explained very briefly. In addition, the circuitry and electrical-optical experimental configurations utilised to conduct transport, photocurrent pump-probe, and fast electrical measurements was described.

The work detailed in chapter 4 has shown that Schottky diodes are successful in developing high speed acoustoelectric detectors for subterahertz compressional and shear acoustic waves. The quasi-longitudinal phonon (QLA) and quasi-

transverse phonon (QTA) modes were detected by a Schottky Diode successfully. The dependence of the QLA and QTA signals on different applied bias, pump powers and temperatures were measured. The important observation from the detected signals is that the first peak is negative for QLA and positive for QTA phonons. The dependence of signals on bias reveals that the temporal position of the signals for QLA and QTA moves slightly earlier times with increasing reverse bias because the width of the depletion layer increases with increasing negative bias. In our work, this shift observed for QLA is 25 ps and for QTA it is 20 ps.

The QLA and QTA signals dependence on different pump laser fluences was investigated. The first peak arrival time for QLA phonons in the measured signal moves to earlier times with increasing pump power. This was caused by the nonlinear acoustic properties of the GaAs substrate. The temporal shift observed in our measurements is ~100 ps which is like the experiments when LA phonons propagate in high-symmetry [100] direction in GaAs. Conversely, the QTA phonon arrival time was not dependent on pump power which indicates the elastic nonlinear effects do not play a crucial role for QTA signals. The QLA and QTA signals were measured at different temperatures up to 298K to investigate the temperature dependence on signals. This temperature dependence investigation reveals that the arrival time changes to later times with increasing temperature because of the decreasing sound velocity with increasing temperature. This shift observed was approximately 1% which agrees with earlier measurements [79].

Schottky diode fabricated on a low-symmetry surface of a semiconductor was shown experimentally to serve as an efficient transducer for longitudinal and transverse coherent phonons with frequencies of about 10 GHz. A theoretical analysis was made to understand the polarity of the experimental signals together with coupling mechanisms of the electrical response of the Schottky contact to the incident coherent phonons. The two-important electron-phonon coupling mechanisms considered in this thesis are deformation potential coupling and piezoelectric potential coupling. Experimental results were compared to the simulated signals of electron-phonon coupling interactions concludes the predominant role of piezoelectric phonon-electric transformation mechanism over

deformational potential. The theoretical calculations show that the piezoelectric mechanism dominates over deformation potential up to frequencies of 70 and 250 GHz for longitudinal and transverse phonons, respectively. Further fast electrical measurements were also performed experiments on Schottky Diodes fabricated on (311A) GaAs surface to confirm the earlier conclusion. The QLA and QTA signals measured on (311A) GaAs surface shows that the polarity of the becomes positive for QLA and negative for QTA which is reverse of what was seen using devices on (311B) GaAs surface. This behaviour agrees with the theoretical predictions of the piezoelectric mechanism. These further experiments on (311A) GaAs surface strongly concludes the dominant role of piezoelectric mechanism over deformational potential.

Low dimensional structures *i.e.* Quantum well embedded *p-i-n* photodiode detector (Q-*p-i-n*), two-dimensional electron gas (2DEG) and two-dimensional hole gas (2DHG), fabricated on (311) GaAs surface, were investigated as detectors for longitudinal and transverse acoustic signals in chapter 5. The first experimental evidence of high a frequency tail in transverse signal is observed using GaAs based Q-*p-i-n* detector. Initially, a GaAs based QW embedded *p-i-n* photodiode detector was used to detect longitudinal and transverse acoustic signals. The longitudinal signal confirms the existence of the GHz oscillations, with the most significant occurring 170 GHz, while in the transverse acoustic signal we observed high frequency tail lasting from 300 ps to 800 ps. Fast Fourier transforms (FFT) analysis of this tail shows the existence of high frequency phonons at 200 GHz. Photocurrent pump-probe measurements was also performed with three different Al film thicknesses (20nm, 30nm and 100nm). Experiments performed with 20nm film thickness clearly shows a weak signal at 250 GHz in the amplitude spectrum which is not observed for 30 nm and 100 nm aluminium films. This observation indicates that the thinner aluminium films can generate high frequency phonons. The detected longitudinal and acoustic signals were also measured at various bias and pump densities to observe the dependence of the signal. Inaddition, photocurrent pump-probe measurements performed on InGaAs quantum well incorporated *p-i-n* photodiode detector. Longitudinal and transverse acoustic signals was observed

successfully. The data taken was not of a sufficient quality to determine the temporal shape of the signals and its dependence on applied bias, power and temperature.

Fast electrical measurements were performed on a two-dimensional electron gas (2DEG) and a two-dimensional hole gas (2DHG) structures fabricated on (311) GaAs substrates. The optical excitation generates compressive strain pulse in the Al film which is at the opposite side of the GaAs substrate. The QLA and QTA phonons generated by this strain pulse were detected successfully, later the dependence of QLA and QTA signals on different applied bias, pump powers were measured. In 2DEG structure, the acoustic modes are due to decrease in carrier density whereas for 2DHG structure, it is due to the increase in carrier density.

## 6.2 Future Research

The findings in the present work gives rise to many potential future research projects related to strain generation and detecting high frequency acoustic phonons. These include investigation of smaller size, hence lower capacitance, Schottky devices to detect higher frequency acoustic phonons experimentally, and optimising the RC 80 sample structure to detect shear acoustic modes. Both these potential projects are discussed briefly in sections 6.2.1 and 6.2.2, respectively. Preliminary fast electrical measurements on a processed 2DEG structure where mobility is on different orientation have been conducted, results and further improvements in this research is provided in section 6.2.3.

### 6.2.1 Investigation of smaller size Schottky Devices to detect high frequency acoustic phonons experimentally

The experiments detailed in chapter 4 showed that Schottky diode fabricated on a low-symmetry surface of a semiconductor serves as an efficient transducer for longitudinal and transverse coherent phonons with frequencies of about 10 GHz. Due to the technical limitations of the experiments, Schottky diodes used in this thesis were not able to detect signals at much higher frequencies. However, by using specially designed microwave holders and Schottky contacts of a few microns in size, with capacitance of order 10 fF, it is possible to detect mm wave signals with

frequencies over 100 GHz [113]. The potential future work is to fabricate smaller Schottky devices to detect high frequency acoustic signals experimentally with the aim of developing coherent phonon-electric transducers in subterahertz frequency range. The schematic shown in figure 6.1 will be used for the future work to fabricate few micron size air-bridge Schottky devices.

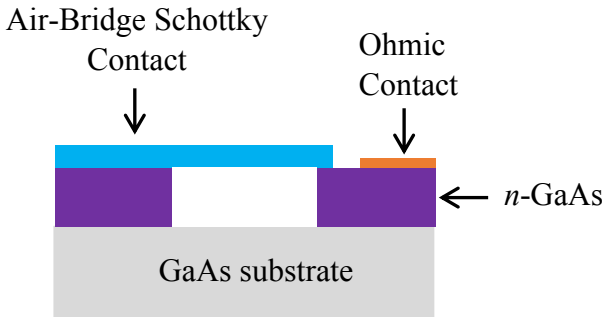



**Figure 6.1:** Schematic of NU927 sample structure modified to fabricate air-bridge Schottky devices.

### 6.2.2 Investigation of shear acoustic modes using *p-i-n* device embedded with InGaAs QW

In chapter 5, a *p-i-n* device embedded with InGaAs QW was fabricated to detect longitudinal acoustic and transverse acoustic waves. The longitudinal acoustic signal was detected after successfully generation in an 30nm aluminium film transducer and propagation through the 448μm (311) substrate but unable to detect transverse modes, which might be due to inadequate quality of the InGaAs quantum well. In future work, the idea is to optimise the RC 80 sample structure by defining excellent quality narrow quantum well to detect high frequency shear modes and to investigate the signal with different aluminium films, power, temperature and bias dependance. A 200nm thin p-type and n-type GaAs layers will be replaced instead of 500nm thick layers to achieve uniform etching.

### 6.2.3 Fast electrical measurements on 2DEG structure processed in different orientation

GaAs (311) A samples exhibit in-plane mobility anisotropy, the anisotropy is caused by irregular corrugations [47,119] during MBE growth. These corrugations run parallel to the $[\bar{2}33]$ direction, causing the mobility along the $[01\bar{1}]$ direction to be significantly smaller than the mobility along $[\bar{2}33]$ direction. A.C. Churchill *et.al.* [120] investigated electron gases grown on (311) B GaAs substrates and observed marked anisotropy in the transport properties, similarly to the hole gases grown on (311) A GaAs surface [121]. The mobility in the $[\bar{2}33]$ direction is 50% higher than in the $[\bar{0}11]$ direction [122,123]. The two-dimensional hole systems at (311) A heterojunctions attribute an anisotropy in the mobility [124, 125], the mobility along $[\bar{2}33]$ direction is 4 times higher in comparison to $[01\bar{1}]$. This anisotropy is due to the anisotropy of the valence band which results in different effective masses in the $[\bar{2}33]$ and $[01\bar{1}]$ directions [124]. Hence, it is interesting to investigate the 2DEG and 2DHG structures fabricated in different orientations.

Preliminary strain pulse based fast-electrical measurements were also performed on a 2DEG structure fabricated in different orientation as shown in figure 6.2 (b) to investigate LA and TA acoustic modes, as it is expected that the mobility of electrons or holes is distinct in different orientation on (311) substrates. The experimental setup is shown in figure 3.16 where the normal lens was replaced with cylindrical lens and all measurements were at T = 5K unless otherwise specified. These measurements are similar to those described in 5.5.2. An example of the temporal trace $\delta V(t)$ measured that includes both QLA and QTA coherent phonons in a full temporal range is shown in figure 6. 4. The trace includes more sharp spikes. Firstly, the spike at time $t$=0 corresponds to the response from optical pump breakthrough. The other spikes marked by vertical arrows are due to coherent phonon wave packets. The second spikes at $t$≈48 ns (figure 6. 4) and at $t$≈99 ns (figure 6. 3) are the QLA and QTA phonons respectively propagating directly from Al film to 2DEG. The third spike at $t$ ≈144 ns (3QLA), is the QLA reflection after three times.

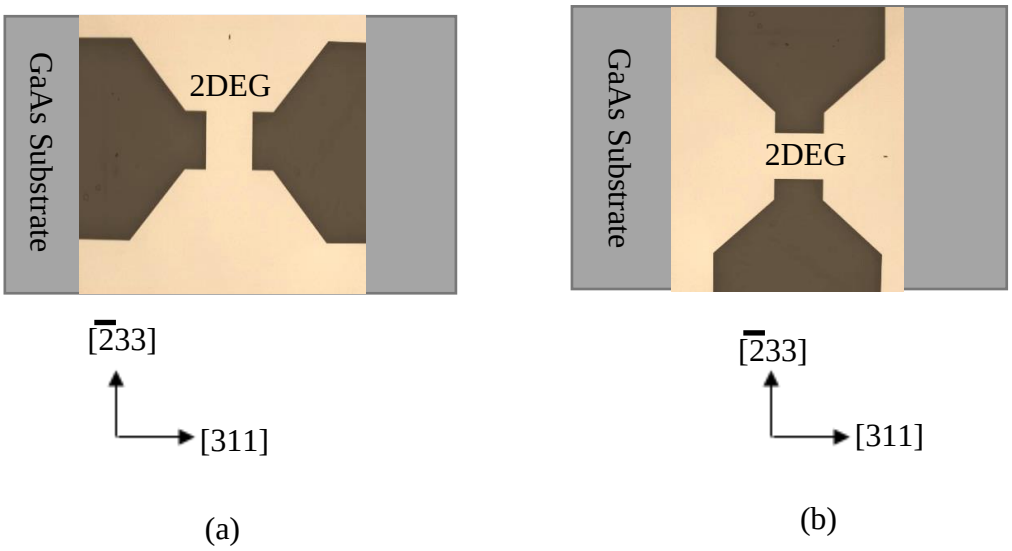



**Figure 6.2:** (a) Schematic of 2DEG sample investigated in chapter 5. (b) Schematic of 2DEG sample fabricated in different orientation.

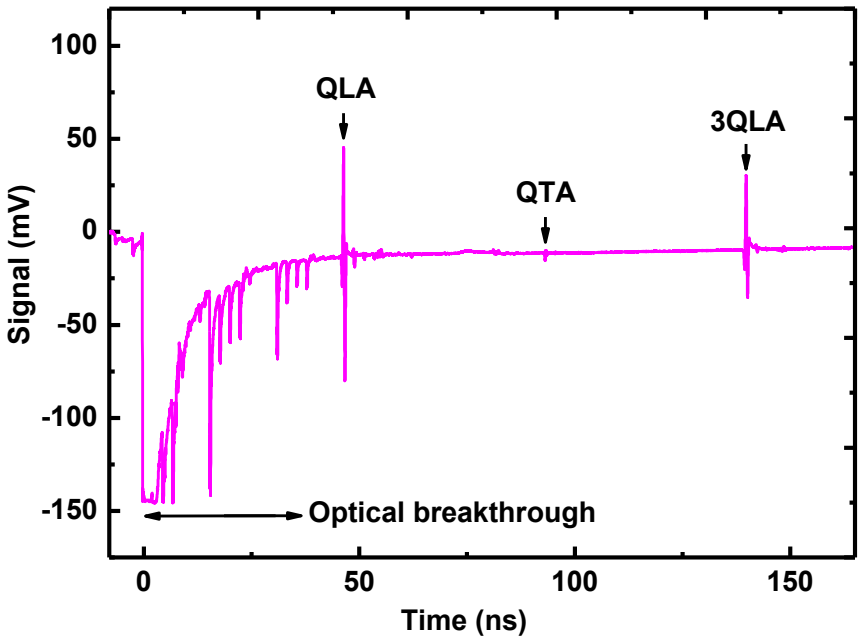



**Figure 6.3:** Electrical response measured from 2DEG structure fabricated in different orientation, consists of both QLA and QTA phonons with a bias of $V_B$ = 500 mV at pump fluence $W$=4.8 mJ/cm$^2$.

The electrical signals (zoomed) for direct QLA and QTA phonons polarity is not clear due to the huge signal behind the contacts, other reason for this might be the inadequate quality of the Al film. In future work, the idea is to decrease the contact size and evaporating superior quality Al film, we might detect superior quality signals and further investigation with different applied bias and powers will be performed. In addition, the 2DHG structures will also be processed in different orientation to detect both QLA and QTA acoustic modes.

# Bibliography

[1] C. Thomsen, H.T. Grahn, H.J. Maris, J. Tauc. Surface generation and detection of phonons by picosecond light pulses. Physical Review B, 34, 4129, 1986.

[2] H. -N. Lin, H.J. Maris, L.B. Freund, K.Y. Lee, H. Luhn, D.P. Kern. Study of vibrational modes of gold nanostructures by picosecond ultrasonics. Journal of Applied Physics, 73, 37, 1993.

[3] H.T. Grahn, H.J. Maris, J. Tauc, B. Abeles. Time-resolved study of vibrations of a-Ge:H/a-Si:H multilayers. Physical Review B, 38, 6066, 1988.

[4] K.C. Bretz, Y.-C. Lee, T.D. Kraus, F.W. Wise, W.H. Sachse. Picosecond acoustics for the characterization of sub-micron polymeric films. Ultrasonics, 34, 513,1996.

[5] B. Bonello, B. Perrin, E. Romatet, J.C. Jeannet. Application of the picosecond ultrasonic technique to the study of elastic and time-resolved thermal properties of materials. Ultrasonics, 35, 223, 1997.

[6] B. Bonello, B. Perrin, C. Rossignol. Photothermal properties of bulk and layered materials by the picosecond acoustics technique. Journal of Applied Physics, 83, 3081,1998.

[7] O.B. Wright, T. Hyoguchi. Ultrafast vibration and laser acoustics in thin transparent films. Optics Letters, 16, 1529, 1991.

[8] O.B. Wright, K. Kawashima. Coherent Phonon Detection from Ultrafast Surface Vibrations. Physical Review Letters, 69, 1668, 1992.

[9] O.B. Wright. Ultrafast nonequilibrium stress generation in gold and silver. Physical Review B, 49, 9985, 1994.

[10] B. Perrin, B. Bonello, J.C. Jeannet, E. Romatet. Interferometric Detection of Hypersound Waves in Modulated Structures. Prog. Natural Sci. (China), S6, 444, 1996.

[11] C. Thomsen, J. Strait, Z. Vardeny, H. J. Maris, J. Tauc, and J. J. Hauser. Phonon Generation and Detection by Picosecond Light Pulses. Physical Review Letters, 53, 989, 1984.

[12] G. L. Eesley, B. M. Clemens, and C. A. Paddock. Generation and detection of picosecond acoustic pulses in thin metal films. Applied Physics Letters, 50,717, 1987.

[13] G. Tas and H. J. Maris. Electron diffusion in metals studied by picosecond ultrasonics. Physical Review B, 49, 15046, 1994.

[14] H.-Y. Hao and H. J. Maris. Dispersion of the long-wavelength phonons in Ge, Si, GaAs, quartz, and sapphire. Physical Review B, 63, 224301, 2001.

[15] A. Bartels, T. Dekorsy, H. Kurz, and K. Kohler. Coherent Zone-Folded Longitudinal Acoustic Phonons in Semiconductor Superlattices: Excitation and Detection. Physical Review Letters, 82, 1044, 1999.

[16] C.-K. Sun, J.-C. Liang, and X.-Y. Yu. Coherent Acoustic Phonon Oscillations in Semiconductor Multiple Quantum Wells with Piezoelectric Fields. Physical Review Letters, 84, 179, 2000.

[17] A. Huynh, B. Perrin, N. D. Lanzillotti Kimura, B. Jusserand, A. Fainstein, and A. Lemaitre. Subterahertz monochromatic acoustic wave propagation using semiconductor superlattices as transducers. Physical Review B, 78, 233302, 2008.

[18] A. J. Kent, G. A. Hardy, P. Hawker, V. W. Rampton, M. I. Newton, P. A. Russell, and L. J. Challis. Detection of Heat Pulses by the Two-Dimensional Electron Gas in a Silicon Device. Physical Review Letters, 61, 180, 1988.

[19] F. F. Ouali, N. N. Zinov'ev, L. J. Challis, F. W. Sheard, M. Henini, D. P. Steenson, and K. R. Strickland. Nonequilibrium Acoustic Phonon- Assisted Tunneling in GaAs/(AlGa)As Double Barrier Devices. Physical Review Letters, 75, 308, 1995.

[20] D. R. Fowler, A. V. Akimov, A. G. Balanov, M. T. Greenaway, M. Henini, T. M. Fromhold, and A. J. Kent. Semiconductor charge transport driven by a picosecond strain pulse. Applied Physics Letters, 92, 232104, 2008.

[21] D. Moss, A. V. Akimov, O. Makarovsky, R. P. Campion, C. T. Foxon, L. Eaves, A. J. Kent, and B. A. Glavin. Ultrafast acoustical gating of the photocurrent in a p-i-n tunneling diode incorporating a quantum well. Physical Review B, 80,113306, 2009.

[22] D. Moss, A. V. Akimov, R. P. Campion, M. Henini, C. T. Foxon, L. Eaves, A. J. Kent, and B. A. Glavin. Picosecond strain pulses probed by the photocurrent in semiconductor devices with quantum wells. Physical Review B, 83, 245303, 2011.

[23] D. M. Moss, A. V. Akimov, B. A. Glavin, M. Henini, and A. J. Kent. Ultrafast Strain-Induced Current in a GaAs Schottky Diode. Physical Review Letters, 106, 066602, 2011.

[24] P. Walker, R. P. Campion, A. J. Kent, D. Lehmann, and Cz. Jasiukiewicz. Excitation and detection of high-frequency coherent acoustic phonons in low-symmetry superlattices. Physical Review B, 78, 233307, 2008.

[25] Aishi Yamamoto, Tomobumi Mishina, and Yasuaki Masumoto. Coherent Oscillation of Zone-Folded Phonon Modes in GaAs-AlAs Superlattices. Physical Review Letters, 73, 740, 1994.

[26] Albrecht Bartels, Thomas Dekorsy, and Heinrich Kurz. Coherent Zone-Folded Longitudinal Acoustic Phonons in Semiconductor Superlattices: Excitation and Detection. Physical Review Letters, 82, 1044, 1999.

[27] M. Trigo, T. A. Eckhause, J. K. Wahlstrand, R. Merlin, M. Reason, and R. S. Goldman. Ultrafast optical generation and remote detection of terahertz sound using semiconductor superlattices. Applied Physics Letters, 91, 023115, 2007.

[28] A. Huynh, B. Perrin, N. D. Lanzillotti-Kimura, B. Jusserand, A. Fainstein, and A. Lemaître. Subterahertz monochromatic acoustic wave propagation using semiconductor superlattices as transducers. Physical Review B, 78, 233302, 2008.

[29] O. Matsuda, O. B. Wright, D. H. Hurley, V. E. Gusev, and K. Shimizu. Coherent Shear Phonon Generation and Detection with Ultrashort Optical Pulses. Physical Review Letters, 93, 095501, 2004.

[30] D.H. Hurley, O.B. Wright, O. Matsuda, V.E. Gusev, O.V. Kolosov. Laser picosecond acoustics in isotropic and anisotropic materials. Ultrasonics, 38, 470, 2000.

[31] Z. V. Popović, H. J. Trodahl, M. Cardona, E. Richter, D. Strauch, and K. Ploog. Folded phonons in (GaAs)n1(AlAs)n2 superlattices grown along the [012] direction. Physical Review B, 40, 1202, 1989.

[32] Z. V. Popovic´, J. Spitzer, T. Ruf, M. Cardona, R. Nötzel, and K. Ploog. Folded acoustic phonons in GaAs/AlAs corrugated superlattices grown along the [311] direction. Physical Review B, 48, 1659, 1993.

[33] Z. V. Popović, E. Richter, J. Spitzer, M. Cardona, A. J. Shields, R. Nötzel, and K. Ploog. Phonon properties of (311) GaAs/AlAs superlattices. Physical Review B, 49, 7577, 1994.

[34] Z.V.Popović, E.Richter, J.Spitzer, M.Cardona, R.Nötzel and K.Ploog. Phonon properties of (211) oriented $(GaAs)_M/(AlAs)_N$ superlattices. Superlattices and Microstructures, 14, 173, 1993.

[35] Z. V. Popović, M. Cardona, E. Richter, D. Strauch, L. Tapfer, and K. Ploog. Phonons in GaAs/AlAs superlattices grown along the [111] direction. Physical Review B, 41, 5904, 1990.

[36] R. N. Kini, A. J. Kent, N. M. Stanton, and M. Henini. Generation and detection of terahertz coherent transverse-polarized acoustic phonons by ultrafast optical excitation of superlattices. Applied Physics Letters, 88, 134112, 2006.

[37] H. Welker. On new semiconducting compounds. Zeitschrift für Naturforschung A7, 744, 1952.

[38] S. M. Sze and K. K. Ng. Physics of Semiconductor Devices. Wiley-Interscience Publication. John Wiley & Sons, Inc., 3rd edition, 2006. ISBN 9780470068304.

[39] M.E. Levinshtein and S.L Rumyantsev. Gallium Arsenide (GaAs). In M.E. Levinshtein, S.L. Rumyantsev, and M. Shur, editors, Handbook Series on Semiconductor Parameters, number 1, chapter 4, pages 77-103. World Scientific Publishing Company, Incorporated, 1996. ISBN 9789810229344.

[40] J. S. Blakemore. Semiconducting and other major properties of gallium arsenide. Journal of Applied Physics, 53, R123, 1982.

[41] S. Adachi. GaAs, AlAs, and $Al_xGa_{1-x}As$: Material parameters for use in research and device applications. Journal of Applied Physics, 58, R1, 1985.

[42] S. Adachi. Physical Properties of III-V Semiconductor Compounds: InP, InAs, GaAs, GaP, InGaAs, and InGaAsP. Wiley-Interscience Publication. John Wiley & Sons, Inc., November 1992. ISBN 9780471573296.

[43] M. R. Brozel and G. E. Stillman, editors. Properties of Gallium Arsenide. Number 16 in EMIS Datareviews Series. INSPEC, The Institution of Electrical Engineers, 3rd edition, 1996. ISBN 9780852968857.

[44] K. K. Ng. Complete Guide to Semiconductor Devices. Wiley-Interscience Publication. John Wiley & Sons, Inc., 2nd edition, 2002. ISBN 9780471202400.

[45] E. S. K. Young, A. V. Akimov, R. P. Campion, A. J. Kent, and V. Gusev. Picosecond strain pulses generated by a supersonically expanding electron-hole plasma in GaAs. Physical Review B, 86, 155207, 2012.

[46] R.Notzel, N.N.Ledentsov, L.Daweritz, M.Hohenstein and K.Ploog. Direct synthesis of corrugated superlattices on non-(100)-oriented surfaces. Physical Review Letters, 67, 3812, 1991.

[47] R.Notzel, N.N.Ledentsov, L.Daweritz, K.Ploog and M. Hohenstein. Semiconductor quantum-wire structures directly grown on high-index surfaces. Physical Review B, 45, 3507, 1992.

[48] Z. M. Wang, V. R. Yazdanpanah, C. L. Workman, W. Q. Ma, J. L. Shultz, and G. Salamo. Origin of step formation on the GaAs (311) surface. Physical Review B, 66, 193313, 2002.

[49] Z. M. Wang, V. R. Yazdanpanah, J. L. Shultz, and G. Salamo. GaAs (311) templates for molecular beam epitaxy growth: surface morphologies and reconstruction. Applied Physics Letters, 81, 2965, 2002.

[50] Y. Li *and* M. Niewczas. Strain relaxation in (100) and (311) GaP⁄GaAs thin films. Journal of Applied Physics, 101, 064910, 2007.

[51] W. I. Wang, E. E. Mendez, T. S. Kuan, and L. Esaki. Crystal orientation dependence of silicon doping in molecular beam epitaxial AlGaAs/GaAs heterostructures. Applied Physics Letters, 47, 826, 1985.

[52] W. Q. Li, P. K. Bhattacharya, S. H. Kwok, and R. Merlin. Molecular-beam epitaxial growth and characterization of silicon-doped AlGaAs and GaAs on (311) A GaAs substrate and their device applications. Journal of Applied Physics, 72, 3129, 1992.

[53] R. Notzel, J. Temmyo, and T. Tamamura. Self-organized growth of strained InGaAs quantum disks. Nature (London), 369, 131, 1994.

[54] S. Lan, K. Akahane, H. Z. Song, Y. Okada, and M. Kawabe. Ordering of $In_xGa_{1-x}As$ quantum dots self-organized on GaAs (311) B substrates. Journal of Vacuum Science & Technology B 17, 1105, 1999.

[55] M. Henini, S. Sanguinetti, S. C. Fortina, E. Grilli, M. Guzzi, G. Panzarini, L. C. Andreani, M. D. Upward, P. Moriarty, P. H. Beton, and L. Eaves. Optical anisotropy in arrow-shaped InAs quantum dots. Physical Review B, 57, R6815, 1998.

[56] J. Bardeen and W. Shockley. Deformation potentials and mobilities in non-polar crystals. Physical Review, 80, 72, 1950.

[57] D. J. Robbins. Properties of gallium arsenide. Institution of Engineering and Technology, 1996.

[58] S. I. Pekar. Electron-phonon interaction proportional to the external applied field and sound amplification in semiconductors. Soviet Physics JETP, 22, 431, 1966.

[59] B. A. Glavin, V. A. Kochelap, T. L. Linnik, and K. W. Kim. Electron-phonon interaction via the pekar mechanism in nanostructures. Physical Review B, 71, 081305, 2005.

[60] P. A. Knipp and T. L. Reinecke. Coupling between electrons and acoustic phonons in semiconductor nanostructures. Physical Review B, 52, 5923, 1995.

[61] Cardona, M., Modulation Spectroscopy. Solid State Physics. 1969, New York: Academic Press.

[62] Blakemore, J.S., Gallium Arsenide. 1987: AIP, P. Y. Yu and M. Cardona. Fundamentals of Semiconductors – Physics and material properties. Springer, second edition, 1999.

[63] P. Y. Yu and M. Cardona. Fundamentals of Semiconductors – Physics and material properties. Springer, fourth edition, 2010.

[64] P. A. Knipp and T. L. Reinecke. Coupling between electrons and acoustic phonons in semiconductor nanostructures. Physical Review B, 52, 5923, 1995.

[65] Davies, J.H., The physics of low-dimensional semiconductors: an introduction. 1998, Cambridge, U.K.; New York, NY, USA: Cambridge University Press.

[66] Madelung, O., Semiconductors: Data Handbook. 3rd ed. 2004: Springer.

[67] C. L. Poyser. The Interaction of Coherent Acoustic Phonons with Electrons in Semiconductor Superlattices. PhD Thesis, The University of Nottingham, 2015.

[68] A. V. Scherbakov, M. Bombeck, J. V. Jäger, A. S. Salasyuk, T. L. Linnik, V. E. Gusev, D. R. Yakovlev, A. V. Akimov, and M. Bayer, Picosecond opto-acoustic interferometry and polarimetry in high-index GaAs, Optics Express 21, 16473, 2013.

[69] H. -Y. Hao and H.J. Maris. Experiments with acoustic solitons in crystalline solids. Physical Review B, 64, 064302, 2001.

[70] Akimov, A.V., A.V. Scherbakov, D.R. Yakovlev, C.T. Foxon, and M. Bayer, Ultrafast band-gap shift induced by a strain pulse in semiconductor heterostructures. Physical Review Letters, 97, 037401, 2006.

[71] Péronne, E. and B. Perrin. Generation and detection of acoustic solitons in crystalline slabs by laser ultrasonics. Ultrasonics, 44 (Supplement 1), 1203, 2006.

[72] Sze, S. and K. Ng. Physics of Semiconductor Devices. Wiley-Interscience, 2006.

[73] Sze, S.M. and K.K. Ng, Metal-Semiconductor Contacts. Physics of Semiconductor Devices. John Wiley & Sons, Inc. 134-196, 2006.

[74] Raki, A.D., Algorithm for the determination of intrinsic optical constants of metal films: application to aluminium. Applied Optics, **34**, 4755, 1995.

[75] Daniel Moss. Ultrafast acoustic modulation of transport in semiconductor devices. PhD Thesis, The University of Nottingham, 2012.

[76] Muskens, O.L. and J.I. Dijkhuis, High Amplitude, Ultrashort, Longitudinal Strain Solitons in Sapphire. Physical Review Letters, 89, 285504, 2002.

[77] Scherbakov, A.V., P.J.S. van Capel, A.V. Akimov, J.I. Dijkhuis, D.R. Yakovlev, T. Berstermann, and M. Bayer. Chirping of an Optical Transition by an Ultrafast Acoustic Soliton Train in a Semiconductor Quantum Well. Physical Review Letters, 99, 057402, 2007.

[78] P. J. S. van Capel and J. I. Dijkhuis. Time-resolved interferometric detection of ultrashort strain solitons in sapphire. Physical Review B, 81, 144106, 2010.

[79] W. Chen, H. J. Maris, Z. R. Wasilewski, and S. Tamura. Attenuation and velocity of 56 GHz longitudinal phonons in gallium arsenide from 50 to 300 K. Philosophical Magazine B, 70, 687, 1994.

[80] H. -N. Lin, R. J. Stoner, H. J. Maris, and J. Tauc. Phonon attenuation and velocity measurements in transparent materials by picosecond acoustic interferometry. Journal of Applied Physics, 69, 3816, 1991.

[81] B. Perrin, C. Rossignol, B. Bonello, and J. -C. Jeannet. Interferometric detection in picosecond ultrasonics. Physica B: Condensed Matter, 263, 571, 1999.

[82] S. M. Sze and K. K. Ng. Physics of semiconductor devices. Wiley, 3rd edition, 1981.

[83] B. G. Streetman. Solid state electronic devices. Prentice-Hall, Inc, 4th edition, 1995.

[84] Buber, T., N. Kinayman, Y. Yong-Hoon, and J. Brogle. Low-loss high-isolation 60-80 GHz GaAs SPST PIN switch. in Microwave Symposium Digest, IEEE MTT-S International. 2003.

[85] Yasui, T., A. Nishimura, T. Suzuki, K. Nakayama, and S. Okajima. Detection system operating at up to 7 THz using quasioptics and Schottky barrier diodes. Review of Scientific Instruments, 77, 066102, 2006.

[86] Maestrini, A., B. Thomas, H. Wang, C. Jung, J. Treuttel, Y. Jin, G. Chattopadhyay, I. Mehdi, and G. Beaudin. Schottky diode based terahertz frequency multipliers and mixers. Comptes Rendus Physique, 11, 480, 2010.

[87] B. G. Streetman, S. K. Banerjee. Solid state electronic devices. Pearson Education Limited, 7th edition, 2015.

[88] S. M. Sze. Semicondctor Devices Physics and Technology. John Wiley & Sons, Inc, second edition, 2002.

[89] B. G. Streetman. Solid State Electronic Devices. Prentice Hall, Inc, fourth edition, 1995.

[90] Hall, H.H., J. Bardeen, and G.L. Pearson, The Effects of Pressure and Temperature on the Resistance of p-n Junctions in Germanium. Physical Review, 84, 129, 1951.

[91] J. F. Creemer, F. Fruett, G. C. M. Meijer, and P. J. French. The piezojunction effect in silicon sensors and circuits and its relation to piezoresistance. Sensors Journal, IEEE, 1, 98, 108, 2001.

[92] Fruett, F., Meijer, and Gerard C.M. The Piezojunction Effect in Silicon Integrated Circuits and Sensors. The Springer International Series in Engineering and Computer Science. Springer, 2002.

[93] W. Shockley, G. L. Pearson and J. R. Haynes. Hole injection in germanium – Quantitative studies and filamentary transistors. The Bell System Technical Journal, 28, 344, 1949.

[94] Stevenson, D.A, William Paul and Douglas M. Warschauer, Eds. McGraw-Hill. Solids Under Pressure. Science, 141(3582), 711, 1963.

[95] Rindner, W. and E. Pittelli. Effects of Stress-Induced Band-Gap Widening and Defects in GaAs Junctions. Journal of Applied Physics, 37, 4437, 1966.

[96] Pollak, F.H., M. Cardona, and K.L. Shaklee. Piezoelectroreflectance in GaAs. Physical Review Letters, 16, 942, 1966.

[97] F. H. Pollak and M. Cardona. Piezo-Electroreflectance in Ge, GaAs, and Si. Physical Review, 172, 816, 1968.

[98] M. Chandrasekhar and F. H. Pollak. Effects of uniaxial stress on the electroreflectance spectrum of Ge and GaAs. Physical Review B, 15, 2127, 1977.

[99] D. M. Moss, A. V. Akimov, R. P. Campion, and A. J. Kent. Ultrafast Strain-Induced Electronic Transport in a GaAs p-n Junction Diode. Chinese Journal of Physics, 49, 499, 2011.

[100] E. Riis M. Wilkinson G.L Oppo, S. M. Barnett, editor. Quantum Dynamics of Simple Systems. Institute of Physics publishing, 1997.

[101] Universities UK (formerly Committee of Vice Chancellors and Principals), 1992. http://optics.eee.nott.ac.uk/optics/safety/documents/

[102] S. L. Shapiro. Ultrashort light Pulses: Picosecond techniques and applications. Springer, New York, second edition, 1986.

[103] I. Vurgaftman and J. R. Meyer. Band parameters for III–V compound semiconductors and their alloys. Journal of Applied Physics, 89, 5815, 2001.

[104] Dmitriev, A.G., Temperature-Dependence of The Width of The GaAs Band-gap. Semiconductors, 29, 227, 1995.

[105] B.A. Auld, Acoustic Fields and Waves in Solids. Wiley, New York, Vol. 1, 191, 1973.

[106] B. A. Glavin, High-Frequency Acoustic Wave Detection in Schottky Diodes. Theory Consideration, 2016. arXiv:1607.04922.

[107] Data in Science and Technology; Semiconductors, Group IV Elements and III V Compounds, edited by O. Madelung, Springer, Berlin, page no. 105, 1991.

[108] J. V. Jäger, A. V. Scherbakov, T. L. Linnik, D. R. Yakovlev, M. Wang, P. Wadley, V. Holy, S. A. Cavill, A. V. Akimov, A. W. Rushforth, and M. Bayer, Picosecond inverse magnetostriction in galfenol thin films. Applied Physics Letters, 103, 032409, 2013.

[109] V.F. Gantmakher Y.B. Levinson. Carrier Scattering in Metals and Semiconductors. Elsevier, Volume 19, 1987.

[110] L. D. Landau and E. M. Lifshitz. Theory of Elasticity. Pergamon, 1986.

[111] K. Lee, M. S. Shur, T. J. Drummond, and H. Morkoq. Low field mobility of 2-d electron gas in modulation doped $Al_xGa_{1-x}As$/GaAs layers. Journal of Applied Physics, 54, 6432, 1983.

[112] P. J. van Hall. Ultrafast processes in Ag and Au: A Monte Carlo study. Physical Review B, 63, 104301, 2001.

[113] S. L. Heywood, B. A. Glavin, R. P. Beardsley, A. V. Akimov, M. W. Carr, J. Norman, P. C. Norton, B. Prime, N. Priestley, and A. J. Kent. Heterodyne mixing of millimetre electromagnetic waves and sub-THz sound in a semiconductor device. Scientific Reports, 6, 30396, 2016.

[114] B. Taylor, H. J. Maris, and C. Elbaum. Phonon focusing in solids. Physical Review Letters, 23, 416, 1969.

[115] S. Schmitt-Rink, D. S. Chemla, and D. A. B. Miller. Linear and nonlinear optical Properties of Semicondctor quantum wells. Advances in Physics, 38, 89, 1989.

[116] D. Srikanthreddy, B. A. Glavin, C. L. Poyser, M. Henini, D. Lehmann, Cz. Jasiukiewicz, A. V. Akimov, and A. J. Kent. Piezoelectric response to coherent longitudinal and transverse acoustic phonons in a semiconductor Schottky diode. Physical Review Applied, 7, 024014, 2017.

[117] A. J. Kent, R. E. Strickland, K. R. Strickland, A. J. Cross, P. Hawker and M. Henini. Heat-pulse study of the phonon emission by hot two-dimensional holes in a gallium arsenide heterojunction. Semiconductor Science and Technology, 12, 849, 1997.

[118] Wiley J. D, R. K. Willardson and A. C. Beer. Transport Phenomena (Semiconductors and Semimetals, vol 10, NewYork: Academic, 1975.

[119] M. Wassermeier, J. Sudijono, M. D. Johnson, K. T. Leung, B. G. Orr, L. Däweritz, and K. Ploog. Reconstruction of the GaAs (311) *A* surface. Physical Review B, 51, 14721, 1995.

[120] A. C. Churchill, G. H. Kim, M. Y. Simmons, D. A. Ritchie, and G. A. C. Jones. Electron focusing in two-dimensional electron gases grown on (311) *B* GaAs substrates. Physical Review B, 50, 17636, 1994.

[121] J. Spector, H. L. Stormer, K.W. Baldwin, L.N. Pfeiffer and K. W. West. Ballistic electron transport beyond 100 microm IN 2D electron systems. Surface Science, 228, 283, 1989.

[122] J. J. Heremans, M. B. Santos, K. Hirakawa, and M. Shayegan. Transverse magnetic focusing and the dispersion of GaAs 2D holes at (311) A heterojunctions. Surface Science, 305, 348, 1994.

[123] A. C. Churchill, G. H. Kim, A. Kurobe, M. Y. Simmons, D. A. Ritchie, M. Pepper, and G. A. C. Jones. Anisotropic magnetotransport in two-dimensional electron gases on (311) B GaAs substrates. Journal of Physics: Condensed Matter, 6, 6131, 1994.

[124] A. G. Davies, J. E. F. Frost, D. A. Ritchie, D. C. Peacock, R. Newbury, E. H. Linfield, M. Pepper, and G. A. C. Jones. The growth and physics of high mobility two-dimensional hole gases. Journal of Crystal Growth, 111, 318, 1991.

[125] J. J. Heremans, M. B. Santos, and M. Shayegan. Observation of magnetic focusing in two-dimensional hole systems. Applied Physics Letters, 61, 1652, 1992.